KEK Proceedings 2008-7
Octorber 2008
R

Proceedings of the Fifteenth EGS Users' Meeting in Japan

August 6 - 8, 2008.

KEK, Tsukuba, Japan

Edited by

Y. Namito, H. Hirayama and S. Ban

High Energy Accelerator Research Organization

High Energy Accelerator Research Organization (KEK), 2008

KEK Reports are available from:

High Energy Accelerator Research Organization (KEK)
1-1 Oho, Tsukuba-shi
Ibaraki-ken, 305-0801
JAPAN

Phone: +81-29-864-5137
Fax: +81-29-864-4604
E-mail: irdpub@mail.kek.jp
Internet: http://www.kek.jp

FOREWARD

The Fifteenth EGS Users' Meeting in Japan was held at High Energy Accelerator Research Organization (KEK) from August 6 to 8. The meeting has been hosted by the Radiation Science Center. More than 100 participants attended the meeting.

The meeting was divided into two parts. Short course on EGS was held at the first half of the workshop using EGS5 code. In the later half, 19 talks related EGS were presented. The talk covered the wide fields, like the medical application and the calculation of various detector responses *etc.* These talks were very useful to exchange the information between the researchers in the different fields.

Finally, we would like to express our great appreciation to all authors who have prepared manuscript quickly for the publication of this proceedings.

Hideo Hirayama
Yoshihito Namito
Syuichi Ban
Radiation Science Center
KEK, High Energy Accelerator Research Organization

CONTENTS

ANALYTICAL PROPERTIES OF THE MOLIÈRE SIMULTANEOUS DISTRIBUTION BETWEEN THE DEFLECTION ANGLE AND THE LATERAL DISPLACEMENT

T. Nakatsuka and K. Okei[†]
Okayama Shoka University, Okayama 700-8601, Japan
[†]*Dept. of Information Sciences, Kawasaki Medical School, Kurashiki 701-0192, Japan*

Abstract

Analytical properties of the Molière simultaneous distribution between the deflection angle θ_y and the lateral displacement y are investigated. The distribution is determined by the same two parameters, the expansion parameter B and the scale angle $\theta_{\rm M}$, as derived for the Molière angular distribution, and expressed by power series of B^{-1} with coefficients of universal functions derived below. The simultaneous distributions at central regions, $\theta_y^2 + (y/t)^2 \ll \theta_{\rm M}^2$, are found to be expressed by the Fermi simultaneous distribution with the scale angle of $\theta_{\rm M}$ irrespective of B, and the distributions at peripheral regions, $\theta_y^2 + (y/t)^2 \gg \theta_{\rm M}^2$, are found to approach to the single-scattering or the double-scattering distributions.

1 Introduction

We proposed the Molière simultaneous distribution between the deflection angle and the lateral displacement in the preceding report [1]. The diffusion equation for the simultaneous distribution was solved analytically in the Fourier frequency space by applying the differential formulation of the Molière theory [2], and the probability density for the distribution was derived accurately by numerical methods [1]. We have continued analytical investigations on the problem and found an important mathematical property of the simultaneous distribution common to the Molière angular distribution. The central and the peripheral features of the simultaneous distribution are also investigated.

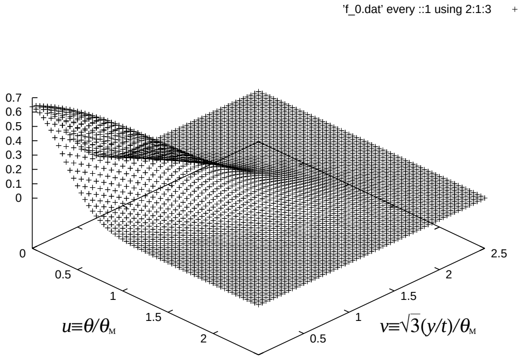

Figure 1: $f^{(0)}(u,v)$ in linear scale.

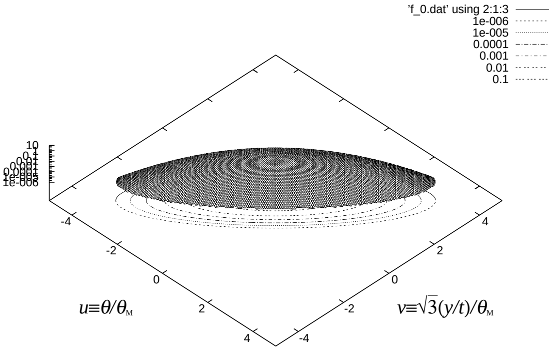

Figure 2: $f^{(0)}(u,v)$ in log. scale ($\geq 10^{-6}$).

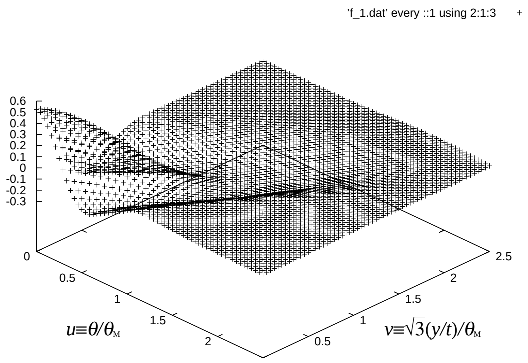

Figure 3: $f^{(1)}(u,v)$ in linear scale.

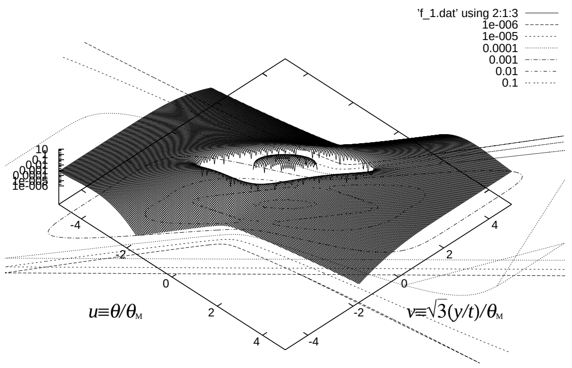

Figure 4: $f^{(1)}(u,v)$ in log. scale ($\geq 10^{-6}$).

2 Molière simultaneous distribution derived by the differential formulation of the theory

We derive the Molière simultaneous distribution $f(\theta_y, y)d\theta_y dy$ between the projected components of deflection angle and the lateral displacement, θ_y and y, under the fixed energy condition. The diffusion equation for the Molière simultaneous distribution was described under the differential formulation of Molière theory [2] as

$$\frac{\partial}{\partial t}\tilde{f}(\zeta,\eta) = \eta\frac{\partial}{\partial\eta}\tilde{f} - \frac{K^2\zeta^2}{4E^2}\tilde{f}\left\{1 - \frac{1}{\Omega}\ln\frac{K^2\zeta^2}{4E^2}\right\}, \tag{1}$$

where $\tilde{f}(\zeta,\eta)$ denotes the double Fourier transforms of the simultaneous distribution, satisfying

$$f(\theta,y)d\theta dy = \frac{d\theta dy}{2\pi}\iint e^{-\theta\zeta - y\eta}\tilde{f}(\zeta,\eta)d\zeta d\eta. \tag{2}$$

The equation was solved as [1]

$$\ln 2\pi\tilde{f} = \frac{1}{\Omega}\frac{\theta_{\rm G}^2}{12\eta t}\left\{(\zeta+\eta t)^3\ln\frac{\theta_{\rm G}^2(\zeta+\eta t)^2}{4te^{2/3+\Omega}} - \zeta^3\ln\frac{\theta_{\rm G}^2\zeta^2}{4te^{2/3+\Omega}}\right\}, \tag{3}$$

where $\theta_{\rm G}^2$ is the gaussian mean square angle introduced by Fermi [3]:

$$\theta_{\rm G}^2 = K^2t/E^2. \tag{4}$$

This solution was identical with Molière's 1955 result [4] of his Eq. (3.3'), where we should remind his ξ_1, ξ_2, $\chi_c'^2 l_0$, and $\gamma^2\chi_a^2/e$ are identical with our ζ, ηt, $\chi_c^2 = \theta_{\rm G}^2/\Omega$, and $(K^2/E^2)e^{-\Omega}$, respectively.

The solution with ζ and ηt was expressed with three parameters, Ω, $\theta_{\rm G}^2$, and t. We have found the explicit parameter t can be removed from the solution by introducing the well known parameters B and $\theta_{\rm M}^2$, derived from [2]

$$B - \ln B = \Omega - \ln\Omega + \ln t, \tag{5}$$

$$\theta_{\rm M} = \theta_{\rm G}\sqrt{B/\Omega}. \tag{6}$$

B and $\theta_{\rm M}$ are called the expansion parameter and the scale angle and have determined the Molière angular distribution [5, 6, 7]. If we introduce the composite variables

$$\mu \equiv \theta_{\rm M}\zeta, \quad \text{and} \quad \nu \equiv \theta_{\rm M}\eta t/\sqrt{3}, \tag{7}$$

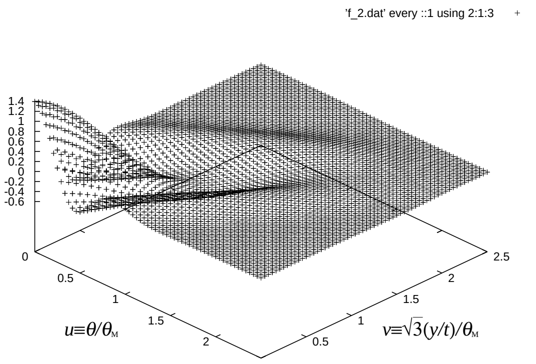

Figure 5: $f^{(2)}(u,v)$ in linear scale.

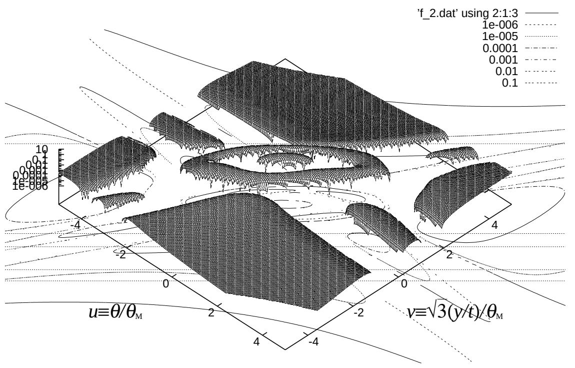

Figure 6: $f^{(2)}(u,v)$ in log. scale ($\geq 10^{-6}$).

then the solution (3) becomes

$$\ln 2\pi\tilde{f} = \frac{1}{B}\frac{\theta_{\mathrm{M}}^2}{12\eta t}\left\{(\zeta+\eta t)^3 \ln\frac{\theta_{\mathrm{M}}^2(\zeta+\eta t)^2}{4e^{2/3+B}} - \zeta^3 \ln\frac{\theta_{\mathrm{M}}^2\zeta^2}{4e^{2/3+B}}\right\} \tag{8}$$

or

$$\tilde{f} = \frac{1}{2\pi}\exp\left(-\frac{\mu^2+\sqrt{3}\mu\nu+\nu^2}{4} + \frac{B^{-1}}{12\sqrt{3}\nu}\left\{(\mu+\sqrt{3}\nu)^3\ln\frac{(\mu+\sqrt{3}\nu)^2}{4e^{2/3}} - \mu^3\ln\frac{\mu^2}{4e^{2/3}}\right\}\right), \tag{9}$$

and the solution with the variables scaled by θ_{M} can be expressed by single parameter B, which fact was not pointed out by Molière himself [4]. We can expand the solution by power series with B^{-1}:

$$\tilde{f} = \frac{1}{2\pi}e^{-\frac{\mu^2+\sqrt{3}\mu\nu+\nu^2}{4}}\sum_{k=0}^{\infty}\frac{1}{k!}\frac{B^{-k}}{(12\sqrt{3}\nu)^k}\left\{(\mu+\sqrt{3}\nu)^3\ln\frac{(\mu+\sqrt{3}\nu)^2}{4e^{2/3}} - \mu^3\ln\frac{\mu^2}{4e^{2/3}}\right\}^k. \tag{10}$$

So we find the Molière simultaneous distribution is expressed as

$$f(u,v) = f^{(0)}(u,v) + B^{-1}f^{(1)}(u,v) + B^{-2}f^{(2)}(u,v) + \cdots, \tag{11}$$

similarly as expressed for the Molière angular distribution, where we have introduced scale variables u and v against the deflection angle θ_y and the cord angle y/t,

$$u \equiv \theta/\theta_{\mathrm{M}}, \quad \text{and} \quad v \equiv (y/t)/(\theta_{\mathrm{M}}/\sqrt{3}), \tag{12}$$

and expressed the universal functions $f^{(k)}(u,v)$, as

$$f^{(k)}(u,v) = \frac{1}{4\pi^2 k!}\int\frac{e^{-u\mu-v\nu}}{(12\sqrt{3}\nu)^k}\left\{(\mu+\sqrt{3}\nu)^3\ln\frac{(\mu+\sqrt{3}\nu)^2}{4e^{2/3}} - \mu^3\ln\frac{\mu^2}{4e^{2/3}}\right\}^k e^{-\frac{\mu^2+\sqrt{3}\mu\nu+\nu^2}{4}}d\mu d\nu. \tag{13}$$

3 Derivation of the universal functions for series expansion of the Molière simultaneous distribution

We practically derive the universal functions (13) for series expansion of the Molière simultaneous distribution. Especially for the first three functions, we have

$$f^{(0)}(u,v) \;=\; \frac{1}{4\pi^2}\iint e^{-u\mu-v\nu}e^{-\frac{\mu^2+\sqrt{3}\mu\nu+\nu^2}{4}}d\mu d\nu = \frac{2}{\pi}e^{-4(u^2-\sqrt{3}uv+v^2)}, \tag{14}$$

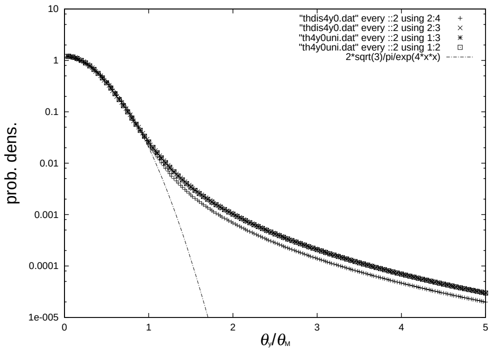

Figure 7: The simultaneous distribution on $y = 0$ derived by series expansion and numerical integration. We find no differences between the both for $B = 10$ (upper) and $B = 15$ (lower). The central region, $\theta_y \ll \theta_{\mathrm{M}}$, is well represented by the Fermi distribution.

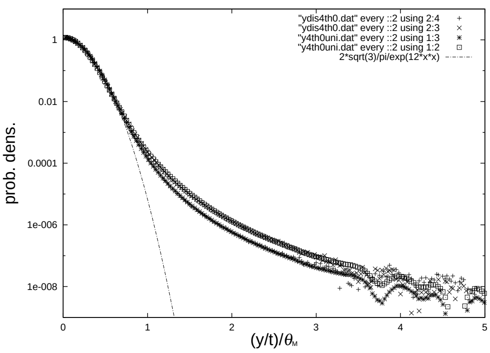

Figure 8: The simultaneous distribution on $\theta_y = 0$ derived by series expansion and numerical integration. We find no differences between the both for $B = 10$ (upper) and $B = 15$ (lower). The central region, $y/t \ll \theta_{\mathrm{M}}$, is well represented by the Fermi distribution.

$$\begin{aligned} f^{(1)}(u,v) &= \frac{1}{4\pi^2}\iint e^{-u\mu - v\nu} e^{-\frac{\mu^2+\sqrt{3}\mu\nu+\nu^2}{4}} \\ &\quad \times \left\{ \frac{\mu^2+\sqrt{3}\mu\nu+\nu^2}{4} \ln\frac{\mu^2}{4e^{2/3}} + \frac{(\mu+\sqrt{3}\nu)^3}{12\sqrt{3}\nu} \ln\left(1+\frac{\sqrt{3}\nu}{\mu}\right)^2 \right\} d\mu d\nu, \quad (15) \\ f^{(2)}(u,v) &= \frac{1}{4\pi^2}\iint \frac{e^{-u\mu - v\nu}}{2} e^{-\frac{\mu^2+\sqrt{3}\mu\nu+\nu^2}{4}} \\ &\quad \times \left\{ \frac{\mu^2+\sqrt{3}\mu\nu+\nu^2}{4} \ln\frac{\mu^2}{4e^{2/3}} + \frac{(\mu+\sqrt{3}\nu)^3}{12\sqrt{3}\nu} \ln\left(1+\frac{\sqrt{3}\nu}{\mu}\right)^2 \right\}^2 d\mu d\nu, \quad (16) \end{aligned}$$

and at $|\frac{\sqrt{3}\nu}{\mu}| \leq 0.01$ we evaluate

$$\frac{(\mu+\sqrt{3}\nu)^3}{12\sqrt{3}\nu} \ln\left(1+\frac{\sqrt{3}\nu}{\mu}\right)^2 \simeq \frac{(\mu+\sqrt{3}\nu)^3}{6\mu}\left(1-\frac{\sqrt{3}\nu}{2\mu}+\frac{\nu^2}{\mu^2}-\cdots\right). \quad (17)$$

$f^{(0)}(u,v)$ derived analytically from (14) is indicated in Figs. 1 and 2, and $f^{(1)}(u,v)$ and $f^{(2)}(u,v)$ derived numerically from (15) and (16) are indicated in Figs. 3-6.

The probability densities for simultaneous distribution derived from the series expansion (11) up to B^{-2} are compared with those derived numerically from (9) in Fig. 7 and 8. The both agree very well. Also we find the probability density at central regions ($\theta_y^2 + y^2/t^2 \ll \theta_{\mathrm{M}}^2$) is well represented by the first term $f^{(0)}$ or Fermi distribution [3] irrespective of B.

4 Contour pattern of Molière simultaneous distribution

Characteristics of the Molière simultaneous distribution are well understood in contour maps [8] as indicated in Fig. 9.

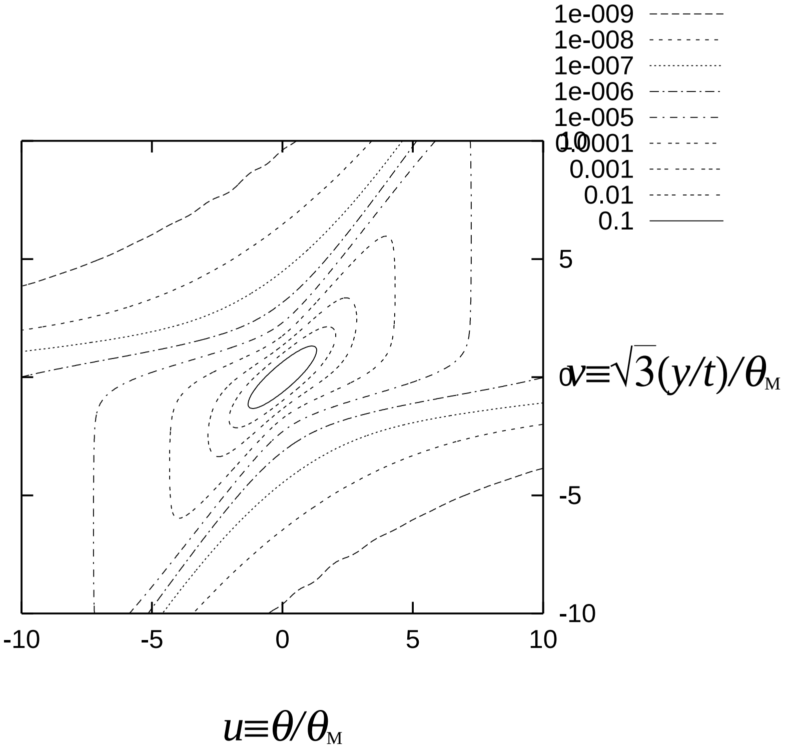

Figure 9: A contour map of Molière simultaneous distribution.

The probability density at central regions, $\theta_y^2 + y^2/t^2 \ll \theta_{\mathrm{M}}^2$, shows an elliptic pattern, which is well represented by the first term (14) of Molière series expansion (11) or the Fermi simultaneous distribution with the scale angle of θ_{M} [3].

The probability density in peripheral regions, $\theta_y^2 + y^2/t^2 \gg \theta_{\mathrm{M}}^2$, with $u(v - \sqrt{3}u) < 0$ depends only on θ_y and does not depend on y/t. We can interpret the simultaneous distribution by the Rutherford single scattering as illustrated in Fig. 10. The single scattering formula is expressed as [2]

$$\frac{N}{A}\sigma(\theta)2\pi\theta d\theta dx = \frac{1}{\pi\Omega}\frac{K^2}{E^2}\theta^{-4}2\pi\theta d\theta dt, \tag{18}$$

so the probability density determined by the single scattering, $f_1(u, v)dudv$, is evaluated as

$$\begin{aligned} f_1(u,v)dudv &= \frac{1}{2\Omega}\frac{K^2}{E^2}d\theta dy \int_0^t \theta^{-3}\delta(y-(t-t')\theta)dt' \\ &= \frac{1}{2\Omega}\frac{K^2}{E^2}\theta^{-4}d\theta dy \\ &= \frac{1}{2B}\theta_{\mathrm{M}}^2\theta^{-4}d\theta d(y/t) \\ &= \frac{1}{2\sqrt{3}B}u^{-4}dudv. \end{aligned} \tag{19}$$

On the contrary in the peripheral regions, $\theta_y^2 + y^2/t^2 \gg \theta_{\mathrm{M}}^2$, with $u(v - \sqrt{3}u) > 0$, we can interpret the simultaneous distribution by the Rutherford double scattering as illustrated in Fig. 10. The

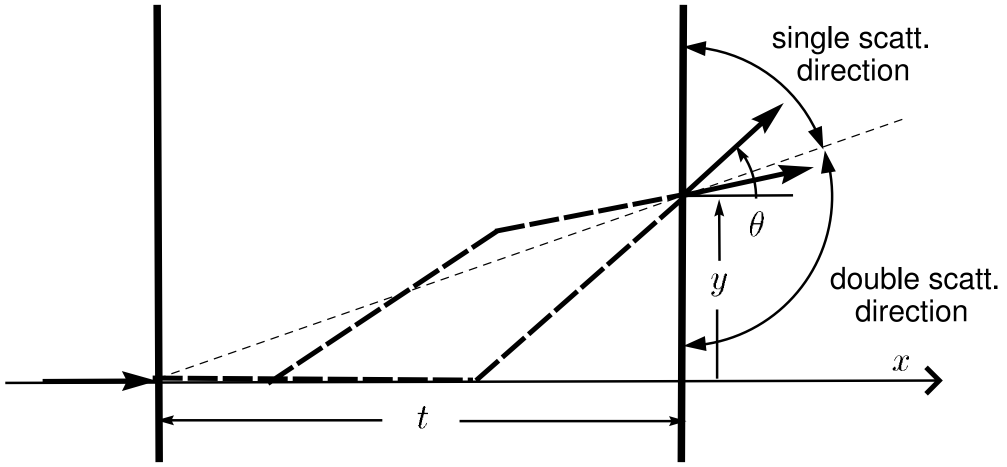

Figure 10: The directions for single and double scatterings in peripheral regions.

probability density determined by the double scattering, $f_2(u,v)dudv$, is evaluated as

$$\begin{aligned} f_2(u,v)dudv &= (\frac{1}{2\Omega}\frac{K^2}{E^2})^2 d\theta dy \int_0^t dt' \int_{\theta+(y-\theta t)/t'}^{\infty} \theta'^{-4}(\theta'-\theta)^{-3}d\theta' \\ &= \frac{dudv}{4\sqrt{3}B^2}\int_0^1 ds \int_{u+(v/\sqrt{3}-u)/s}^{\infty} \frac{1}{u'^4}\frac{1}{(u'-u)^3}du'. \end{aligned} \tag{20}$$

A contour map derived from $f_1(u,v)$ of (19) and $f_2(u,v)$ of (20) is evaluated by a formula manipulating tool, *mathematica* [9], and is indicated in Fig. 11. We find good agreement between the Figs. 9 and 11 in peripheral regions.

5 Conclusions and discussions

Analytical properties of the Molière simultaneous distribution between the projected components of deflection angle and the lateral displacement are investigated under the fixed energy condition. The distribution is determined by the same two parameters, the expansion parameter B and the scale angle θ_{M}, as derived to determine the Molière angular distribution. The simultaneous distribution can also be expressed in series expansion with B^{-1} as expressed for the Molière angular distribution. The universal functions $f^{(k)}(u,v)$ as the coefficients of B^{-k} for the series expansion are derived analytically for $k=0$ and numerically for $k=1,2$. The distribution at central regions, $\theta_y^2 + y^2/t^2 \ll \theta_{\mathrm{M}}^2$, is well represented by the Fermi simultaneous distribution with the scale angle of θ_{M}, irrespective of B. The distributions for peripheral regions, $\theta_y^2 + y^2/t^2 \gg \theta_{\mathrm{M}}^2$, are well represented asymptotically by the single scattering in the area of $u(v-\sqrt{3}u)<0$ and by the double scattering in the area of $u(v-\sqrt{3}u)>0$.

The present results will be valuable for benchmark tests of simulation codes to trace passage of fast charged particles [10, 11, 12, 13, 14, 15], as well as more accurate designs and analyses of experiments concerning fast charged particles.

References

[1] T. Nakatsuka, K. Okei, and N. Takahashi, *"Proceedings of the Thirteenth EGS4 User's Meeting in Japan,"* KEK Proceedings 2006-4, 18(2006).

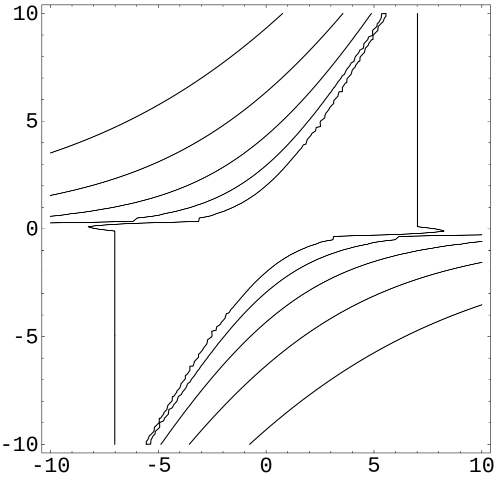

Figure 11: A contour map from $f_1(u,v)$ and $f_2(u,v)$ derived using *mathematica*.

[2] T. Nakatsuka and J. Nishimura, Phys. Rev. **E78**, 021136(2008).

[3] B. Rossi and K. Greisen, Rev. Mod. Phys. **27**, 240(1941).

[4] G. Molière, Z. Naturforsch. **10a**, 177(1955).

[5] G. Molière, Z. Naturforsch. **2a**, 133(1947).

[6] G. Molière, Z. Naturforsch. **3a**, 78(1948).

[7] H.A. Bethe, Phys. Rev. **89**, 1256(1953).

[8] K. Okei and T. Nakatsuka, *"Proceedings of the Fourteenth EGS User's Meeting in Japan,"* KEK Proceedings 2007-5, 6(2007).

[9] S. Wolfram, *The Mathematica Book,* 4th ed. (Cambridge University Press, Cambridge, UK, 1999).

[10] T.W. Jenkins, W.R. Nelson, and A. Rindi (eds.), *Monte Carlo Transport of Electrons and Photons* (Plenum, New York, 1988).

[11] W.R. Nelson, H. Hirayama, and D.W.O. Rogers, "The EGS4 Code System," SLAC-265, Stanford Linear Accelerator Center (Dec. 1985).

[12] D. Heck, J. Knapp, J.N. Capdevielle, G. Shatz, and T. Thouw, Forschungszentrum Karlsruhe Report FZKA6019(1998).

[13] S.M. Selzer, in Ref. [10], pp. 153-182.

[14] J.A. Halbleib, R.P. Kensek, T.A. Mehlborn, G.D. Valdez, S.M. Selzer, and M.J. Berger, ITS Version 3.0: The Integrated TIGER Series of Coupled Electron/Photon Monte Carlo Transport Codes, Sandia report SAND91-1634, 1992.

[15] GEANT4 Collaboration, Nucl. Instr. Meth. **A506**, 250(2003).

Charged particle transport calculation with GPU

K. Okei[†] **and T. Nakatsuka**[‡]
[†]*Kawasaki Medical School, Kurashiki 701-0192, Japan*
[‡]*Okayama Shoka University, Okayama 700-8601, Japan*

Abstract

A GPU (graphics processing unit) was examined to see if it accelerates charged particle transport simulations. Having performed Monte Carlo simulations of Coulomb scattering, we found that a GPU (NVIDIA GeForce 8800 GTX) outperforms a general purpose CPU (Intel Core2Duo E6700) by more than an order of magnitude.

1 Introduction

A GPU (graphics processing unit) is a special-purpose processor for graphics and was originally used for tasks such as accelerating 3D rendering. Since modern GPUs are programmable and have tremendous computational power and memory bandwidth [1], they are used not only for graphics, but also for a wide variety of applications, e.g., astrophysics, fluid dynamics, molecular dynamics, seismic data processing, computational finance and more [2, 3, 4].

When addressing the transport of charged particles in matter, there is a huge number of interactions to be considered, and it would be beneficial if the transport calculations could be accelerated by exploiting the programmable GPU.

To examine the effectiveness of the GPU computing for the charged particle transport, Monte Carlo simulations of Coulomb scattering are performed on a GPU (NVIDIA GeForce 8800 GTX) using CUDA [1] and the execution time is compared with the CPU (Intel Core2Duo E6700) execution time. As an example application, a new method to generate large deflection angles due to multiple Coulomb scattering is developed and validated by comparison of the angular distributions obtained from the new method and from exact single scattering simulations with the GPU.

2 Coulomb scattering

Charged particles passing through matter suffer deflections due to Coulomb scattering, and the process is the main source of the angular and lateral spreads. An approximated form of the single scattering differential cross section including the screening effect for a spin $\frac{1}{2}$ incident particle as a function of angle θ can be written as

$$f(\theta)\,\mathrm{d}\theta \propto \left(1-\beta^2\sin^2\frac{\theta}{2}\right)\frac{\sin\theta}{\left(\sin^2\frac{\theta}{2}+\frac{\chi_\mathrm{a}^2}{4}\right)^2}\,\mathrm{d}\theta, \tag{1}$$

and for small θ, it reduces to the small-angle screened Rutherford cross section,

$$f(\theta)\,\mathrm{d}\theta \propto \frac{\sin\theta}{(\theta^2+\chi_\mathrm{a}^2)^2}\,\mathrm{d}\theta, \tag{2}$$

where β is the particle velocity relative to the speed of light and χ_a is the screening angle (see, for example, refs. [5, 6, 7, 8]). Making the substitution $\mu=\cos\theta$, we obtain

$$f(\mu)\,\mathrm{d}\mu \propto \left(1-\frac{1-\mu}{2}\beta^2\right)\frac{1}{\left(1-\mu+\frac{\chi_\mathrm{a}^2}{2}\right)^2}\,\mathrm{d}\mu. \tag{3}$$

Below we consider, for simplicity, highly relativistic cases ($\beta = 1$) only and proportionality (3) becomes

$$f(\mu)\,\mathrm{d}\mu \propto (1+\mu)\,\frac{1}{\left(1-\mu+\frac{\chi_\mathrm{a}^2}{2}\right)^2}\,\mathrm{d}\mu. \tag{4}$$

(Note that we omit trivial constants in above expressions.)

To generate random variates from $f(\mu)$, first we sample the Rutherford part, $1/(1-\mu+\chi_\mathrm{a}^2/2)$, using the inversion method and then apply the rejection method to realize the spin effect factor. Figure 1 shows the pseudo code of an implementation of random number generation from $f(\mu)$.

```
do{
  r=getURand();
  $\mu = 1 + \frac{\chi_\mathrm{a}^2}{2} - \frac{\frac{\chi_\mathrm{a}^2}{2}\left(2+\frac{\chi_\mathrm{a}^2}{2}\right)}{2\mathtt{r}+\frac{\chi_\mathrm{a}^2}{2}}$;
  r=getURand();
}while($1-2\mathtt{r} > \mu$);
```

Figure 1: An implementation of random number generation from $f(\mu)$. The function `getURand()` is supposed to return a uniform random variate between 0 and 1.

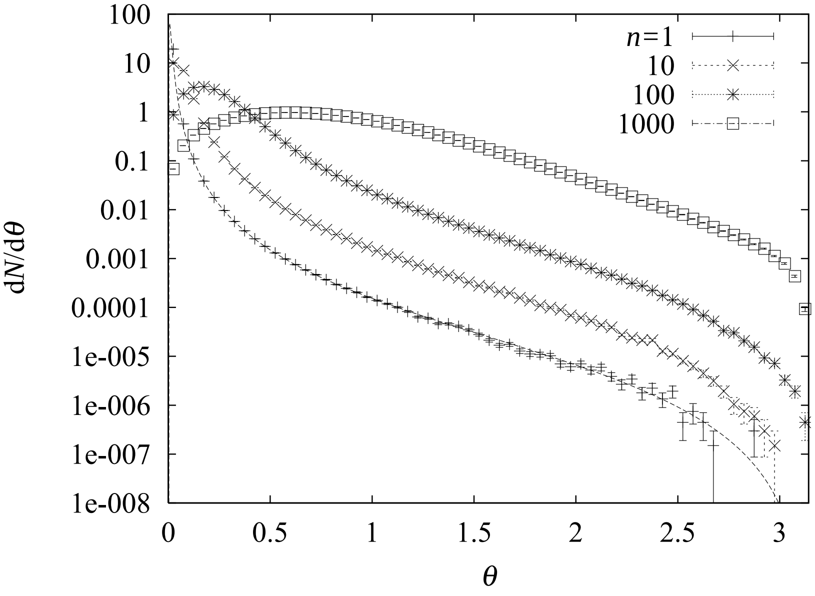

Figure 2: The distribution of the polar angle after n Coulomb scattering processes for $\chi_\mathrm{a} = 0.01$.

3 Monte Carlo simulation

To evaluate the processing ability of GPU, we have written a simple Monte Carlo code using CUDA [1]. The code simulates changes of the direction of a charged particle's motion due to n times of Coulomb scattering. The scattering polar angle $\Delta\theta$ is sampled according to $f(\mu)$ and the azimuthal angle $\Delta\phi$ is drawn from the uniform distribution of $[0,2\pi)$. The change of the direction is calculated as

$$\begin{aligned} \sin\theta_i\cos\phi_i &= \cos\Delta\theta\sin\theta_{i-1}\cos\phi_{i-1} + \sin\Delta\theta(\cos\Delta\phi\cos\theta_{i-1}\cos\phi_{i-1} - \sin\Delta\phi\sin\phi_{i-1}) \\ \sin\theta_i\sin\phi_i &= \cos\Delta\theta\sin\theta_{i-1}\sin\phi_{i-1} + \sin\Delta\theta(\cos\Delta\phi\cos\theta_{i-1}\sin\phi_{i-1} + \sin\Delta\phi\cos\phi_{i-1}) \\ \cos\theta_i &= \cos\Delta\theta\cos\theta_{i-1} - \sin\Delta\theta\cos\Delta\phi\sin\theta_{i-1} \end{aligned}$$

where θ_i and ϕ_i are the polar and azimuthal angles after the i-th scattering respectively. To generate uniform pseudo random numbers, "taus88" described in L'Ecuyer [9] is used. Since the simulation is processed in parallel on the GPU, the seed values are initialized by random numbers for each thread.

Figure 2 shows the distribution of the polar angle relative to the initial direction after Coulomb scattering processes for $\chi_{\rm a} = 0.01$, $n = 1, 10, 100$ and 1000. The execution time of the Monte Carlo simulation, for example, for $n = 1000$ using a GPU (NVIDIA GeForce 8800 GTX) and a CPU (Intel Core2Duo E6700) are shown in table 1. It can be seen that the GPU simulation is about 52 times faster than the CPU version. That is, a one year task for the CPU can be computed in a week by using the GPU.

Table 1: Comparison of the execution time for $n = 1000$.

processor	number of events	execution time	time per event
GPU (GeForce 8800 GTX)	$2^{24} = 16777216$	94.3 sec.	5.62×10^{-3} sec.
CPU (Core2Duo E6700 2.66GHz)	$2^{18} = 262144$	76.8 sec.	2.93×10^{-1} sec.

4 Large angle multiple scattering

We have developed a method for simulating multiple Coulomb scattering [10, 11, 12, 13]. Though the method can take a constant energy loss per unit length into account and generate the joint distribution of the deflection angle and the lateral displacement, it is only applicable for small angle multiple scattering.

In this section, we present a new method to generate large deflection angles due to multiple Coulomb scattering. The single scattering differential cross section is assumed to have the form $f(\mu)$. Angular distributions obtained using the new method are validated by comparison with the distributions obtained by GPU direct simulations, since GPUs can compute Coulomb scattering processes so fast as described in the previous section.

Our sampling method is constructed by dividing the differential scattering cross section into the moderate scattering and the large angle scattering [10, 11]. Owing to the central limit theorem, the sum of many small angle deflections less than the dividing angle $\theta_{\rm s}$ can be simulated by a Gaussian random number. On the other hand, the large scattering is rare and directly sampled from the scattering cross section. However, when $\theta_{\rm s}$ is large, we must consider dispersion on a sphere,

$$f(\theta_{\rm s}) = \frac{1}{2}\sum_{n=0}^{\infty}(2n+1)P_n(\cos\theta_{\rm s}){\rm e}^{-\frac{1}{4}n(n+1)V}\sin\theta_{\rm s} \tag{5}$$

where V is the dispersion parameter and P_n is the Legendre polynomial of order n. This can be approximated by Gaussian (for small V),

$$f_{\mathrm{G}}(\theta_{\mathrm{s}}) = \frac{\theta_{\mathrm{s}}}{\sigma^2} \mathrm{e}^{-\frac{\theta_{\mathrm{s}}^2}{2\sigma^2}} \tag{6}$$

or the von Mises-Fisher distribution,

$$f_{\mathrm{vMF}}(\theta_{\mathrm{s}}) = \frac{\kappa}{2\sinh\kappa} \mathrm{e}^{\kappa\cos\theta_{\mathrm{s}}} \sin\theta_{\mathrm{s}} \tag{7}$$

by suitable adjustment of the parameters σ^2 and κ [14, 15]. The best fit values σ_{fit} and κ_{fit} were obtained numerically. Figures 3 and 4 show these values as functions of $\sigma_0 = \sqrt{V/2}$ respectively. With these parameters, we generate θ_{s} from f_{G} for $\sigma_0 \le 1.5$ and from f_{vMF} for $\sigma_0 > 1.5$. To sample random numbers from the von Mises-Fisher distribution, we use the method described in Wood [16].

The multiple scattering angular distributions generated using the new method are compared with those obtained by direct single scattering simulations with GPU in figure 5. We see fairly good agreement from relatively small angle scattering (top left) to the almost uniform distribution (bottom right).

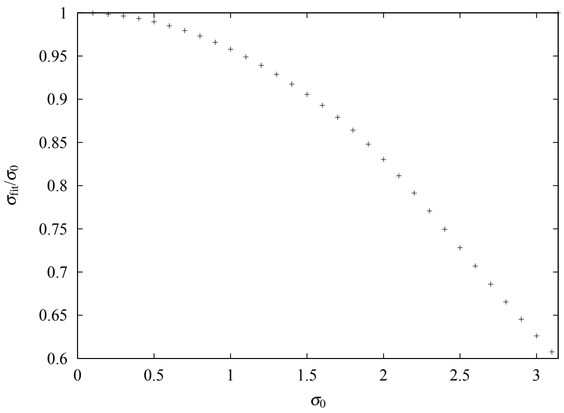

Figure 3: The best fit value σ_{fit}.

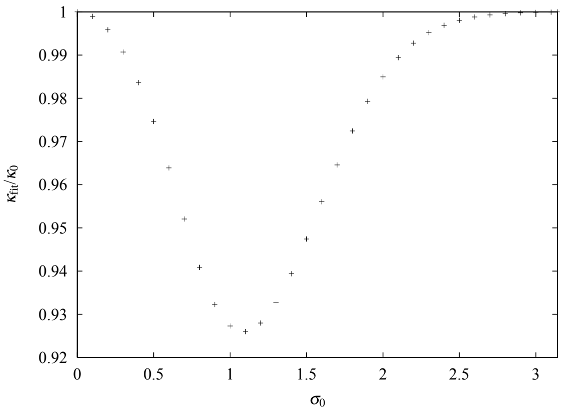

Figure 4: The best fit value κ_{fit} ($\kappa_0 = 1/\sigma_0^2$).

5 Conclusion

We have tested the effectiveness of the GPU computing for the charged particle transport. It was found that a GPU (NVIDIA GeForce 8800 GTX) accelerates Monte Carlo simulations of Coulomb scattering by about 50 times over a CPU Intel Core2Duo E6700). A new method for simulating large angle multiple scattering which includes the spin effect has been developed and validated by exploiting the processing power of GPU. Though the performance gain depends on a particular application and/or processor, GPUs seem promising for the charged particle transport computation.

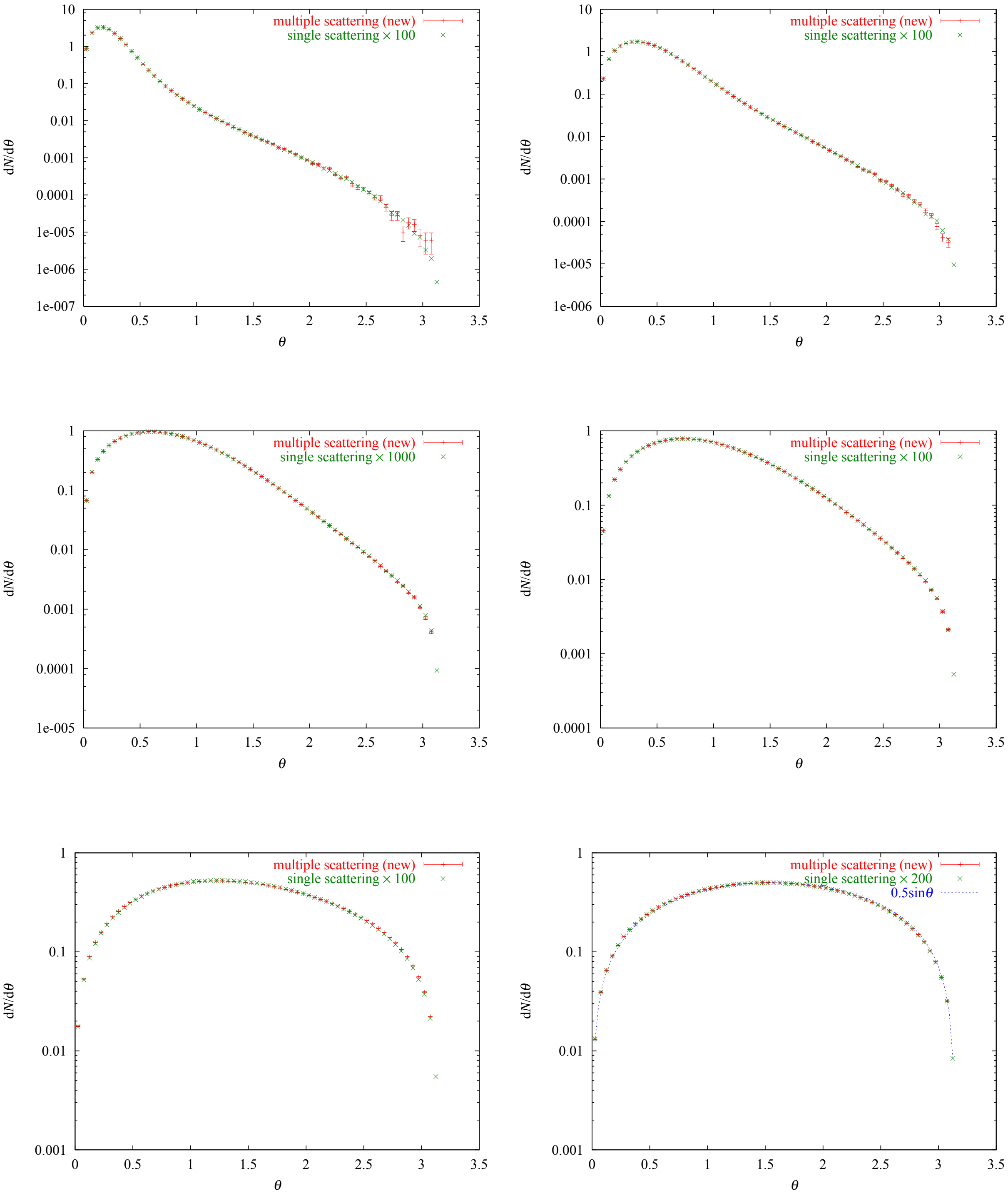

Figure 5: Comparison of multiple scattering angular distributions obtained by the new cross section dividing method and direct single scattering simulations with GPU (top left: $\chi_{\mathrm{a}} = 0.01, n = 100$, top right: $\chi_{\mathrm{a}} = 0.02, n = 100$, middle left: $\chi_{\mathrm{a}} = 0.01, n = 1000$, middle right: $\chi_{\mathrm{a}} = 0.05, n = 100$, bottom left: $\chi_{\mathrm{a}} = 0.1, n = 100$, bottom right: $\chi_{\mathrm{a}} = 0.1, n = 200$).

References

[1] NVIDIA CUDA Compute Unified Device Architecture Programming Guide ver. 2.0 (2008)

[2] `http://www.gpgpu.org/`

[3] `http://www.nvidia.com/object/cuda_home.html`

[4] H. Nguyen, ed.,*GPU Gems 3*, Addison-Wesley (2007)

[5] B. Rossi and K. Greisen, *Rev. Mod. Phys.* **13**, 240 (1941)

[6] G. Molière, *Z. Naturforsch.* **2a**, 133 (1947).

[7] G. Molière, *Z. Naturforsch.* **3a**, 78 (1948).

[8] H.A. Bethe, *Phys. Rev.* **89**, 1256 (1953).

[9] P. L'Ecuyer, *Mathematics of Computation* **65**, 203 (1996)

[10] K. Okei and T. Nakatsuka, *Proc. 11th EGS4 Users' Meeting in Japan*, KEK Proceedings 2003-15, 9 (2004).

[11] K. Okei and T. Nakatsuka, *Proc. 3rd International Workshop on EGS*, KEK Proceedings 2005-7, 57 (2005).

[12] K. Okei, N. Takahashi and T. Nakatsuka, *Proc. 13th EGS Users' Meeting in Japan*, KEK Proceedings 2006-4, 28 (2006).

[13] K. Okei and T. Nakatsuka, *Proc. 14th EGS Users' Meeting in Japan*, KEK Proceedings 2007-5, 26 (2007).

[14] R.A. Fisher, *Proc. Roy. Soc.* A **217**, 295 (1953)

[15] P.H. Roberts and H.D. Ursell, *Philos. Trans.* A **252**, 317 (1960)

[16] A.T.A. Wood, *Commun. Statist. –Simula* **23**, 157 (1994)

Comparison of Several Monte Carlo Codes with Electrion Backscattering Experiments

Y. Kirihara, Y. Namito†, H. Hirayama†, and H. Iwase†
The Graduate University for Advanced Studies, Oho1-1, Tsukuba, Ibaraki 305-0801, Japan
†*KEK High Energy Accelerator Research Organization, Oho1-1, Tsukuba, Ibaraki 305-0801, Japan*

Abstract

We have performed a comparison of an electron backscattering coefficient between experiments and calculations. Electron backscattering coefficients η were measured previously for a few keV to tens of MeV mono-energetic electrons on targets of Z=4 to 92 materials. We calculated the η using Monte Carlo codes as EGS5, EGSnrc, PENELOPE and ITS3.0, and compared with the experiments. Those codes uses Goudsmit-Sounderson scattering model for a multiple scattering, and considers spin relativistic effect. For Al, Cu and U target, EGS5, EGSnrc and PENELOPE calculations were agree within about 10%, and ITS3.0 calculation was lower than other calculations in whole. In addition, the η was calculated using EGS5 code with applying spin relativistic effect to GS model (Spin-GS) and Molière model (Spin-Molière) and ignored spin relativistic effect to Molière model (NoSpin-Molière). The η of those models and the experiments agreed within 25% for Cu target and 16% for U target, respectively. The η using the Spin-GS and the Spin-Molière were nearer the experiments than that using the NoSpin-Molière for several hundred keV to 20 MeV.

1 Introduction

A lot of experiments of electron backscattering have been performed so far. Electron backscattering coefficient η, which was a ratio of backscattering electron from target to incident electron, was measured for a few keV to tens of MeV mono-energetic electrons on targets of Z=4 to 92 materials in the experiments [1]. We calculated η using the codes as EGS5 [2], EGSnrc [3], PENELOPE [4] and ITS3.0 [5] on the same condition, and compared with the experiments. Those code uses Goudsmit-Sounderson scattering model (GS model) of the multiple scattering [6, 7] and spin relativistic effect are considered.

2 Calculation and comparison

2.1 Calculation condition

The η was calculated using the Monte Carlo codes as EGS5, EGSnrc, PENELOPE and ITS3.0 on the same condition. The cutoff energy of the codes was set to 1 keV. The energies of incident electron were set from 2 keV to 20 MeV. Target materials were Be, Al Cu and U, and those thicknesses were set Continuous-Slowing-Down-Approximation (CSDA) range. The backscattering electrons were counted in a whole of backward of the target. The number of incident electron was adjusted so that $\Delta\eta/\eta$ to be less than 2%. Here $\Delta\eta$ is the statistical error (one σ) of η.

2.2 Comparison between experiments and calculations

The experimental and calculated η of Be, Al, Cu and U target are shown in Fig. 1. The η decrease with increasing incident energy on all target. The calculations were decreased at 10 keV or less because of the cutoff energy as 1 keV. ITS3.0 calculation was lower than other calculations in whole. For Al, Cu and U target, EGS5, EGSnrc and PENELOPE calculations were agree within about

10%, and the calculations and the experiments were good agreement. In contrast, for Be target, the calculations and the experiments had the discrepancy.

3 Applying spin relativistic effect to Molière scattering

EGS5 code has two modes for electron transport. One is GS model of the multiple scattering and spin relativistic effect was considered (Spin-GS) and the other, Molière model [8] of the multiple scattering with ignoring spin relativistic effect (NoSpin-Molière). In previous section, we calculated η by the Spin-GS mode in EGS5 code.

To see effect of multiple scattering model and spin relativistic effect separately, we added another mode for EGS5 to calculate electron transport using Molière while considering spin relativistic effect (Spin-Molière). In this section, first, we describe how spin relativistic effect was applied to Molière multiple scattering for EGS5 code. Next, EGS5 calculations of the Spin-GS, the NoSpin-Molière and the Spin-Molière were performed.

3.1 Rutherford scattering and Mott scattering

The Rutherford scattering cross section of the electron single scattering is expressed by following formula:

$$\frac{d\sigma}{d\Omega} = Z^2 r_0^2 \frac{(1-\beta^2)}{\beta^4} \frac{1}{(1-\cos\theta)^2} \tag{1}$$

where Z was atomic number, r_0 was classical electron radius, β was the ratio of the initial electron velocity to the velocity of light, and θ was the angle between the scattered and the incident electron. Mott scattering cross section is a elastic scattering cross section of atom for electron while considering spin relativistic effect. A tabulation of the ratio of the Mott cross section to the Rutherford cross section for electrons and positrons was made by R. Idoeta and F. Legarda [9], and is shown in Fig. 2 at Be and U target. For the Be target, the large angle scattering decreased with increasing energy. For the U target, the ratio is changeful in the respective energy.

3.2 Rejection method

We employed a rejection method to include spin relativistic effect to the Molière model in EGS5 code. We added rejection routine for SUBROUTINE MSCAT (multiple scattering sampling routine in EGS5 code). A new routine, SUBROUTINE MRCAL, was added to EGS5 code to interpolate the ratio of the Mott cross section to the Rutherford cross section along energy and angle. Flow diagrams of the additional part of SUBROUTINE MSCAT and the new routine, SUBROUTINE MRCAL, were shown in Fig. 3 and Fig. 4, respectively.

3.3 Comparison

The electron backscattering coefficients η at Be, Al, Cu and U target were calculated using EGS5 code in three different conditions. Those conditions were (1) GS model with spin relativistic effect (Spin-GS), (2) Molière model with spin relativistic effect (Spin-Molière) and (3) Molière model without spin relativistic effect (NoSpin-Molière). As shown in Fig. 5, for 10 keV to 20 MeV, those modes and the experiments agreed within 25% for Cu target and 16% for U target, respectively.

The Spin-Molière and the Spin-GS were close for several hundred keV to 20 MeV. Spin-GS is not available for 20 MeV or more energy in EGS5 code. As a result, Spin-Molière seem to be suitable for several hundred keV or more energy. On the other hand, for below several hundred keV, there was a difference between the Spin-GS and the Spin-Molière mode. This difference was caused by application limitation of the Molière model for low energy. Thus the GS model is more reliable than the Molière model for several hundred keV or less energy.

The Spin-Molière and the NoSpin-Molière modes were close below a few 10 keV. The spin relativistic effect is weak in this energy region. The models with the spin relativistic effect were nearer the experiments than the model without that for several hundred keV to 20 MeV.

References

[1] Y. Kirihara et al., *"Proceedings of the Fourteenth EGS Users' Meeting in Japan,"* KEK Proceedings 2007-5, 7 (2007).

[2] H. Hirayama, Y. Namito, A. F. Bielajew, S. J. Wilderman and W. R. Nelson, The EGS5 Code System. Report SLAC-R-730, Stanford Linear Accelerator Center, Stanford, CA, (2005).

[3] I. Kawrakow and D. W. O. Rogers, The EGSnrc Code System: Monte Carlo simulation of electron and photon transport, Ionizing Radiation Standards National Research Council of Canada, NRCC Report PIRS-701 (2006).

[4] F. Salvat, J. M. Fernández-Varea, E. Acosta and J. Sempau, PENELOPE - A Code System for Monte Carlo Simulation of Electron and Photon Transport, Nuclear Energy Agency OECD/NEA, Issy-les-Moulineaux, France, (2001).

[5] J. A. Halbleib, R. P. Kensek, G. D. Valdez, T. A. Mehlhorn, S. M. Seltzer and M. J. Berger, ITS: The integrated TIGER series of coupled electron/photon Monte Carlo transport codes - Version 3.0, IEEE Trans. Nucl. Sci. **39** 1025-1030 (1992).

[6] S. A. Goudsmit and J. L. Saunderson, Phys. Rev. **57** 24 (1940).

[7] S. A. Goudsmit and J. L. Saunderson, Phys. Rev. **58** 36 (1940).

[8] G. Z. Molière, Z. Naturforsch. **2a**, 133 (1947).

[9] R. Idoeta and F. Legarda, Nucl. Instr. Meth. Phys. Res. **B71,** 116-125 (1992).

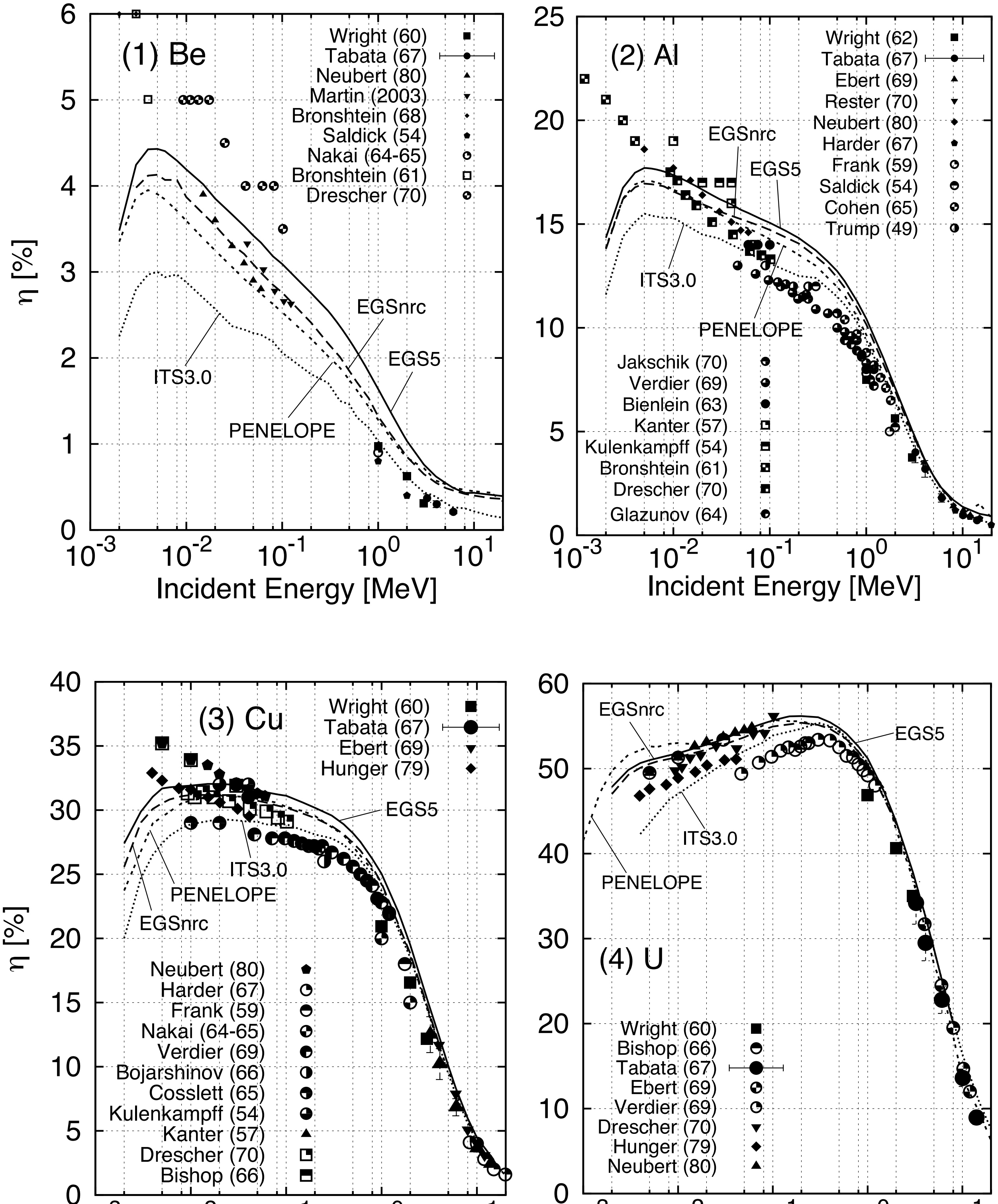

Figure 1: Electron backscattering coefficient η of (1) Be, (2) Al, (3) Cu and (4) U target. The experiments are shown in dots. The calculations are shown in lines.

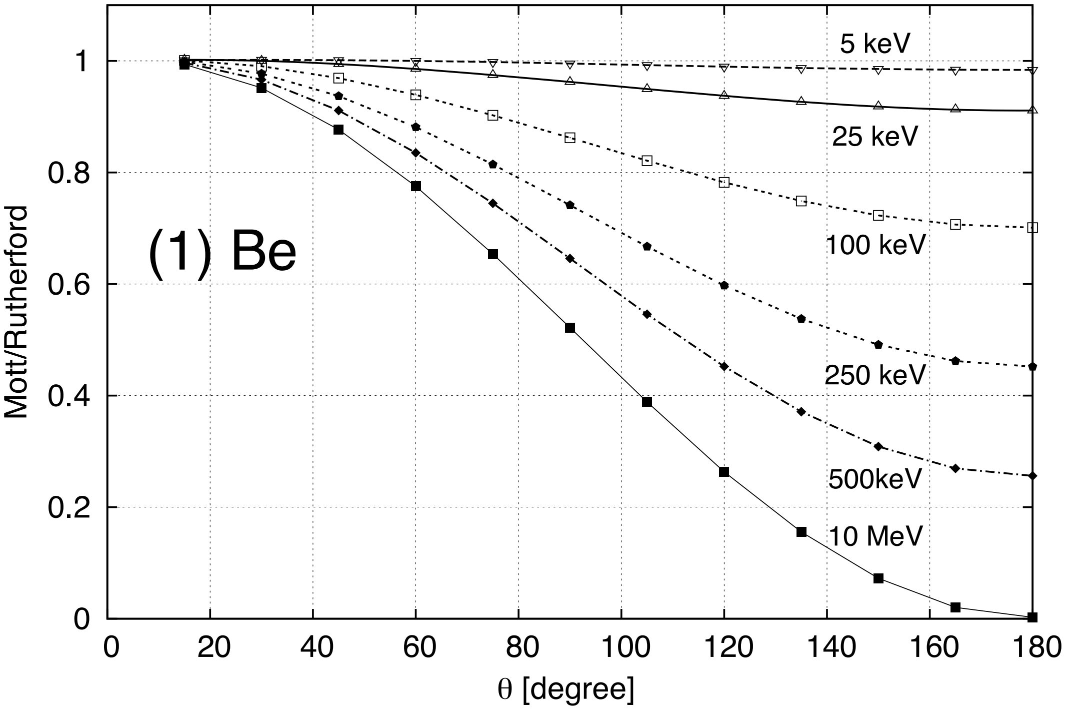

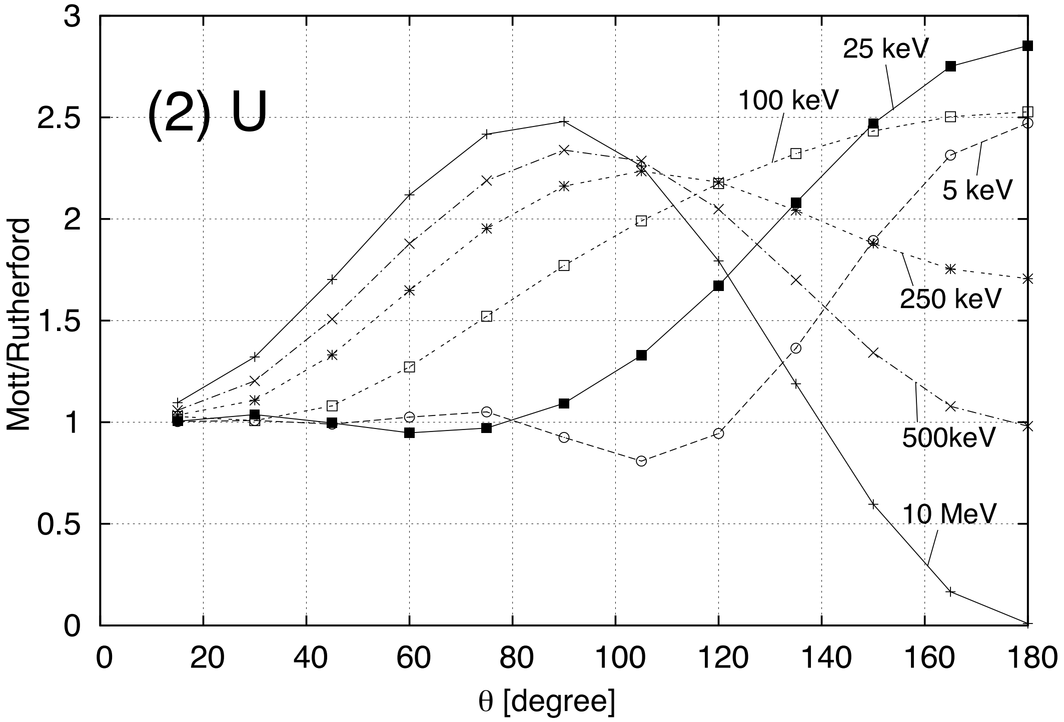

Figure 2: The ratio of the Mott to the Rutherford cross section for electrons at (1) Be and (2) U target[9].

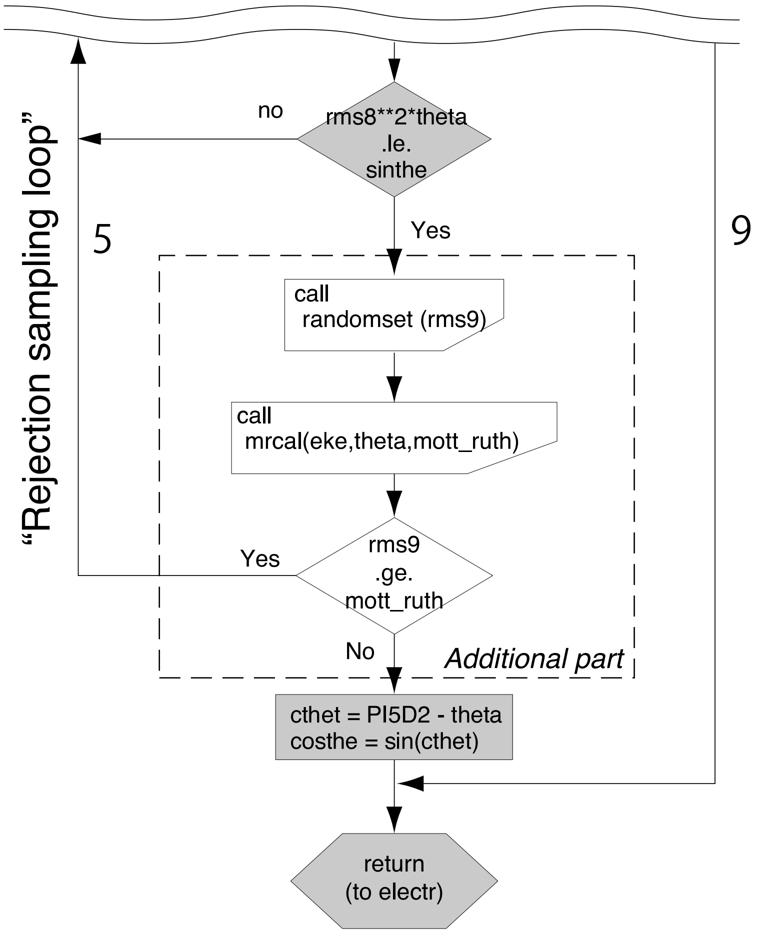

Figure 3: The flow diagram of SUBROUTINE MSCAT (Additional part).

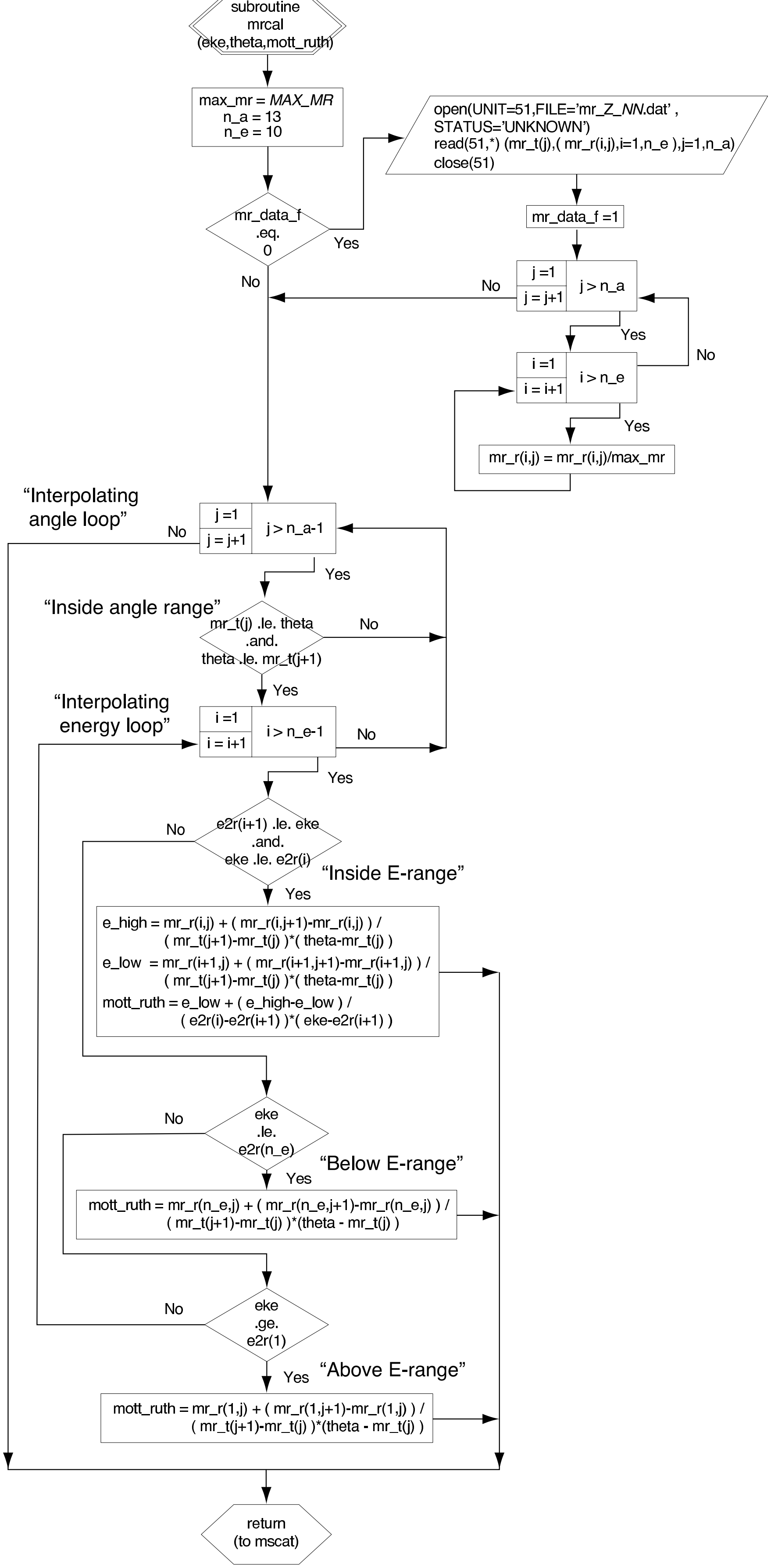

Figure 4: The flow diagram of SUBROUTINE MRCAL.

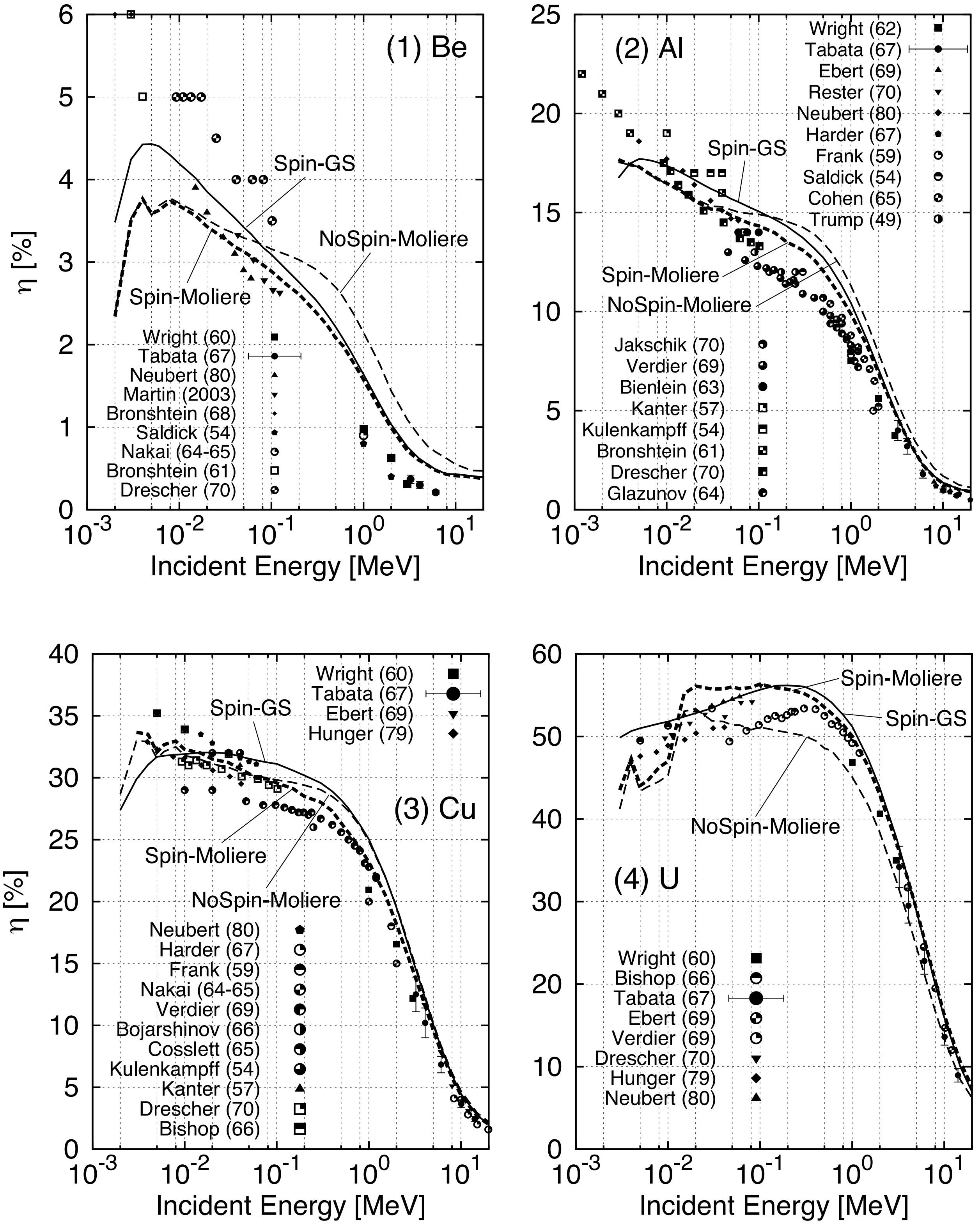

Figure 5: The electron backscattering coefficients η at (1) Be, (2) Al, (3) Cu and (4) U target were calculated using EGS5 code in three different conditions. The Spin-GS, the Spin-Molière and the NoSpin-Molière mode are in solid, thick dash and thin dash lines, respectively. The experiments are shown in symbols.

DESIGN STUDY FOR MONOCHROMATIC X-RAY TUBE USING EGS5

Shoichi Yoshida

Graduate School of Medical and Pharmaceutical Science for Research,
University of Toyama, Toyama 930-0194, Japan
e-mail: syoshida@las.u-toyama.ac.jp

Abstract

In this paper, we present a design study for monochromatic X-ray tube using Monte Carlo simulation (EGS5). This tube is designed for medical diagnostics and it can reduce dose delivered to patients.

1. Introduction

Diagnostic X-rays have been reported to be the largest artificial source of radiation for the general population. Their use involves the risk of developing cancer [1] so that various efforts to reduce dose are performed. One of the most effective methods to reduce dose is to use monochromatic X-rays of the best energy.

Monochromatic X-rays are produced by two-step process. As an ordinary X-ray tube, the electrons which are incident on the primary target produce Bremsstrahlung X-rays (primary X-rays). These X-rays which are incident on secondary target produce fluorescent X-rays (monochromatic X-rays) [2].

2. Basic Concept of Monochromatic X-ray Tube

The tube is a rotary anode type and the configuration is shown in Figure 1 and Figure 2. The primary thin gold target with a thickness of 15 μm is located near the edge of rotary anode surface. Gold is chosen because of its high atomic number and high thermal conductivity. The secondary cerium target is located under the primary target. Cerium is chosen because it emits the fluorescent X-rays of the best energy for medical diagnostic. There is beryllium layer between primary and secondary target which is transparent to X-rays. The heat conductivity of beryllium is relatively high so that the heat produced by the interaction with the electrons in the primary target can be dissipated. The fluorescent X-rays pass through the slit but the primary X-rays are not able to pass through the slit directly because they are absorbed in primary target.

3. Results and Discussion

Figure 3 shows the energy spectrum of X-rays which pass through the slit. The X-ray flux is normalized by the number of incident electrons. The X-rays produced by this tube is almost monochromatic and the amount of monochromatic X-rays is nearly comparable to the amount of Bremsstrahlung X-rays produced by the ordinary X-ray tube with a tungsten target. Figure 4 shows the exit angle dependence of X-rays. The exit angle θ is defined in Figure 2. This angle dependence is suitable for X-ray CT.

Acknowledgments

This work was supported by Grant-in-Aid for Scientific Research (C), 19500383.

References

1) Amy Berrington de Gonzalez, Sarah Darby, Risk of cancer from diagnostic X-rays: estimates for the UK and 14 other countries, The Lancet, vol. 363, 345-351, 2004
2) Harding G. and Schreiber B., X-ray source having a liquid metal target, US Patent 6185277, 1999

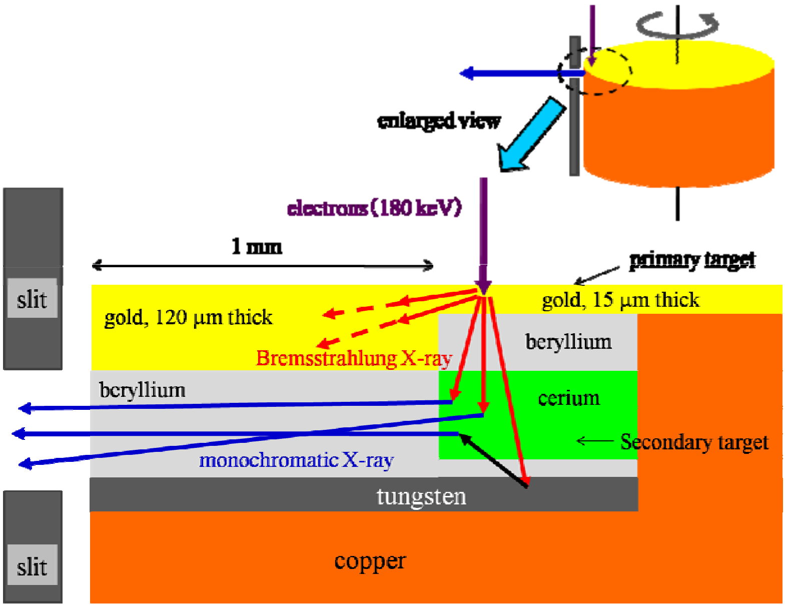

Figure 1. Schematic drawing of rotary anode

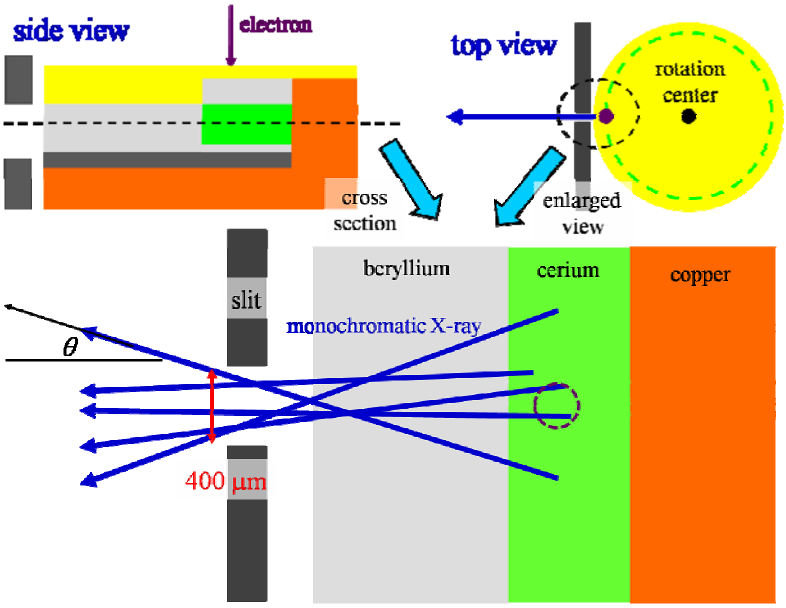

Figure 2. cross section of the rotary target

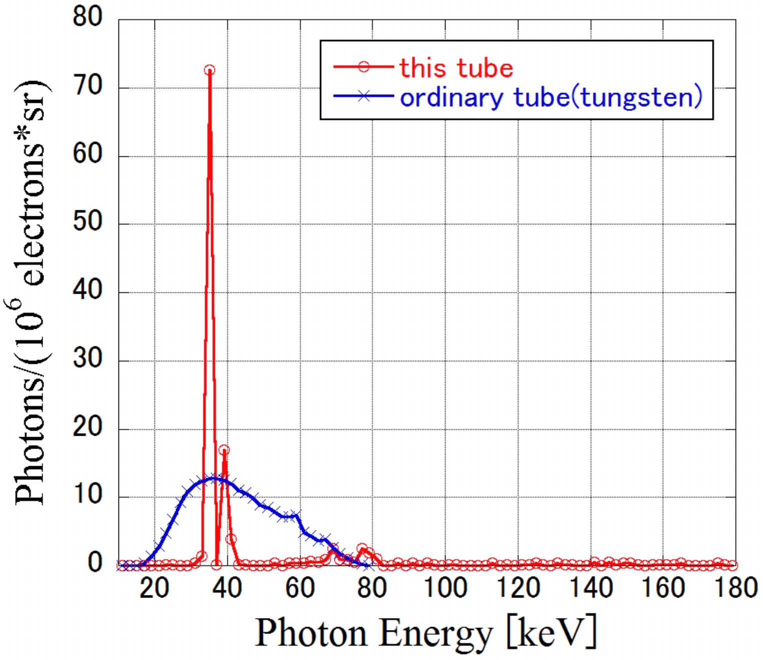

Figure 3. Energy spectrum of X-ray photons

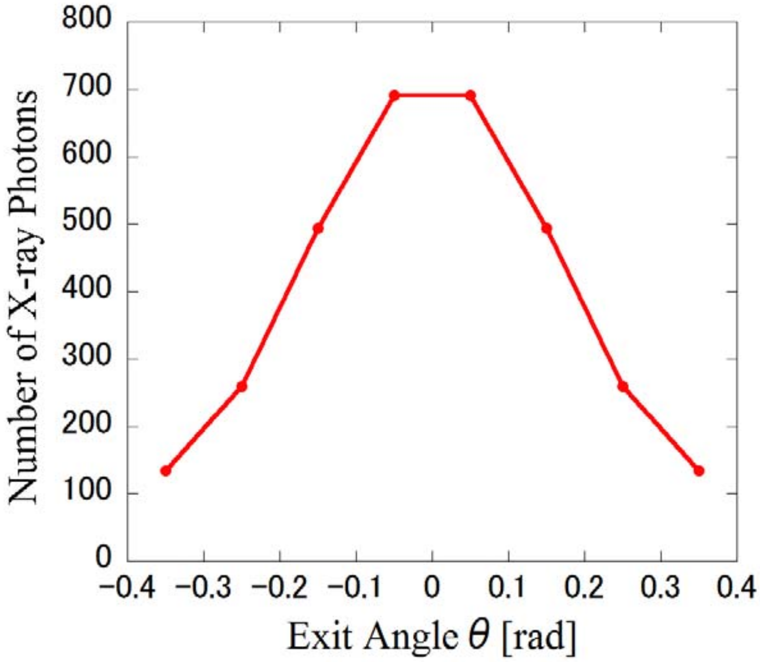

Figure 4. exit angle dependence of X-rays

Estimation of Radioactivity Produced in Cooling Water for High Energy Electron Linear Accelerator Facility

T. Itoga and Y. Asano
RIKEN, XFEL Project Head Office, Hyogo 679-5148, Japan

Abstract

The radioactivity produced in the cooling water was estimated for the XFEL 8 GeV beam dump. The EGS5 code was used to calculate the photon flux and the ratio of deposition energy in the cooling water. The activation cross section of ^{16}O for photo nuclear reactions were evaluated from the JENDL/PD2004 data library and data calculated theoretically with the TALYS code. The estimated radioactive concentrations are below the regulation limit.

1 Introduction

The Japanese hard x-ray free electron laser (XFEL/SPring-8) is under construction in the SPring-8 site. This facility will generate hard x-ray laser based on an 8 GeV electron linear accelerator and in-vacuum undulator. After the lasing, the 0.48 kW electron beam is disposed into a beam dump, but it is thought that cooling the beam dump is necessary for future multi-bunch operation (19.2 kW). When an electron beam loss occurred, the cooling water might become radioactive, and the estimation of the radioactivity produced in the cooling water is important from the view point of radiation safety.

The estimation of radioactivity in the water from the saturation activities per electron power is mentioned in IAEA Technical Report Series No. 188[1]. However, it is difficult to estimate precisely the power of electrons contributing to the activation and this may cause large overestimate when a primary particle does not deposit its energy directly into the cooling water like a beam dump. Therefore we calculated the gamma ray energy spectrum in the cooling water for the beam dump with EGS5[2] to perform a more detailed estimation of the activity in the cooling water.

Table 1: Photo activation products and saturation activities from ^{16}O in water[1].

Reaction	Nuclide	half life	A_S (GBq/kW)
γ,n	^{15}O	123 s	330
γ,2n	^{14}O	70.91 s	3.7
γ,2np	^{13}N	9.96 m	3.7
γ,3n2p	^{11}C	20.34 m	15
γ,4n2p	^{10}C	19.48 s	3.7
γ,5n4p	^{7}Be	53.6 d	1.5
γ,^{3}H	^{3}H	12.262 a	7.4

2 Estimation Method

The following three methods were used to estimate the radioactivity with EGS5.

Method A use ratio F of the energy deposited in the cooling water calculated with EGS5, and the saturation activity given by IAEA shown in table 1.

$$A_{IAEA} = A_S \cdot F \tag{1}$$

Method B use the gamma ray energy spectrum in the cooling water calculated with EGS5, and the evaluated photonuclear reaction cross section for ^{16}O of the JENDL/PD2004 data library[3](only for ^{3}H and ^{15}O).

$$A_{JENDL} = \phi \cdot \sigma_{JENDL} \cdot N \tag{2}$$

Method C use the gamma ray energy spectrum in the cooling water calculated with EGS5, and the photonuclear reaction cross section for ^{16}O calculated by using TALYS code[4].

$$A_{TALYS} = \phi \cdot \sigma_{TALYS} \cdot N \tag{3}$$

N is the number of ^{16}O atom in the cooling water. The ratio of deposition energy was obtained with the subroutine *ecnsv1.f* in EGS5 and the γ ray spectrum obtained with the *track length estimator* (eq.4) in EGS5 with the variable *tvstep*.

$$\phi(E) = \frac{\sum_{i=1}^{n} \Big(wt(np) \times tvstep \Big)_{i,E}}{\Delta V \times \Delta E \times n_0} \tag{4}$$

Since the upper limit of the cross section given by JENDL/PD2004 and calculated by TALYS are 150 and 250 MeV respectively. In higher energy region the cross section is assumed to be constant and equal to the value at 150 or 250 MeV, therefore giving an overestimation of the activity.

To estimate the radioactivity concentration in the cooling water, the following two equations were used in all methods. For long life nuclides with half lives long enough when compared to the water cycling time, the radioactivity concentration was calculated for the annual operation as,

$$C_{Long} = A_{\infty} \cdot P \cdot \Big\{ 1 - exp(-\lambda \cdot T) \Big\} \cdot V^{-1} \tag{5}$$

For short life nuclides, the equation 6 is used considering the decay time back from the beam dump to cooling water room.

$$C_{Short} = A_{\infty} \cdot P \cdot \Big\{ 1 - exp(-\lambda \cdot T) \Big\} \cdot exp(-\lambda \cdot t) \cdot V^{-1} \tag{6}$$

Here, C is the activity concentration in the cooling water, P is the average electron beam power, λ is the decay constant, T is the irradiation time, t is the cooling time and V is the total volume of the cooling water.

3 Comparison with the IAEA method

To confirm the validity of theses methods, we assumed a cylindrical water dump with a 33 cm radius (4 times of a Molière radius) and 720 cm long (20 radiation length) in the beam axial direction. Theses dimensions correspond to an 8 GeV electron depositing almost all its energy in the water dump. As a result, 97.9 % of the energy was deposited in the water dump. In the case of method B, the total neutron production cross section were used as ^{16}O(γ,n)^{15}O and total triton production cross section were used for tritium. In the case of method C, the cross sections for all target nuclides were derived by using the TALYS code with the Hartree-Fock QRPA theory.

Table 3 shows the saturation activity per electron power obtained with each method. The result calculated by method A was found to be in good agreement with that of method B. However, the result of method C is considerably smaller than that of the other methods. This is caused by the small cross section for ^{16}O(γ,n)^{15}O obtained with TALYS as shown in fig. 1. On the other hand, the result of method B might be overestimated because it using the total neutron production cross section.

Table 2: Saturation activity (GBq/kW).

Nuclide	A_{IAEA}	A_{JENDL}	A_{TALYS}
^{15}O	323	350	155
^{14}O	3.62	-	0.52
^{13}N	3.62	-	6.24
^{11}C	14.7	-	6.54
^{10}C	3.62	-	0.11
^{7}Be	1.47	-	0.84
^{3}H	7.24	7.68	4.28

4 Estimation of radioactivity concentration

The radioactivity concentration in the cooling water of the XFEL 8 GeV beam dump as been estimated with the three methods described in section 2. Figure 2 shows the structure of 8 GeV beam dumps. The beam dump consists of a core part made of graphite, a copper jacket and an outside iron shield. Cooling water goes along the pipes in each four sides of the jacket and cools the core part indirectly. This structure was reproduced in EGS5 precisely to calculate the γ ray energy spectrum induced in the cooling water and the ratio of deposition energy in cooling water, when 8 GeV electron induced on the beam dump core center.

Figure 3 shows the γ ray energy spectrum induced in the cooling water. The ratio of deposition energy in the cooling water is 1.28×10^{-3}%. As the operating condition, we assume an 8 GeV electron beam running in multi bunch mode with 1 nC/bunch, 40 bunch/pulse, at 60 Hz. All nuclides except ^{3}H and ^{7}Be are counted as short life nuclides and the radioactivity concentration after 1 cycle is calculated with equation 6. In this case T is about 4 seconds and t is about 37 seconds (time from the closest beam dump to the cooling water room). On the other hand, the concentrations for ^{3}H and ^{7}Be were calculated by equation 5 for 9 days (corresponding to 365 days / 40). Table 4 shows the radioactive concentration in the cooling water by each method and the regulation limit of the radioactive consentration for the draining water in Japan. All results are less than the regulation limit.

Table 3: Activity consentration in cooling water (Bq/cm^3).

Nuclide	Method A	Method B	Method C	Regulation limit
^{15}O	4.61	2.73	2.15	5
^{14}O	7.64×10^{-2}	-	3.66×10^{-3}	5
^{13}N	1.27×10^{-2}	-	5.26×10^{-3}	5
^{11}C	2.57×10^{-2}	-	3.94×10^{-3}	40
^{10}C	0.102	-	1.38×10^{-4}	0.1
^{7}Be	0.133	-	4.43×10^{-3}	30
^{3}H	8.31×10^{-3}	2.16×10^{-3}	1.02×10^{-3}	60

5 Summary

The radioactive concentration in cooling water was estimated for the 8 GeV beam dump of the XFEL facility with EGS5 and found to be below the regulation limit for all nuclides, independently of the method used. The results using the saturation activity and the ratio of deposited energy

(IAEA+EGS5) are in good agreement with the results using the γ spectrum and photonuclear cross section (JENDL+EGS5). The IAEA+EGS5 method is confirmed as a good approximation for the calculation of induced activity. The results obtained with the gamma spectrum and photonuclear cross-section calculated with EGS5 and TALYS smallest value in comparison with other method. However, it is useful method for a nuclide without an evaluated cross section like ^{7}Be although further investigations are necessary to confirm the values of the cross sections.

References

[1] W.P.Swanson, Radiological Safety Aspects of the Operation of Electron Linear Accelerators, Technical report series No. 188, (1978).

[2] H. Hirayama, Y. Namito, A.F. Bielajew, S.J. Wilderman and W.R. Nelson, The EGS5 Code System, SLAC-R-730, 2005 and KEK Report 2005-8, (2005).

[3] Norio Kishida, Toru Murata, Tetsuo Asami, Kazuaki Kosako, Kouichi Maki, Hideo Harada, Young-Ouk Lee, Jonghwa Chang, Satoshi Chiba, and Tokio Fukahori, JENDL Photonuclear Data File, AIP Conf., **769**, 199, (2005).

[4] A.J. Koning, S. Hilaire and M.C. Duijvestijn, TALYS: Comprehensive Nuclear Reaction Modeling, AIP Conf., **769**, 1154, (2005).

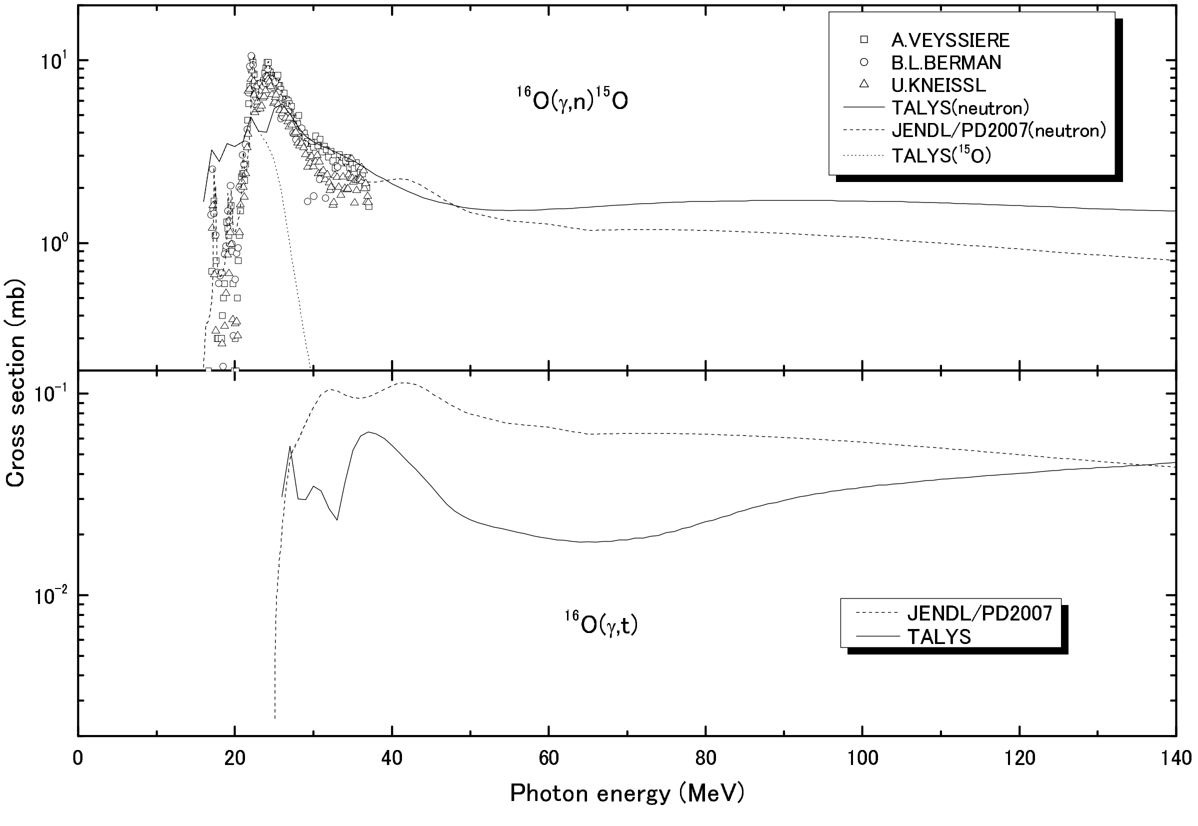

Figure 1: Comparison between JENDL/PD2004 and TALYS results.

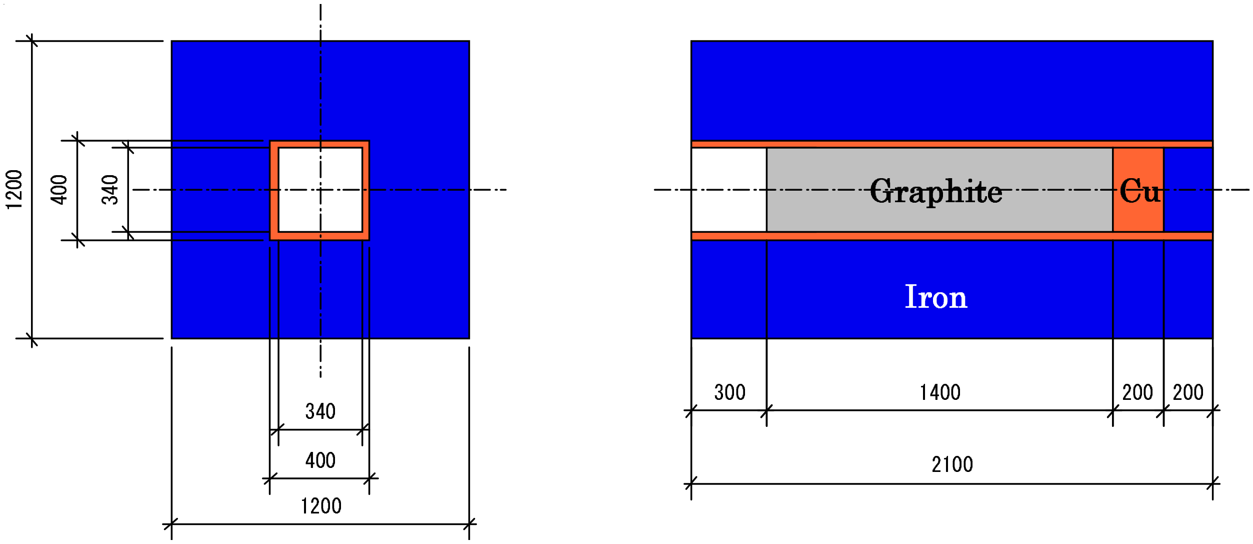

Figure 2: Schematic view of XFEL 8 GeV beam dump.

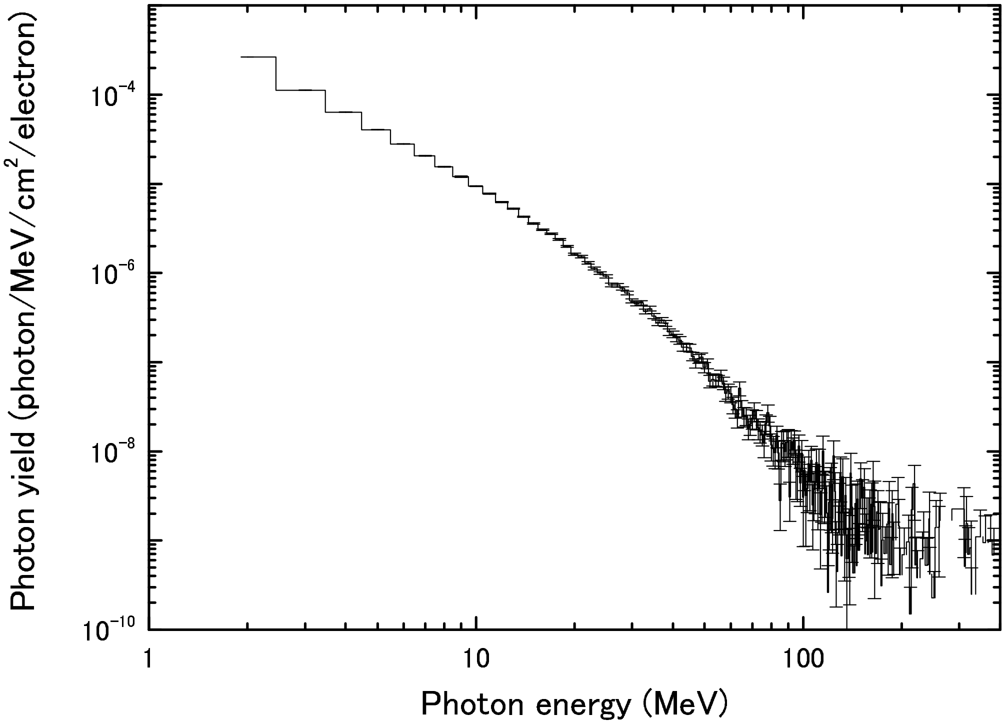

Figure 3: γ ray energy spectrum induced in cooling water.

EVALUATION FOR NON-UNIFORMITY EFFECT OF A LARGE SPHERICAL CHAMBER USING EGS5 CODE

Y. Unno[1], T. Kurosawa[1], Y. Sato[1], T. Yamada[1, 2], A. Yunoki[1], Y. Hino[1]

[1]National Metrology Institute of Japan, National Institute Advanced Industrial Science and
Technology, 1-1-1 Umezono, Tsukuba, Ibaraki 305-8563, Japan
[2] Japan Radioisotope Association
28-45, Honkomagome2, Bunkyo-ku, Tokyo, 113-8941, JAPAN
e-mail: y.unno@aist.go.jp

Abstract

A spherical ionization chamber was used in measurement of an iodine-125 seed source. The spherical chamber was calibrated previously in terms of protection level air kerma at National Metrology Institute of Japan (NMIJ). The volume of chamber is as large as approximately 4 L. The chamber was placed at near position from the seed source in order to obtain enough ionization current. However, it causes that we could not neglect the different situation between parallel beams at air kerma standard in NMIJ and isotropic radiation at the actual measurement for the seed source. We evaluated a correction factor for the non-uniformity effect using EGS5 code. The non-uniformity collection factor was applied to the measurement and the results exhibits good agreement with the result from a well-type ionization chamber which is traceable to the National Institute of Standards and Technology (NIST).

1. Introduction

The brachytherapy for prostate cancer employing iodine-125 seed sources is rapidly spreading in last 5 years in Japan [1]. We aim establishment of national traceability in Japan for the seed sources [2]. It is required by Japan society of medical physics in order to deliver accurate dose for cancer. The standard is in terms of air kerma strength, which is defined at The American Association of Physicists in Medicine (AAPM) Report 84 [3]. According to the report, air kerma strength S_k is the air kerma rate in vacuo $\dot{K}_\delta(d)$ multiplied by the square of distance *d*, concerning the higher energy photons than δ= 5 keV.

$$S_k = \dot{K}_\delta(d) \cdot d^2 [\mu\mathrm{Gy\ m^2\ h^{-1}}]$$

In National Metrology Institute of Japan (NMIJ), there is protection level air kerma standard, which contain a parallel-plate free air chamber [4]. However, the free air chamber is too small and has no longer any enough sensitivity for the seed sources. Therefore, we managed to assemble a new large free air chamber for primary standard. We also used a spherical chamber in order to confirm consistency between the conventional and new standard.

The spherical chamber is as large as approximately 4 liters in order to gather ionized current enough. The large spherical chamber has been used as secondary standard in Japan Radioisotope Association (JRIA) and has proven stability against thorny noise. We adopt this chamber for measurement of iodine-125 seed sources because of its successful measurement in order to realize the establishment of standard earlier. However, the energy response of the chamber has an edge just around 30 keV. The energy region corresponds to the region of photon spectrum emitted from iodine-125 seed sources as shown in Fig.1. Therefore, we should consider the energy dependency to evaluate a calibration factor for iodine-125 seed source in terms of air kerma strength. We derived the calibration factor from the protection level air kerma standard in NMIJ.

On the other hand, the spherical chamber was placed at near position from a seed source in order to measure at large solid angle. It causes that we should collect the non-uniformity effect. It was evaluated with EGS5 code [5] because it was difficult to evaluate in measurement.

The measurement results of air kerma strength with non-uniformity correction were compared with the measured air kerma strength by a well-type ionization chamber which is traceable to National Institute of Science and technology (NIST).

2. Materials and Methods

2.1 Iodine-125 seed sources

We should calibrate two types of iodine-125 seeds which are usually used in Japan. Their types are IMC6711 (Oncoseed) and STM1251 (Bard Brachysource). The seeds are looked like small capsules, and the length is 5mm and the diameter is 1mm approximately. They have different spectra each other as shown in Fig.1. The spectra were measured using a CdTe detector (RAMTEC413, TOYO MEDIC Co. Ltd.). It is declared that a seed source called IMC6711 has a softer spectrum than STM1251. The spectra have several peaks derived from γ-ray and Te-K x-ray emitted by electron capture decay of iodine-125 around 30 keV. A peak of Ag-K x-ray around 22 keV was found only in the spectrum of IMC6711. Additionally, it is known that Ti-K x-ray 4.5 keV is emitted from the seed source [6], but the low energy x-ray was neglected because the large spherical chamber has no sensitivity below 10 keV. The difference in the energy spectra mainly affects a calibration factor of the spherical chamber.

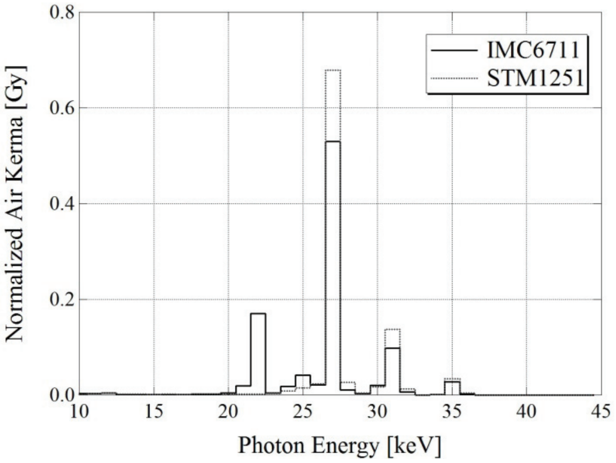

Fig. 1 Photon energy spectra from two types of an iodine-125 seed source

2.2 Experimental setup

We measured an IMC6711 seed with the large spherical chamber. The large spherical ionized chamber is vented to atmosphere and has electrode at the center. It has 5 mm thick wall of polymethyl methacrylate (PMMA). We used a charge-up type electrometer (model2961 Applied Engineering Inc.). The distance between the seed and the center of the ionization chamber is 30 cm, 50 cm, and 100 cm.

Using this large spherical chamber, we measured the seeds in terms of air kerma strength with a following equation.

$$S_k = N_k \cdot \dot{M}_u \cdot k_{scat} \cdot k_{air} \cdot k_n \cdot d^2$$

N_k means a calibration factor for the spherical chamber in terms of air kerma strength, and $\dot{M}_u$ means a measurement of collected current, and k_{scat}, k_{air}, k_n means correction factors for scattering, air attenuation, and non-uniformity. The calibration factor N_k was derived from the calibration factor at protection level air kerma standard in NMIJ. Response function of the chamber was obtained by unfolding method with photon energy spectra of air kerma standard in NMIJ and calibration factors obtained there. The response function was weighted by photon energy spectra of the seed source and summed to the calibration factor N_k [7]. Additionally, we evaluated both scattering k_{scat} and attenuation factor in air k_{air}. We evaluated the scattering factor k_{scat} as 0.988 at 30 cm by measurement using a shadow bar. We also evaluated the attenuation factor k_{air} as 1.021 at 30 cm from “Tables of X-Ray Mass Attenuation Coefficients and Mass Energy-Absorption Coefficients” at NIST [8].

2.3 Non-uniformity correction factor

As mentioned above, the large spherical chamber was at the near distance from the iodine-125 seed source in order to gather enough ionization current. However, it causes that we should evaluate the non-uniformity correction factor that converts the irradiation situation in front of the iodine-125 seed source into the situation at the air kerma primary standard of NMIJ. We cannot measure the correction factor because it is difficult to measure the ionization current at the far position where the beam could be assumed as parallel. Therefore, we used EGS5 code in order to evaluate the non-uniformity correction factor. We calculated deposited energy in the spherical chamber in the simulations, and the deposited energy was normalized by photon fluencies at the center of the chamber. The lower cutoff energy was 1 keV, and the upper was 100 keV. The diameter of a spherical chamber was 11 cm, and the thickness was 0.5 cm. The diameter of a spherical electrode was 0.6 cm, and the thickness was 0.1 cm. The diameter of a cylindrical pole for the electrode was 0.4 cm, and the thickness was 0.1 cm. The space in the equipment was filled with atmosphere, and the wall was composed of PMMA. At the simulation of parallel field at NMIJ, the photons were emitted perpendicularly from uniformly spread surface (Fig.2 (A)). At the simulation of isotropic field, the source was at 30 cm, 50 cm, and 100 cm on the perpendicular straight line from center of the spherical chamber and emitted photons as cone beam which contains the spherical chamber completely (Fig.2 (B)). The incident photons had mono-energy for each simulation around 10 keV to 40 keV in increments of 1 keV.

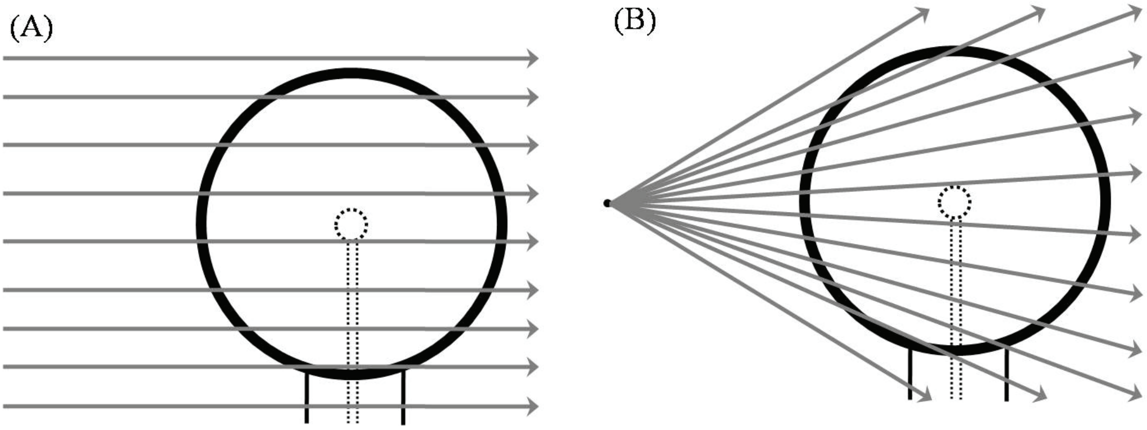

Fig. 2 The geometry of parallel (A) and cone (B) beams in the simulation

3. Results

The non-uniformity correction factor functions $k_n(E)$ characterized by incident photon energy E are evaluated from ratio of the deposit energy $D_{para}(E)/D_{iso}(E)$ as shown in Fig.3. It is clear that we should take into account the non-uniformity effect especially at 30 cm from Fig.3. The non-uniformity correction factors were weighted with the air kerma spectrum at the actual field and summarized at Table.1. The correction factors at near position reported by S. Shimizu [9] were also shown in Table.1. The evaluation was based on measurement using a Co-60 point source and calculation of its geometric parameter. The present evaluation agreed

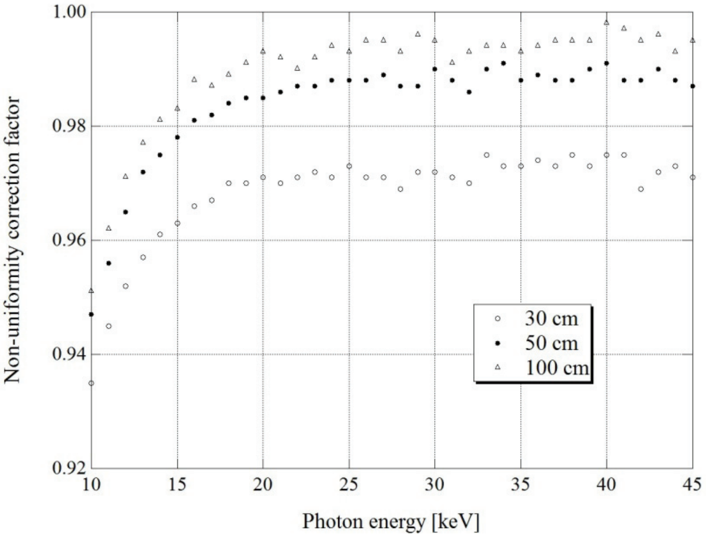

Fig. 3 The calculated non-uniformity correction functions

with the previous report within 0.5 %.

The present measurement was conducted at 30 cm, and the results multiplied the correction factors were compared with reference data which were obtained from NIST traceable ionization chamber (Table.2).

Table 2 The evaluated non-uniformity correction factor for each distance from the seed source

Distance from the seed source	Non-uniformity correction factor k_n	S. Shimizu [9]
30 cm	0.971	0.976
50 cm	0.987	0.991
100 cm	0.993	0.998

Table 1 Comparison between the present and reference results

	Present μGy m^2 h^{-1}	Reference μGy m^2 h^{-1}	Ratio
#1	0.5038	0.5045	0.999
#2	0.5129	0.5145	0.997
#3	0.5024	0.5079	0.989
#4	0.4975	0.5011	0.993
#5	0.5097	0.5104	0.999

4. Conclusions

We arranged the spherical chamber at near position from the iodine-125 seed source in order to collect ionized current enough. The non-uniformity effect should be considered because the spherical chamber was calibrated by the parallel beam at primary air kerma standard in NMIJ. We applied EGS5 code to evaluate the correction factor instead of measurement. The result agreed with the reference data which are traceable to NIST. We will adopt the spherical chamber for the benchmark experiment which confirms the consistency between primary air kerma standard and the new standard field for the iodine-125 seed source.

References

[1] Japan Radioisotope Association: Stastics on the distribution of radioisotopes and disposal of radioactive wastes in Japan, 2008

[2] A. Yunoki: A survey on the radiation exposure and activity standards of iodine-125 small sealed source for brachytherapy, AIST Bulletin of Metrology, 4-3 (2006) 201 (in Japanese)

[3] Mark J. Rivard et.al: Update of AAPM Task Group No. 43 Report : A revised AAPM protocol for brachytherapy dose calculations, Med. Phys., 31 (3), March 2004, 633

[4] A. Nohtomi: A surver on establishment of exposure standards for low energy x-rays, AIST Bulletin of Metrology, 2-4 (2004), 627 (in Japanese)

[5] H. Hirayama et.al: The EGS5 code system, SLAC-R-730 (2005)

[6] Stephen M. Seltzer et.al: New national air-kerma-strength standards for ^{125}I and ^{103}Pd brachytherapy seeds, J. res. Natl. Inst. Stand. Technol. 108, 337-358 (2003)

[7] Y. Unno et.al: Measurement of air kerma strength for I-125 seed sources with a sphere chamber (1) Estimation of the calibration coefficient into air kerma strength (in Japanese)

[8] J. H. Hubbell, S. M. Seltzer: Tables of X-ray mass attenuation coefficients and mass energy -absorption coefficients (ver. 1.4), National Institute of Standards and Technology, http://physics.nist.gov/PhysRefData/XrayMassCoef/cover.html

[9] S. Shimizu, JAERI-Review 95-020 (in Japanese)

EVALUATION OF COUNTING EFFICIENCY OF WHOLE-BODY COUNTER USING "MAX06" VOXEL PHANTOM

M. Takahashi[1], **S. Kinase**[1] **and R. Kramer**[2]

[1] *Japan Atomic Energy Agency, 2-4 Shirakata-Shirane, Tokai-mura, Ibaraki 319-1195, Japan*
[2] *Universidade Federal de Pernambuco, Av. Prof. Luiz Freire 1000, Cidade Universitaria, CEP 50740-540, Recife, PE, Brazil*

Abstract

In 2007, the International Commission on Radiological Protection (ICRP) recommended that effective doses be calculated using reference phantoms of the human body based on medical tomographic images. From the standpoint of internal dosimetry services, calibration methods of whole-body counters using the reference phantoms are of considerable practical interest. The purpose of the present study is to evaluate counting efficiencies of a whole-body counter for a voxel phantom "MAX06" that was developed as the first human phantom which corresponds to the reference male anatomical data in ICRP Publ. 89. The whole-body counter has been installed with three p-type high-purity Ge closed-ended coaxial detectors and normally calibrated using BOMAB phantoms. The counting efficiencies for the MAX06 phantom were found to be smaller than those for the BOMAB phantom defined as adult males. This is due to geometrical differences between the MAX06 and the BOMAB phantoms. The results suggest that the MAX06 phantom can be significant tool for calibration of whole-body counters because calibrations with the BOMAB phantoms could cause to underestimate radioactivities in human body.

1 Introduction

In the 2007 recommendations by ICRP, it is mentioned that effective doses from internal or external sources be calculated using the reference phantoms of the human body based on medical tomographic images [1]. The reference phantoms, which consist of voxels that make up defined organs, have been adjusted to approximate the organ masses assigned to the reference male and reference female in ICRP Publ. 89 [2]. For internal exposures, the reference voxel phantoms will be used to calculate conversion coefficients from radioactivities to average absorbed doses in any organs specified in the reference humans. For the internal exposure monitoring, instruments to measure radioactivities in human body e.g., whole-body counters are applied. The whole-body counters are generally calibrated using simple geometrical phantoms [3]. To make accurate assessment of radioactivity in the whole-body or a region of the body, the calibrations of whole-body counters using voxel phantoms are needed. From the point of view of internal dosimetry services, calibration methods of whole-body counters using the reference voxel phantoms are of considerable practical interest. The purpose of the present study is to develop the calibration methods using voxel phantoms and to evaluate counting efficiencies of a whole-body counter at the Japan Atomic Energy Agency (JAEA) for a voxel phantom which has organ and tissue masses adjusted to the reference masses given in ICRP Publ. 89.

2 Materials and methods

2.1 MAX06 phantom

The voxel phantom used in the present study was "MAX06" phantom that was developed by Kramer *et al.* [4] as the first human phantom which corresponds to the male anatomical data recommended in ICRP Publ. 89. The MAX06 phantom is based on segmented images from patients. The voxel size is 1.2 × 1.2 × 1.2 mm^3 and 97 organs or tissues are specified. Figure 1 shows the images of the MAX06 phantom of (a) entire body and (b) cross section in the heart region. The MAX06 phantom is compiled as a data set of 474 columns × 222 rows × 1461 slices and consequently the total number of voxels are 153,738,108, of which 41,461,410 voxels are filled with human tissues. Ten materials shown in table 1 were defined for the MAX06 phantom. The elemental compositions and the densities were taken from ICRP Publ. 89. Table 2 shows the heights, weights and masses of some organs and tissues for the MAX06 phantom and the reference male in ICRP Publ. 89. It can be seen in the table that the organ and tissue masses of the MAX06 phantom agree well with the reference masses.

2.2 Whole-body counter and BOMAB phantom

A bed-type whole-body counter is installed with three p-type high-purity Ge closed-ended coaxial detectors at JAEA. The Ge detectors have approximately 80 % peak efficiency, which is relative to that of a 76.2 mm diameter × 76.2 mm thick NaI(Tl) crystal measured for 1333 keV photons from a source of ^{60}Co at 25 cm. The Ge detectors are located in a shielding room to reduce background radiations such as cosmic rays. The shielding room consists of iron with 200 mm thickness, lead with 3 mm, copper with 1 mm and faced plastic wall. The inner size of the shielding room is 2.0 m width × 2.5 m distance × 2.5 m height. As shown in figure 2(a) , a bed is located at 1 m above the bottom inside the shielding room and one of the Ge detectors are placed above the bed and the others under the bed.

The whole-body counter is normally calibrated with BOttle Manikin ABsorption (BOMAB) phantoms [5]. The specifications of the BOMAB phantom were defined by the American National Standards Institute (ANSI) as the standard of a anthropomorphic phantom for calibrations of whole-body counters [6]. Geometrical parameters of the MAX06 and BOMAB phantoms are summarized in table 3. The BOMAB phantom consists of 10 cylindrical containers formed into various sizes to represent any parts of a human, as shown in figure 3(a). Two materials, shells and fillers, for the containers have been defined by ANSI. The shells are high-density polyethylene with a density of 0.95 g/cm^3 and the thickness is 0.5 cm except for the top of the cylinders, which is 1.5 cm as illustrated in figure 3(b). Radioactive sources are homogeneously distributed in the filler material that is composed of a tissue-substitute polyurethane compound. The sources include 4 nuclides, ^{133}Ba, ^{137}Cs, ^{60}Co and ^{40}K .

2.3 Monte Carlo calculations

Counting efficiencies of the whole-body counter for the MAX06 phantom were calculated using EGS4 code in conjunction with UCWBC [7]. The photon sources were assumed to be homogeneously distributed in the all organs and tissues of the MAX06 phantom laid on the bed. The counting efficiencies were calculated at 12 mono-energies in the photon energy range between 81 and 1333 keV. The counting efficiencies were evaluated by dividing the number of photons, which deposited its total energy in the detectors, by the number of histories. The number of histories was determined to be 10 million so that statistical uncertainties were below 5 %.

Figure 2(a) and (b) show the calculation geometries of the whole-body counter and the Ge detectors, respectively. The calculation model was constructed to represent the actual whole-body counter. It was assumed that thicknesses of dead layers on the outer surface of the Ge crystals were 0.9 mm.

The cut-off energies for the transport calculations were set 1 keV for photons and 10 keV for electrons in the regions around the detectors. In the other regions, the cut-off energies were set half of the source energies for photons and more than source energies for electrons in order to reduce calculation times. The cross section data for photons were taken from PHOTX [8], and data for electrons from ICRU report 37 [9].

Counting efficiencies for the BOMAB phantom were also calculated in order to compare with those of experiments for validation of the simulation methods.

3 Results and discussion

Figure 4 shows the results of the calculations and experiments for the BOMAB phantom. The measurement data are indicated with error bars representing uncertainties relating to the source activities and counting statistics. It can be seen that the counting efficiencies by the calculations are consistent with those by the experiments within the error bars. From the results, the simulation methods of this study were found to be valid in the photon energy range from 81 to 1333 keV.

Figure 5 shows the counting efficiencies for the MAX06 and BOMAB phantoms. It was found that the efficiencies for the MAX06 phantom are smaller than those for the BOMAB phantom over the energy range of the simulations. The discrepancies between them are from 3 to 10 %, of which the maximum discrepancy is found at the photon energy of 1333 keV. These discrepancies are probably due to geometrical differences between the two phantoms. As shown in table 3, there is significantly difference on volumes of the source regions because the BOMAB phantom has the shell regions including no sources.

The counting efficiencies for real humans are expected to be similar to those for the MAX06 phantom more than those for the BOMAB phantom. This results lead to a conclusion that measured radioactivities in human body with whole-body counters could be underestimated, assuming that the whole-body counters were calibrated using only the BOMAB phantom.

4 Conclusions

The calibration methods of whole-body counters using Monte Carlo simulation and voxel phantoms have been developed. The counting efficiencies of a whole-body counter at JAEA were also simulated using the two type phantoms, the MAX06 and the BOMAB phantoms. It was found that the counting efficiencies for the MAX06 phantom are smaller than those for the BOMAB phantom in the energy range between 81 and 1333 keV. The discrepancies between the efficiencies for the two phantoms were approximately 10 % at the muximam. It was also been found from this results that measurements with whole-body counters calibrated using the BOMAB phantoms possibly lead to underestimates of radioactivities in human body.

Based on these findings, we can conclude that the calibration method of the JAEA whole-body counter using the MAX06 phantom is useful for the reliable assessments of internal exposures. We plan in the near future to study calibration methods of whole-body counters for a reference female and Japanese average persons.

References

[1] ICRP, "The 2007 Recommendations of the International commission on Radiological Protection," ICRP Publ. 103, Elsevier(2007).

[2] ICRP, "Basic Anatomical and Physical Data for Use in Radiological Protection: Reference Values," ICRP Publ. 89, Pergamon Press, Oxford(2002).

[3] ICRU, "Phantoms and Computational Models in Therapy, Diagnosis and Protection," ICRU Report 48, Bethesda (1992).

[4] R. Kramer, H. J. Khoury, J. W. Vieira and V. J. M. Lima, "MAX06 and FAX06: update of two adult human phantoms for radiation protection dosimetry," Phys. Med. Biol., **51**, 3331-3346(2002).

[5] Y. Ohi, "Geometry and Peak Efficiencies of the Whole-body Counter with Maze-type Shielding Room," JAERI-Review, 2003-034, 127-129(2003).

[6] ANSI, "Specifications for the Bottle Manikin Absorption Phantom," ANSI/HPS N13.35-1999(2000).

[7] S. Kinase, S. Takagi, H. Noguchi, K. Saito, "Application of Voxel Phantoms and Monte Carlo Method to Whole-body Counter Calibration," Radiat. Prot. Dosim., 125, 189-193(2007).

[8] RSIC, DLC-136/PHOTX Photon Interaction Cross Section Library (contributed by National Institute of Standards and Technology)(1989).

[9] ICRU, "Stopping Powers for Electrons and Positrons," ICRU Report 37, Bethesda, Md.(1984).

Table 1: Human tissue materials defined for the MAX06 phantom.

Material	Density (g/cm^3)
Cortical bone	1.92
Trabecular bone	1.18
Marrow	0.98
Cartilage	1.10
Skin	1.09
Muscle	1.05
Lung	0.26
Soft tissue	1.03
Adipose	0.95
Air	1.205×10^{-3}

Table 2: Comparison of geometrical parameters between the MAX06 phantom and the ICRP reference male.

	MAX06	ICRP ref. male	Difference (%)
Height (cm)	175.3	176	-0.4
Weight (g)	72500	73000	-0.7
Organ and tissue (g)			
Brain	1450	1450	
Connective tissue	2600	2600	
Liver	1800	1800	
Adipose	14544	14500	+ 0.3
Skin	3383	3300	+ 2.5
Muscle	29000	29000	
Lungs	1200	1200	
Skeleton	9950	10500	- 5.2

Table 3: Geometrical parameters of the MAX06 and BOMAB phantoms.

	MAX06	BOMAB
Height (cm)	175.3	175.8
Weight (g)	72500	69000
Source region volume (cm^3)	71600	57300

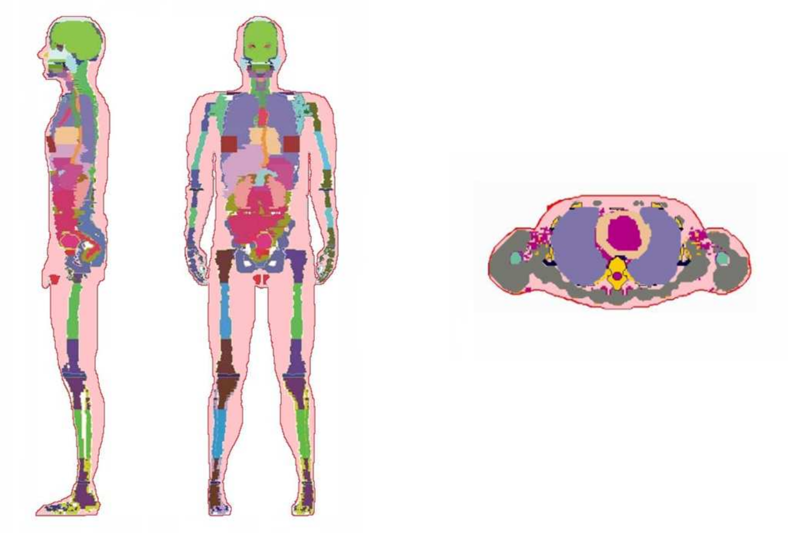

(a) Whole body images (b) A traversal image on No. 350 slice

Figure 1: MAX06 voxel phantom.

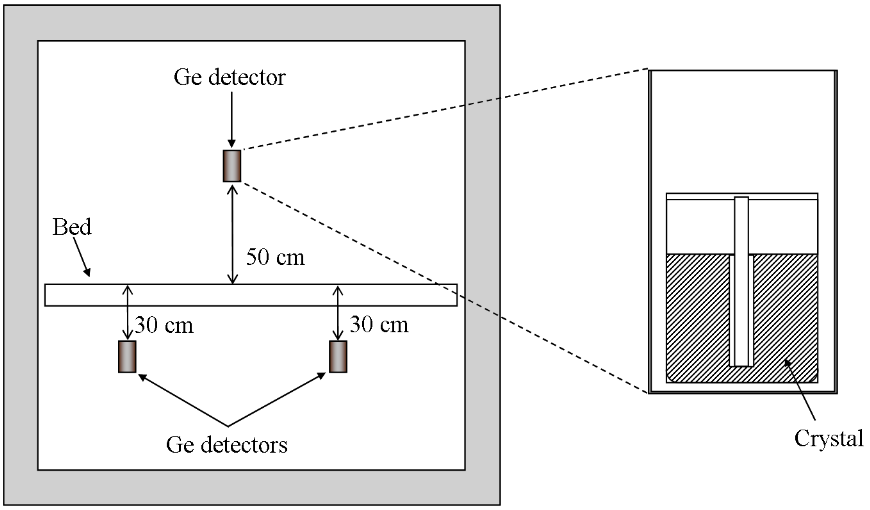

(a) Whole-body counter (b) Details of Ge detectors

Figure 2: Geometrical models of the whole-body counter and the Ge detectors.

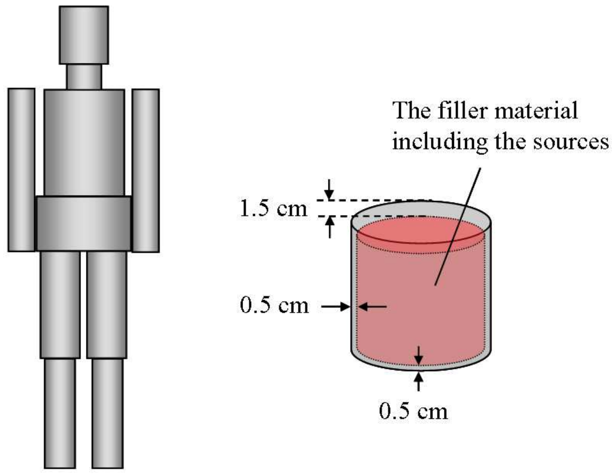

(a) Whole exterior (b) A cylindrical container for a part of the BOMBA phantm

Figure 3: BOMAB phantom.

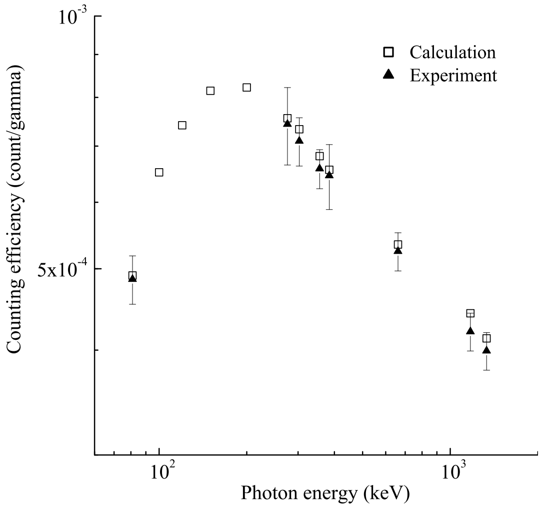

Figure 4: Comparison of the counting efficiencies by the simulations and the measurements.

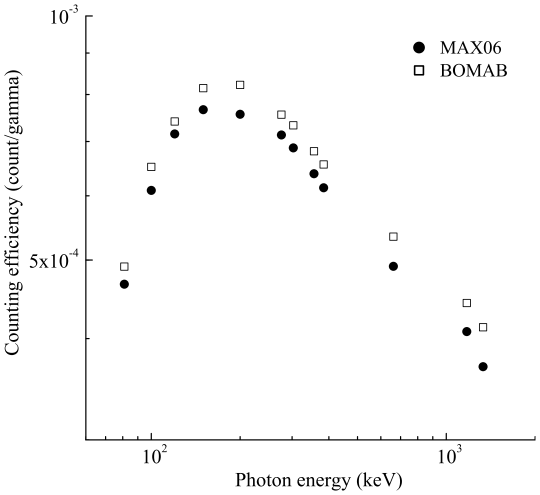

Figure 5: Comparison of the counting efficiencies for the MAX06 and BOMAB phantoms.

MONTE CARLO SIMULATION CT

S. Kitou[1], K. Hanai[1] and Y.Obata[2]

[1]*National Cancer Center Hospital East, Chiba 277-8577, Japan*
[2]*Department of Radiological Technology, Graduate School of Medicine, Nagoya University*
1-1-20 Daikou-Minami, Higashi area, Nagoya city, Japan
E-mail: skitou@east.ncc.go.jp

Abstract

X-ray Computed Tomography (CT) to acquire the arbitrary section image of a human body has a lot of technology in the system. By simulating the CT device and the reconstruction process of the CT image, we can analyze the information that it is difficult to obtain it in the measurement, and the reason of the artifact. Using Monte-Carlo (MC) method, we can also simulate the effect of the statistical noise. On the other hand, It is useful for an educational purpose to develop such a simulation. In this research, it aims to understand the device of the CT by MC simulation and the principles of the CT reconstruction process. In this study, Electron Gamma Shower Version 5 (EGS5) was used to simulate the CT device. In the EGS5 geometry, the mass density voxel phantom of a human body that was obtained from actual CT Image was arranged in the MC CT gantry. And the X-ray transmission data from the multidirection were acquired by MC simulation. About CT reconstruction algorism, CT image was reconstructed by the method of filtered back projection. On the other hand, theoretical algorism simulator based on Radon Transfer algorism (RTS) was also developed by Visual C++. Then, the theoretical transmission data were obtained by RTS. The image reconstructed from RTS data dose not includes the influence of a statistical noise. Therefore the image based on RTS is similar to the original image, the algorism of the CT reconstruction is functioning well. In the result of MC simulation, the image quality of CT is improved when the number of histories increases. However, even in case of the condition of 100×1000000 histories, the noise of the image is considerably strong. Therefore, the smoothing process might be given to the transmission data and the image after reconstruction. Thus, the simulation developed by this study is useful to recognize CT system.

1. Introduction

X-ray Computed Tomography (CT) to acquire the arbitrary section image of a human body has a big role on a present medical treatment site. For example, filtered back projection method and image smoothing filter, there are a lot of technology to actualize CT images in the CT system.

By simulating the CT device and the reconstruction process of CT image, we can analyze the information that it is difficult to obtain it in the measurement, and the reason of the artifact (false signal that is deterioration of quality of image). Using Monte-Carlo (MC) method, we can also simulate the effect of the statistical noise. On the other hand, It is useful for an educational purpose to develop such a simulation. In this research, it aims to understand the device of the CT by Monte-Carlo simulation and the principles of the CT reconstruction process.

2. Materials and Methods

2.1 Theory of Computed Tomography

CT is the section image that is reconstructed from the transmission data that is acquired by irradiating X-rays from the multiway to a subject. The elements of the picture are relative X-ray linear attenuation coefficient.

Figure 1 shows the geometry of the CT. It is called Radon transform to obtain (logarithm) transmission data function g(X,θ) for all directions from the distribution of linear attenuation coefficient μ(x,y). The equation is

$$g(X,\theta)=\ln[\frac{I_0}{I(X,\theta)}]=\int_{-\infty}^{\infty}\mu(x,y)dY\ ,$$

where Io is the intensity of the incident X-ray, I(X, θ) is the intensity of the X-ray that transmits a subject from the angle of θ for X number detector.

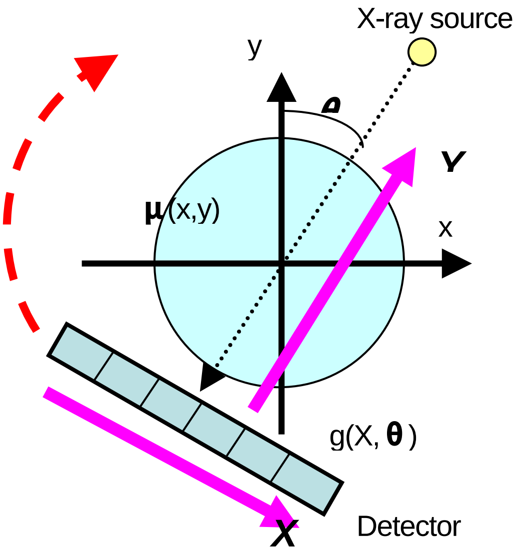

Figure 1. Geometry of CT.

Data that is the Fourier transform of g(X,θ) is corresponding to the data of the same angle that passes the origin point of two-dimensional data that is the two-dimensional Fourier transform of a original image. Therefore, μ (x,y) is obtained by two-dimensional Fourier reverse transforming the data that is the Fourier transform of g(X,θ) for all θ. This relation is called central slice theorem. However, the image quality is deteriorated because of the interpolation error caused when Fourier reverse transform.

To calculate all in real space, the next equation

$$\mu(x,y)=\frac{1}{4\pi}\int_0^{2\pi}\left[\frac{1}{2\pi}\int_{-\infty}^{\infty}\left\{\int_{-\infty}^{\infty}g(X,\theta)e^{-i\omega X}dX\right\}|\omega|e^{-i\omega X}d\omega\right]$$

developed by previous equation is used in the following method called filtered back projection.

Filtered back projection method is the technique that obtains μ(x,y) by convoluting filter function that corresponds to |ω| into transmission data g(X,θ) in frequency space (Figure 2). Theoretically, it should be ｜ω｜ in frequency space, but the function has the characteristic in which the high frequency noise is increased. Therefore, in this study, Shepp and Logan function which expressed as

$$\frac{2W}{\pi}\cdot\left|\sin\left(\frac{\pi\omega}{W}\right)\right|$$

in frequency space, or

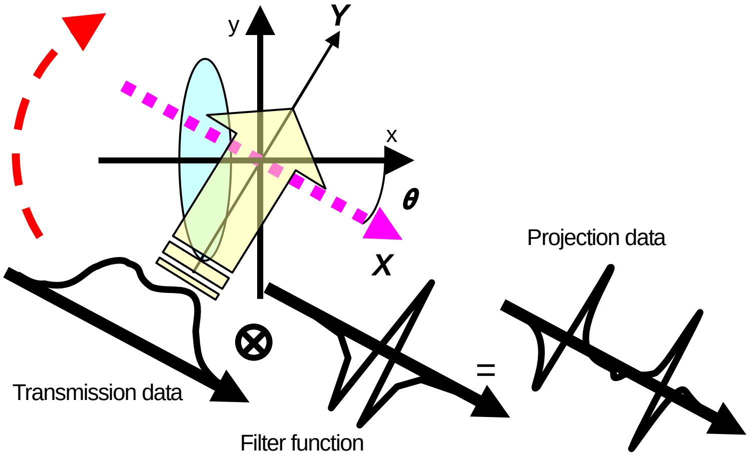

Figure 2. Filtered back projection method.

$$\frac{2}{\pi^2 a^2 \left(1-4k^2\right)} \quad \left(k = 0, \pm 1, \pm 2 \cdots\right)$$

in real space, where a is sampling interval, is used as the filter function. This filter decreases the high frequency noise compared with that filter.

2.2 Construction of the CT Gantry in EGS5

In this study, Electron Gamma Shower Version 5 (EGS5) was used to simulate a CT device. Figure 3 shows the schematic view of the Monte-Carlo simulation. In the EGS5 geometry, the mass density voxel phantom of the human body that was obtained from actual CT Image was arranged in the MC CT gantry. The mass density data of the human body were arranged at 321×321×5 voxels, and the voxel size was 0.875 × 0.875 × 1.0 mm^3 at the central slice of the voxel phantom. And the X-ray transmission data from the multidirection were acquired every 0.5 degrees by MC simulation.

X-ray source was positioned at 80 cm far from the isocenter of the MC CT Gantry, and generated photons were emitted with 30 degrees fan beam (slit width was 0.05cm at the isocenter). The photon energy was set 40 keV mono-energy, and the cut-off energies for transport calculation of electron (ECUT) and photon (PCUT) were set to 521keV and 1keV, respectively. The numbers of histories were 1,000,000 particles × 10, 20, 50 and 100 batches to evaluate the statistical noise of the MC CT image.

The table that converts CT values to mass density was obtained from CT values of the materials with already-known density. Those CT values were obtained by scanning CMS phantom in which those materials were inserted with Toshiba Asteion CT for 120kV (Figure 4).

2.3 Development of CT Reconstruction Software

CT reconstruction algorism was programmed by Visual C++ 2008 professional. First, raw data obtained by MC simulation were transferred to logarithm value. Second, because those data were fan beam transmission data, those data were converted to parallel beam transmission data numerically. Third, the data were converted into projection data which were convoluted Shepp and Logan filter by First Fourier Transform technique. Finally, CT image was reconstructed by FBP.

On the other hand, Theoretical algorism simulator based on Radon Transfer algorism (Radon Transfer Simulator : RTS at the following) was also developed by Visual C++. Then, the theoretical transmission data were obtained at almost same the MC geometry by RTS. RTS data were used to check the functioning of the reconstruction algorism. Therefore, the image reconstructed from RTS data dose not includes the influence of a statistical noise.

3. Results and Discussion

Figure 5 shows the comparison of the original CT and the CT reconstructed from RTS data. Therefore the image based on RTS is similar to the original image, the algorism of the CT reconstruction is functioning well. However, it is thought that the image quality of RTS CT is deteriorated because the histograms of the original CT and the RTS CT are a little different (Figure 6).

It is guessed that it is caused in the interpolation of the transmission data and the filter function in the reconstruction algorism because the deterioration in the image quality of the RTS CT is not due to a statistical noise.

In the result of MC simulation, the image quality of the CT is improved when the number of histories increases. However, even in case of the condition of 100×1,000,000 histories, the noise of the image is considerably strong. Therefore, the smoothing process might be given to the transmission data and the image after reconstruction. Thus, the reconstruction algorism developed by this study is very helpful to analyze CT system.

4. Conclusions

In this study, Monte-Carlo simulation CT was constructed by the EGS5 code. The reconstruction algorism of the CT developed by this study is functioning well. It is necessary to improve the deterioration in the image quality by a statistical noise for Monte-Carlo CT. However, it is useful for an educational purpose.

References

1) Kouzou Hanai, Tetsuya Horiuchi, Junko Sekiguchi, Yoshihisa Muramatsu, Ryutaro Kakinuma, Noriyuki Moriyama, Ryosuke Tuchiya, and Noboru Niki, “Computer-Simulation Technique for Low Dose Computed Tomographic Screening” J Comput Assist Tomogr, 30, 955 (2006).
2) Hideo Hirayama, Yoshihito Namito, Alex F. Bielajew, Scott J. Wilderman and Walter R. Nelson, “EGS5 USER MANUSAL SLAC-730/KEKE-2004-5,” SLAC web site, 2004
3) H. Hirayama and Y.Namito, “Lecture Notes of EGS4 Course at KEK(Japanese Part),” KEK Internal 99-5. 2, 2003
4) S. J. Wilderman and A. F. Bielajew, “Modified Random Hinge Transport Mechanics and Multiple Scattering Step-Size Selection in EGS5,” KEK Proceedings 2005-3. 3, 1-18(2005)

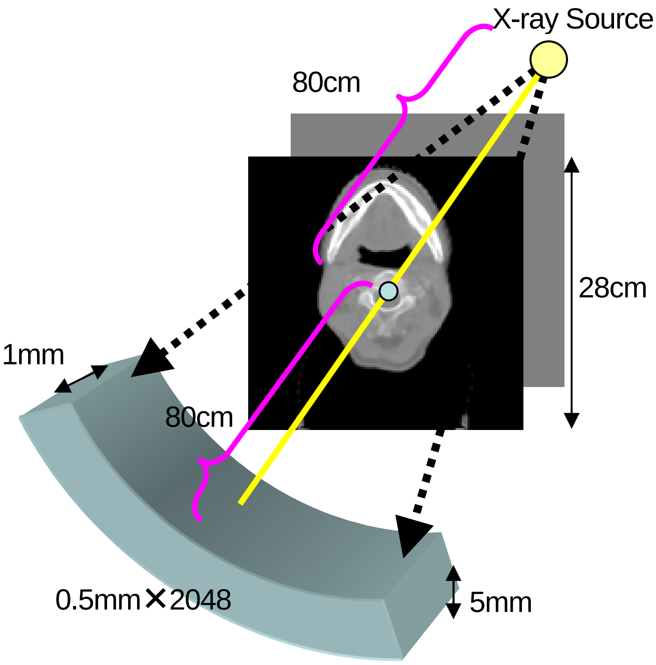

Figure 3. Shematic view of Monte-Carlo CT.

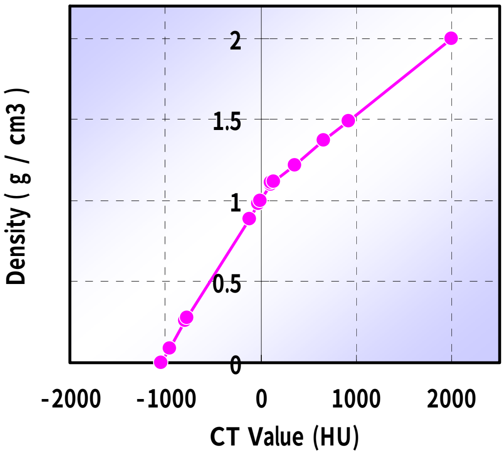

Figure 4. CT value to density transfer table.

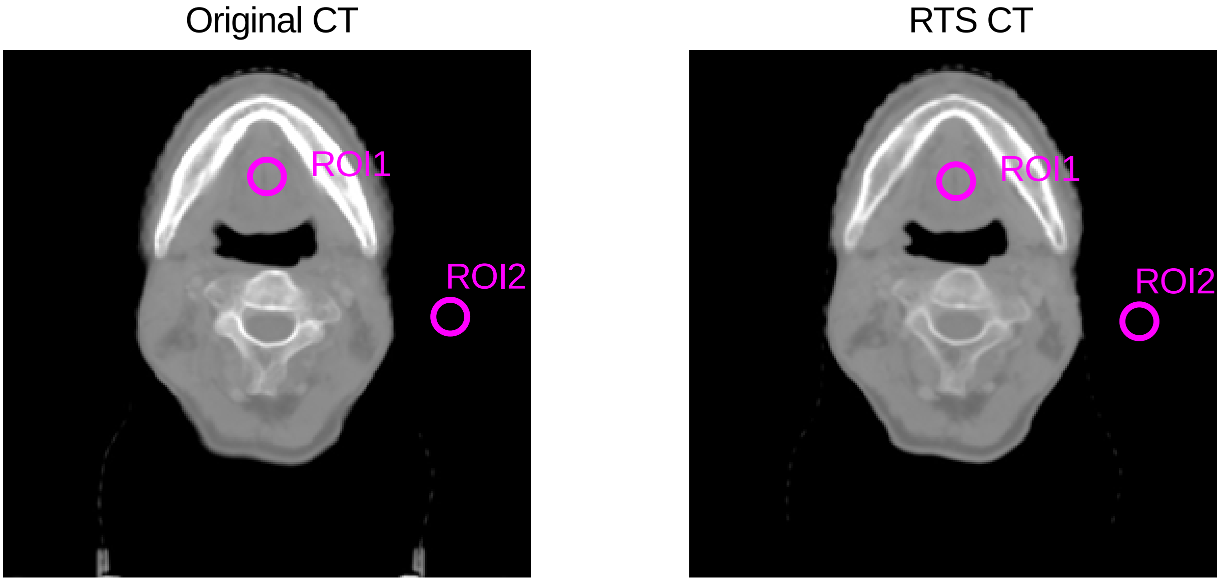

Figure 5. Comparison of Original CT and RTS CT.

Table 1. Comparison of the statistical values of Original CT and those of RTS CT.

		Original CT	**RTS CT**
ROI1	**Average**	**68.42**	**68.42**
	STDEV	**20.17**	**16.99**
ROI2	**Average**	**-1115.13**	**-1115.13**
	STDEV	**71.46**	**70.56**

CT values of both images are calibrated by average values of ROI1 and ROI2.

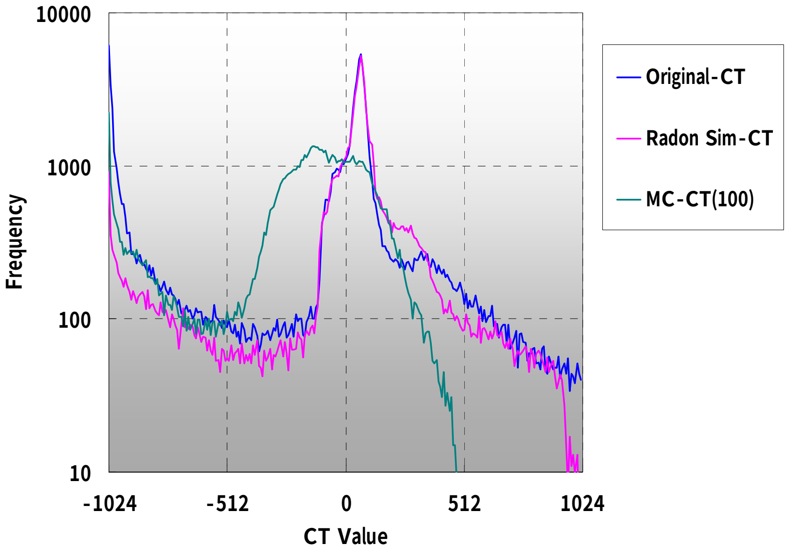

Figure 6. CT Image Histgram.

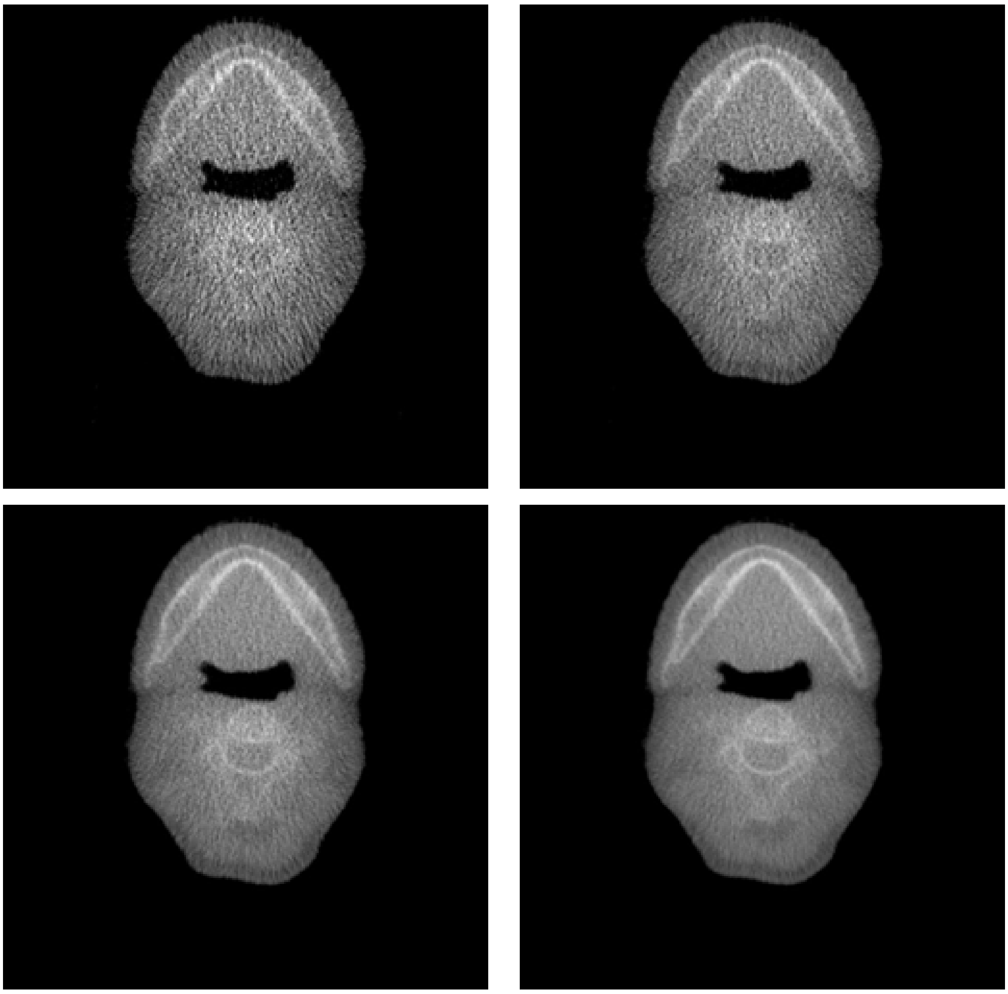

Figure 7. Comparison of statistical noise of MC CT. (Left top: 10, Right top: 20, Left down: 50 and Right down: 100 batches × 1,000,000 histories, respectively)

Table 2. Comparison of statistical noise for each history

	ROI1		ROI2	
	Average	STDEV	Average	STDEV
MC(10)	68.42	159.07	-1115.13	188.35
MC(20)		110.04		140.36
MC(50)		68.34		102.66
MC(100)		51.31		88.86

DEVELOPMENT AND VALIDATION OF A MONTE CARLO MODELING OF MILLENNIUM MLC

Y.Ishihara[1], T. Yamamoto[1,2], Y. Miyabe[2], T. Mizowaki[2], Y. Narita[2], S. Yano[3], T. Teshima[1], and M. Hiraoka[2]

[1]Department of Medical Physics & Engineering,
Osaka University Graduate School of Medicine, Osaka 565-0871, Japan
[2]Department of Therapeutic Radiology and Oncology,
Kyoto University Graduate School of Medicine, Kyoto 606-8507, Japan
[3]Clinical Radiology Service, Kyoto University Hospital, Kyoto 606-8507, Japan
e-mail: y.ishi@sahs.med.osaka-u.ac.jp

Abstract

Most of the commercial treatment planning systems doesn't take into account multileaf collimator (MLC) design which causes the leakage radiation, the tongue-and-groove effect, beam hardening and rounded leaf tip effect in intensity-modulated radiotherapy (IMRT) field. We were to develop an integrated Monte Carlo (MC) dose calculation system called MCRTV (Monte Carlo for Radiotherapy Treatment plan Verification) as a routine verification tool of radiotherapy. In this study we try to construct accurate model of the Varian Millennium 120-leaf MLC and validate the model using the EGS4/PRESTA MC code. Leakage, picket fence, and sliding window tests were calculated using well-commissioned 15MV photon beam. These results were compared and validated measured dataes. All MC simulations matched measured ones less than 2.0 %. Leaf leakage radiation was 1.38% on average. Tongue-and-groove design caused 8.3% underdose on average. According to these results, we could constructed precise Millennium model and accuracy were validated to develop a MCRTV for IMRT.

1. Introduction

The goal of radiotherapy is to control the tumor by delivering high dose only to the target without injuring the surrounding normal tissues. Toward this goal, intensity-modulated radiotherapy (IMRT) was developed. IMRT can achieve the ideal dose distribution to effectively treat a cancer, which is calculated by inverse treatment planning, by employing a computer-controlled multileaf collimator (MLC) and a medical linear accelerator. A several investigators reported that IMRT achieved higher local control rate and lower occurrence of a complication than conventional radiotherapy in prostate, head and neck cancer. [1, 2]

MLC design causes specific effects, which include the leakage radiation, [3] the tongue-and-groove effect, [4,5] beam hardening [3] and rounded leaf tip effect. [6] Leaf leakage is radiation through the very small gap between two adjacent leaves. The two adjacent leaves are coupled together through the tongue-and-groove to reduce the radiation leakage. When two adjacent leaves have different degrees of extension, the tongue side of the move extended leaf produces an underdose region near the leaf edge. This phenomenon is called tongue-and-groove effect. The dose calculation algorithms used in commercial treatment planning systems cannot calculate accurate dose which is concerned by these effects such as IMRT field. For this reason, we need more accurate calculation algorithm which can take into these effects account to simulate precisely.

In general, it is now well accepted that Monte Carlo (MC) is the most accurate dose calculation method. The strength of MC stems from the fact that it can realistically model radiation transport and interaction processes through the accelerator head, beam modifiers and the patient geometry. Many investigators have used MC for IMRT dose calculations. [7-10] Ma et al. had reported that the discrepancy between the dose distributions calculated by a finite-size pencil beam (FSPB) algorithm and MC simulation were more than 20 %. [11] The effective treatment of cancers by radiotherapy needs an accuracy of about 2 or 3 % in the dose delivery. MLC delivery issues and electron disequilibrium must be precisely considered to implement IMRT of sufficient quality.

We had been to develop an integrated MC dose calculation system called MCRTV (Monte Carlo for radiotherapy treatment plan verification) as a routine verification tool of radiotherapy treatment plans which could solve these problems. [12] The MCRTV system was developed using EGS4/PRESTA code. This system was consisted of three realistic models which were the accelerator treatment head, the MLC and the in-patient anatomy. The MC models of the 15 MV photon beam from Varian Clinac 2300C/D linear accelerator, the MLC and in-patient anatomy model built from treatment planning CT images were developed and implemented to MCRTV by Yamamoto et al. [12] Now, we try to construct accurate model of the Varian Millennium 120 - leaf MLC for dealing with this model in MCRTV. The purpose of this study was to validate 120-leaf MLC model.

2. Materials and Methods

2.1 MC modeling of the Varian Millennium MLC

We have developed the MC models of the Varian 120-leaf Millennium MLC for a 15 MV photon beam. Figure 1 shows schematic drawings of the Millennium MLC. The EGS4 MC code with the PRESTA algorithm [13] was used in this study. To model the treatment head with the MLC, they were divided into the field-independent part (i.e. from target to mirror) and the field-dependent part (i.e. jaws and MLC). Specific design of the Varian 120-leaf Millennium MLC was accurately modeled in great detail fully considering the inter-leaf minute air gap, the tongue-and-grove design, the rounded leaf tip and the leaf alignment parallel to the beam divergence. The dynamic motion of the MLC leaves is simulated by sampling the leaf positions for each incident history using a cumulative probability distribution function of each leaf position, which can be created from a relationship between the fractional number of monitor units (MUs) and the corresponding leaf positions specified in the .mlc leaf sequence file. A similar method was employed by Liu *et al* [14] for the DMLCQ component module in the EGS4/PRESTA code.

2.2 Validation of the MC models of the MLC

To benchmark the MLC model, results obtained with the model were compared with measurements and other MC calculations for a variety of test cases. Validation tests were performed using the 15 MV beam from our Varian Clinac 2300C/D. The solid water phantom (Gammex RMI, Middleton, WI) was employed for subsequent experiments. The cut-off energies for transport calculation of electron (ECUT) and photon (PCUT) in all calculations of this study were set to 521 keV and 10 keV, respectively.

The static tests for validation of the MLC model were implemented for investigation of the following effects: leaf leakage and picket fence effect. These effects are strongly affected by geometry of the MLC model. Figure 2 shows the MLC leaf settings in the beam's eye view for investigation of above MLC dosimetric effects. Dose profiles were simulated and measured with Kodak XV II films at 2cm shift from central axis. The measurements were taken with a source axis distance of 100 cm (source surface distance = 90cm, depth = 10cm), and the jaws were opened $10\times30\text{cm}^2$. The spatial resolutions used to calculate the dose were $2.0\times0.1\times0.5\text{cm}^3$ in leaf leakage case and $2.0\times0.1\times2.0\text{cm}^3$ in picket fence case.

The sliding window test to investigate the case incorporating the dynamic leaf motion was also implemented. The widths of the sliding windows were 1, 5, 10, 20, 50, 70, and 100 mm. Point doses were simulated and measured with ion chamber (JARP) at central axis, and the jaws were opened $10\times10\text{cm}^2$. T he spatial resolutions used to calculate the dose were $0.5\times2.0\times0.5\text{cm}^3$.

3. Results

Figure 3 shows a comparison of the MC calculated and measured profiles of leaf leakage. The doses were normalized at central axis dose at 10 cm depth. The peaks and the valleys of the profile due to the leakage and transmission were clearly reproduced by MC calculation. Difference of MC and measured is less than 0.5%. In this study MLC leakage was 1.38% on average. The peak positions of the MC profile almost agreed to the measurement.

Figure 4 shows the dose profiles of the MC and the measurement for the complementary field depicted in Figure 2. All data were normalized to the 10 x 10 cm^2 open field central axis dose at the depth of 5 cm. Figure 4(a) shows profile that is opened even leaves, and Figure 4(b) shows that odd leaves are opened. The averaged discrepancy of MC and measured is 1.9%.

Table 1 summarizes results for the sliding window fields. All data were normalized at the same situation of picket fence profiles. When sliding window width is 1mm, the difference is over 1.0%. In other cases errors are less than 1%. This results show that sliding window width is narrower, discrepancy of MC and measured is larger.

4. Discussion

MLC models have been developed by various reasons [15-18]. In this study we reconstructed the precise MLC model in order to deal with this model in MCRTV. MLC leakage reported by other studies were 1.51% (Siebers J F et al. [18]), 1.50% (Kim J O et al.[6]) and 1.58% (Jang Y et al.[16]). In this study MLC leakage was 1.38% on average and less than those reports by several investigators. Measurement profile is not sharper than MC. We propose this result as a cause of film measurement at depth 10cm. Siebers J F et al. and Jang Y et al. showed that the underdose due to the tongue-and-groove effect could amount to about 8% [18-19].17-18) From picket fence profiles in this study, tongue-and-groove effect reduced dose by 8.3% on average. This is in good agreement with other reports.

On modern accelerators, the MLC system is a critical and integral component for the delivery and modulation of the IMRT dose distributions. The commercial MLC have evolved to have very sophisticated designs. An approach to modeling the geometry of MLC, in which only photon attenuation and first Compton scattered photons were modeled through the MLC geometry, has been developed by Keall et al[19]18) and Siebers et al.[18]17) Fix et al [20-21]19-20) modeled the Varian 80 - leaf MLC. The leaf edges parallel to leaf motion were modeled with the tongue-and-groove, but the rounded leaf tips were simplified and modeled as planes focused at the source. Thus, although most investigators tried to reduce CPU time with variance reduction techniques, we developed accurate MLC model to provide benchmark data of dose calculation as accurate as possible.

A future direction for this study will construct precise the Millennium model for IMRT without variance reduction techniques. Then we must compare measurements and simulation to validate the Millennium model in clinical patients' case.

5. Conclusions

An EGS4 MC dose calculation system for dynamic IMRT was developed. MLC dosimetric effects were then successfully reproduced well for both of the static and the dynamic test patterns. This system will be developed into the QA system for the routine verification of the commercial treatment planning system for dynamic IMRT.

References

1) Zelefsky M J, Fuks Z, Happersett L, et al., Clinical experience with intensity modulated radiation therapy (IMRT) in prostate cancer, Radiat. Oncol. Biol. Phys. 55: 241-249 (2000)
2) Su A W, Gratzle J, Correa D, et al., Comparison of Chronic GI and GU Toxicity of Patients With Prostate Cancer Undergoing IMRT vs Conventional Radiotherapy Using Localized Fields, Radiat. Oncol. Biol. Phys. 66: 374-379 (2006)
3) Mohan R, Tong S, Arnfield S, et al., The impact of fluctuations in intensity patterns on the number of monitor units and the quality and accuracy of intensity modulated radiotherapy, Med. Phys. 27: 1226-1237 (2000)
4) Deng J, Pawlicki T, Chen Y, et al., The MLC tongue-and-groove effect on IMRT dose distributions, Phys. Med. Biol. 46: 1039-1060 (2001)
5) Hsu I C, Pickett B, Shinohara K, et al., Normal tissue dosimetric comparison between HDR prostate implant boost and conformal external beam radiotherapy boost: Potential dose escalation, Int. J. Radiat.Oncol. Biol. Phys. 46: 851-858 (2000)
6) Kim J O, Siebers J F, and Keall P J, A Monte Carlo study of radiation transport through multileaf collimators, Med.Phys. 28: 2497-2506 (2001)
7) Jeraj R and Keall P J, Monte Carlo-based inverse treatment planning, Phys. Med. Biol. 44: 1885-1896 (1999)
8) Laub W, Alber M, Birkner M, et al., Monte Carlo dose computation for IMRT ptimization Phys. Med. Biol. 45: 1741-1754 (2000)
9) Pawlicki T and Ma C M, Monte Carlo simulation for MLC-based intensity-modulated radiotherapy, Med. Dosim. 26: 157-168 (2000)
10) Ma C M, Mok E, Kapur A, et al., Clinical implementation of a Monte Carlo treatment planning system, Med. Phys. 26: 2133-2143 (1999)
11) Ma C M, Pawlicki T, Jiang S B, et al., Monte Carlo verification of IMRT dose distributions from a commercial treatment planning optimization system, Phys. Med. Biol. 45: 2483-2495 (2000)
12) Yamamoto T, Mizowaki T, Miyabe Y, et al., An integrated Monte Carlo dosimetric verification system for radiotherapy treatment planning, Phys. Med. Biol. 52: 1-18 (2007)
13) A. F. Bielajew A F and D. W. O. Rogers, PRESTA: The parameter reduced electron-step transport algorithm for electron Monte Carlo transport, Nucl. Instrum. Methods B. 18: 165-181 (1987).
14) Liu H H, Verhaegen F and Dong L, A method of simulating dynamic multileaf collimators using Monte Carlotechniques for intensity-modulated radiation therapy, Phys. Med. Biol. 46: 2283- 2298 (2001).
15) Walle J V, Martens C, Reynaert N, et al., Monte Carlo model of the Elekta SLiplus accelerator: validation of a newMLC component module in BEAM for a 6 MV beam, Phys. Med. Biol. 48: 371-385 (2003)
16) Jang S Y, Vassiliev O N, Liu H H, et al. , Development and commissioning of a multileaf collimator model in Monte Carlo dose calculations for intensity-modulated radiation therapy, Med. Phys. 33: 770-781 (2005)
17) Heath E and Seuntjens J, Development and validation of a BEAMnrc component module for accurate Monte Carlo modelling of the Varian dynamic Millennium multileaf collimator, Phys. Med. Bio. 48: 4045-4063 (2003)
18) Siebers J V, Keall P J, Kim J O, et al. ,A method for photon beam Monte Carlo multileaf collimator particle transport, Phys. Med. Biol. 47: 3225-3249 (2002)
19) Keall P J, Siebers J V, Arnfield M, et al., Monte Carlo dose calculations for dynamic IMRT treatments, Phys. Med. Biol. 46: 929-941 (2001)
20) Fix M K, Manser P, Born E J, et al., Monte Carlo simulation of a dynamic MLC based on a multiple source model, Phys. Med. Biol. 46: 3241-3257 (2001)
21) Fix M K, Manser P, Born E J, et al., Monte Carlo simulation of a dynamic MLC: implementation and applications Z, Med. Phys. 11: 163-170 (2001)

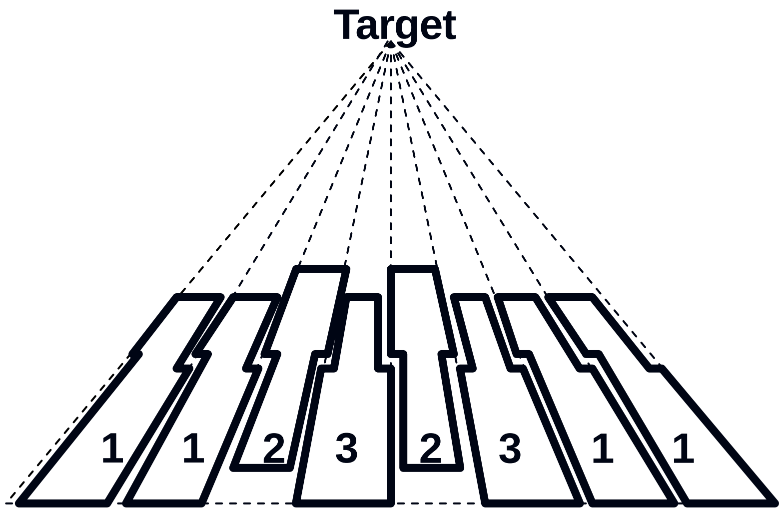

Figure 1. Schematic diagram of the MLC models which focus towards the target. Leaf number 1, 2, and 3 is full-leaf, target-leaf, and isocenter-leaf respectively.

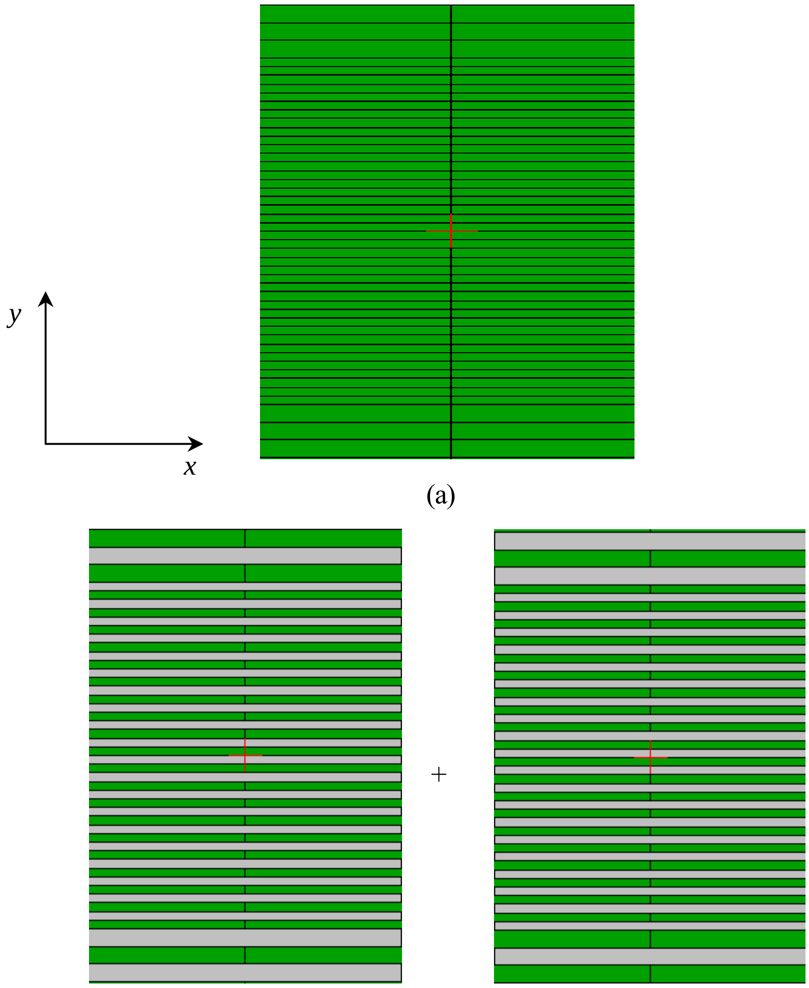

(a)

(b)

Figure 2. MLC leaf settings in the beam's eye view: (a) for leakage (b) for picket fence tests

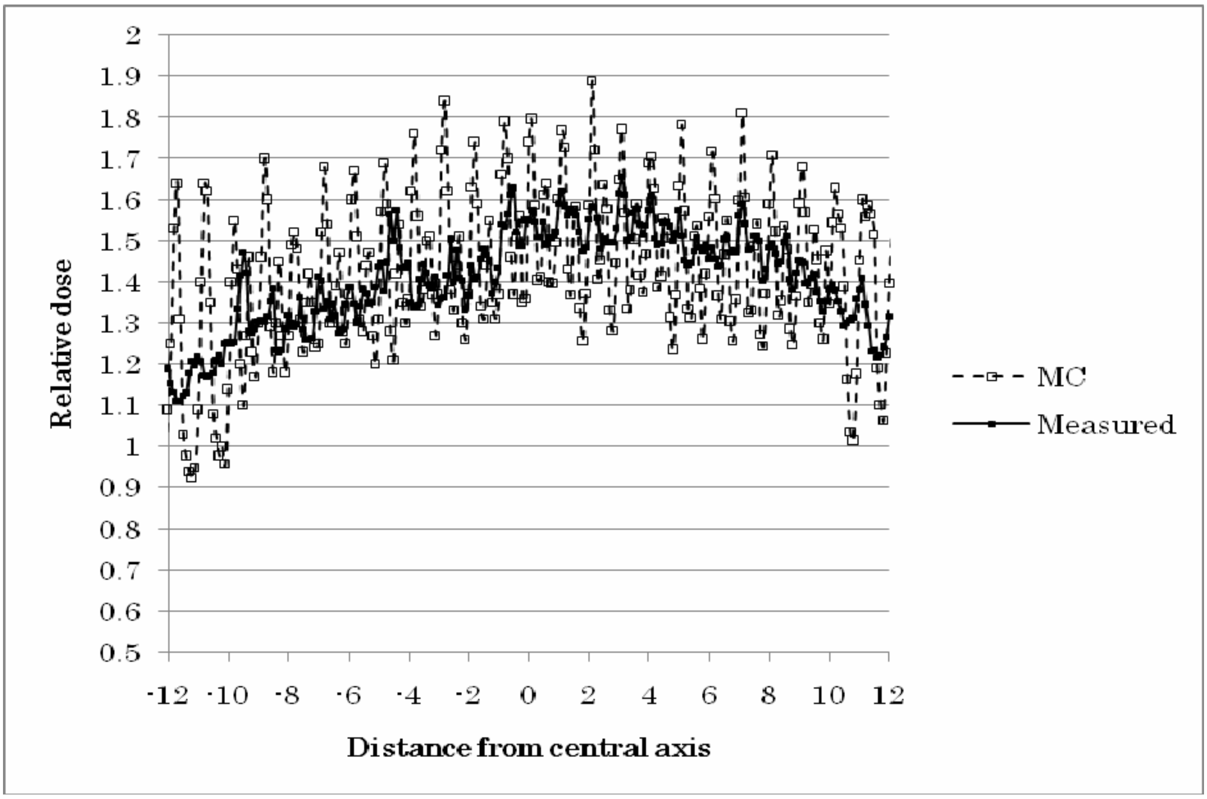

Figure 3. Dose profiles in *y*-direction at *x* = 2.0 cm of the fields with the MLC leaf setting depicted in Figure 2(a).

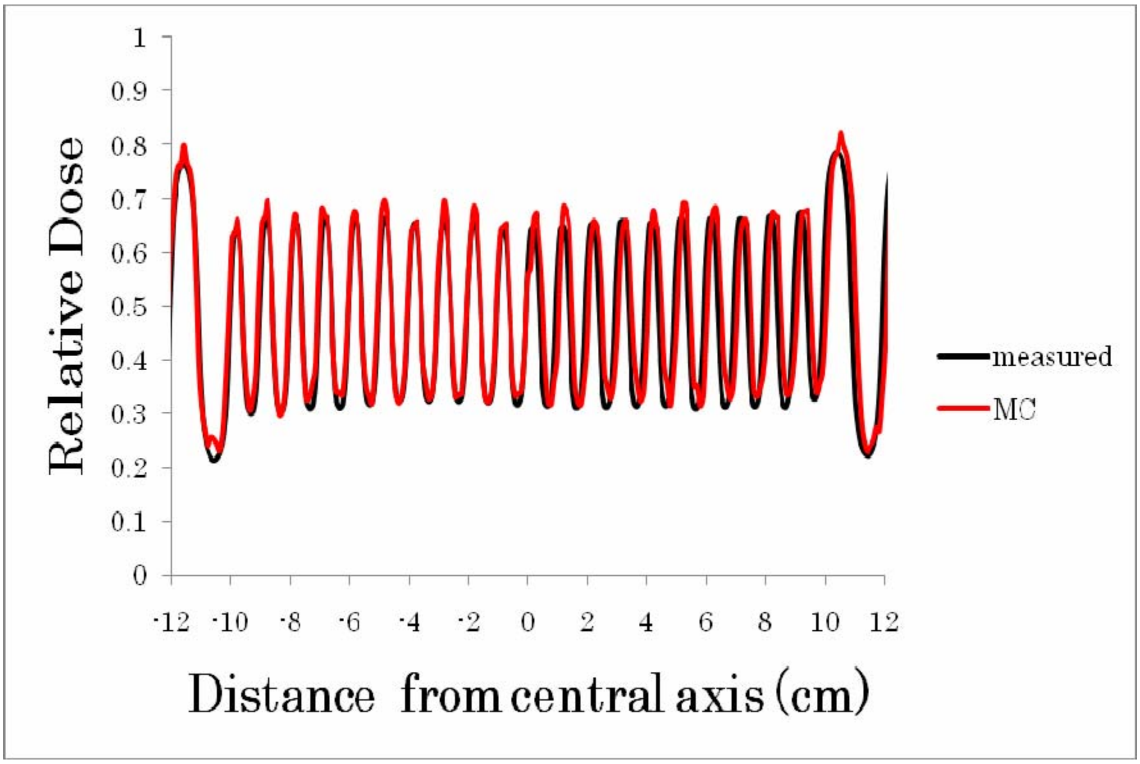

(a)

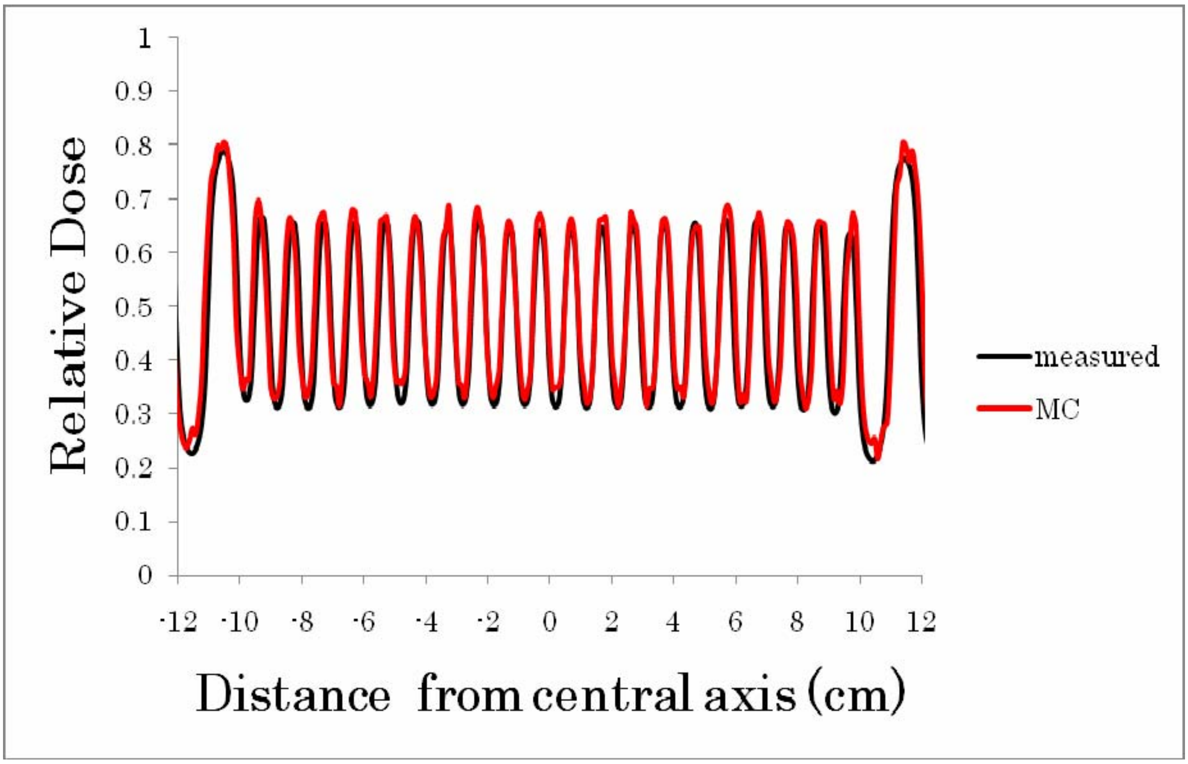

(b)

Figure 3. Picket fence test profiles: (a) even leaves open, (b) odd leaves open.

Window width (cm)	Measured (%)	MC (%)	Difference (%)
1	5.03	3.98	1.05
5	8.61	7.69	0.92
10	12.69	12.00	0.68
20	19.92	19.17	0.75
50	35.68	35.25	0.43
70	43.19	42.71	0.48
100	51.73	51.72	0.34

Table 1. Results of sliding window test.

Investigation for the calculation of absolute dose exposed from a brachy therapy source with Monte Carlo simulation

H. Shibata[1], K. Tabushi[2], K. Narihisa[3], Y. Aoyama[1,4], and Y. Obata[2]

[1]Department of Radiological Technology, Graduate School of Medicine, Nagoya University
1 - 1 - 20 Daikou - Minami, Higashi-ku, Nagoya, Japan
[2]Department of Radiological Technology, School of Health Science, Nagoya University
[3]Department of Radiology, Meijo Hospital
[4]Department of Radiology, Nagoya University Hospital
e-mail: shibata.hiroki@f.mbox.nagoya-u.ac.jp

Abstract

In these day, Monte Carlo (MC) simulation has been used in radiological studies frequently, and its simulation results are often output as relative values which are normalized with a value at a reference point. In the calculation of the relative dose with MC simulations, the deposited energies are calculated. Moreover, the deposited energy is calculated as the energy per incident particle, commonly. Therefore, we thought that the absolute dose was calculable only with the MC simulations using the deposited energy, and we computed the absolute exposure rate distribution exposed from a brachy therapy source in water with EGS5 and GEANT4. The simulated distributions and their profiles on the long axis and the short axis of the source were evaluated by comparison with the measured data quoted from the literature. In the comparison of the distribution, the significant difference between the simulated distribution and the measured one was found around the long axis of the source. The simulated profiles along the long axis of the source was compared with the literature data measured with film and showed agreement with it within about 7% in difference. In the comparison among the simulated profiles along the short axis of the source, the literature data using film, and the data with an ion chamber showed agreement with each other. It was shown that the absolute dose was calculable with MC simulations because the simulated profiles along the short axis of the source agreed with the measured profile with the ion chamber.

1. Introduction

Recently, Monte Carlo (MC) simulation has been utilized in radiological studies frequently. In the use of the simulations for those studies, there are many advantages such as that we can obtain the dose without real irradiation equipments and measuring devices and we can calculate the amount which is difficult to measure like energy spectra of secondary particles and the dose at the location where measuring devices are not able to be put in. In the discussions about the absorbed doses with MC simulations, the relative doses are calculated and commonly evaluated by the comparison in relative values with measured doses.

For obtaining the relative doses, deposited energies at each region of interest are computed through the simulations and normalized with the energy at a reference point. The deposited energies are usually expressed as those per incident particle. Therefore, we conceived that the absolute dose could be obtained only with MC simulations applying the deposited energies per incident particle when the amount of incident particles that were exposed at the measurement time was already known. In this investigation, the absolute exposure rate distribution from a brachy therapy source was calculated with the two MC simulation codes EGS 5 and GEANT 4 and evaluated by comparison with a literature data [1].

2. Materials and Methods

2.1 Modeling of the brachy therapy source

In the calculation of the absolute dose with MC simulations, as described above, it is needed the amount of incident particles is known. A brachy therapy source is covered with a metal capsule which is contained radioisotope, and the amount of its emissive photons per time is calculable from a half-life of radioisotope inside it. Therefore, the brachy therapy source was selected as the model of this simulation.

The selected source was a custom-made ^{137}Cs tubular source (The Radiochemical centre, Amersham) described the literature. The length and the diameter of its stainless capsule were 21 mm and 2.3 mm, respectively (fig.1). The thickness of the capsule was 0.5 mm, and the active length of the source was 15 mm. The model source was reconstructed referring it. As shown in fig.1, the real source has the hole to knot colored strings for distinguishing the sources. However, the model source was constructed without the hole for simplifying. The materials of the source and its compositions are shown in table.1. In this simulation, the emitted particle from ^{137}Cs was regarded as only 662 keV gamma ray.

2.2 Calculation of the absolute dose distribution

For calculating the absolute dose distribution, the deposited energy distribution in water was simulated with the model source using EGS5 and GEANT 4. The geometry is shown in fig.2. The model source was placed in the center of an aquarium which size was 30 x 30 x 30 cm^3. The data acquisition regions were allocated from 0 cm to 5 cm on the first quadrant of the y-z plane in the aquarium. The size of each region was 0.1 x 0.1 x 0.1 cm^3. The simulation result was expressed as the deposited energy per unit volume per the incident photon at each region.

The absolute dose distribution was calculated as exposure dose rate per hour [R/h] since the literature data was expressed by this unit. The calculations at each region are as follows; at first, the absorbed dose per incident photon D_{Gy} $[\mathrm{Gy/incident}]$ is calculated,

$$D_{Gy} = E \cdot \frac{10^3}{d_w \cdot J},$$

where E is the deposited energy per unit volume per incident photon [MeV/cm^3/incident photon], d_w is the density of water, 1.00 [g/cm^3], and J is the conversion constant from eV to joule.

Secondarily, the absorbed dose D_{rad} [rad/incident] is obtained,

$$D_{rad} = D_{Gy} \cdot 100.$$

Finally, the absolute exposure dose rate $\dot{R}$ [R/h] is obtained by following formula.

$$\dot{R} = D_{rad} \cdot \frac{N \cdot 3600}{C} \cdot r_d,$$

where N was the amount of decay per second [Bq], C [rad/R] is the conversion constant from roentgen to rad, and r_d is the emissive rate of 662 keV gamma ray.

2.3 Measurement of dose distribution

In this investigation, the measurement data was quoted from a literature [1]. In the literature, the exposure dose rate distribution was obtained with measurement using film and the calculation of the exposure dose rate. The distribution is shown in fig.3. The profile measured with an ion chamber in water along the short axis of the source was also quoted.

3. Results and Discussions

Figs.4(a) and 4(b) show the absolute exposure dose rate distributions calculated with EGS 5 and GEANT 4, respectively. They exhibit the similar distribution, and significant differences are not observed between them. To compare them with the distribution of the measurement, the simulated and measured distributions were overlapped as shown in fig.5 and fig.6. Both of the simulated results show an ellipsoidal distribution like the measured results along the short axis of the source. However, along the long axis, the difference between two distributions is found. In the measured distribution, the isodose rate curves are domed on the side of the source around the long axis, whereas this tendency is not shown in the simulated distributions. It is presumed the difference was caused by the edge shape of the model source, because the domed parts of the measured isodose rate curves are placed on the line extended from the edge of the source. Since the model source was reconstructed according only to the literature data, the shape of the edge might be inaccurate in this simulation.

The profiles on the long axis and the short axis are shown in fig.7 and fig.8, respectively. As shown in fig.6, the simulated profiles and quoted profiles measured with the film were shown the same tendency. The differences between them were around 15 % in the region of 3 cm in distance, and within 7 % except that region. This exhibits the simulated results along the long axis agree with the quoted data obtained with film on some level just on the long axis. In fig.8, the quoted profile with the ion chamber is plotted additionally. The all profiles along the short axis show agreement with each other. As seen in the profiles, the absolute exposure dose rates with simulations get closer to the quoted results measured with the ion chamber at the region of 1 cm in distance. The exposure dose rate of the quoted profile obtained with film is the calculated values. In this calculating method, the radioactive part of the source is assumed to the line source, and this assumption increases the error near the source. This is speculated as the cause why the simulated profiles showed better agreement with the quoted profiles obtained with the ion chamber than that with film.

4. Conclusions

In this work, computing the absolute doses with MC simulations was examined through the calculation of the exposure dose rate from ^{137}Cs brachy therapy source. In the evaluation of the calculation, exposure dose rate distribution and the profiles along the source axis in water were compared with the literature data. In the comparison of the distribution, the significant difference between the simulated distribution and that of the literature was found around the long axis of the source. The simulated profiles along the long axis of the source were compared with the literature data obtained with film and showed agreement with it within around 7% in difference. On the other hand, in the comparison among the simulated profiles along the short axis of the source, the literature data obtained with film, and that with the ion chamber showed agreement with each other.

In summary, since the simulated profiles along the short axis of the source agreed with the quoted profiles measured with the ion chamber, it was shown that the absolute dose was calculable with MC simulations.

References

1) E. Tazaki, K. Kawashima, T. Hiraoka, H. Matsuzawa, and T. Arai, “The dose distribution of the Cesium tubular source,” Jpn. J. Clin. Radiol. 17, 359-363 (1972)
2) H. Hirayama, Y. Namito, A.F. Bielajew, S.J. Wilderman and W.R. Nelson, “The EGS5 Code System,” SLAC-R-730 (2005)
3) GEANT4 Collaboration, “GEANT4 User's Guide for Application Developers” [online], available at http://geant4.web.cern.ch/geant4/support/userdocuments.shtml

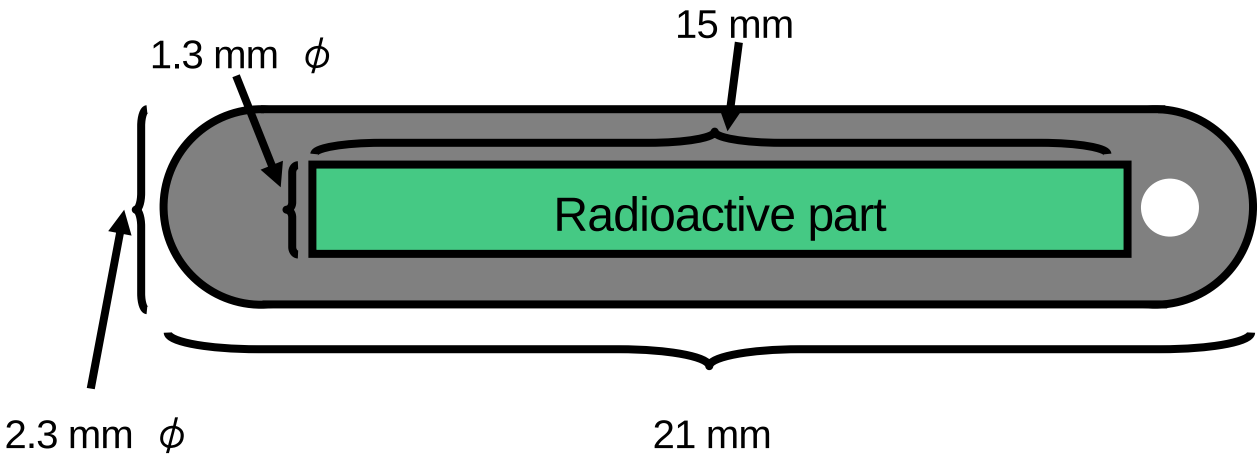

Fig.1 Overview of the 137Cs tubular brachy therapy source

Table.1 the compositions of the materials of the ^{137}Cs tubular source

Component	Material	Atomic composition (%)	Density [g/cm^3]
Source capsule	SUS 316 Stainless steel	C(0.04), Si(0.61), Mn(0.81), P(0.025), S(0.001), Ni(11.23), Cr(16.64), Mo(2.27), N(0.073), Fe(68.301)	7.98
^{137}Cs	Borosilicate glass	Si(26.18%), Ti(3%), Al(1.59%), B(3.73%), Mg(1.21%),Ca(2.86%), Na(12.61%), Cs(0.94%), O(47.89%)	2.9

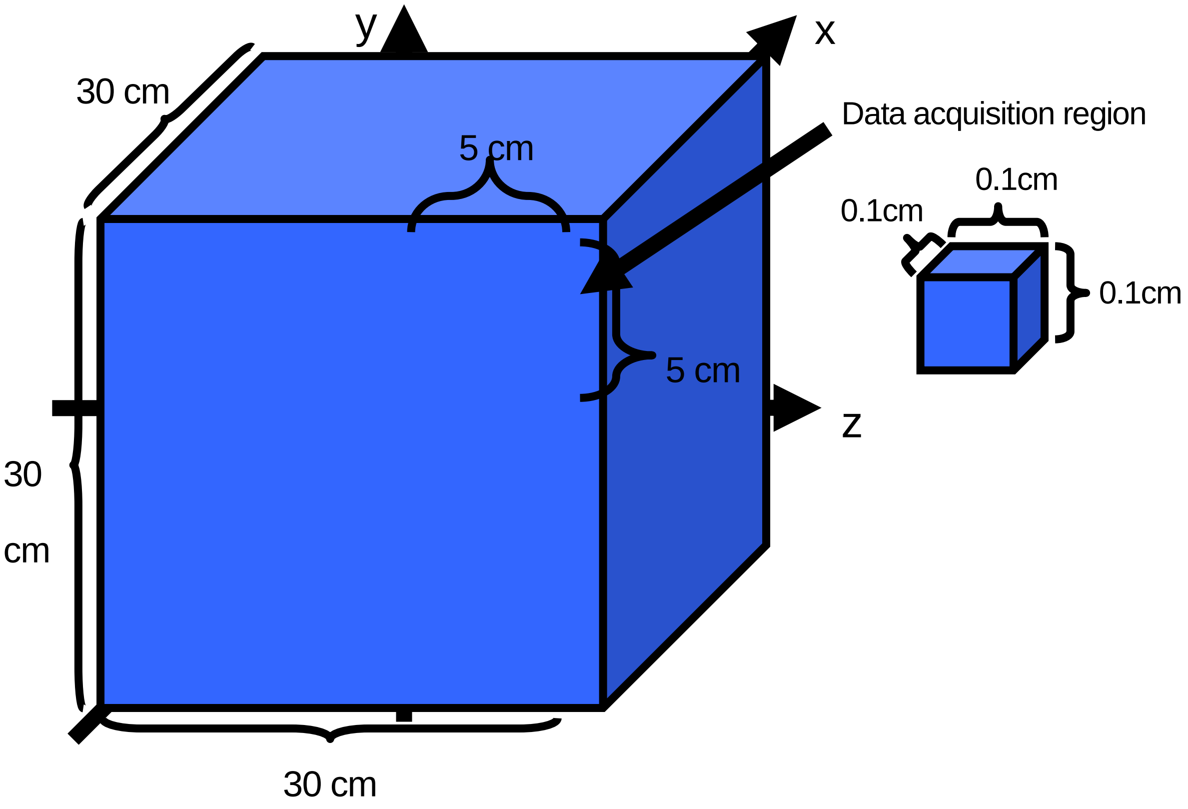

Fig.2 Overview of the geometry calculating the deposited energy distribution

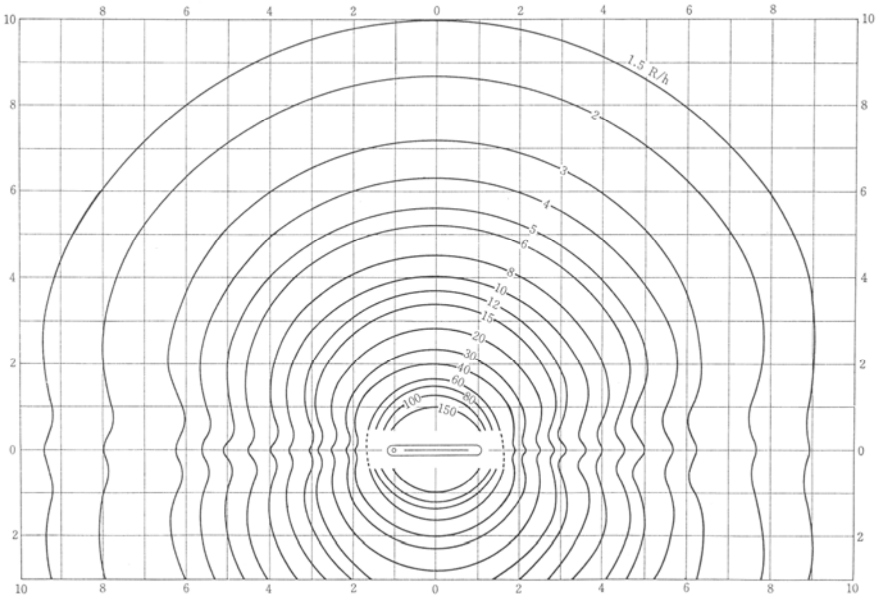

Fig.3 the exposure dose rate distribution measured with the film from the literature

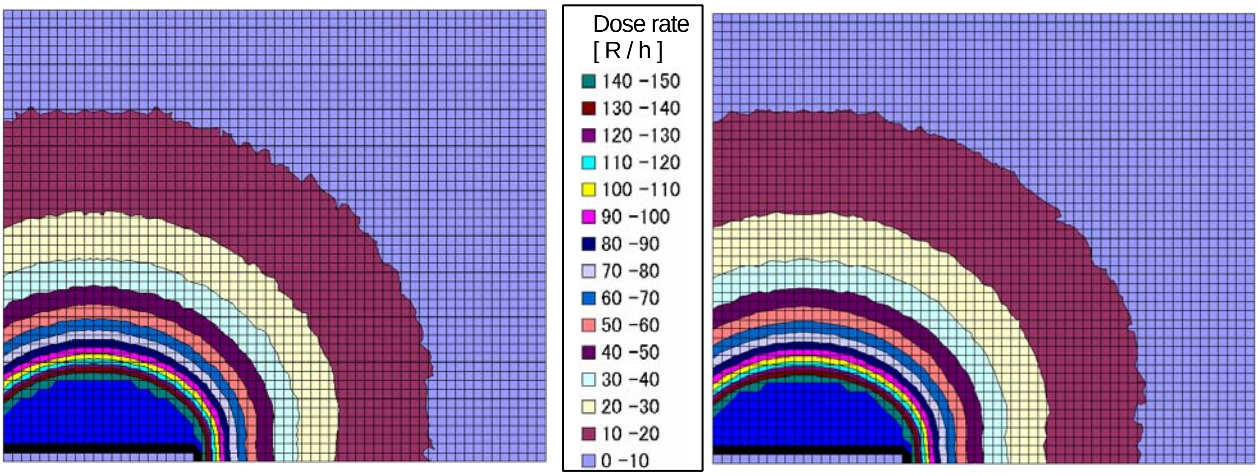

(a) (b)

Fig.4 the simulated distribution with EGS 5 and GEANT4:
(a) calculated with EGS5 (b) calculated with GEANT4

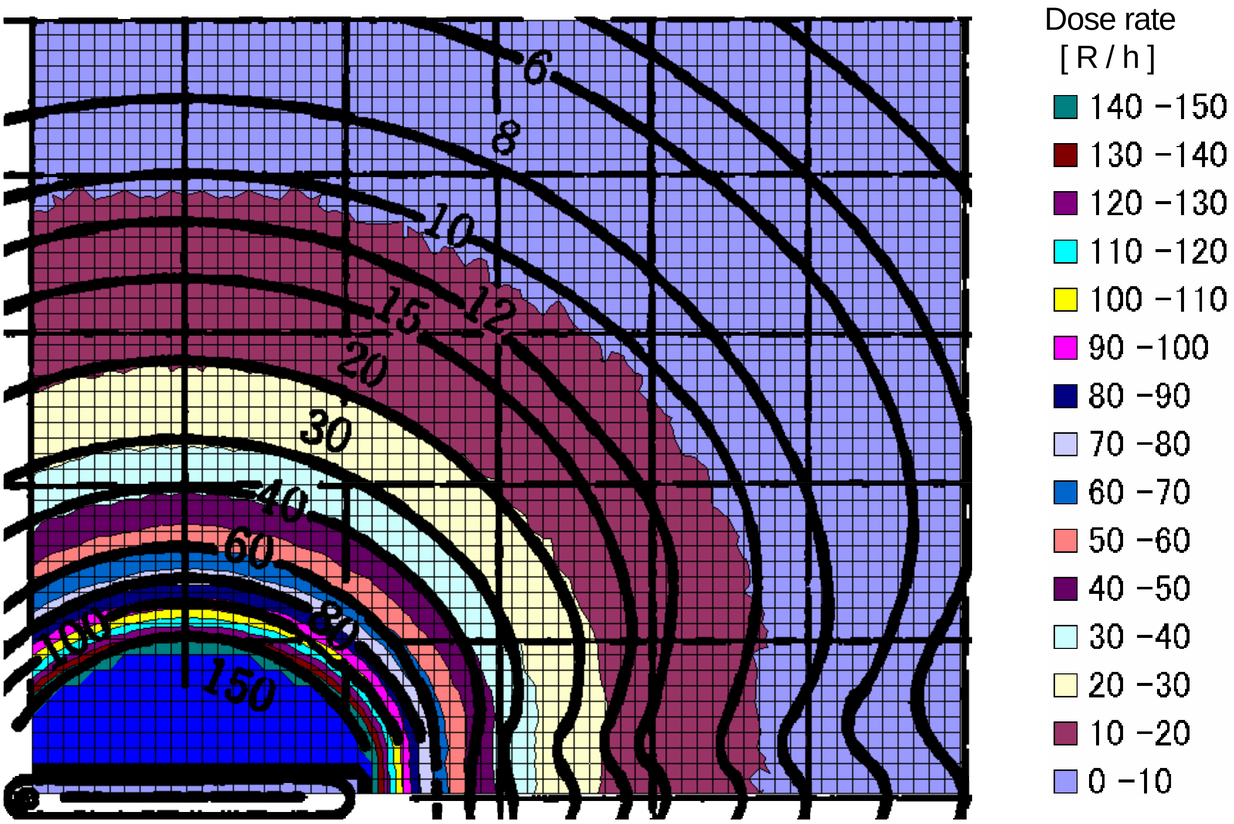

Fig.5 the simulated distribution with EGS 5 and the overlapped measured distributions from the literature

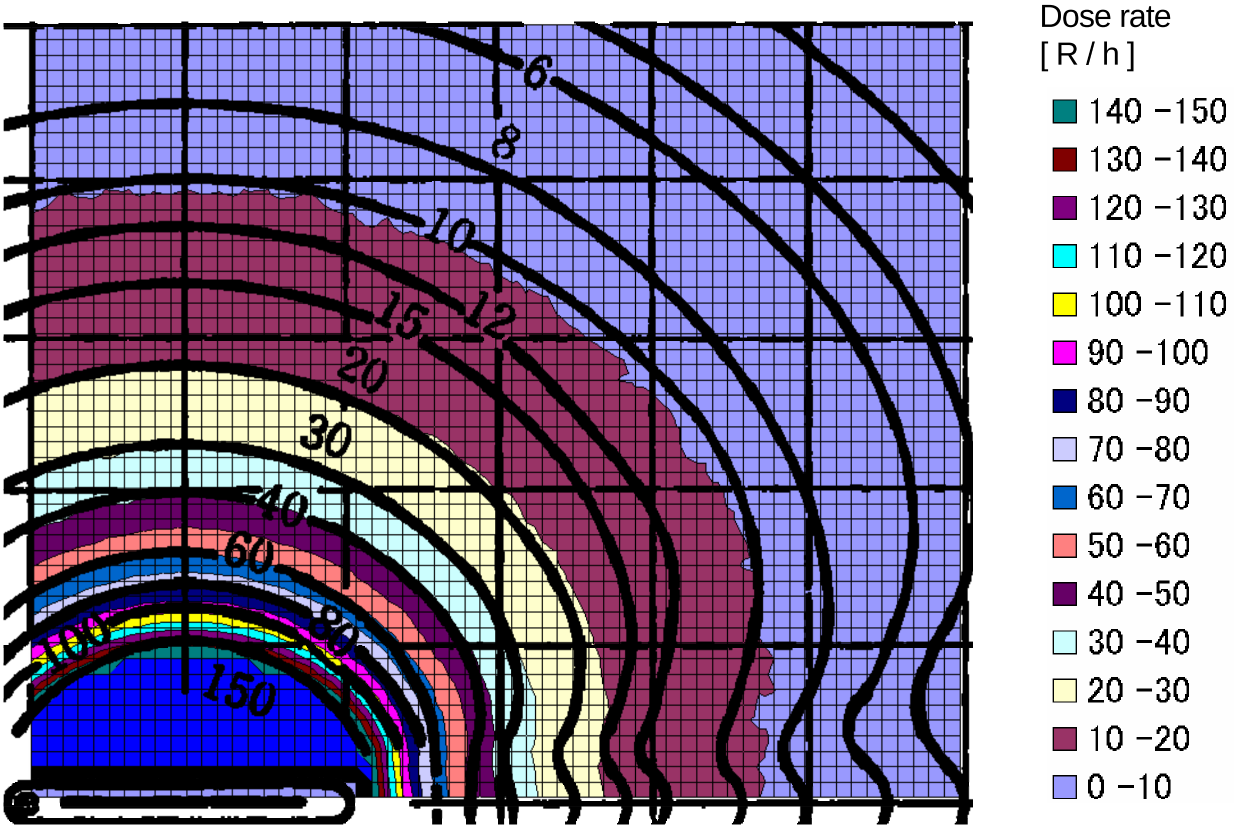

Fig.6 the simulated distribution with GEANT 4 and the overlapped measured distributions from the literature

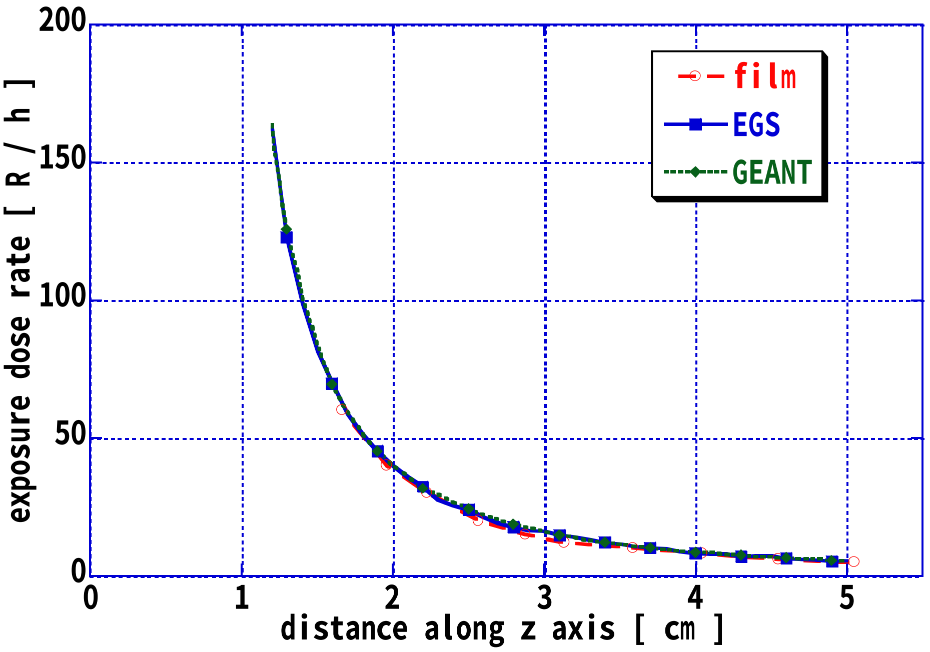

Fig.7 the profiles along the long axis of the ^{137}Cs tubular source

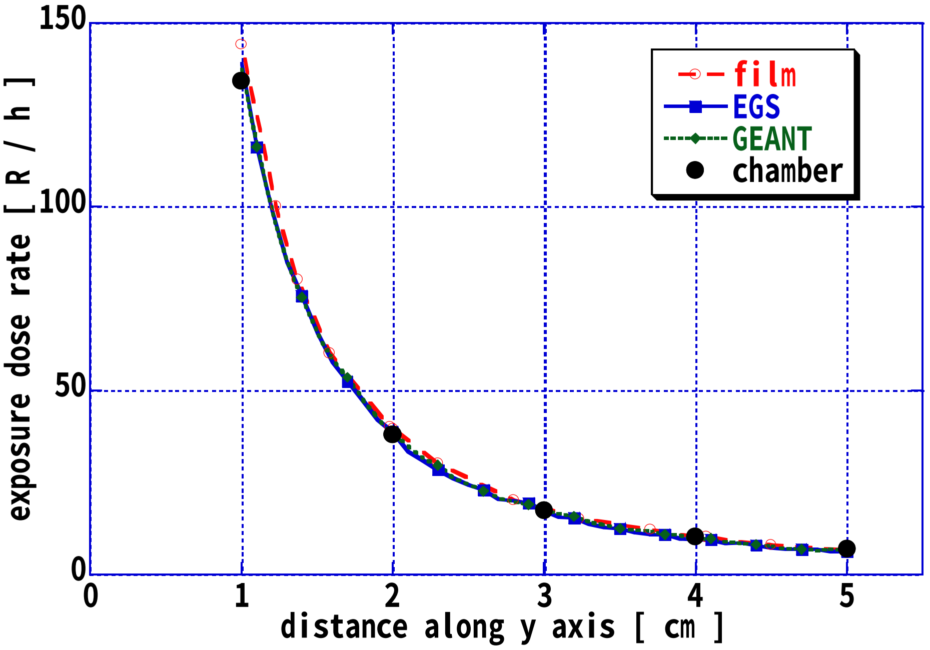

Fig.8 the profiles along the short axis of the ^{137}Cs tubular source

THE ACCURACY OF CALCULATION USING RADIATION TREATMENT PLANNING SYSTEM WITH TITANIUM IN A HUMAN BODY

K. Yasui[1], T. Shimozato[2], Y. Aoyama[3], K. Okudaira[3], R. Kawanami[1],
K. Habara[1], H. Shibata[1], T. Oshima[1] and Y. Obata[2]

[1]Department of Radiological Technology, Graduate School of Medicine, Nagoya University
1-1-20 Daiko-Minami, Higashi-ku, Nagoya, Japan
[2] Nagoya University School of Health Science
[3]Division of Radiology, Nagoya University Hospital
e-mail: yasui.keisuke@a.mbox.nagoya-u.ac.jp

Abstract

A radiation treatment planning, which was calculated using Radiation Treatment Planning Systems (RTPS) has been unsuccessful in the correct calculation of dose perturbations for high-density substances. High-density metal objects such as prosthetic dental implants, metal hip prosthesis, and others are implanted occasionally into human bodies. In this work, the dose distributions inside a tough water phantom with titanium irradiated by 4 MV and 10 MV photon beams for a 5 x 5 cm^2 field size were evaluated. Dose distributions were measured using Gafchromic Film RT-QA and calculated by Monte Carlo (MC) simulation or RTPS. By these evaluations, we investigated the accuracy of the calculation using RTPS for the existence of titanium. Depth-dose profiles obtained using the film and the MC simulation agreed within ±5 %. The rate of changes (RC) between the MC simulations and the RTPS calculations were -13.2 % (4 MV) or -17.2 % (10 MV) in front of titanium, and 15.8 % (4 MV) or 3.9 % (10 MV) at behind of titanium (shown in Table 1), where RC (%) = ((D_{xio} - D_{EGS}) / D_{EGS}) x 100, D is relative dose. For the depth deeper than 7 cm, the results show no much difference.

1. Introduction

In radiotherapy, dose distributions inside patients are calculated using Radiation Treatment Planning Systems (RTPS). The correct dose calculation in the radiation treatment planning is a crucial component as significant deviations from the prescribed dose may change the outcome of the treatment. However, the RTPS has been unsuccessful in the correct calculation of dose perturbations for high-density substances (such as a bone or a metal). [1]

High-density metal objects such as prosthetic dental implants, metal hip prosthesis, and others are implanted occasionally into human bodies. Some of prostheses are mainly composed of titanium, and titanium causes the dose perturbation at its interface. In this work, dose distributions inside a tough water phantom (Kyoto kagaku co.,LTD) with 1.0 x 1.0 x 30.0 cm^3 titanium bar were evaluated. Dose distributions were obtained using film measurements, Monte Carlo (MC) simulations and RTPS calculations. By these evaluations, the accuracy of the calculation using RTPS for the existence of titanium was investigated.

2. Materials and Methods

2.1 Film measurements to obtain density-dose conversion curve and depth-dose profiles

We used a though water phantom and Gafchromic Film RT-QA (ISP.inc) with the same lot number. This film was selected due to its characteristics that it can be used in bright light, closely contacts to the titanium and the phantom, etc [2]. As reported by Miyazawa [3], the uncertainty of measurement using the Gafchromic Film RT-QA was approximately 5.0 %. 4 MV and 10 MV photon beams from a medical linear accelerator Clinac 21 EX (Varian,inc) were used to obtain the density-dose conversion curve and depth-dose profiles. To obtain the density-dose conversion curve, calibration films were placed in the perpendicular to the central axis of the beam, and exposed 16 steps of monitor-units (MU) from 0 MU to 700 MU for a 10 x 10 cm^2 field size at 10 cm depth (100 MU = 1 Gy at depth of dose maximum for each energies). In film calibrations, source surface distance (SSD) was 90 cm. Measurement films to obtain depth-dose profiles were placed in the parallel to the central axis of the beam and exposed 600 MU for a 5 x 5 cm^2 field size at the surface. In film measurements, SSD was 100 cm and the geometry is shown in Fig. 1. All films were digitalized by a commercial scanner (EPSON Offirio ES 10000G) and analyzed by DD-system (R-TECH.INC).

2.2 Monte Carlo simulations to obtain depth-dose profiles

The MC simulation code Electron Gamma Shower 5 (EGS5) was used. In the comparison of depth-dose profiles between the film measurement and the MC simulation, the simulation geometry was reconstructed accurately from the measurement geometry (shown in Fig. 1). The composition of the film was H: 39.7, Li: 0.3, C: 42.3, N: 1.1, O: 16.2 and Cl: 0.3 (percentage by weight, %) and the density was 1.13 g/ cm^3. The density of the tough water phantom was 1.02 g/ cm^3. Data acquisition regions were allocated on the central axis of the beam and each voxel size was 0.5 x 0.01 x 0.1 cm^3. Fig. 2 shows the geometry in the comparison of depth-dose profiles between the MC simulation and the RTPS calculation. Data acquisition regions were allocated on the central axis of the beam and each voxel size was 0.5 x 0.5 x 0.1 cm^3 from the surface to 30 cm depth.

Energy spectra of photon beams excerpted from published data for 4 MV and 10 MV photon beams of Varian in all simulations[4]. Statistical uncertainties of the MC simulations were less than 2.0 % at all depths.

2.3 RTPS calculations to obtain depth-dose profiles

A commercial RTPS XiO (Version 4.3.1, CMS.Inc) was adopted and the superposition algorithm was selected for all XiO calculations because the superposition algorithm is more accurate than other algorithms including convolution, pencil beam, and Clarkson[5]. The dose distribution calculated using the superposition algorithm was fitted in that of the same linear accelerator used in the measurement. As reported by Miften et al. [6], the uncertainty of the calculation result using the superposition algorithm was estimated as 2 % or 2 mm for a homogeneous media and 3 % or 3 mm for an inhomogeneous phantom.

The tough water phantom and titanium regions are shown in Fig. 2. A computed-tomography (CT) number-electron density conversion table is required for the treatment planning based on CT images. Materials those relative electron density is higher than 2.0 (particles/m^3) are not automatically assigned the proper CT number because the relative electron density of the calibration phantoms typically used to make the CT number-electron density conversion table ranges from air to bone (0.001-1.737, particles/m^3). Since relative electron density of titanium is higher than 2.0, that was assigned manually to the proper contoured volume, not relying on the CT number to electron density table.

3. Results and discussion

3.1 Comparison between the film measurement and the MC simulation

Fig.3 shows percentage depth dose (PDD) curves for 4 MV. To 15 cm depth, PDD curves agreed within ±2.0 % among the MC simulation, the film measurement and the ion chamber measurement except the buildup region. The dose measured using film was less than 2.0 % at 15 cm depth and 5.4 % at 25 cm depth for those measured by the ion chamber. Fig. 4 shows depth-dose profiles along the central axis of the beam inside the tough water phantom for the existence of titanium bar for 4 MV. The depth-dose profiles of the MC simulation and the film measurement agreed within ±5.0 % dose discrepancy at all depths except the buildup region. As shown in Figs. 3 and 4, the accuracy of MC simulation for the existence of titanium was confirmed in this study.

3.2 Comparison between the MC simulation and the RTPS calculation

Figs. 5 and 6 shows the depth-dose profiles simulated using the MC and calculated using XiO with superposition algorithm for 4 MV and 10 MV photon beams respectively. The MC simulation and the XiO calculation produced different results at the titanium interface. Simulation results of MC show that the back scatter radiation contributes a peak at depth 4.5 – 5.0 cm and re-buildup region appears at behind of titanium. In these regions, the rate of changes (RC) between the MC simulations and the RTPS calculations were -13.2 % (4 MV) or -17.2 % (10 MV) in front of titanium, and 15.8 % (4 MV) or 3.9 % (10 MV) at behind of titanium (shown in Table 1), where RC (%) = ((D_{xio} - D_{EGS}) / D_{EGS}) x 100, D is relative dose. RTPS cannot calculate precisely the dose of the backscatter radiation from titanium. As reported by Kurooka [7], the inhomogeneity correction on the basis of the density scaling theorem has limitations. The results of this study were affected by such limitations. For the depth deeper than 7 cm, the results show no much difference.

Figs. 7 and 8 show energy spectra of backscatter photons and electrons by titanium simulated by EGS5 code for 4 MV and 10 MV beams respectively. As shown in Figs. 7 and 8, most of compositions of backscatter energy spectra were low-energy photons. Thus, it will be able to prevent these backscatters by covering the prosthesis.

4. Conclusions

The accuracy of XiO calculation for the existence of titanium was investigated in this work. Depth-dose profiles obtained using the film agreed with the MC simulation. In the comparison of depth-dose profiles between the MC simulation and the XiO calculation, the dose calculated using XiO was higher than that simulated by MC at the anterior surface of titanium. Thus, for the existence of prosthesis, the treatment planning calculated using the XiO with superposition algorithm have possibilities to underestimate the prescribed dose and may cause damage to healthy tissue at the surface of prosthesis. In the region behind of prosthesis, it may cause under dosage to the tumor because the dose calculated using the XiO were higher than that simulated by MC. For the depth deeper than 7 cm, the result shows no much difference.

References

1) T.Krieger and O.Sauer. “Montecarlo versus pencilbeam collapsed-cone-dose calculation in a heterogeneous multilayer phantom.” Phys Med Biol, **50**; 859–868. (2005).
2) MJ. Butson, T. Cheung and Y. PKN. “Absorption spectra variations of EBT-radiochromic film from radiation exposure.” Phys Med Biol, **50**; 135–140. (2005).
3) M.Miyazawa. “The dosimetry procedure of Gafchromic Film RT-QA” Jpn.J.Radiol.Technol,**62**; 1428-1436 (2006)

4) D. Sheikh-Bagheri and D. W. O. Rogers. “Monte Carlo calculation of nine megavoltage photon beam spectra using the BEAM code” Med. Phys. **29**; 391-402, (2002)

5) S. Spirydovicha, L. Papieza, M. Langera, G. SandisonbaV. Thaia, “High density dental materials and radiotherapy planning: Comparison of the dose predictions using superposition algorithm and fluence map Monte Carlo method with radiochromic film measurements,” Radiother Oncol.**81**; 309-314, (2006)

6) M. Miften, M. Wiesmeyer, S. Monthofer and K.Krippner. “Implementation of FFT convolution and multigrid superposition models in the FOCUS RTP system.” Phys Med Biol **45**; 817–833. (2000).

7) M.Kurooka. “Validation of inhomogeneity correction on the basis of the density scaling theorem by the Monte Carlo method.” Ph.M,thesis, (2003)

8) L. Sung-Yen, C. Tieh-chi, L. Jao-Peerng and L. Mu-Tai. “The effect of a metal hip prosthesis on the radiation dose in therapeutic photon beam irradiations.” Appl. Radiat. Isot., **57**; 17-23 (2002).

9) M.D.R. Thomas and A.P. Warrington “Gafchromic® RTQA film for routine quality assurance of high-energy photon beams” Phys Med Biol, **51**; 1439-1447, (2006)

Table. 1 The rate of change (RC) between the MC simulations and the RTPS calculations

	4 MV	**10 MV**
Front of titanium	**-13.2 %**	**-17.2 %**
Behind of titanium	**+15.8 %**	**+3.9 %**
Greater depths	**Not much difference**	**Not much difference**

RC (%) = $((D_{xio} - D_{EGS}) / D_{EGS})$ x 100, D is relative dose

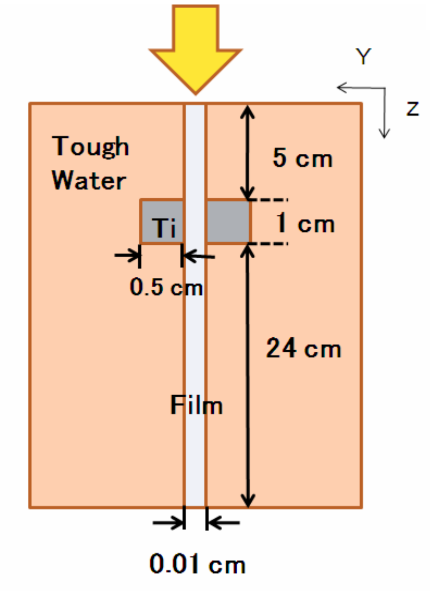

Fig. 1 The geometry of film measurement

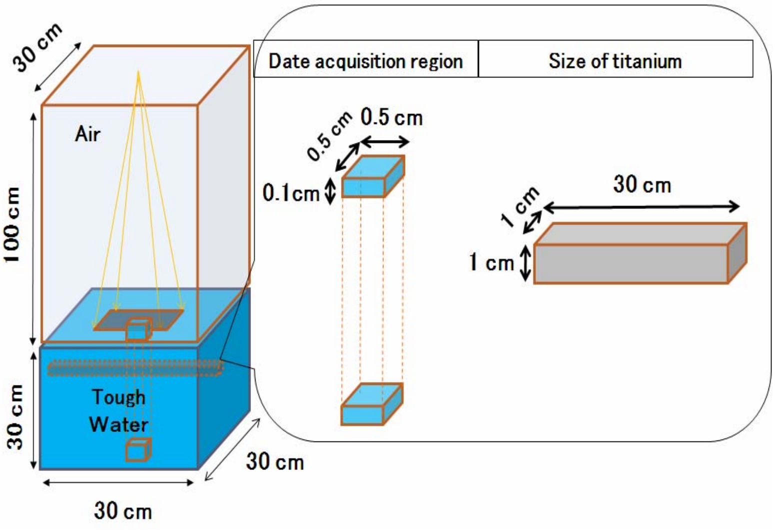

Fig. 2 The geometry of RTPS calculation

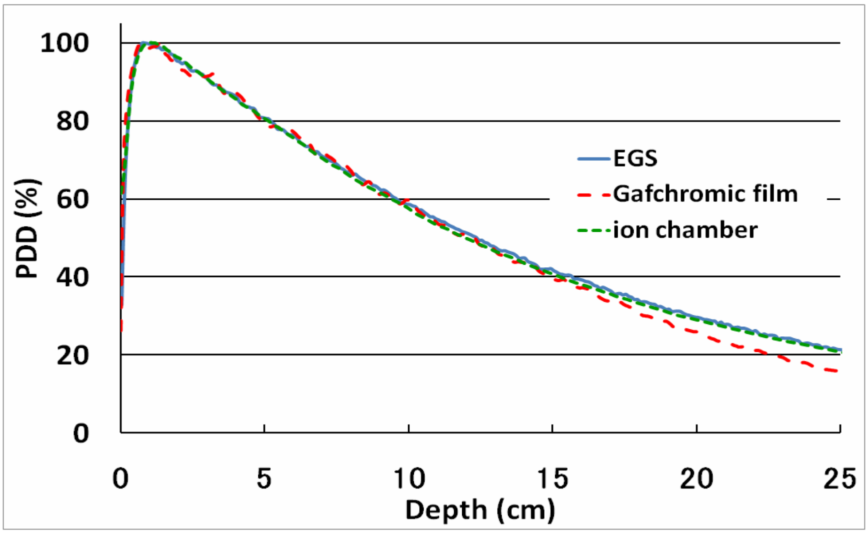

Fig. 3 PDD curves of the EGS simulation, the film measurement and the ion chamber measurement for 4 MV

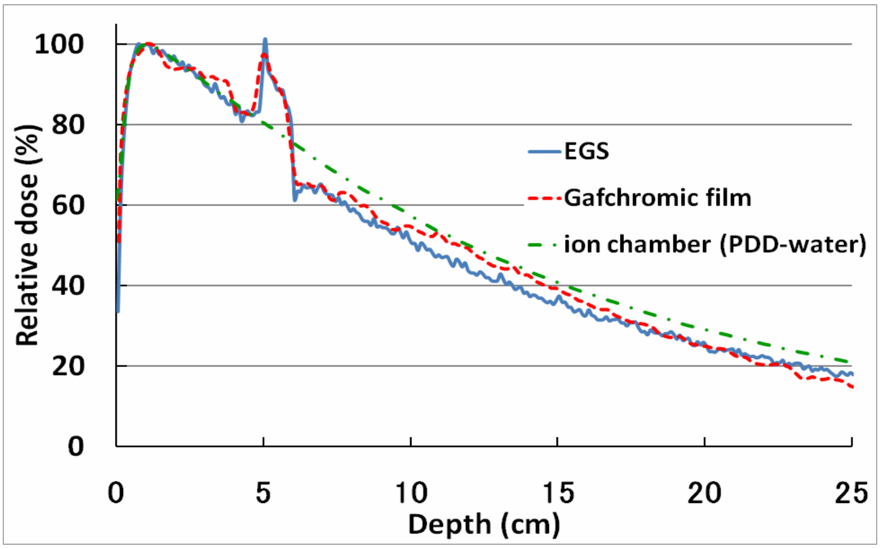

Fig. 4 Relative dose curves of the EGS simulation and the film measurement with titanium for 4 MV

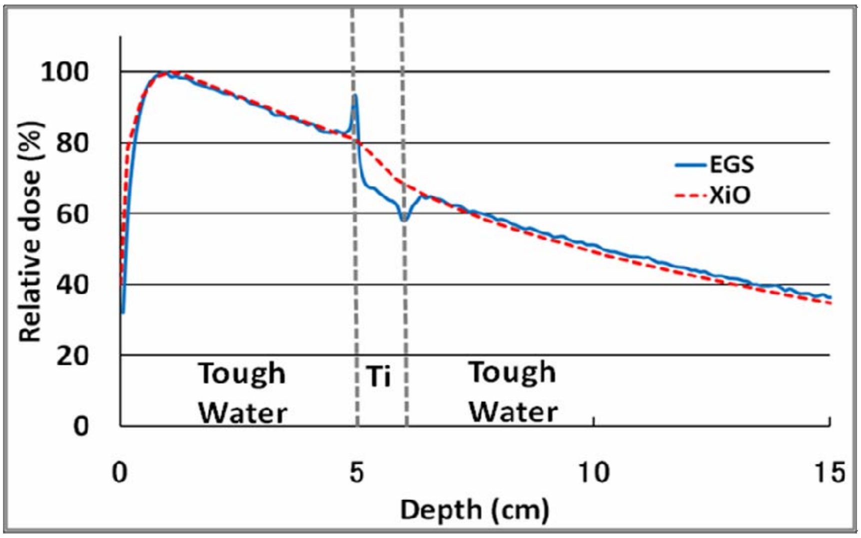

Fig. 5 Relative dose curves with titanium of the EGS simulation and the RTPS calculation for 4 MV

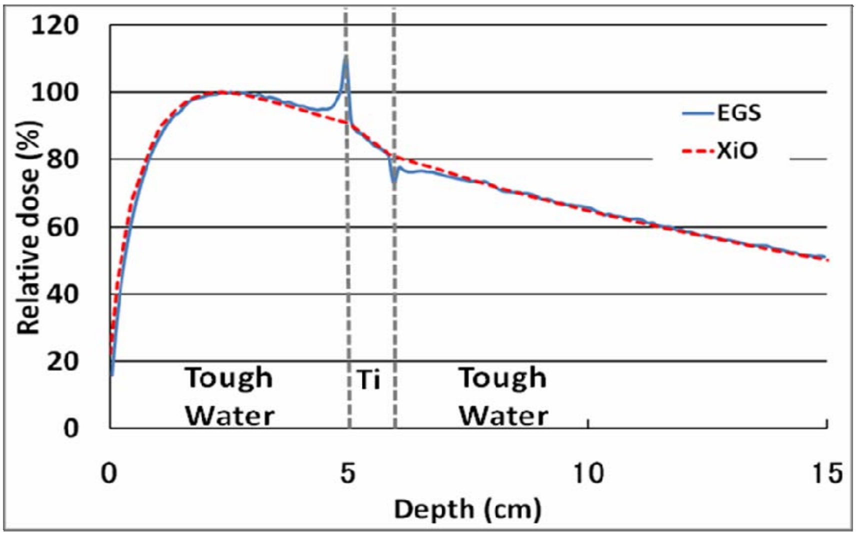

Fig. 6 Relative dose curves with titanium of the EGS simulation and the RTPS calculation for 10 MV

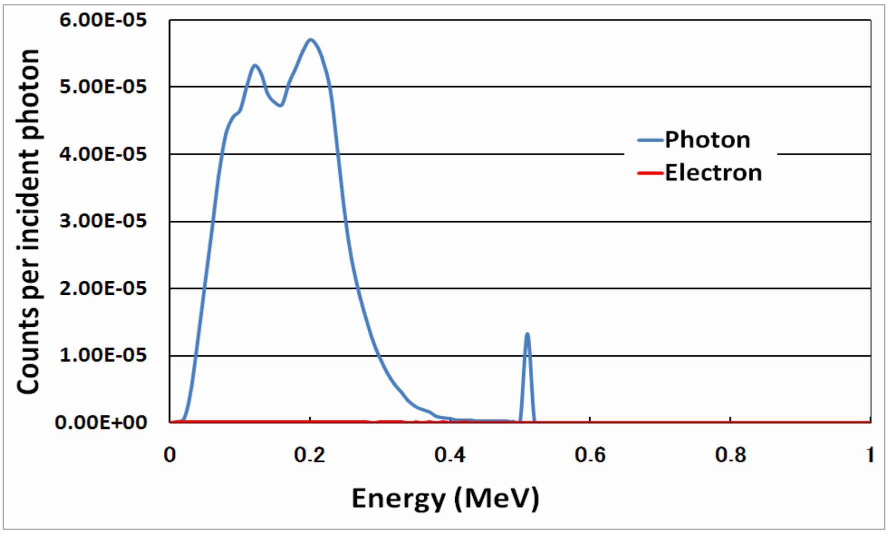

Fig. 7 Energy spectra of backscatter photons and electrons for 4 MV

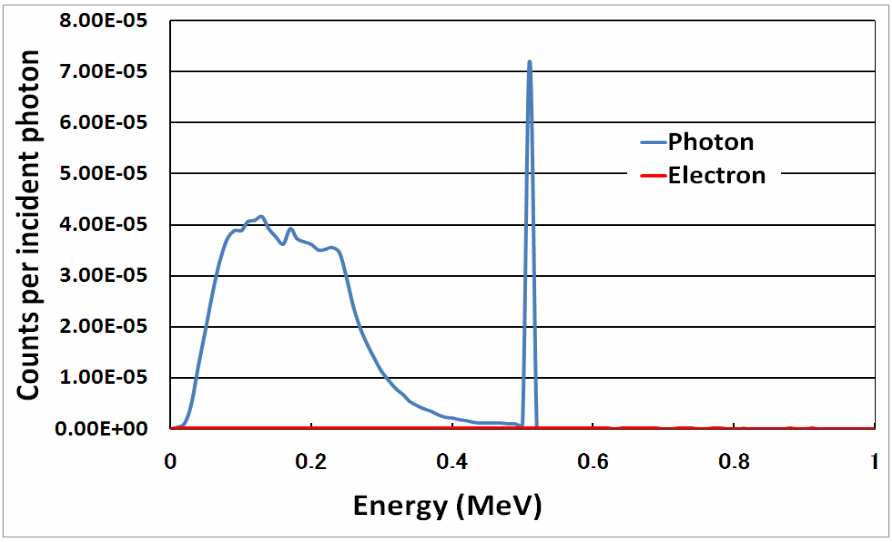

Fig. 8 Energy spectra of backscatter photons and electrons for 10 MV

IMPROVEMENT OF A SPECIALLY DESIGNED SHIELDING PLATE FOR INTRAOPERATIVE ELECTRON BEAM RADIOTHERAPY OF BREAST CANCER

T. Oshima[1], Y. Aoyama[2], T. Shimozato[3], K. Tabushi[3], and Y. Obata[3]

[1]Nagoya University Graduate School of Medicine
1-1-20 Daikou-Minami, Higashi-ku, Nagoya-city, Aichi, 461-8673, Japan
[2]Division of Radiology, Nagoya University Hospital
[3]Department of Radiological Technology, Nagoya University school of Health Science
e-mail: oshima.takashi@a.mbox.nagoya-u.ac.jp

Abstract

Intraoperative electron beam radiotherapy (IOERT) is one of intraoperative radiotherapy techniques. In IOERT for breast cancer, electron beam is irradiated to subclinical tumor cells after breast conserving surgery and some normal tissues are also irradiated simultaneously. To protect the normal tissues, a pair of metal disks called an attenuation plate is generally inserted between pectoralis major muscle and mammary gland. In previous study, a new attenuation plate called a shielding plate, which significantly diminished electron beam without influence of backscattered electrons at R_{90} which was the depth of 90 % of percentage depth dose, was designed. In this study, the shielding plate was further improved so that it could be available at shallower depth than R_{90}. The structure of the improved shielding plate was composed of three layers; an absorption layer, a buffer layer, and a shielding layer and these three layers were packed with synthetic resin coating. The best materials for the three layers and the coating were selected among several option materials using Monte Carlo simulations. The optimal materials for the absorption layer, the buffer layer, the shielding layer, and the coating were graphite, Al_2O_3, W, and PET, respectively, and thicknesses for the layers and the coating were 0.5, 0.1, 0.1, and 0.15 cm, respectively. We hope that usage of this improved shielding plate would open up the options for energy selection in IOERT and lead to the improvement of treatment results.

1. Introduction

Intraoperative radiotherapy (IORT) is an approach to deliver a single-fraction high dose to residual tumor or tumor bed during surgery. Some techniques for IORT have been reported [1, 2, 3] and intraoperative electron beam radiotherapy (IOERT) is one of those techniques. IOERT has also been investigated [4, 5] and is becoming popular as dedicated mobile linear accelerators (LINAC), which can be installed without significant modification of operating room, were developed. In IOERT for breast cancer, electron beam is irradiated to subclinical tumor cells after breast conserving surgery and several results for this treatment have been reported [6, 7, 8].

Since not only cancer cells but also normal tissues such as pectoralis major muscle, lung, and heart are irradiated when IOERT for breast cancer is performed, a pair of metal attenuation disks, which is called an attenuation plate, is inserted between pectoralis major muscle and mammary gland to protect the normal tissues [9, 10]. Several combinations of metal disks were investigated and optimal combination was determined by Martignano *et al* [11]. They concluded that an attenuation plate should consist of two layers and the first layer, which stops low energy backscatter electrons from the second layer, should be composed of a low atomic number substance and the second, which stops electron beam completely, should be composed of a high atomic number substance. However, all materials investigated by them were metal and the materials caused more backscattered electrons than tissue. Moreover, this backscattered electrons lead to unpredicted and unfavorable dose increment.

In previous study, we made a new attenuation plate called a shielding plate, which significantly diminished electron beam without influence of backscattered electrons. The shielding plate consisted of poly-methyl methacrylate (PMMA) layer and copper layer. However, the plate was designed so as to show its best performance when it was set at R_{90} where was the depth of 90 % of percentage depth dose (*PDD*) and it could not prevent the influence of backscattered electrons when it was located at shallower depth than R_{90}. In this study, we designed an improved shielding plate which could be available at shallower depth than R_{90} by reviewing its structure and materials.

2. Materials and Methods

2.1 Policy of design

In actual IOERT, depth where an attenuation plate is set is equal to a thickness of breast and the thickness is varied for each patient. Thus, it is difficult to normalize the depth where the plate is located and to determine a specific depth which represents all depths which are shallower than R_{90}. Additionally, electron beam energies used in IOERT are 6, 9, and 12 MeV and one of them is chosen according to the thickness. In previous study, the shielding plate was designed for use at R_{90} and the used energy for plate designing was 12 MeV since its energy spectra had the largest maximal energy of the 3 energies above at R_{90} as shown in Fig.1. This indicated that the largest incident energy spectra showed the largest maximal energy at the same depth when several incident energy spectra were irradiated. Accordingly, the improved shielding plate was designed so that it blocked electron beam while constraining the influence of backscattered electrons when it was set at R_{90} of 12 MeV electron beam (= 3.8 cm) and irradiated with 15 MeV electron beam. A spectrum at the R_{90} for 15 MeV electron beam was almost the same as one at 2.8 cm for 12 MeV electron beam as shown in Fig. 2, that is to say, the assumed condition in this study was comparable with a case when it was allocated at 2.8 cm and 12 MeV electron beam was irradiated.

2.2 Structure of the improved shielding plate

In previous study, a shielding plate was composed of two layers. The first layer was for absorption of backscattered electrons and attenuation of electron beam and the second layer was for shielding of electron beam. Under the assumed condition, designing the improved shielding plate with this two-layer structure would lead the plate to be thick. Consequently, the improved shielding plate consisted of three layers. The first layer and the third layer had the same roles as the first layer and the second layer of two-layer structure, respectively. The second layer of the three-layer structure was introduced to attenuate backscattered electrons to the first layer and electron beam to the third layer. In this study, the first, the second, and the third layers were called an absorption layer, a buffer layer, and a shielding layer, respectively. In addition to these three layers, the layers were packed by thin coating to prevent them from the corrosion in sterilization process. Meanwhile, the thickness of the improved shielding plate should be thin enough so that it could be inserted between pectoralis major muscle and mammary gland and the thickness could be up to 1.0 cm. Therefore, the thickness of the plate was decided at 1.0 cm and thicknesses of the absorption layer, the buffer layer, and the shielding layer were decided as 0.4, 0.1, and 0.1 cm, respectively, on the basis of preliminary investigations. Thickness of the coating was set at 0.2 cm.

2.3 Materials of the improved shielding plate

In terms of attenuating or shielding electron beams, materials for the plate should be high effective atomic number (Z_{eff}) and high density substances since electrons lose their energy more in an electron-dense substance. However, magnitude of backscattered electrons increases as Z_{eff} of a scatterer becomes large [12]. A material for the coating should have almost the same Z_{eff} as water and be suitable for packing the layers. From the aspect of packing, synthetic resin was appropriate and PMMA, polyethylene terephthalate (PET), and Teflon were employed as options for coating material. The absorption layer should be made of a material which have almost the same Z_{eff} as water and have high density. Options for the absorption layer were graphite, cubic boron nitride (c-BN), and Teflon. The shielding layer should consist of a high Z_{eff} and high density material to block electron beam completely. Probable materials for the shielding layer were ruthenium (Ru), rhodium (Rh), silver (Ag), and tungsten (W). Although the buffer layer should be composed of a high Z_{eff} and high density material to attenuate backscattered electrons and electron beam, a range of backscattered electrons from the buffer layer should be within the thickness of (the coating + the absorption layer). Thus, aluminum oxide (Al_2O_3), silicon carbide (SiC), aluminum (Al), and titanium (Ti) were employed as options for the buffer layer since they had moderate Z_{eff} and high density. The Z_{eff} and density of each material above are summarized in Table 1.

To select the best material for each layer and the coating among option materials for the layers and the coating, magnitude and range of backscattered electrons from each material and its shielding capability were investigated by calculating depth doses deposited by backscattered electrons (backscatter doses) and total absorbed doses with Monte Carlo simulations. Since it was difficult to determine the optimal materials for the layers and the coating at the same time, the coating material was examined first. Secondly, the material for the absorption layer was decided and the material for the buffer layer was chosen after the selection of the absorption layer material. Finally, the shielding layer material was selected. In the simulations for the coating material and absorption layer material, a 1.0-cm layer made of the option material was set at R_{90} of 12 MeV electron beam in a water phantom and a monoenergetic pencil electron beam of 15 MeV was irradiated at 100 cm of source-to-surface distance. In the simulations for the buffer layer material, the layer was located under the 0.2 cm coating material layer and the 0.4 cm absorption layer. In the final simulations the shielding layer was located under the three layers whose optimum materials were previously determined. Statistical uncertainty was less than 0.2 % in all simulations and voxel size was 1.0 x 1.0 x 0.05 cm^3.

3. Results and Discussion

3.1 Coating material

Figs. 3(a) and 3(b) show backscatter dose curves and total absorbed dose curves calculated for the coating materials and water, respectively. Both curves for the same material were normalized to the dose at d_{max} of the total absorbed dose curve. Although Teflon reduced electron beam the most in Fig. 3(b), the magnitude and the range of backscattered electrons from Teflon were the largest as shown in Fig. 3(a). Those from PMMA and PET were almost the same as those from water and PET diminished electron beam more than PMMA. Therefore, PET was the most adequate for the coating material.

3.2 Absorption layer material

Figs. 4(a) and 4(b) show backscatter dose curves and total absorbed dose curves calculated for the coating materials and water, respectively. Both curves for the same material were normalized to the dose at d_{max} of the total absorbed dose curve. As seen in Fig. 4(a), the magnitude and the range of backscattered electrons from Teflon were the largest of the materials. On the other hand, c-BN considerably attenuated electron beam and reduction of electron beam by graphite was equivalent to that by Teflon. Although c-BN was the best material for the layer from a perspective of its performance, it was extremely expensive. Thereby, c-BN was not desirable because of its cost and Teflon was not suitable because of its large backscattered electrons. Thus, graphite was employed.

3.3 Buffer layer material

In the selection of buffer layer material, the magnitude and the range of backscattered electrons were estimated by calculating a difference between depth dose at the source side surface of the coating with and without the layers and its criterion was 1.0 %. The differences for Al_2O_3, SiC, Al, and Ti are shown in Table 2 and Fig. 5 shows total absorbed dose curves for the materials and water. Although differences for Al and Ti were lager than 1.0 % as seen in Table 2, those for

Al_2O_3 and SiC were below 1.0 %. Consequently, Al and Ti were unsuited and Al_2O_3 and SiC were available for the layer. Moreover, Al_2O_3 decreased electron beam better than SiC due to difference of their Z_{eff}. Accordingly, Al_2O_3 was the optimal material for the buffer layer.

3.4 Shielding layer material

The options for the shielding layer material were assessed by the same way as buffer layer material selection. Table 3 shows the differences for Ru, Rh, Ag, and W and Fig. 6 shows total absorbed dose curves for the materials and water. As seen in Fig. 6, all materials except W could not block electron beam sufficiently. Therefore, Ru, Rh, and Ag were not appropriate for the shielding layer material. However, influence of backscattered electrons from W was observed as shown in Table 3. As W was suited for the shield layer material, the combination of the thickness assumed first for each the layers and the coating could not absorb the backscattered electrons. Thus, the thicknesses should be changed and those of the absorption layer and the coating were modified from 0.4 and 0.2 cm to 0.5 and 0.15 cm, respectively. Additional calculation was performed and the results indicated that the modified structure could shield electron beam completely without influence of backscattered electrons.

4. Conclusions

In a current IOERT, a pair of metal disks is used for protection of normal tissues from unnecessary irradiation. However, the disks are made of metals and cause increments of the dose on the source side of them due to backscattered electrons from them. In this work, a shielding plate, which could shield electron beam without influence of backscattered electrons and be available at shallower depth than R_{90}, was designed using Monte Carlo simulations. The shielding plate consisted of three layers; the absorption layer, the buffer layer, and the shielding layer. Furthermore, the three layers were packed with the coating to prevent them from the corrosion in sterilization process. The thicknesses for the absorption layer, the buffer layer, the shielding layer, and the coating were 0.5, 0.1, 0.1, and 0.15 cm, respectively, and the materials for the layers and the coating were graphite, Al_2O_3, W, and PET, respectively.

We hope that usage of this improved shielding plate would open up the options for energy selection in IOERT and lead to improvement of treatment results.

References

1) E. V. Limbergen and C. Weltens, “New trends in radiotherapy for breast cancer,” Curr. Opin. Oncol. **18**, 555-562 (2006).
2) O. Nairz, H. Deutschmann, M. Kopp, K. Wurstbauer, G. Kametriser, G. Fastner, F. Merz, R. Reitsamer, C. Menzel, and F. Sedlmayer, “A dosimetric comparison of IORT techniques in limited-stage breast cancer,” Strahlenther. Onkol. **182**, 342-348 (2006).
3) G. J. Moore-Higgs, “Radiation options for early stage breast cancer,” Semin. Oncol. Nurs. **22**, 233-241 (2006).
4) S. Mussari, W. S. della Sala, L. Busana, V. Vanoni, C. Eccher, B. Zani, L. Menegotti, and L. Tomio, “Full-dose intraoperative radiotherapy with electrons in breast cancer,” Strahlenther. Onkol. **182**, 589-595 (2006).
5) R. Reitsamer, F. Peintinger, M. Kopp, C. Menzel, H. D. Kogelnik, and F. Sedlmayer, “Local recurrence rates in breast cancer patients treated with intraoperative electron-boost radiotherapy versus postoperative external-beam electron-boost irradiation,” Strahlenther. Onkol. **180**, 38-44 (2004).
6) D. W. Ollila, N. Klauber-DeMore, L. J. Tesche, C. M. Kuzmiak, D. Pavic, L. K. Goyal, J. Lian, S. Chang, C. A. Livasy, R. F. Sherron, and C. I. Sartor, “Feasibility of breast preserving therapy with single fraction in situ radiotherapy delivered intraoperatively,” Ann. Surg. Oncol. **14**, 660-669 (2007).
7) R. Orecchia, M. Ciocca, R. Lazzari, C. Garibaldi, M. C. Leonardi, A. Luini, M. Intra, G. Gatti, P. Veronesi, J. I. Petit, and U. Veronesi, “Intraoperative radiation therapy with electrons (ELIOT) in early-stage breast cancer,” The Breast

12, 483-490 (2003).

8) A. S. Beddar, P. J. Biggs, S. Chang, G. A. Ezzell, B. A. Faddegon, F. W. Hensley, and M. D. Mills, "Intraoperative radiation therapy using mobile electron linear accelerators," Report of AAPM TG-72.
9) R. Orecchia and U. Veronesi, "Intraoperative electrons," Semin. Radiat. Oncol. **15**, 76-83 (2005).
10) M. Intra, A. Luini, G. Gatti, M. Ciacca, O. D. Gentilini, A. AC. Viana, E. M. Chagas, A. Berrettini, F. Schuh, D. Scarpa, R. Orecchia, and U. Veronesi, "Surgical technique of intraoperative radiation therapy with electrons (ELIOT) in breast cancer: A lesson learned by over 1000 procedures," Surgery **140**, 467-471 (2006).
11) A. Martignano, L. Menegotti, and A. Valentini, "Monte Carlo investigation of breast intraoperative radiation therapy with metal attenuator plates," Med. Phys. **34**, 4578-4584 (2007).
12) C. Frujinoiu and R. R. Brey, "A Monte Carlo investigation of electron backscattering," Radiation Protection Dosimetry **97**, 223-229 (2001).
13) G. X. Ding, D. W. O. Rogers, "Energy spectra, angular spread and dose distribution of electron beam from various accelerators used in radiotherapy," National Research Council of Canada, PIRS-0439 (1995).
14) H. Hirayama, Y. Namito, A. F. Bielajew, S. J. Wilderman, and W. R. Nelson "The egs5 code system," SLAC-R-730.

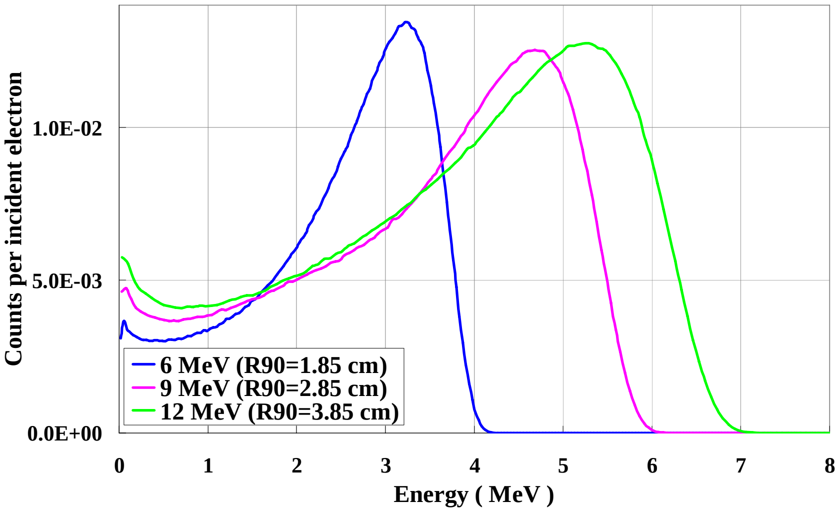

Fig. 1 Energy spectrum at each R_{90} for 6, 9, and 12 MeV electron beam.

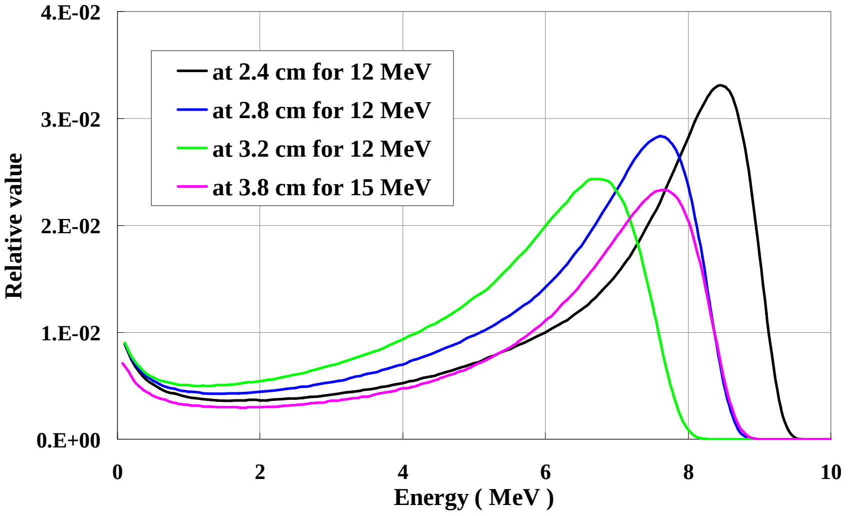

Fig.2 Spectra at several depths for 12 MeV electron beam and spectrum at R_{90} of 12 MeV electron beam for 15MeV electron beam.

Table 1 Effective atomic number and density of all materials for simulations.

Material	†Z_{eff}	Density (g/cm^3)	Material	Z_{eff}	Density (g/cm^3)
water	7.42	1.0	SiC	12.54	3.22
PMMA	6.47	1.19	Al	13	2.70
PET	6.64	1.37	Ti	22	4.54
Teflon	8.43	2.20	Ru	44	12.2
Graphite	6	2.26	Rh	45	12.5
c-BN	6.31	3.48	Ag	47	10.5
Al_2O_3	11.14	3.97	W	74	19.3

†: effective atomic number

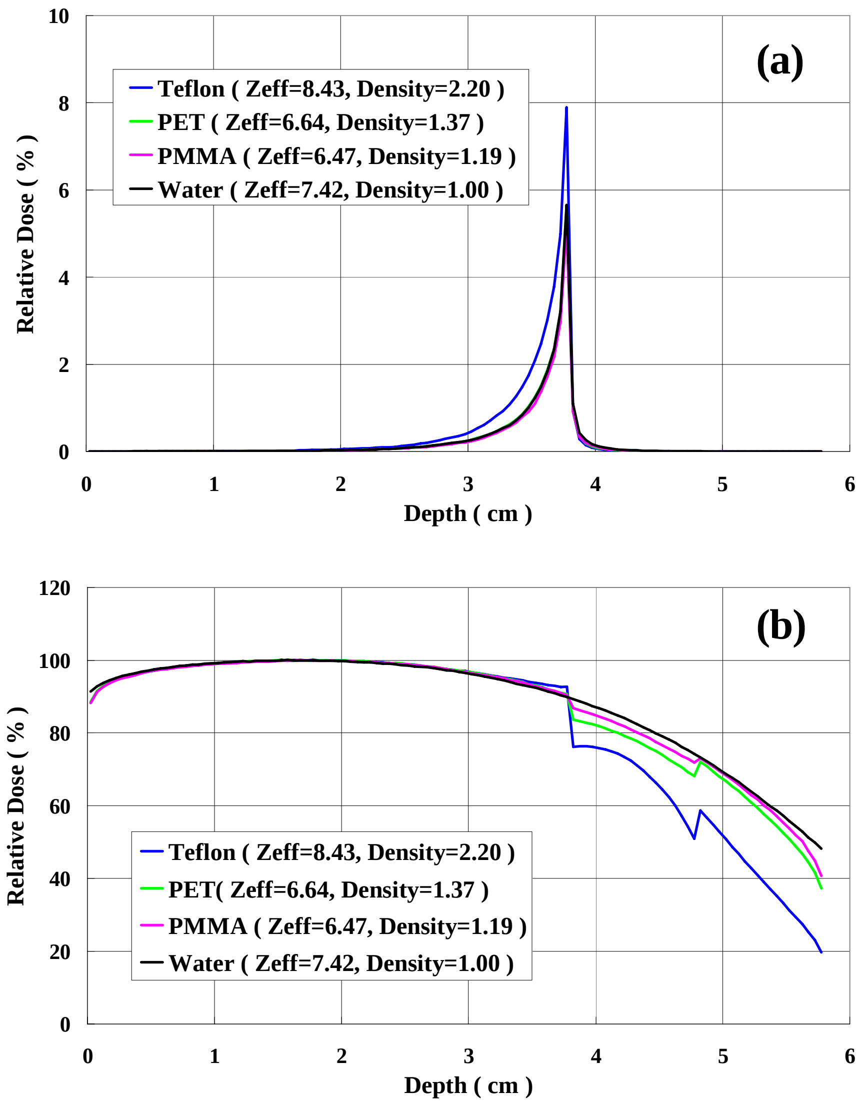

Fig. 3 (a) Backscatter dose curves and (b) total absorbed dose curves for the coating materials and water.

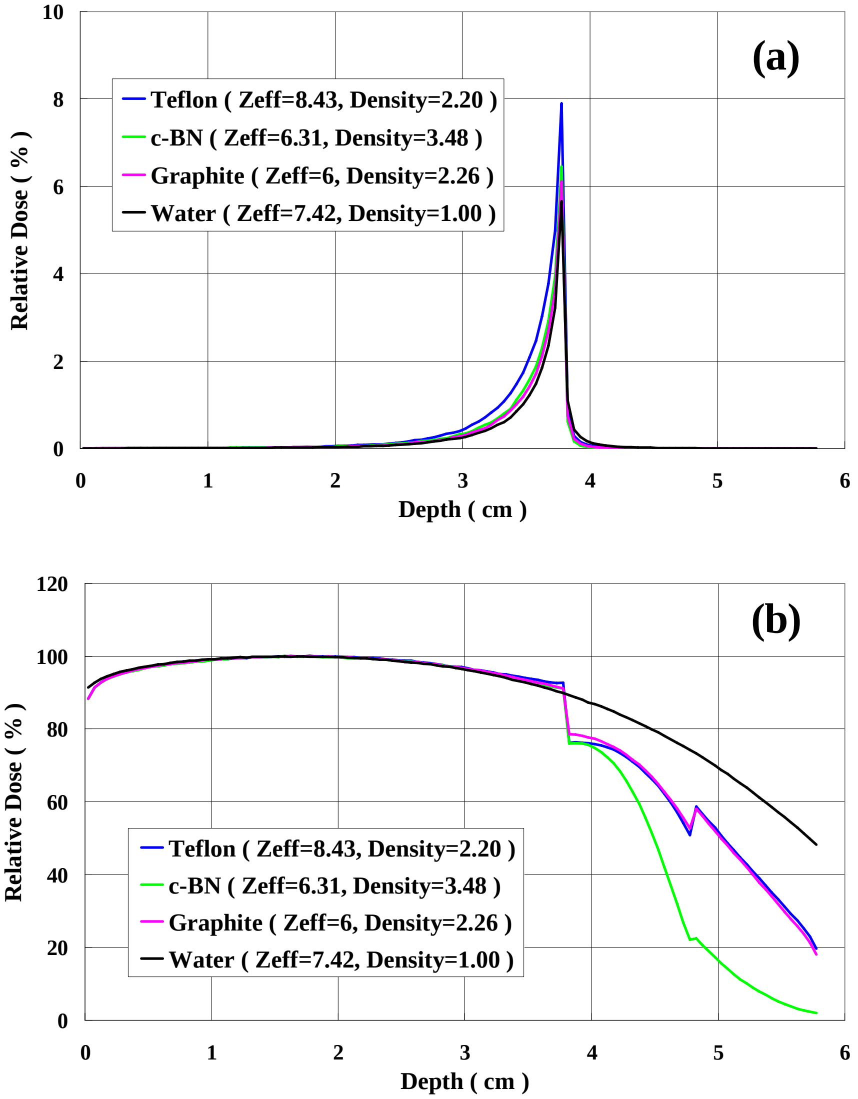

Fig. 4 (a) Backscatter dose curves and (b) total absorbed dose curves for the absorption layer materials and water.

Table 2 Differences between depth dose at the source side surface of the coating with and without the layers for the buffer layer materials.

Material	Al_2O_3	SiC	Al	Ti
$^{*}D_{\mathrm{diff}}$	+ 0.78	+ 0.90	+ 1.03	+ 1.24

*: $D_{\mathrm{diff}} = D_{\text{with the layers}} - D_{\text{without the layers}}$

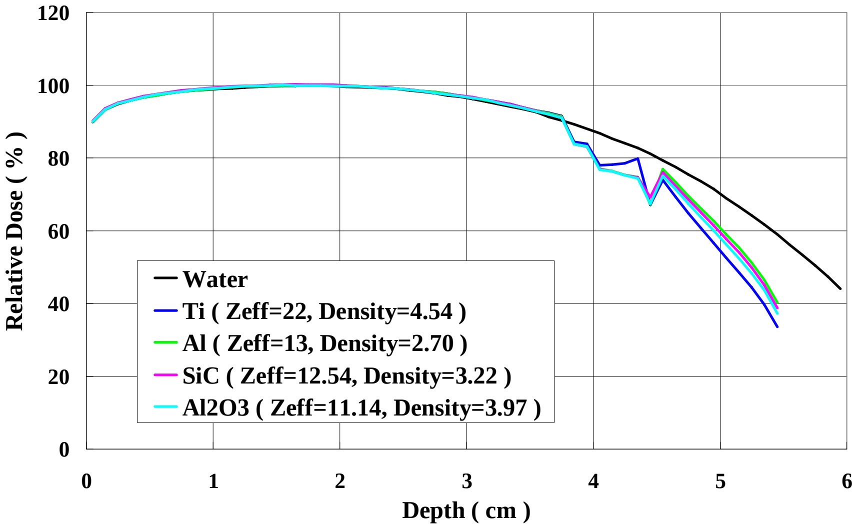

Fig. 5 Total absorbed dose curves for the buffer layer materials and water.

Table 3 Differences between depth dose at the source side surface of the coating with and without the layers for the shielding layer materials.

Material	Ru	Rh	Ag	W
$^{*}D_{\mathrm{diff}}$	+ 0.68	+ 0.65	+ 1.05	+ 1.61

*: $D_{\mathrm{diff}} = D_{\text{with the layers}} - D_{\text{without the layers}}$

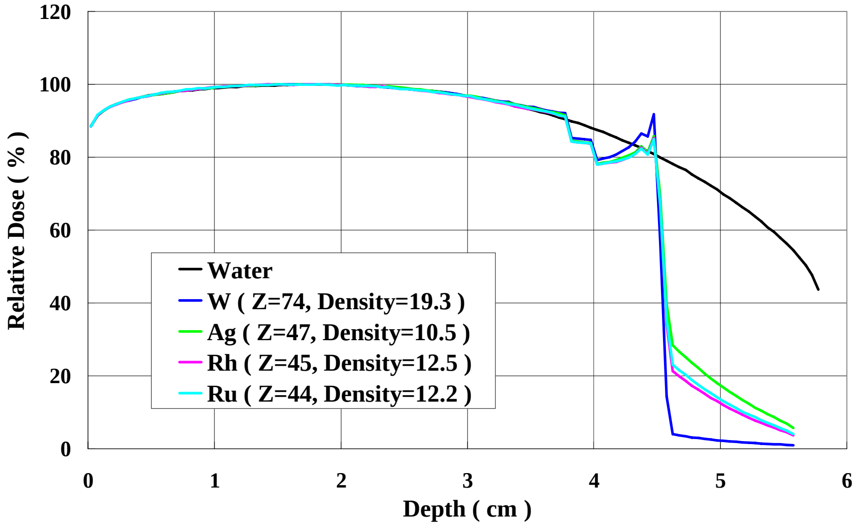

Fig. 6 Total absorbed dose curves for the shielding layer materials and water.

COMPARISON OF PDD CURVES OBTAINED BY THERAPEUTIC FILMS AND CALCULATED BY EGS5

R. Kawanami[1], C. Nejigaki[2], T. Shimozato[3], K. Yasui[1], K. Habara[1], K. Okudaira[4],
Y. Aoyama[1,4], H. Shibata[1], T. Oshima[1] and Y. Obata[3]

[1]*Department of Radiological Technology, Graduate School of Medicine, Nagoya University*
1-1-20 Daiko-Minami, Higash-ku, Nagoya, Japan
[2]*Tosei General Hospital*
[3]*Nagoya University School of Health Science*
[4]*Division of Radiology, Nagoya University Hospital*

Abstract

Recently, dose delivery techniques are evolved rapidly in radiotherapy. Intensity-modulated radiotherapy (IMRT) enables a non-uniform complex dose distribution. Therefore, it is necessary to obtain data of two dimensional (2D) dose distribution. Radiographic films are more commonly used in this situation. The radiographic film features high resolution, and obtains 2D data easily. However, the standard method of the radiographic film dosimetry has not been established in radiotherapy. In this study, the radiographic film EDR2 (Kodak) and Gafchromic Film RT-QA (ISP. INC) were used and compared by measurements and Monte Carlo simulations. Both films were digitalized using a scanner (EPSON Offirio ES 100000G) and analyzed by the DD-system (R-TECH. INC). Density-dose conversion curves were plotted and percentage depth dose (PDD) curves were calculated by the DD-system. The simulation geometry was the same as the film measurement arrangement. In comparison of PDD curves for EDR2, the calculated curve was lager than the curve obtained by an ion chamber and the curve measured by the film dosimetry and PDD curves for RT-QA was smaller than the curve by the ion chamber. Thus, the calculated curve was overestimated and the curve by the film dosimetry was underestimated. On the other hand, calculated PDD for RT-QA was smaller than the PDD by the ion chamber and the curve measured by RT-QA agreed with the PDD by the ion chamber.

1. Introduction

Recently, intensity-modulated radiotherapy (IMRT) and dynamic delivery techniques are evolved rapidly in radiotherapy. IMRT enables a non-uniform complex dose distribution. Therefore, it is necessary to obtain data of two dimensional (2D) dose distribution. A film dosimetry is a convenient method to measure the relative dose distributions. The film dosimetry has been an important method of verifying IMRT and radiographic films are commonly used in the film dosimetry. However, the radiographic film dosimetry has some problems such as the film handling and the quality control. In particular, the response of the film to radiation dependents significantly on the film type. Additionally, the standard method of the radiographic film dosimetry has not been established in radiotherapy and the method of the radiographic film dosimetry is different in each institute. In this study, the dependence of the film response on the film type was investigated by measurements and Monte Carlo simulations (EGS5) for radiographic film EDR2 and Gafchromic Film RT-QA.

2. Materials and Methods

2.1 Film measurements for PDD

EDR2 and RT-QA were used for the film measurement. EDR2 is affected by the processing and shows an over-response by low-energy photons. This film has been reported to be the dose error by approximate 3 %. RT-QA can be used in water and in bright light. Furthermore, this film can be used by cutting freely. However, the disadvantage like as a moiré effect needs careful usage of this film.

10 MV X-ray beams were delivered from Varian Clinac 21 EX, at 100 cm source surface distance (SSD), for the field size of 10 x 10 cm^2. A Tough water phantom (Kyoto kagaku Co., LTD) of the size of 30 x 30 x 30 cm^3 was used. The film calibration for EDR2 was carried out at depth of 10 cm for 13 points of monitor units (from 0 to 450 MU): 100 MU = 1 Gy at the dose of depth maximum. The film calibration for RT-QA was carried out at depth of 10 cm for 14 points of monitor units (from 0 to 500 MU). The values of MU were calibrated by a farmer type ion chamber with 0.6 cm^3 ionization region (TM 30013 PTW Freiburg) and MU-dose linearity was confirmed. In the film calibration, the calibration films were irradiated by 10 x 10 cm^2 field size in the tough water phantom at depth of 10 cm and the distance from source to film was 90 cm. Fig.1 shows that EDR2 was protruded from the surface of phantom. Fig 2 shows the geometry of RT-QA measurement. EDR2 films were placed parallel to the central axis of photon beam and irradiated the dose 200 MU and the irradiated films were processed under the same conditions using an automatic film processor. RT-QA films were placed parallel to the central axis of photon beam and irradiated the dose 300 MU and the irradiated films were analyzed at same time. Both films were digitalized using a scanner (EPSON Offirio ES 100000G) and analyzed by the DD-system (R-TECH.INC). The density-dose conversion curves were plotted and PDD curves were plotted by the DD-system.

2.2 Monte Carlo simulation using EGS5 for PDD

The simulation geometry was modeled accurately on the film measurement arrangement [Fig. 3 and Fig. 4]. The composition of the EDR2 film was C: 22.0, H: 2.4, O: 47.0, N: 9.9, Ag: 10.0 and Br: 7.7 (percentage by weight, %); and the density was 1.731 g / cm^3 [1]. The composition of the paper used for EDR2 to prevent light-transmittance was assumed cellulose (C_6HO_8) and its density was 0.805 g / cm^3. The composition of the RT-QA film was H: 39.7, Li: 0.3, C: 42.3, N: 1.1, O: 16.2, and Cl: 0.3; (percentage by weight, %) and the density was 1.13 g/ cm^3 [2]. The incident energy spectrum was used from published data for 10 MV from Varian Clinac 21 EX [3] and the irradiation field size was 10 x 10 cm^2 in all simulations. Fig. 5 shows PDD curves of water calculated by EGS5 and measured in water. The calculation of EGS5 was thoroughly accurate.

3. Results and Discussions

3.1 Film measurement for PDD

Fig. 6 shows PDD curves by both films and by the ion chamber. In the region from the surface to 12 cm depth, PDD curves of EDR2 and the ion chamber agreed within 0.5% and EDR2 measurement overestimated the dose by 1.7 % at the depth of 25 cm. This overestimation was caused by the over-response of the film to low-energy photons. On the other hand, in the region from the surface to 10 cm, PDD curves of RT-QA and the ion chamber agreed within 1.2% and RT-QA underestimated the dose by 6.2 % at the depth of 19 cm. This is conceivable that RT-QA has low sensitivity in low dose region. In the dose measurement, EDR2 is more accurate than RT-QA. From this result, it is necessary to verify the characteristics of RT-QA.

3.2 Monte Carlo calculation for PDD

Fig.7 shows the PDD curves calculated by EGS5. The PDD curve for EDR2 overestimated the dose between 1.8 and 3.0 % comparing with the measured one by the ion chamber. This overestimation might be caused by the existence of silver particle, that is to say, more energy might be deposited in active layers. The PDD curve for RT-QA underestimated the dose by 3.0 % in the build-up regions of curves in comparison with the ones by the ion chamber. Moreover, those agreed within 1.0 % with the ones by the ion chamber in the other regions. This is conceivable that the effective atomic number of Gafchromic Film RT-QA is similar to that of water,

5. Conclusions

In this study, two types of film measuring method were investigated. In the measurements, the PDD curve of EDR2 overestimated PDD curve of measurement. The PDD curve of RT-QA underestimated PDD curve of measurement. From this result, it is necessary to verify the characteristics of RT-QA. In the Monte Carlo simulation, the PDD curve of EDR2 was overestimated. The PDD curve of Gafchromic Film RT-QA agreed with the PDD carve of the ion chamber. When the absolute dose measurement is not required, RT-QA is convenient since this film can be used in water and in bright light and can be used by cutting freely. For the subject of future investigation, we would reconstruct more accurate geometry. We would obtain the PDD curves of RT-QA in water phantom. Additionally, we hope evaluate the film that obtained in water phantom.

References

1) Å. Plam, A. S. Kirov and T. LoSasso, "Predicting energy response of radiographic film in a 6 MV x-ray beam using Monte Carlo calculated fluence spectra and absorbed dose," Med. Phys. 31 (12), 3168-3178 (1004).
2) D. Sheikh-Bagheri and D.W.O. Rogers, "Monte Carlo calculation of nine megavoltage photon beam spectra using the BEAM code," Med. Phys. 29 (3), 391-402 (2002).
3) Inhwan J. Yeo, C-K Chris Wang and Sandra E. Burch, "A filtration method for improving film dosimetry in photon radiation therapy," Med. Phys. 24 (12), 1943-1953 (1997).
4) N. Dogan, L. B. Leybovich and A. Sethi, "Comparative evaluation of Kodak EDR2 and XV2 films for verification of intensity modulated radiation therapy," Phys. Med. Biol. 47, 4121-4130 (2002).
5) M. D. R. Thomas and A. P. Warrington, "GafChromic® RTQA film for routine quality assurance of high-energy photon beams," Phys. Med. Biol. 51, 1439-1447 (2006).

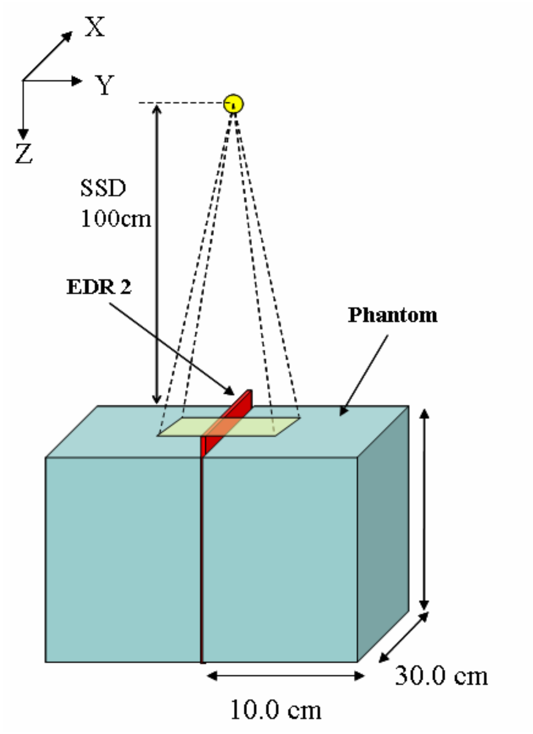

Fig. 1 The geometry of EDR2 measurement

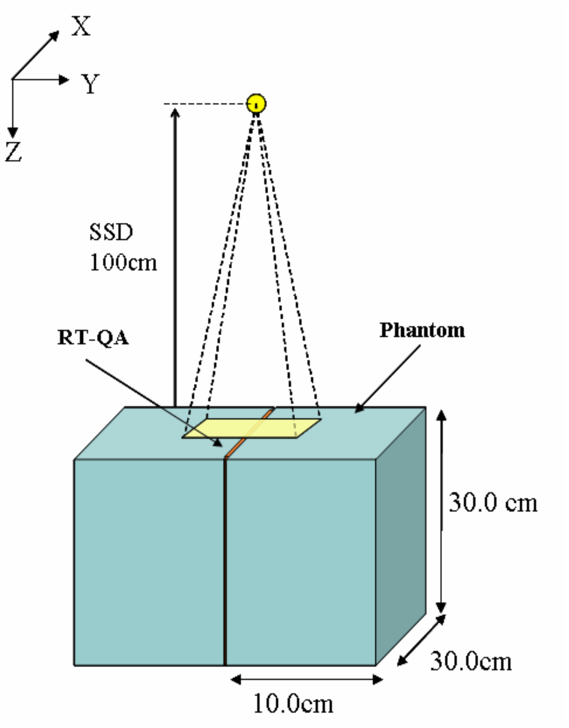

Fig. 2 The geometry of RT-QA measurement

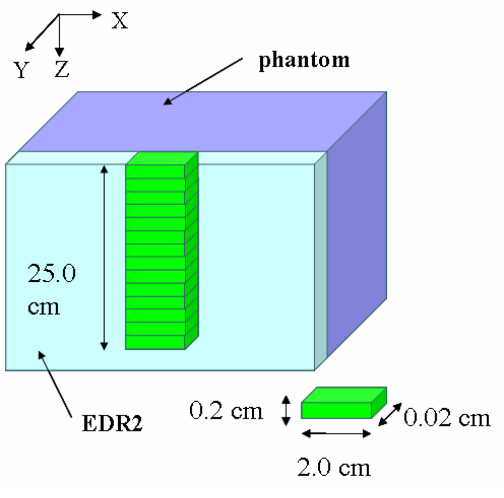

Fig. 3 The geometry of EDR2 calculation

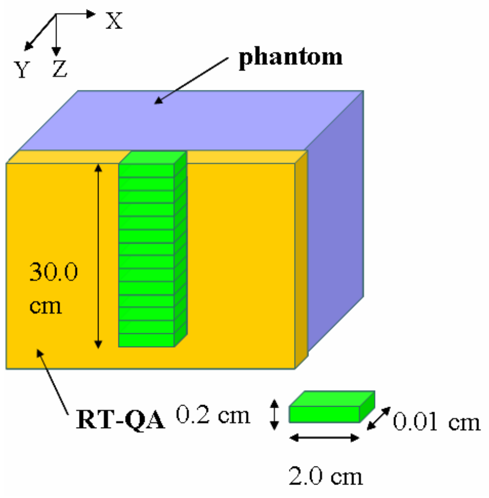

Fig. 4 The geometry of RT-QA calculation

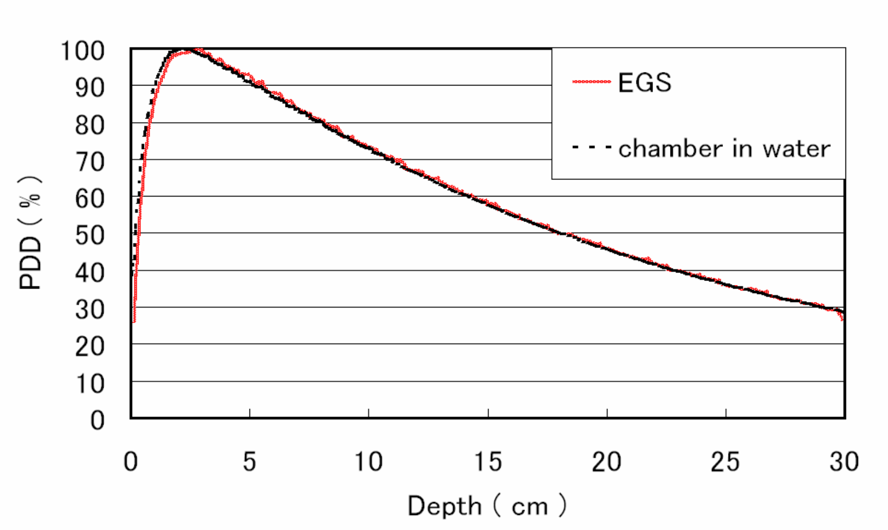

Fig. 5 PDD curves of water calculated by EGS and measured in water

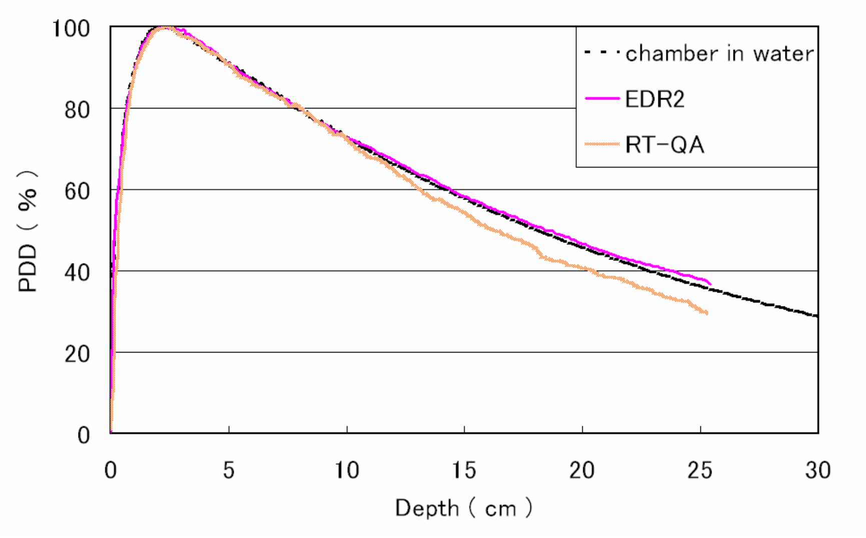

Fig. 6 PDD curves by both films and by ion chamber

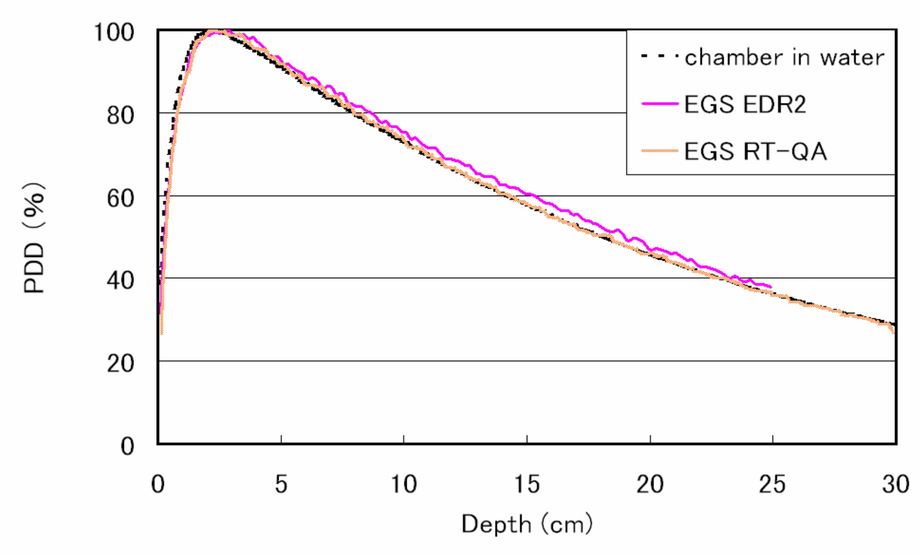

Fig.7 PDD curves calculated by EGS and measured by ion chamber

THE ESTIMATION OF DOSE DISTRIBUTION OF MRI-LINAC WITH EGS4

H. Itoh[1], Y. Narita[2], Y. Iwashita[1], M. Hiraoka[2] and A. Noda[1]

[1]*Accelerator Laboratory, Advanced Research Center for Beam Science, Institute for Chemical Research,*
Kyoto University, Kyoto 611-0011, Japan
[2]*Department of Therapeutic Radiology and Oncology,*
Kyoto University Graduate School of Medicine, Kyoto 606-8507, Japan
e-mail: itoh@kyticr.kuicr.kyoto-u.ac.jp

Abstract

The radiation therapy techniques advance from day to day. Image guided radiation therapy (IGRT) is particularly of current interest all over the world. The use of magnetic resonance imaging (MRI) is one of the IGRT techniques. In a magnetic fieid, charged particles are subjected to Lorentz force and bent. So we calculated dose distribution in the magnetic field with EGS4 and discussed their features. As calculation models, stereotactic radiotherapy for lung cancer was assumed. The application of the magnetic field to the radiation therapy made the more dose convergence than that of normal radiation therapy, but unfavorable middle dose regions appeared at heart and chest wall due to the homogeneity of magnetic field. Some kind of improvement methods are needed in order to overcome this defect.

I. Introduction

One of the important issues in the radiation therapy is dose convergence at tumor sparing normal tissues. In this view point, image guided radiation therapy (IGRT) is developed all over the world. IGRT, which uses gating and tracking irradiation, is one of the methods to avoid unnecessary exposure. It is invasive to acquire the images directly with kV or MV X-ray. One of the noninvasive methods is prospective gating method with a CCD camera and an infrared laser. Another is the use of magnetic resonance imaging (MRI). In a magnetic fieid, charged particles are subjected to Lorentz force and those tracks are bended. The dose distribution in the magnetic field has been investigated by many researchers [1-21], and C. Kirkby et. al.[22] reported that beam kernels in the magnetic field are calculated and optimized, then dose distribution is almost same as intensity modulated radiation therapy (IMRT) in the non-magnetic field. However, in my opinion, we should try to use the effect of magnetic field to the full extent and create new methods to improve the dose distribution. In this study, we calculated the dose distribution in the MRI and reported the availability of magnetic field in the radiation therapy.

II. Material and Methods

Calculation model

Secondary electrons have long stopping range in the low density region, return backward and deposit their energies in the high density region. So the effect of magnetic field is remarkable in the lung region of human body.

For this reason, the calculation model based on CT images of lung cancer was built with *MATLAB*[23]. **Fig.1** shows calculation model. Four thretholds were established from the difference of CT values: air, lung, soft tissue and bone. Simulated tumor was manually added. Isocenter (IC) was set in the center of tumor and the source to target distance was 1m. The size of calculation voxels was 1mm x 1mm x 1mm. Lower limit energies of electron and photon were 10 keV and 521 keV, respectively.

User Code

HOWFAR was built based on sample code:*UCBEND.MOR*.[24] **Eq.1**, **Eq.2** and **Eq.3** reflected the effect of magnetic field as deviations of vector. However, those equations don't work properly in the low density region such as air. This means that *USTEP* tends to be long and particles aren't bent smoothly in the low density region. On this account, We made *USTEP* divided into some batches of unit length that fulfilled **Eq.4**. Particles moved through that unit length and then those direction changed by the amount determined by **Eq.1** and **Eq.2**. This step was iterated until the sum of unit length became larger than *USTEP*. After the iteration, new *USTEP* was established. **Fig.2** shows this modification. As to the transport of electrons of lower energy, *PRESTA* was used.[25]

$$\hat{v} = \hat{B}\left(\hat{v}_0 \cdot \hat{B}\right) + \left\{\hat{v}_0 - \hat{B}\left(\hat{v}_0 \cdot \hat{B}\right)\right\}\cos\alpha - \hat{v}_0 \times \hat{B}\sin\alpha \qquad \textbf{(Eq.1)}$$

$$\hat{v} = \left(v_x, v_y, v_z\right) = \left(\left(v_{x0} + \alpha v_{z0}\right)F, v_{y0}, \left(v_{z0} - \alpha v_{x0}\right)F\right) \qquad \textbf{(Eq.2)}$$

$$F = \frac{1}{\sqrt{1+\alpha^2}} \qquad \textbf{(Eq.3)}$$

$$\alpha = \frac{\Delta l}{R} << 1 \qquad \textbf{(Eq.4)}$$

Beam arrangement

The initial energies of particles were determined by the energy spectrum of varian 6MV Linac.(See **Fig.3**.)[26] Two beam arrangements were considered: coplanar and non-coplanar. **Fig.4** shows positional relation of X-ray fields and the magnetic field. Assumed the magnet of MRI, the magnetic field was homogeneous and faced craniocaudal direction. **Table.1** and **Table.2** show coplanar beam arrangement and non-coplanar beam arrangement, respectively.

III. Results

Fig.5 and **Fig.6** show dose distributions of six coplanar fields and non-coplanar fields, respectively. In each graph, left side represents color-wash map of the dose distribution and right side is contour plot. Dose distribution was normalized at IC dose in each graph. **Fig.5** and **Fig.6** show similar tendencies as a whole. In the non-magnetic field (graph (a)), high dose converged on tumor, but low dose region that are represented with between 5% and 30% lines expanded like star shape in the lung. In the magnetic field of 0.5 [T] (graph(b)), the volume of low dose region in the lung decreased. Magnetic field of 1.5 [T] (graph(c)) made more dose convergence than that of 0.5 [T]. In particular, the volume of 15% dose decreased. Although the convergences of dose distribution to tumor were improved in the magnetic field, unfavorable middle dose regions appeared at heart and chest wall.

IV. Discussions

As mentioned in **Calculation model**, the effect of magnetic field is remarkable in the region that the density shifted from high to low. This was called Electron Return Effect (ERE).[16-21] As homogeneous magnetic field was assumed, ERE occured not only at tumor but at heart and chest wall. In order to prevent the appearance of middle dose region at heart and chest wall, the magnetic field needs to be inhomogeneous. It is considered that magnetic field absorpstion material such as iron is established at patient surface. If the magnetic field is absorbed and weakened at chest wall, ERE doesn't occur. As to heart, dose distribution is improved by the rearrangement of beams to avoid heart.

V. Conclusion

The application of the magnetic field to photon therapy seems to be useful. ERE due to the effect of the magnetic field generally make the dose convergences at tumor, but unfavorable middle and low dose region may appear at normal tissues. In that case, some kind of improvement strategy is needed.

Acknowledgement

The author would like to thank Dr. Hirayama and Dr. Yamamoto. Dr. Hirayama gave very helpful comments to apply the magnetic field to EGS4. Dr. Yamamoto taught the EGS4 code system from the basics.

References

1) W. H. Bostick, "Possible techniques in direct-electron-beam tumor therapy", Phys. Rev. **77**, 564-565(1950)
2) C. C. Shih, "High energy electron radiotherapy in a magnet field", Med. Phys. **2**, 9-13(1975)
3) D. P. Whitmire, D. L. Bernard, M. D. Peterson and J. A. Purdy, "Magnetic enhancement of electron dose distribution in a phantom", Med. Phys. **4**, 127-131(1977)
4) R. Nath and R. J. Schulz, "Modification of electron-beam dose distributions by transverse magnetic fields", Med. Phys. **5**, 226-230(1978)
5) B. H. Paliwal, A. L. Wiley, B. W. Wessels and M. C. Choi, "Magnetic field modification of electron-beam dose distributions in inhomogeneous media", Med. Phys. **5**,404-408(1978)
6) M. S. Weinhous, R. Nath and R. J. Schulz, "Enhancement of electron beam dose distributions by longitudinal magnetic field: Monte Carlo simulation and magnetic system optimization", Med. Phys. **12**, 598-603(1985)
7) E. Nardi and G. Barnea, "Electron beam therapy with transverse magnetic fields", Med. Phys. **26**,967-973(1999)
8) A. F. Bielajew, "The effect of strong longitudinal magnetic fields on dose deposition from electron and photon beams", Med. Phys. **20**, 1171-1179(1993)
9) L. Reiffel, A. Li, J. Chu, R. W. Wheatley, S. Naqvi, R. Pillsbury and A. Saxena, "Control of photon beam dose profiles by localized transverse magnetic fields", Phys. Med. Biol. **45**, 177-182(2000)
10) X. Allen Li, L. reiffel, J. Chu and S. Naqvi, "Conformal photon-beam therapy with transverse magnetic fields:

A Monte Carlo study", Med. Phys. **28**,127-133(2001)

11) J. Chu, L. Reiffel, W. Hsi and A. Saxena, "Modulation of radiotherapy photon beam intensity using magnetic field", Int. J. Cancer **96**, 131-137(2001)
12) D. W. Litzenberg, B. S. Fraass, D. L. Mcshan, T. W. O'Donnell, D. A. Roberts, F. D. Becchetti, A. F. Bielajew and J. M. Moran, "Experimental apparatus to measure the effects of strong longitudinal magnetic fields on photon and electron radiotherapy beams", Phys. Med. Biol. **46**, 105-115(2001)
13) F. D. Becchetti, D. W. Litzenberg, J. M. moran, T. W. O'Donnell, D. A. Roberts, B. A. Fraass, D. L. McShan and A. F. Bielajew, "Magnetic confinement of radiotherapy beam-dose profiles", Proc. Cyclotrons and their applications 2001, 16th international conference(AIP press), 44-46(2001)
14) Y. Chen, A. F. Bielajew, D. W. Litzenberg, J. M. moran and F. D. Becchetti, "Magnetic confinement of electron and photon radiotherapy dose: A Monte Carlo simulation with a nonuniform longitudinal magnetic field", Med. Phys. **32**, 3810-3818(2005)
15) J. C. H. Chu, L. Reiffel, S. Naqvi, X. A. Li, S-J. Ye and A. Saxena, "The use of magnetic fields to improve photon dose distributions for radiation – a possible approach to "poor man's proton" beam properties", Proc. Engineering in Medicine and Biology Society, 22nd Annual International conference of IEEE, 2000
16) B. W. Raaymakers, A. J. E. Raaijmakers, A. N. T. Kotte, D. Jette and J. J. W. Lagendijk, "Integrating a MRI scanner with a 6MV radiotherapy accelerator: dose deposition in a transverse magnetic field", Phys. Med. Biol. **49**, 4109-4118(2004)
17) A. J. E. Raaijmakers, B. W. Raaymakers and J. J. W. Lagendijk, "Integrating a MRI scanner with a 6MV radiotherapy accelerator: dose increase at tissue-air interfaces in a lateral magnetic field due to returning electrons", Phys. Med. Biol. **50**, 1363-1376(2005)
18) J. E. Raaijmakers, B. W. Raaymakers, S. van der Meer and J. J. W. Lagendijk, "Integrating a MRI scanner with a 6MV radiotherapy accelerator: impact of the surface orientation on the entrance and exit dose due to the transverse magnetic field", Phys. Med. Biol. **52**, 929-939(2007)
19) J. E. Raaijmakers, B. W. Raaymakers and J. J. W. Lagendijk, "Experimental verification of magnetic field dose effects for the MRI-accelerator", Phys. Med. Biol. **52**, 4283-4291(2007)
20) J. E. Raaijmakers, B. Hardemark, B. W. Raaymakers, C. P. J. Raaijmakers and J. J. W. Lagendijk, "Dose optimization for the MRI-accelerator: IMRT in the presence of a magnetic field", Phys. Med. Biol. **52**, 7045-7054(2007)
21) J. J. W. Lagendijk, B. W. Raaymakers, A. J. E. Raaijmakers, J. Overweg, K. J. Brown, E. M. Kerkhof, R. W. van der Put, B. Hardemark, M. van Vulpen, Unlke A. van der Heide, "MRI/linac integration", Radiother. Oncol. **86**, 25-29(2008)
22) Kirkby, T. Stanescu, S.Rathee, M. Carlone, B. Murray and B. G. Fallone, "Patient dosimetry for hybrid MRI-radiotherapy systems", Med. Phys. **35**, 1019-1027(2008)
23) MATLAB *http://www.cybernet.co.jp/matlab/*
24) W. R. Nelson, D. W. O. Rogers and H. Hirayama, *The EGS4 Code System*, Stanford Linear Accelerator Report No.SLAC-265, Stanford, CA, 1985
25) A .F. Bielajew and D. W. O. Rogers, "PRESTA-the Parameter Reduced Electron-Step Transport Algorithm

for electron Monte Carlo transport", Nucl. Instrum. Methods B **18**, 165-181(1987)

26) S .B.Daryoush et.al., "Monte Carlo calculation of nine megavoltage photon beam spectra using the BEAM code", Med.Phys., **29**(2002)

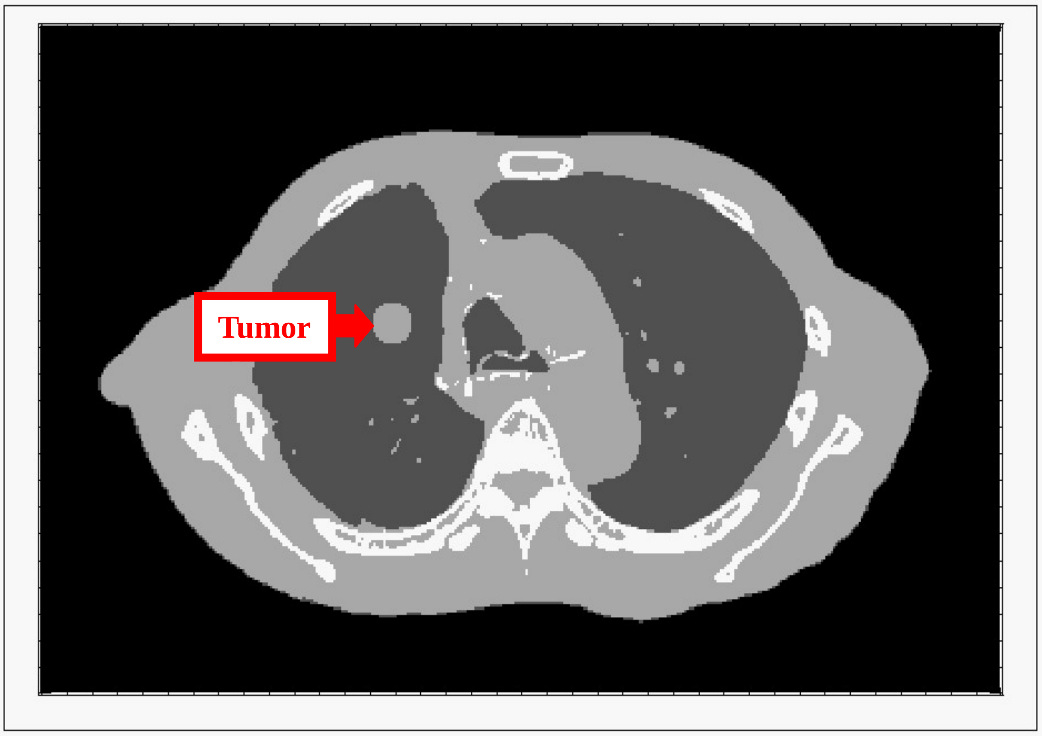

Fig.1 Calculation model based CT images of lung cancer

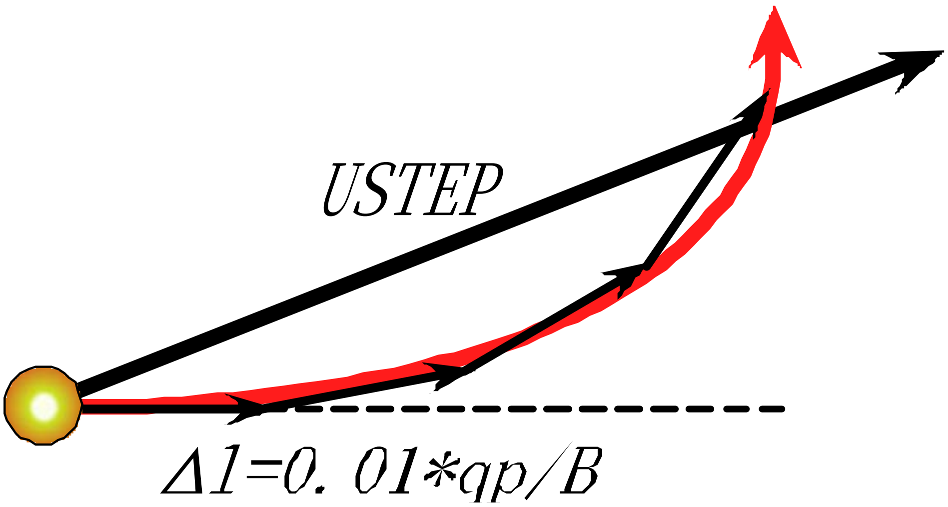

Fig.2 Modification of direction vector in *HOWFAR*

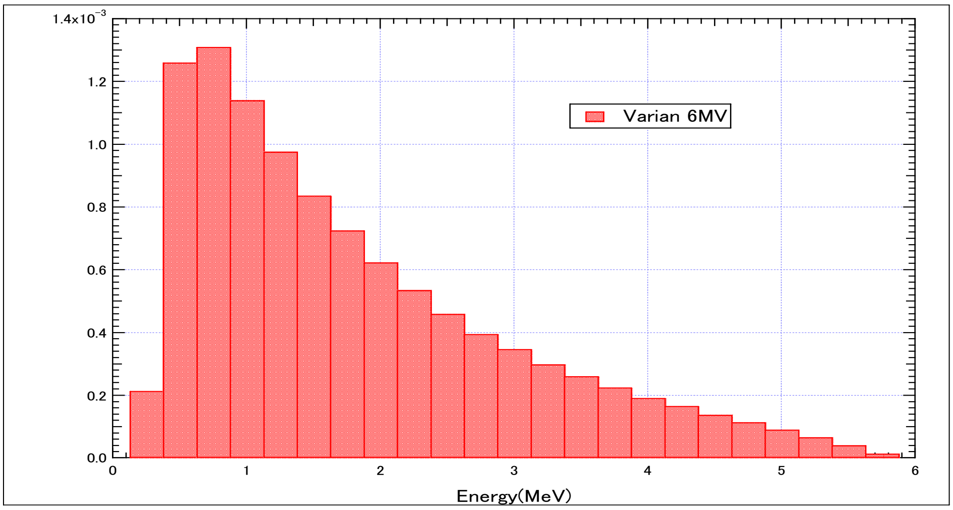

Fig.3 Energy spectrum of Varian 6MV Linac

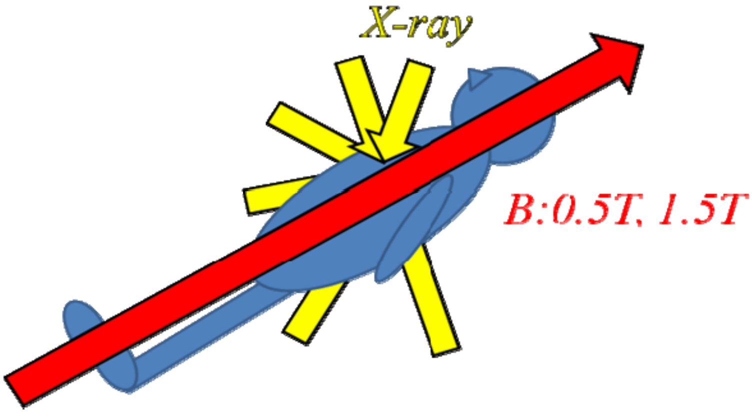

Fig.4 The positional relation of X-ray fields and magnetic field

Table.1 The coplanar beam arrangement

Field #	**1**	**2**	**3**	**4**	**5**	**6**
Gantry	**20**	**335**	**300**	**260**	**240**	**175**
Couch	**0**	**0**	**0**	**0**	**0**	**0**

Table.2 The non-coplanar beam arrangement

Field #	**1**	**2**	**3**	**4**	**5**	**6**
Gantry	**20**	**335**	**300**	**260**	**240**	**175**
Couch	**0**	**320**	**30**	**330**	**15**	**0**

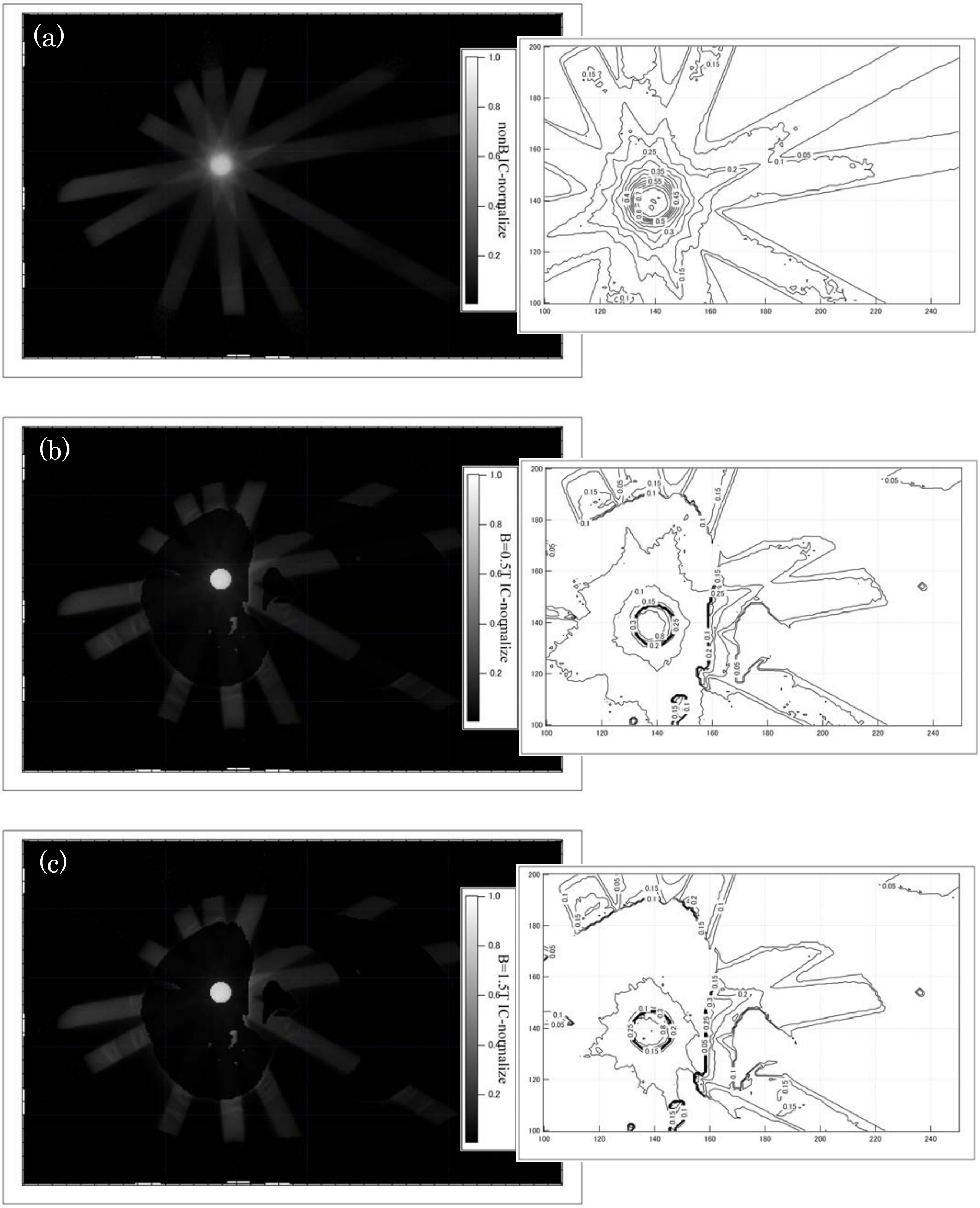

Fig.5 Dose distribution of coplanar beams

(a) Non-magnetic field, (b) B = 0.5 [T], (c) B = 1.5 [T]

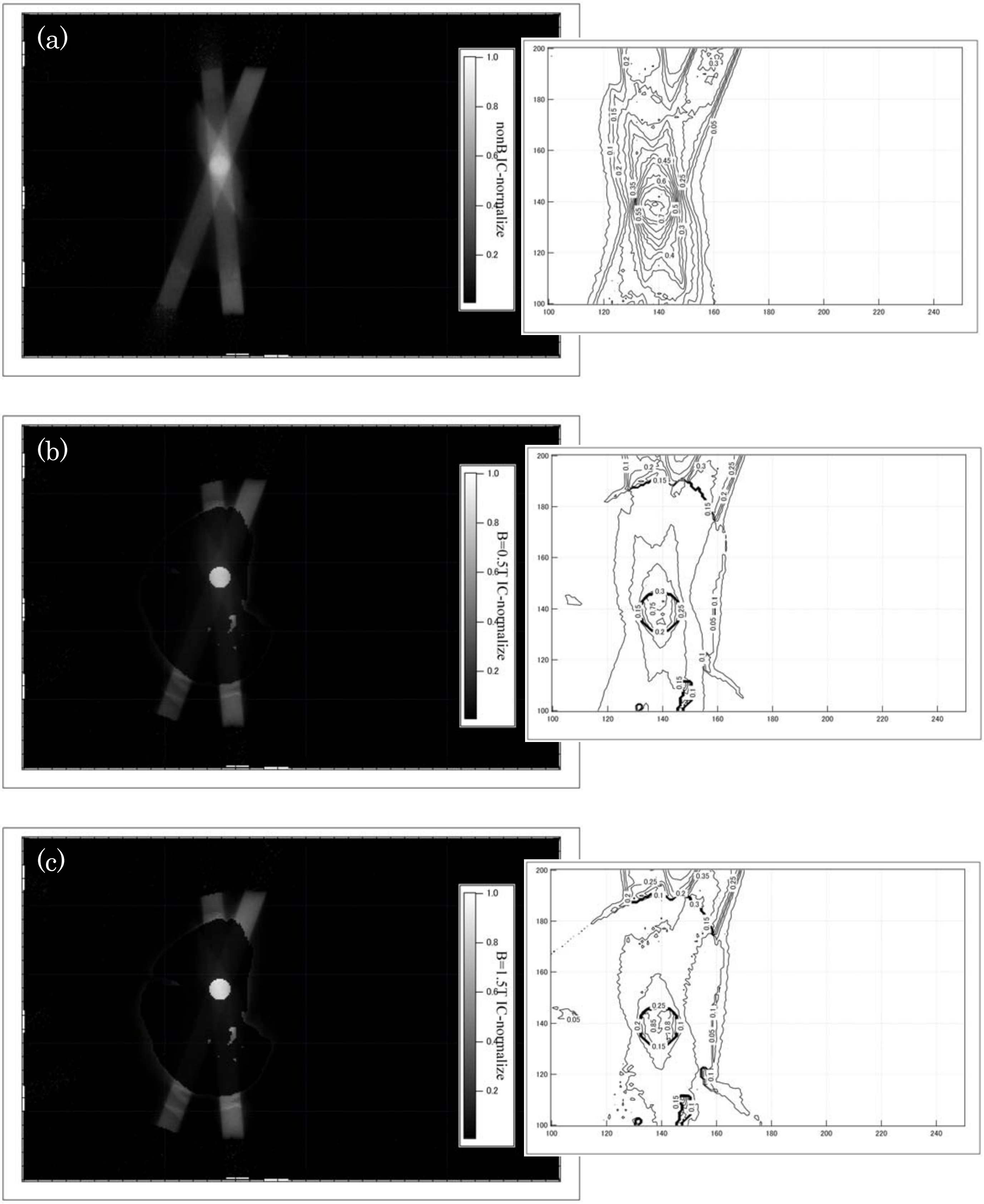

Fig.6 Dose distribution of non-coplanar beam

(a) Non-magnetic field, (b) B = 0.5 [T], (c) B = 1.5 [T]

Photon Energy Spectra in Water Phantom: Monte Carlo Simulation Study with EGS5

Satoshi Miyajima and Kiyomitsu Shinsho

Institute of Health Sciences, Junshin Junior College
1-1-1 Chikushigaoka, Minami-ku, Fukuoka 815-1510, Japan

Abstract

Photon energy spectra in a water phantom were calculated with the Monte Carlo method. The code Electron-Gamma Shower version 5 (EGS5) was used in the calculations. Monoenergetic pencil beams from 10 keV to 150 keV impinged on the center of the flat surface of a cylinderical water phantom perpendicularly. The results indicate that the energy spectra in water are quite different from the incident ones, and are dependent on the depth in the beam direction and the distance from the beam axis. The effects of variations of the energy spectra in a water phantom on the patient dosimetry were discussed. The results indicate that dosimeters with tissue-equivalent materials are suitable for the patient dosimetry in the diagnostic energy range (i.e. below 150 keV).

1 INTRODUCTION

Photon energy spectra in a phantom are of primary concern in the patient dosimetry, because the detector response is a function of photon energy. However, the energy spectra are usually unknown in the patient dosimetry.

Photon energy spectra in water have been determined both theoretically and experimentally. The energy spectra of scattered photons had been measured extensively with a NaI scintillation spectrometer in 1950-60's [1]-[8]. Photons passing through a hollow tube extended from the center of a water phantom were measured with a NaI spectrometer as a function of scattering angle. The results were integrated over the angle to obtain the photon energy spectra at the center of the phantom. In 1990's, a thimble-type Si-diode detector was utilized in the in-phantom x-ray spectroscopy [9]. A Si-diode chip with quasi-uniform angular sensitivity was enclosed in the tip of the stem.

Photon energy spectra in a water phantom have also been calculated mainly by the Monte Carlo method. Bruce et al. calculated the spectra of primary photons with the analytical calculations, and those of secondary (i.e. scattered) photons with the Monte Carlo method [10]. The energy range was from 50 to 250 keV. Petoussi et al. calculated photon energy spectra in the standard phantoms irradiated by photons in the diagnostic energy range with the Monte Carlo method [11]. Cunningham et al. calculated photon energy spectra in a water phantom irradiated by MeV photons used in the radiotherapy. The average stopping-power and mass energy absorption coefficient ratios of water, graphite and tissue-equivalant materials to air were calculated from the energy spectra for high-energy x-ray dosimetry [12, 13]. Miyajima et al. calculated photon energy spectra in a water phantom during the Computed Tomography (CT) scanning [14]. The effects of the spectral variation on the detector response were estimated from the calculated spectra [15].

Photon energy spectra in a cylindrical water phantom were calculated using the Monte Carlo method in this study. The incident photons were monoenergetic pencil beams with 0 mm diameter. The photon energy was from 10 to 150 keV. The pencil beam impinged on the center of the cylindrical phantom perpendicularly, along with the axis of the water cylinder. Variations of the energy spectra in the phantom were shown as a function of the depth in the beam direction and the

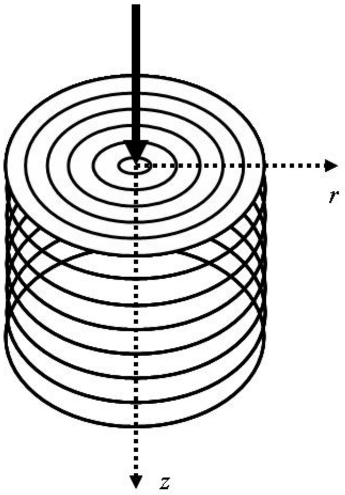

Figure 1: The cylindrical water phantom used in the EGS5 calculations in this study. The phantom was 100 cm thick and 201 cm diameter. The phantom was composed of the multi-slab in the z-direction (Δz = 1 cm) and the multi-cylinder in the r-direction (Δr = 1 cm). The solid arrow shows the direction of the pencil beam of incident photons.

distance from the beam axis (i.e. from the axis of the water cylinder). The effects of the spectral variations on the detector response were discussed.

2 MATERIALS AND METHODS

The water phantom was composed of the multi-slab and multi-cylinder (Fig. 1). The dimensions of the phantom were 100 cm in thickness and 201 cm in diameter. Both the increment Δz of the multi-slab and Δr of the multi-cylinder were 1 cm.

The incident beam was a pencil beam of monoenergetic photons from 10 to 150 keV in 10 keV increments. The beam diameter was 0 mm. The pencil beam was incident on the center of the flat surface of the cylindrical water phantom perpendicularly (i.e. along with the axis of the cylinder), as shown in Fig. 1.

Electron-Gamma Shower version 5 (EGS5) was utilized in the Monte Carlo calculations [16]. The binding of electrons to the nucleus was taken into account in the Rayleigh scattering and the Compton scattering (i.e. $IRAYLR = 1$ and $INCOHR = 1$ in the usercode). The generation of K- and L-characteristic x-rays was included (i.e. $IEDGFL = 1$). The cutoff energy for photons was 1 keV ($PCUT = 0.001$) in all the calculations. As the range of secondary electrons is far small compared with Δz and Δr, the electron path was neglected. It should be noted that the mean free path of 1 keV photons in water is about 0.025 mm [17], and the CSDA range of 150 keV electrons is less than 0.3 mm [18].

2.1 Photon energy spectra in water phantom

The photon energy and IRL (the region number in EGS) of the region were recorded everytime the photon crossed the region in the water phantom. As a result, photon energy spectra were obtained as a function of the depth z and the direction from the beam axis r (Fig. 1). The calculated spectra per unit incident photon, normalized to the unit central cylindrical volume (i.e. (0.5 cm × 0.5 cm × π) × 1 cm), were shown. Note that the calculated results should be rotationally symmetrical in this geometry.

2.2 Average photon energy in water phantom

The average photon energy at each *IRL* was obtained from the photon energy spectra calculated in this study. The average energy was also shown as a function of the depth z and the direction from the beam axis r.

2.3 Average number of Compton scattering in water phantom

The number of Compton scattering experienced was recorded as a function of z and r, everytime the Compton scattering occurred. The variable *LATCH* was utilized in the subroutine *AUSGAB* for this. The average number of Compton scattering at each region was calculated from the data after all histories end.

3 RESULTS

3.1 Photon energy spectra in water phantom

Figure 2(a) shows the variation of photon energy spectra at the depth of 10 cm, when a monoenergetic pencil beam of 30 keV photons impinged on the water phantom. The results for different r are shown in the figure. Figure 2(b) is the results for the depth of 20 cm, and Fig. 2(c) for 30 cm. Figures 3 to 5 show the variations of photon energy spectra at the depth of 10 cm, 20 cm and 30 cm, when a monoenergetic pencil beam of 60 keV, 90 keV and 120 keV photons impinged on the water phantom.

Figures 2 to 5 show that photons with lower energy than the incident photon exist in a water phantom. The energy spectra are dependent on r: the larger the distance from the beam axis (in other words, the larger the r), the fewer the high-energy photons. On the contrary, the dependence of the energy spectra on z is not very apparent in the range of $z = 10$ cm to 30 cm. The lower limit of photon energy in a water phantom is around 20 keV. This value is independent of the incident photon energy and the depth z in a water phantom. The edges on the energy spectra are prominent for $r = 0$ in Figs. 3 to 5: 42 keV/49 keV for the incident energy of 60 keV (Fig. 3), 53 keV/67 keV for 90 keV (Fig. 4) and 62 keV/82 keV for 120 keV (Fig. 5).

3.2 Average photon energy in water phantom

Figure 6 shows the average photon energy in the water phantom as a function of the distance from the beam axis r for 30 keV, 60 keV, 90 keV and 120 keV incident photons at the depths from 1 cm to 30 cm. The results indicate that the larger the distance from the beam axis (in other words, the larger the r), the lower the average photon energy. This tendency agrees with the spectral variation shown in Figs. 2 to 5. The average energy decreases steeply near the beam axis. The dependence of the average energy on the depth z is rather small in the range from $z = 1$ cm to 30 cm, though the average energy for $z = 1$ cm is slightly higher than the others. This is probably due to the lack of contributions of back-scattered photons from the slab above it: no water slab exists over the slab of $z = 1$ cm. The fluctuations at large r are due to small number of photons reaching there.

3.3 Average number of Compton scattering in water phantom

Figure 7 shows the average number of Compton scattering experienced in the water phantom, as a function of the distance from the beam axis r for 30 keV, 60 keV, 90 keV and 120 keV incident photons.

The figures show the followings: the higher the incident photon energy, the larger the average number of Compton scattering; the larger the distance from the beam axis (in other words, the larger the r), the larger the average number of Compton scattering; the larger the distance from

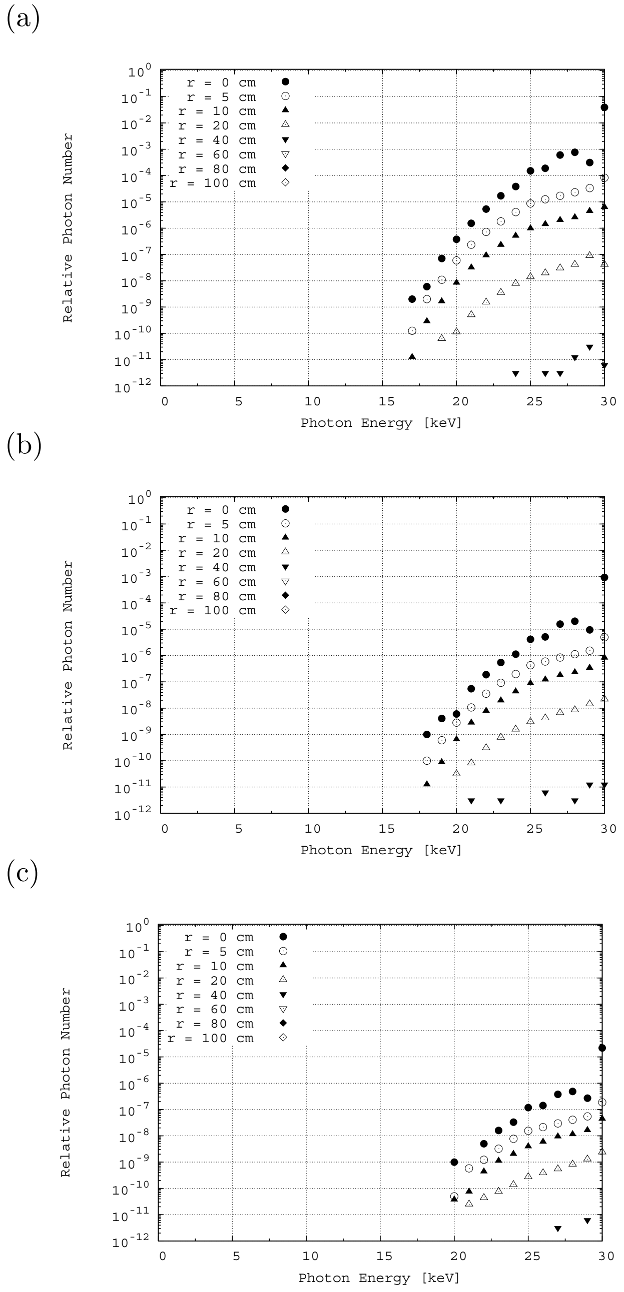

Figure 2: Calculated photon energy spectra in water at the depth of (a) 10 cm, (b) 20 cm and (c) 30 cm. The parameter r is the distance from the beam axis. The incident photon energy is 30 keV.

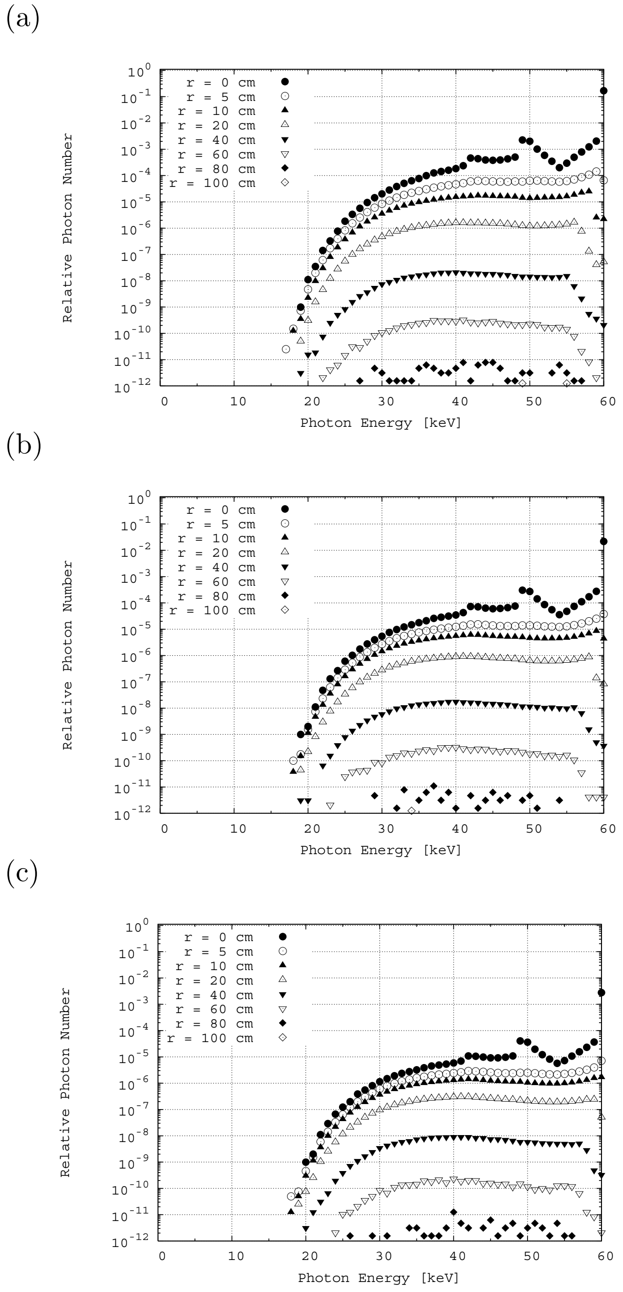

Figure 3: Calculated photon energy spectra in water at the depth of (a) 10 cm, (b) 20 cm and (c) 30 cm. The parameter r is the distance from the beam axis. The incident photon energy is 60 keV.

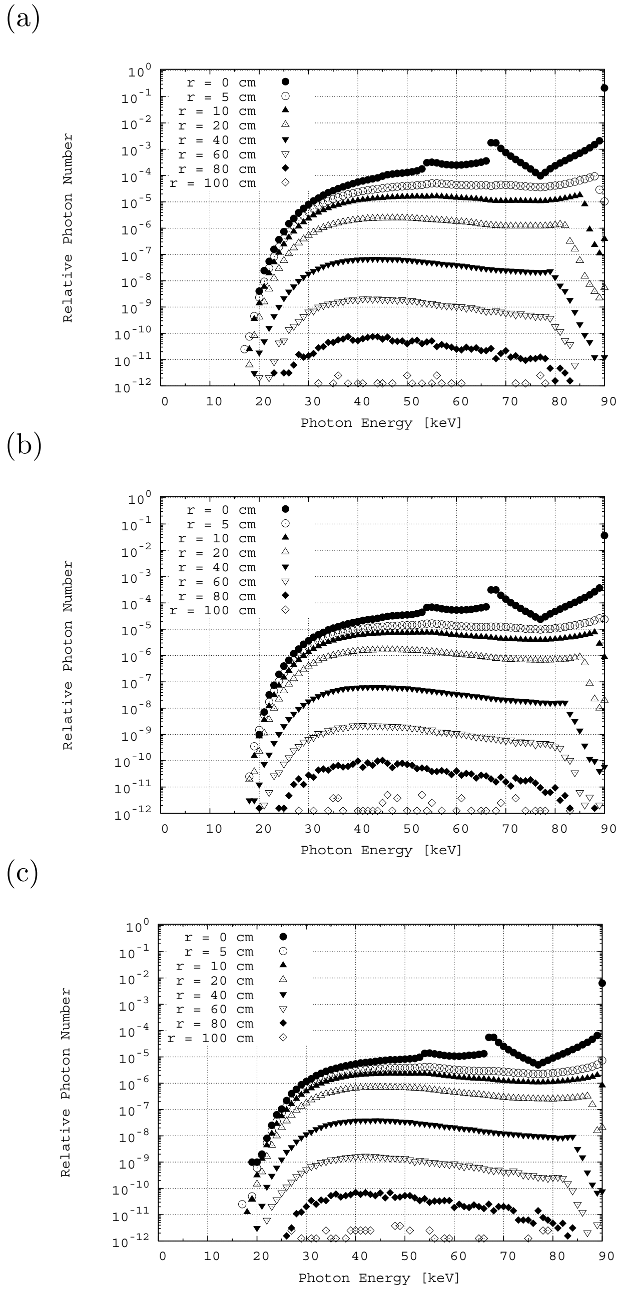

Figure 4: Calculated photon energy spectra in water at the depth of (a) 10 cm, (b) 20 cm and (c) 30 cm. The parameter r is the distance from the beam axis. The incident photon energy is 90 keV.

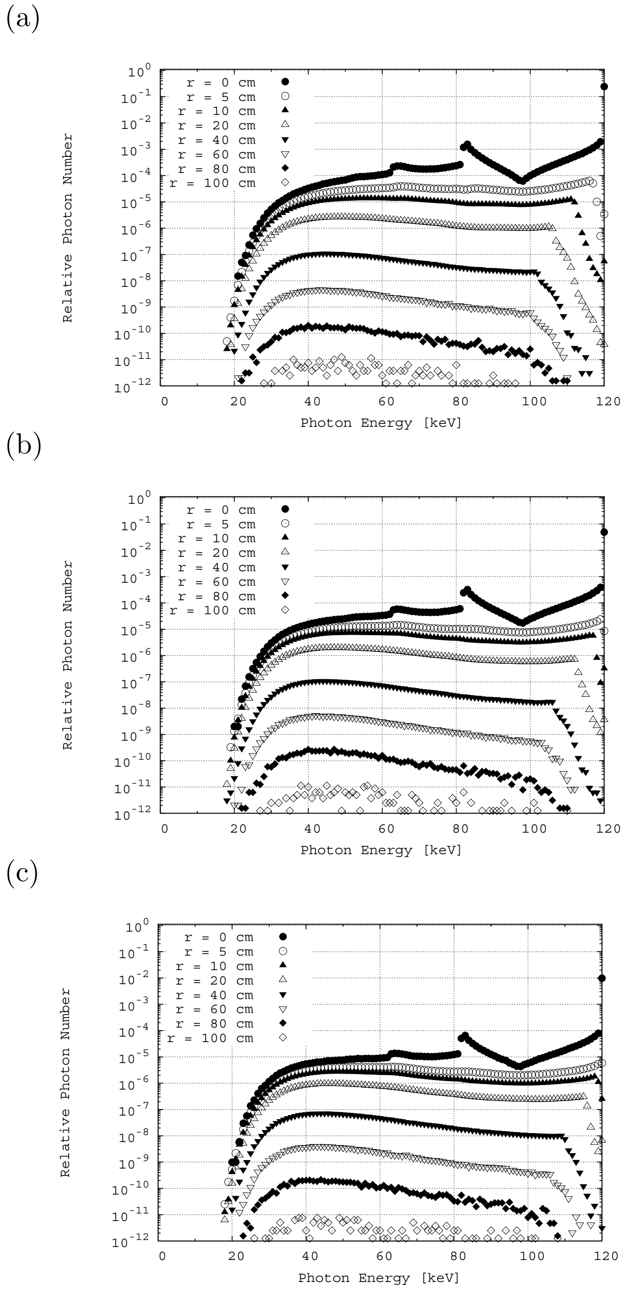

Figure 5: Calculated photon energy spectra in water at the depth of (a) 10 cm, (b) 20 cm and (c) 30 cm. The parameter r is the distance from the beam axis. The incident photon energy is 120 keV.

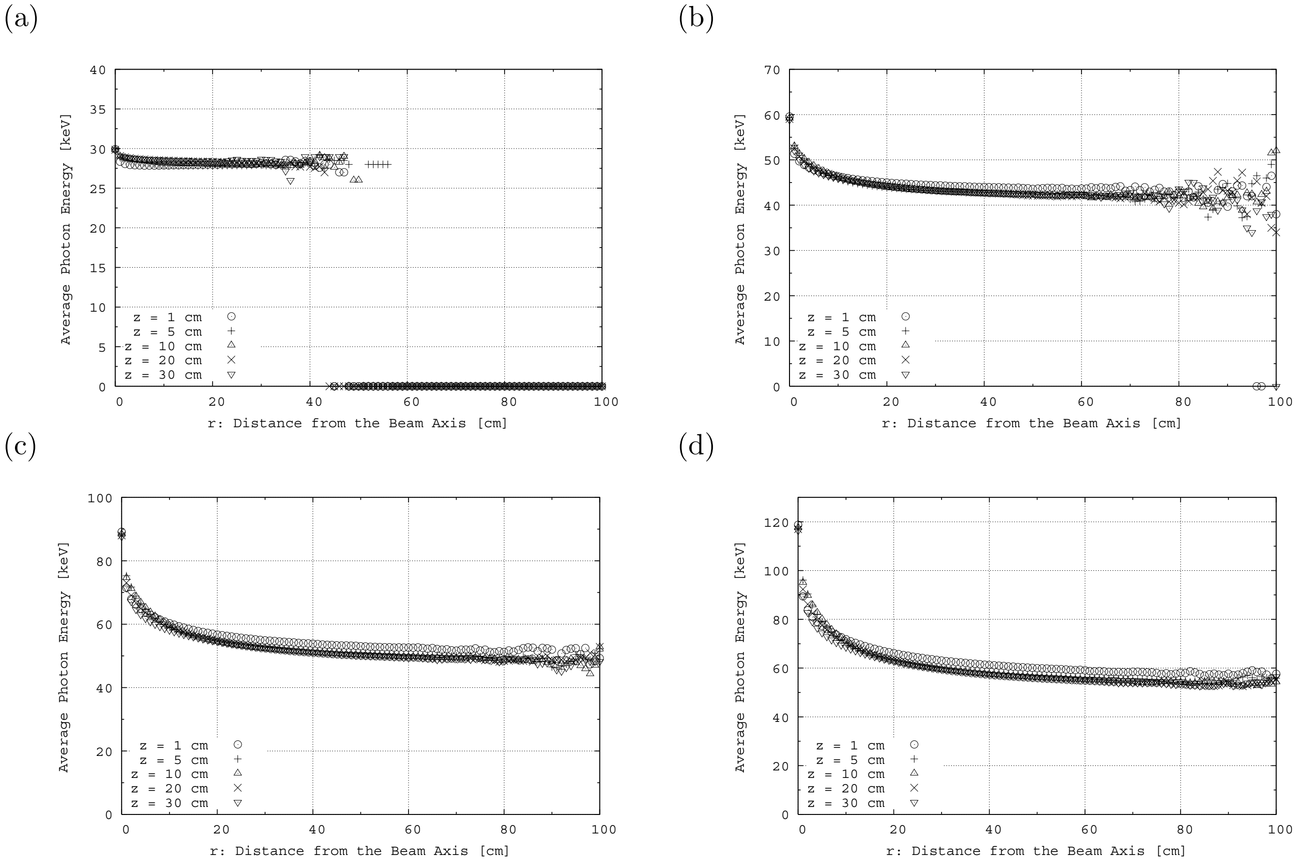

Figure 6: Average photon energy in water. The incident photon energy is (a) 30 keV, (b) 60 keV, (c) 90 keV and (d) 120 keV. The parameter z is the depth in the beam direction, and the r is the distance from the beam axis.

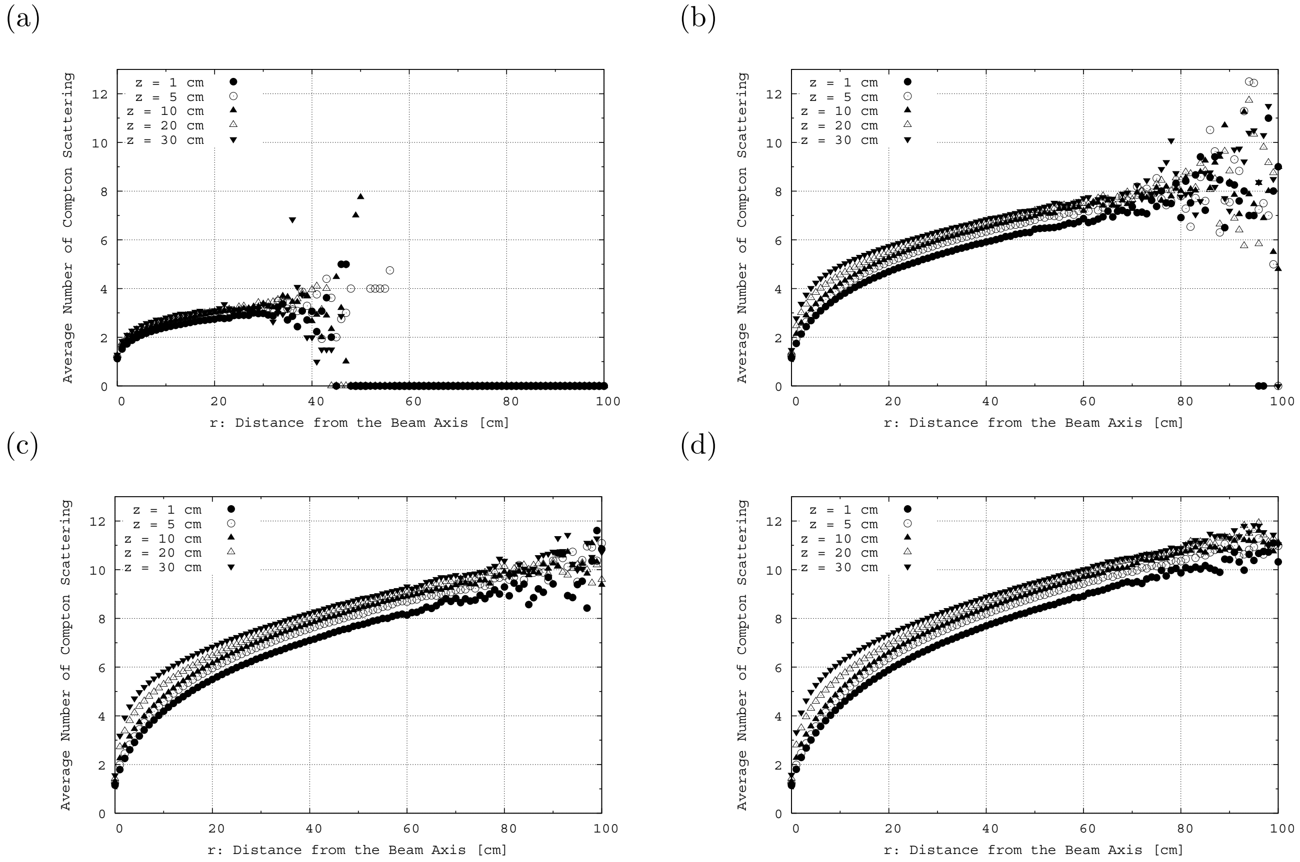

Figure 7: Average number of Compton scattering in water. The incident photon energy is (a) 30 keV, (b) 60 keV, (c) 90 keV and (d) 120 keV. The parameter *z* is the depth in the beam direction, and the *r* is the distance from the beam axis.

the incident surface (i.e. the deeper), the larger the average number of Compton scattering. The fluctuations at large *r* are also due to small number of photons reaching there.

4 DISCUSSION

4.1 Pencil beam of monoenergetic photons used in this study

Monoenergetic incident photons are used in this study. A typical photon source (for example, an x-ray tube) is polyenergetic in the patient dosimetry. As the results with polyenergetic photons are considered to be the weighted sum of monoenergetic results, the results obtained in this study are valid not only for monoenergetic photon beams, but for polyenergetic photon beams. The same can be said for a pencil beam used in this study. As the results with the fields of arbitrary shapes or directions (for example, a broad beam, an irregular field and the rotational irradiation) are the convolution of those with a pencil beam, the results are also valid for a broad beam with arbitrary shapes or the rotational irradiation, etc.

4.2 Interactions in water

The linear attenuation coefficients of water and their compositions are shown in Fig. 8. The curves indicate the followings:

- The photoelectric effect is dominant in the energy below around 30 keV in water.

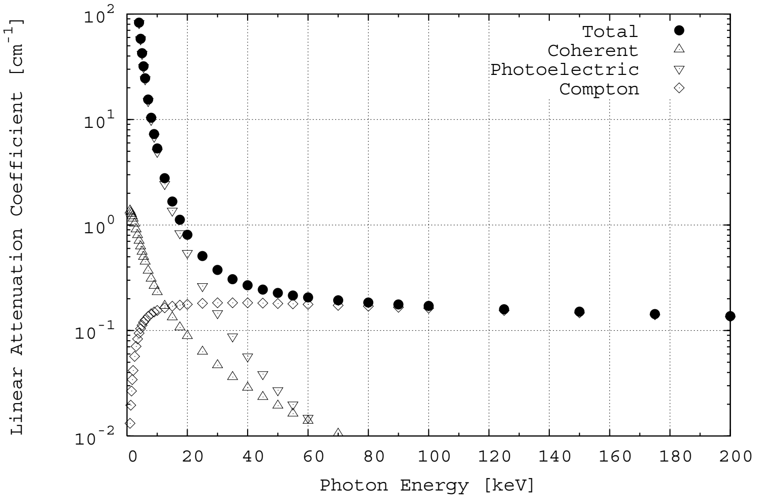

Figure 8: The linear attenuation coefficients of water [17]. The total linear attenuation coefficients are composed of the linear attenuation coefficients for the coherent scattering, the photoelectric effect and the Compton scattering in this energy range.

- The Compton scattering is dominant in the energy above 30 keV.
- The contribution of the coherent scattaring is minimal.

Figure 9 shows the mean free path (MFP) of photons in water. The MFP is the recirocal of the linear attenuation coefficient. The curve for the Compton scattering is almost flat (around 5-7 cm) in this energy range. This means that the Compton scattering occurs every 5-7 cm on average in water, independent of photon energy in the diagnostic energy range.

The energy of Compton-scattered photons depends on the incident photon energy and the scattering angle. The relations between the energy of Compton-scattered photon and the scattering angle in the compton scattering are shown as a function of incident photon energy in Figure 10. The discrepancy between the energy of incident photons and that of scattered photons is dependent on the incident energy: the higher the incident energy, the larger the discrepancy. The energy of Compton-scattered photons depends on the scattering angle: the energy of the scattered photon is lower with larger scatting angle. It should be noted that the maximum energy loss occurs in the Compton scattering with the scattering angle of 180 degrees.

4.3 Average photon energy and average number of Compton scattering

Figure 6 shows that the decrease of the average photon energy is steep near the beam axis. In addition, the decrease is larger in case of incident photons with higher energy. This is because the Compton scattering is dominant in the higher energy region (Fig. 8) and higher energy photons tend to experience larger energy loss during the Compton scattering (Fig. 10). It should be noted that the photons near the axis have higher energy (see Figs. 2 to 5).

Figure 7 shows that incident photons with higher energy allow larger number of Compton scattering. This is because of the lower probability of the photoelectric effect in the higher energy region (Fig. 8). The figure also shows that the longer distance in r and z causes larger number of Compton scattering. This means that the chance of the Compton scattering is larger for the longer distance. Note that the MFP of the Compton scattering in water is around 6 cm in this energy range, irrespective of photon energy (Fig. 9).

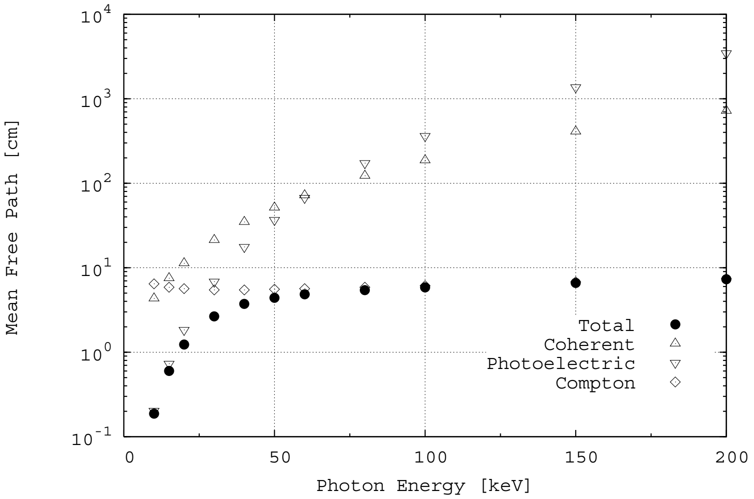

Figure 9: The mean free path (MFP) of photons in water. The data in this figure are calculated from the linear attenuation coefficients in Fig. 8 [17]. Note that the MFP is the reciprocal of the linear attenuation coefficient.

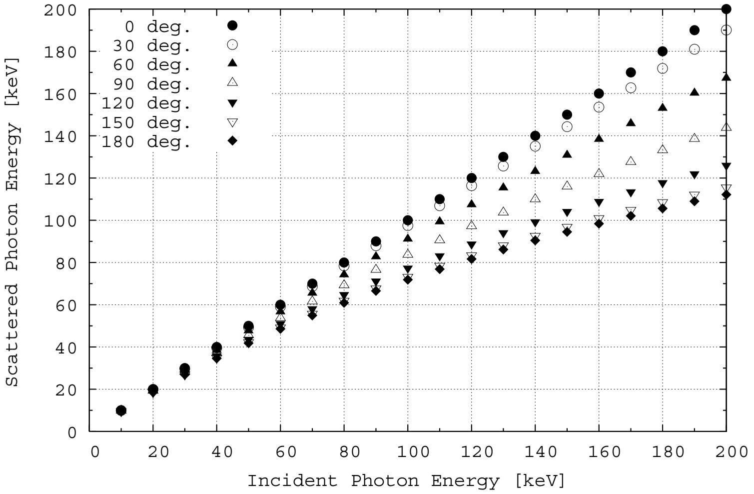

Figure 10: The energy-angle relations in the Compton scattering. The data are calculated using the equations in the footnote[1].

Photons lose its energy during the Compton scattering. Therefore, the larger number of Compton scattering means lower photon energy there. The data in Figs. 2 to 5 and Fig. 6 reflect the results in Fig. 7.

4.4 Edges on photon energy spectra

As shown in Figs. 3 to 5, the edges on the proton energy spectra are apparent especially for $r = 0$. Judging from the energy, the edges are due to Compton-scattered photons with the scattering angle of 180 degrees. For example, the edge is prominent at around 82 keV in Fig. 5(a). When the energy of the incident photon is 120 keV, the energy of 180 degs. Compton-scattered photon is 81.7 keV. When the 180 degs. scattered photon (81.7 keV) experiences 180 degs. scattering again, the resultant energy of the scattered photon is 62.1 keV, corresponding to the energy of the second edge at around 62 keV[1] (see Fig. 10). As the scattering angle with the maximum energy loss in the single Compton scattering is 180 degrees, the discontinuities occur at the energy corresponding to 180 degrees Compton-scattered photons: the continuum exists in the higher energy region of the edge due to Compton-scattered photons with the scattering angles smaller than 180 degrees.

4.5 Lower limit of photon energy in a water phantom

Figures 2 to 5 show that the lower limit of photon energy in the water phantom is around 20 keV, irrespective of incident photon energy. This means that scattered photons with the energy below 20 keV are rare in water.

As shown in the section 4.2, the main interactions in the diagnostic energy range are the photoelectric effect and the Compton scattering. High-energy photons tend to interact with media by the Compton scattering. Photons lose its energy by giving the energy to the recoil electron during the Compton scattering. Meanwhile, low-energy photons tend to interact with media by the photoelectric effect. In the photoelectric interaction, photon energy is absorbed completely by media and photon disappears. Therefore, high-energy photons lose its energy by the Compton scattering and low-energy photons disappear by the photoelectric effect on the whole. With these two interactions, the limit appears around 20 keV. Note that the probability of the Compton scattering is far smaller than that of the photoelectric effect, and the energy transfer to the recoil electron is quite small during the Compton scattering in the low-energy region below 20 keV (see Fig. 10). This means that a large energy loss of photons is not probable in this energy region.

4.6 Effects of variations of photon energy spectra on patient dosimetry

The calibration of detector is usually done with the incident photon beams, because the energy spectra at the site of a detector are unknown. However, as shown in Figs. 2 to 5, photon energy spectra in the water phantom are quite different from those of incident photons. In addition, the energy spectra depend on the position in the water phantom. If the response of a detector used in the patient dosimetry is dependent on photon energy, the calibration with the incident photon beams may cause an error in the dosimetry.

---

[1] The energy of the Compton-scattered photons is calculated by the following equation [19]:

$$E_{scat} = E \cdot \frac{1}{1 + \alpha(1 - cos\theta)}$$

where

$$\alpha = \frac{E}{m_0 c^2}$$

E is the incident energy, and E_{scat} is the energy of the scattered photon. The parameter α is the ratio of the energy of the incident photon to the rest energy of the electron (i.e. $m_0 c^2$).

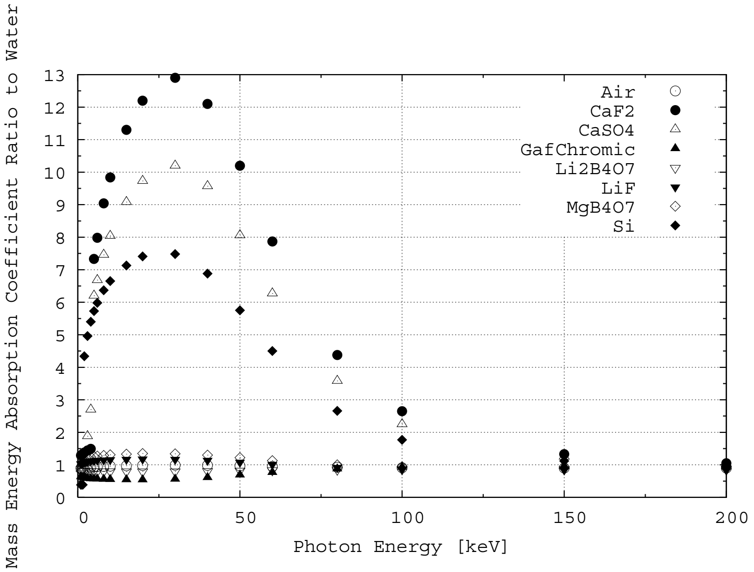

Figure 11: The mass energy absorption coefficient ratios of typical detector materials in the patient dosimetry to water [20].

Usually water is substituted for the soft-tissue in a human body in the patient dosimetry. In this case, the ideal detector in the patient dosimetry is the one whose detector response is proportional to the absorbed dose in water. However, the mass energy absorption coefficients of materials, especially with high effective atomic numbers, are rather different from those of water. Figure 11 shows the mass energy absorption coefficient ratios of typical detector materials to water [20]. The curves indicate that the ratios of detector materials with a high effective atomic number (such as CaF_2, $CaSO_4$ and Si) are far larger than unity in the energy range below 100 keV. This means that the detectors with a high effective atomic number may show the over-response in this energy range. The results in this study indicate that the use of tissue-equivalent materials is preferred in the patient dosimetry because of the spectral variations in a water phantom.

5 CONCLUSIONS

Calculated photon energy spectra in a water phantom were shown as a function of incident photon energy and the position in the phantom. The photon energy spectra in water were quite different from those of incident photons. However, the energy spectra at the site of a detector in a phantom are usually unknown in the patient dosimetry. As the detector response depends on photon energy, the use of tissue-equivalent materials for a dosimeter is recommended in the patient dosimetry, judging from the spectral variations in a water phantom calculated in this study.

References

[1] D. V. Cormack, T. J. Griffith and H. E. Johns, *"Measurement of the spectral distribution of scattered 400 kVp x rays in a water phantom"* Brit. J. Radiol. **30** (1957) 129-135.

[2] D. V. Cormack, W. E. Davitt, D. G. Burke and E. G. Rawson, *"Spectral distributions of 280 kVp x rays"* Brit. J. Radiol. **31** (1958) 565-570.

[3] D. V. Cormack and G. Burke, *"Spectral distrubutions of primary and scattered 140kVp x-rays"* Radiology **74** (1960) 743-752.

[4] G. Hettinger and K. Liden, *"Scattered radiation in a water phantom irradiated by roentgen photons between 50 and 250 keV"* Acta Radiol. 53 (1960) 73-92.

[5] G. Hettinger and N. Starfelt, *"Energy and angular distribution of scattered radiation in a water tank irradiated by x-rays"* Ark. Fysik. **14** (1959) 497-511.

[6] E. R. Epp and H. Weiss, *"Spectral fluence of scattered radiation in a water medium irradiated with diagnostic x-rays"* Radiat. Res. **30** (1967) 129-139.

[7] S. Mak and D. V. Cormack, *"Spectral distributions of scattered x rays at points lying off the beam axis"* Brit. J. Radiol. **33** (1959) 362-367.

[8] L. D. Skarsgard and H. E. Johns, *"Spectral flux density of scattered and primary radiation generated at 250 kV"* Radiat. Res. **14** (1961) 231-260.

[9] K. Aoki and M. Koyama, *"A silicon diode in a thimble-type mount for measurement of diagnostic x-ray spectra"* Phys. Med. Biol. **35** (1990) 1505-1517.

[10] W. R. Bruce and H. E. Johns, *"The spectra of x rays scattered in low atomic number materials"* Brit. J. Radiol. **Suppl. 9** (1960) 1-57.

[11] N. Petoussi, M. Zankl, W. Panzer and P. Nette, *"Photon spectra in standard dosimetric phantom or imaging phantoms calculated with Monte Carlo methods"* Radiat. Prot. Dosim. **43** (1992) 147-149.

[12] J. R. Cunningham and R. J. Schulz, *"On the selection of stopping-power and mass energy-absorption coefficient ratios for high-energy x-ray dosimetry"* Med. Phys. **11** (1984) 618-623.

[13] J. R. Cunningham, M. Woo, D. W. O. Rogers and A. F. Bielajew, *"The dependence of mass energy absorption coefficient ratios on beam size and depth in a phantom"* Med. Phys. **13** (1986) 496-502.

[14] S. Miyajima, K. Imagawa and M. Matsumoto *"Variations of x-ray spectra in water phantom during CT scanning: simulation study"* KEK Proceedings **2002-12** (2002) 164-174.

[15] S. Miyajima, *"The variations of mean energy absorption coefficient ratios in water phantoms during x-ray CT scanning"* KEK Proceedings **2002-18** (2003) 74-83.

[16] *"The EGS5 code system"*, **SLAC-R-730/KEK 2005-8**.

[17] *"XCOM: Photon Cross Sections Database"*, http://physics.nist.gov/PhysRefData/Xcom/Text/XCOM.html.

[18] *"ESTAR"*, http://physics.nist.gov/PhysRefData/Star/Text/ESTAR.html.

[19] H. E. Johns and J. R. Cunningham, *"The Physics of Radiology, 4th ed."* (1983), Charles C. Thomas Publisher.

[20] J. H. Hubbell and S. M. Seltzer, *"Photon mass attenuation and energy-absorption coefficients from 1 keV to 20 MeV for elements Z = 1 to 92 and 48 additional substances of dosimetric interest"* NISTIR **5632** (1995).

Investigation on photon energy response of amorphous silicon EPID using a Monte Carlo method

Yukio Fujita, Hidetoshi Saitoh and Atsushi Myojoyama

Graduate School of Human Health Sciences, Tokyo Metropolitan University,
Tokyo, 116-8551, Japan

ABSTRACT

In recent radiation therapy, the electronic portal imaging device (EPID) is significant as a quality assurance (QA) tool for intensity modulated radiation therapy (IMRT). Some QA software for delivered dose verification is commercially available. Such software can compare images of actually delivered fluence and predicted image by convolution of planned fluence distribution and point spread function in EPID. Only single spread function is usually provided for an accelerate potential, and it is adjusted to get a good agreement between predicted image and actual EPID image of the reference field. However, variation of photon energy spectrum between the IMRT and the reference field can be expected because the IMRT fields consist of various segmented fields and off-set fields. Therefore, this study investigates photon energy response of EPID and develops a method to correct for energy dependence of EPID response. To investigate the response of EPID for photon, the point spread functions in EPID for several mono energies were calculated by Monte Carlo simulation. As a result, it is obvious that the variation of point spread function is negligible for energy. However, the energy absorption in phosphor layer varied with photon energy. Therefore, the EPID image can be predicted by convolution of planned fluence distribution and point spread function which is corrected with local energy spectrum. And it is confirmed that the predicted image well agreed with actual acquired image.

1. INTRODUCTION

Amorphous silicon (a-Si) EPID is originally designed for patient position verification. Moreover EPID is utilized for verification of pre-treatment dose and delivered dose because of their linear response to absorbed dose [1-3]. Some QA software for delivered dose verification is commercially available. Such software can compare images of actually delivered fluence and predicted image by convolution of planned fluence distribution and point spread function in EPID. For the prediction method, only single spread function is usually provided for an accelerate potential, and it is adjusted to get a good agreement between predicted image and actual EPID image of the reference field.

However, variation of photon energy spectrum between the IMRT and the reference field can be expected since the IMRT fields consist of various segmented fields and off-set fields. Therefore, photon energy response of EPID was investigated and a correction method for energy dependence of EPID was proposed in this study.

2. MATERIALS AND METHODS

2.1 Detector description

The aS500 (Varian Medical Systems, Palo Alto, CA) was modeled as a sample of EPID. This EPID is mounted on a linear accelerator gantry as shown in Fig.1-(a) and a cross sectional view of the detector is shown in Fig.1-(b). The detector consists of a copper plate and a phosphor layer which converts incident photon into visible light and the light is sensed by an array of photodiodes. The signal of light intensity is digitized by a 14 bit analog to digital converter. The sensitive area of the detector is 40 cm×30 cm and each pixel size is 0.784 cm×0.784 cm.

2.2 Calculation of EPID response for several photon energies

To investigate the response of EPID for mono energetic photons, the detector response functions in EPID were calculated by the EGS Monte Carlo simulation. The simulation geometry of image detection unit (IDU) in the aS500 is shown in Fig.2. The geometry and material compositions were based on the information provided by manufacturer. For the a-Si EPID, it is estimated that 99.5 % of the signal is generated by photon and electron interactions within the phosphor layer [4]. The remaining 0.5 % of the total signal is due to direct photon and electron interactions with the photodiodes. Furthermore, it is known that the response of the photodiode is proportional to the energy absorption of the phosphor [4,5]. Therefore, the EPID response was calculated by sampling of energy absorption of the phosphor layer in this study. Energy absorption in equally spaced radial bins (Δr=0.0392 cm as 1/2 of pixel width) was sampled using the DOSRZnrc code [6] as shown in Fig.3.

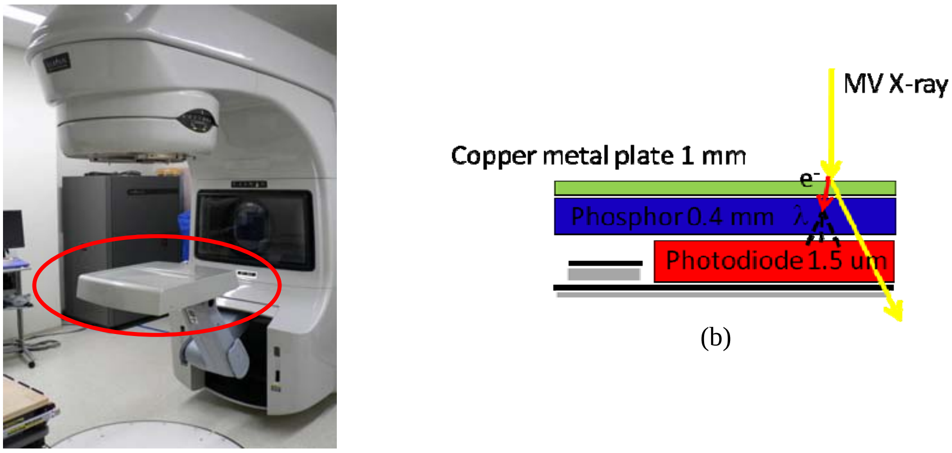

(b)

(a)

Fig.1 Electronic Portal Imaging Device (a) general view and (b) Cross sectional view of EPID.

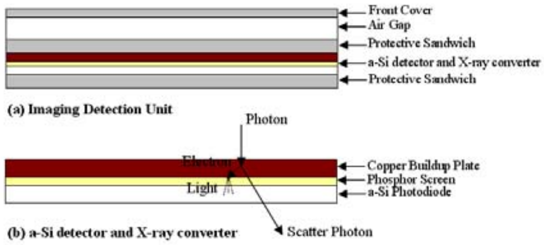

Fig.2 Cross-sectional view of (a) the image detection unit and (b) the a-Si detector and X-ray converter (Varian aS500 EPID).

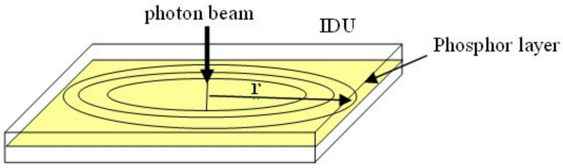

Fig.3 Simulation geometry of point spread functions in EPID.

3. RESULTS AND DISCUSSION

3.1 Pencil beam response in EPID

Dose spread functions for several photon energies are shown in Fig.4. The spread functions were normalized to absorbed dose of central bin. It is obvious that the variation of normalized point spread function is negligible for photon energy.

Absorbed dose of phosphor layer as a function of photon energy is shown in Fig.5. The energy absorption in phosphor layer varied with photon energy.

Therefore, the image prediction algorithm by convolution of planned fluence distribution and single spread function can not predict the EPID image accurately. Consequently, the energy correction for point spread function is required to accurately predict EPID image.

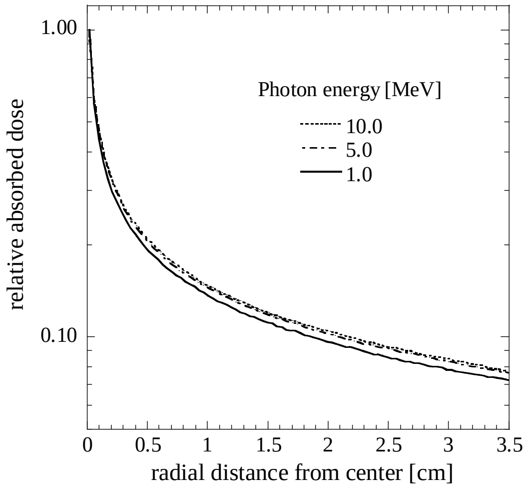

Fig.4 Point spread functions in phosphor layer for several photon energies.

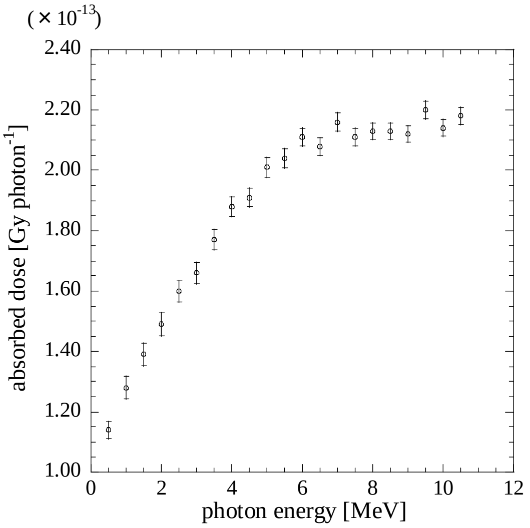

Fig.5 Absorbed dose of phosphor layer as a function of photon energy.

3.2 **Comparison between predicted and actual image**

It is obvious that the EPID image can be accurately predicted by convolution of planned fluence distribution and point spread function corrected spectral variation. Therefore, the point spread function was corrected with local energy spectrum in this study. In order to evaluate improved image prediction method, predicted image was compared with actually acquired image.

Figure 6 shows comparison of profiles between predicted and acquired image for (a) static field of 10 cm×10 cm and (b) dynamic 30 degree wedge field of 10 cm×10 cm. These results were evaluated by the gamma evaluation method [7]. It was confirmed that there is good agreement between predicted and acquired image because gamma indexes were below 1.0 for 98 % of whole field.

4. CONCLUSION

To investigate the energy dependence of EPID, point spread function for pencil beam of several mono energy photons was simulated using Monte Carlo method. The result clarifies that normalized point spread function is independent of energy of photon, however, the energy absorption in phosphor layer varied with photon energy. The predicted image using corrected point spread functions were shown a good agreement with actual acquired image. Consequently, it is confirmed that energy correction for point spread function is required to predict EPID image accurately.

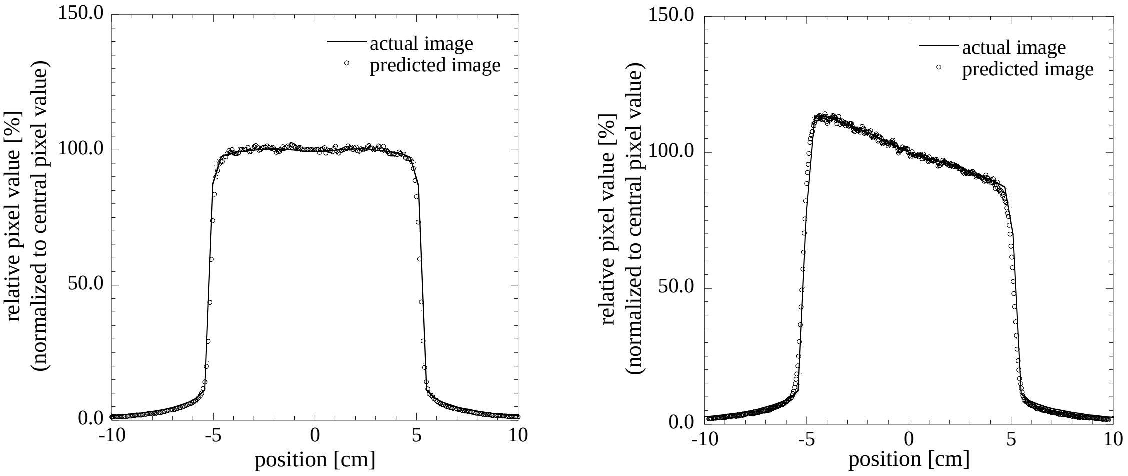

(a) (b)

Fig.6 Comparison between predicted and acquired profile of pixel value for (a) static field of 10 cm×10 cm and (b) dynamic 30 degree wedge field of 10 cm×10 cm.

5. REFERENCES

1) Y. El-Mohri, L. E. Antonuk, J. Yorkston, K. W. Jee, M. Maolinbay, K. L. Lam, and J. H. Siewerdsen: Relative dosimetry using active matrix flatpanel imager (AMFPI) technology. Med. Phys. 26:1530-1541 (1999)
2) B. M. McCurdy, K. Luchka, and S. Pistorius: Dosimetric investigation and portal dose image prediction using an amorphous silicon electronic portal imaging device. Med. Phys. 28:911-924 (2001)
3) G. V. Menon and R. S. Sloboda: Compensator quality control with an amorphous silicon EPID. Med. Phys. 30:1816-1824 (2003)
4) P. Munro and D. C. Bouius: X-ray quantum limited portal imaging using amorphous silicon flat-panel arrays. Med. Phys. 25:689-702 (1998).
5) L. E. Antonuk, Y. El-Mohri, W. Huang, K. W. Jee, J. H. Siewerdsen, M. Maolinbay, V. E. Scarpine, H. Sandler, and J. Yorkston: Initial performance evaluation of an indirect-detection, active matrix flat-panel imager (AMFPI) prototype for megavoltage imaging. Int. J. Radiat. Oncol., Biol., Phys. 42**:**437-454 (1998).
6) Report No. PIRS-701: *The EGSnrc Code System*: Monte Carlo Simulation of Electron and Photon Transport. National Research Council of Canada, Ottawa, ON (2002).
7) Daniel A. Low, William B. Harms, Sasa Mutic, and James A. Purdy: A technique for the quantitative evaluation of dose distributions. Med. Phys. 25:656-661 (1998).

EVALUATION OF PATIENT DOSE IN CEREBRAL ANGIOGRAPHY EXAMINATIONS

Y.Emoto[1], S.Koyama[2]

[1]Department of Radiological Technology, Graduate School of Medicine,
Nagoya University
1-1-20 Daikou – Minami, Higashi-ku, Nagoya, Japan
[2]Nagoya University School of Health Sciences
e-mail: emoto.yuki@f.mbox.nagoya-u.ac.jp

Abstract

Medical exposure has been increasing with the development of new radiological equipment and new diagnostic techniques like Interventional radiology (IVR). In cerebral IVR procedure, large numbers of angiographic images are obtained in various irradiation conditions and x-ray incident directions. The purpose of this study is to investigate whether absorbed dose for organ can be estimated using Monte Carlo simulation code EGS5. We compared between measurement dose and calculation dose in two types of direction, PA-projection and cranio15°, and several irradiation conditions. Difference of maximum 40 % was caused between the measurement dose and the calculation dose. It was thought to be causally related to difference of phantom between measurement and calculation. Tendency of calculation dose in all conditions and directions agreed with those of measurement dose. Application of voxel phantom modeled on physical phantom will make a good agreement between measurements and calculations. Evaluation of patient dose using Monte Carlo simulation in cerebral angiography is useful to get information of patient exposure under various conditions.

1. Introduction

Medical exposure has been increasing with the development of new radiological equipment and new diagnostic techniques like Interventional radiology (IVR). To control medical exposure, it is important to understand the patient exposure undergoing each diagnostic technique. IVR is a less-invasive diagnostic and therapeutic procedure which is performed under fluoroscopic guidance. With the developments of equipments like angiocatheter and x-ray image detector, number of cerebral IVR cases is increasing. In cerebral IVR procedure, large numbers of angiographic images are obtained under various irradiation conditions and x-ray incident directions. Therefore, it is difficult to measure patient exposure under all conditions of operation. To estimate patient exposure in large numbers of conditions, Monte Carlo simulation method is very useful. In this study, we calculate absorbed dose of body organs using EGS5 and measure the organ doses using anthropomorphic phantom and semiconductor dosimeters. By comparing the calculation dose with the measured dose, the efficacy of Monte Carlo simulation in the cerebral IVR is evaluated.

2. Materials and Method

2.1 Organ dose measurements

In the measurement, an organ dose measuring system constructed by an anthropomorphic phantom and semiconductor dosimeters was used. The anthropomorphic phantom (THRA-1, Kyoto Kagaku Co. LTd., Kyoto) was constructed with soft tissue equivalent, bone equivalent and lung tissue equivalent materials. It was modeled a standard Japanese adult man.

A semiconductor dosimeter was made by two silicon photodiodes (S2506-04, Hamamatsu Photonics K.K., Hamamatsu) which were glued together back-to-back to obtain isotropic sensitivity of x-rays1). The dosimeters were installed in centroid position of radiation-sensitive organs in the phantom as defined in ICRP (International Commission on Radiation Protection).

The phantom was set on couch of angiographic device (AXION Artis dBA, Simence Medical Solutions, Munich), and the irradiation field size was 32 cmx32 cm and 22 cmx22 cm on the surface of image receptor (flat panel detector). Tube voltage and tube current were automatically adjusted to patient body thickness. Source-to-image distance (SID) was 100 cm, and x-ray incident angle was posteroanterior direction called "PA-projection". PA-projection was parallel to orbito-meatal line which was shown in Fig.1(a). X-ray incident angle inclined from PA-projection to 15° further craniocaudal axis was called "cranio 15°" which was shown in Fig.1(b). Patient exposure was measured under condition of digital subtraction angiography.

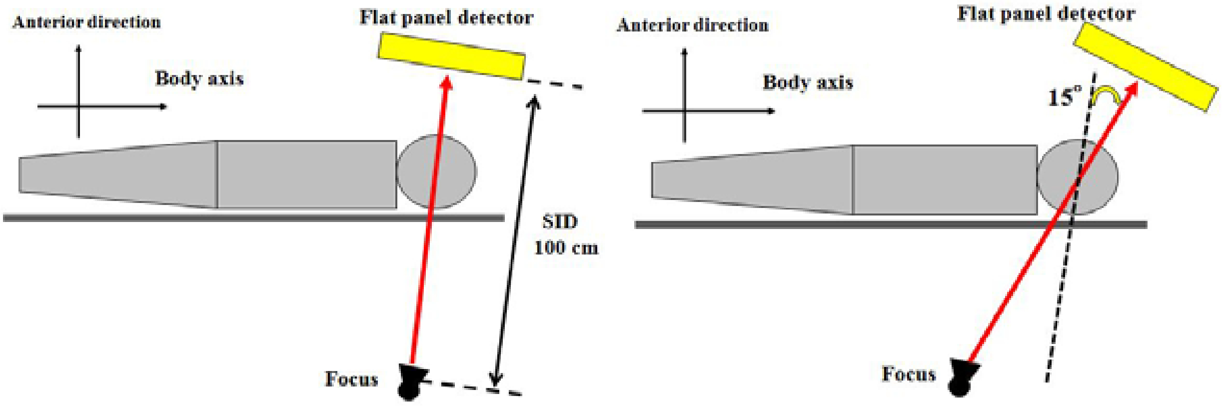

(a) PA-projection (b) cranio15°

Fig.1. X-ray incident angle

2.2 Monte Carlo simulation using EGS5

Simulation geometry was constructed with the same geometry of the measurement and Medical Internal Radiation Dose (MIRD) type phantom was used as the mathematical anthropomorphic phantom. X-ray tube voltage was set at 70 kV, 83 kV and 92 kV for PA-projection and set at 84 kV and 91 kV for cranio15°, and x-ray spectra were calculated by Birch's formula. The number of photons was set to become less than 2 % of fractional standard deviation (FSD) at the region of thyroid. The cut-off energy was 5 keV for photons and 1 keV for electrons.

In EGS5 simulation, it is difficult to get absolute amount of absorbed dose. So a deposit energy ratio of each organ to x-ray entrance skin was calculated and the organ absolute dose was obtained by multiplying the deposit energy ratio by entrance skin dose measurements.

2.3 Calculation of organ doses

In the measurement, output voltage signals generated from the photodiode dosimeters were read out, and each signal was converted to the absorbed dose for soft tissue by using the conversion factor. In the calculation, the deposited energy in the region allocated in each organ was divided in the mass of the organ to calculate the absorbed dose.

Dose for red bone marrow, $D_{bone\ marrow}$, was evaluated from the equation

$$D_{bone\ \ marrow} = \sum_i D_{soft\ \ tissue,i} \cdot A_i \quad ,$$

where $D_{soft\ tissue,i}$ is the absorbed dose for soft tissue at each measuring point in the various points of bone marrow. This is because mass energy-absorption coefficients for red bone marrow coincided with those for soft tissue within 5 % in diagnostic x-ray energy of >30 keV$^{2)}$. A_i is the weight fraction of each red bone marrow, the values of which were shown in Table 1. The weight fraction, i.e. contribution of individual red bone marrow in total weight, could be quoted from ICRP Publication 70$^{3)}$.

Dose for the bone surface, $D_{bone\ surface}$, was evaluated from the equation

$$D_{bone\ \ surface} = \left\{ \sum_i D_{soft\ \ tissue,i} \cdot M_i \right\} \times \frac{1}{2} \left\{ \frac{(\mu_{en}/\rho)_{soft\ \ tissue} + (\mu_{en}/\rho)_{bone}}{(\mu_{en}/\rho)_{soft\ \ tissue}} \right\} \quad ,$$

where M_i is the weight fraction of mineralized bone as indicated in Table 2, and $(\mu_{en}/\rho)_{\text{soft tissue}}$ and $(\mu_{en}/\rho)_{\text{bone}}$ are the mass energy-absorption coefficients for soft tissue and bone, respectively.

For the evaluation of skin dose, absorbed doses at the entrance of x-ray was measured by using an extra dosimeter attached to the surface of the phantom. A dose value of the surface dosimeter was multiplied by the ratio of the irradiated skin area to the gross surface skin area of the phantom to calculate average organ dose for the skin.

Table 1. Weight fraction of red bone marrow (A_i)

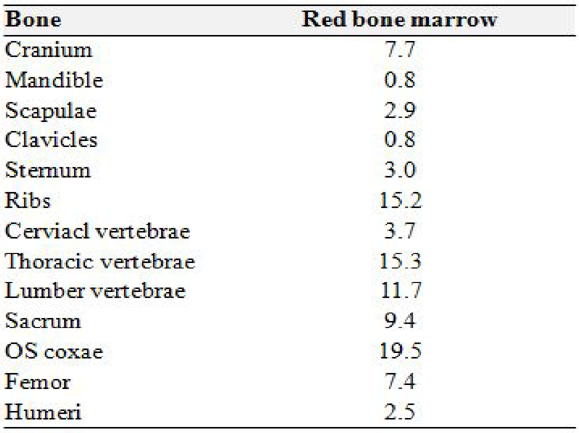

Bone	Red bone marrow
Cranium	7.7
Mandible	0.8
Scapulae	2.9
Clavicles	0.8
Sternum	3.0
Ribs	15.2
Cerviacl vertebrae	3.7
Thoracic vertebrae	15.3
Lumber vertebrae	11.7
Sacrum	9.4
OS coxae	19.5
Femor	7.4
Humeri	2.5

Table 2 . Weight fraction of mineralized bone (M_i)

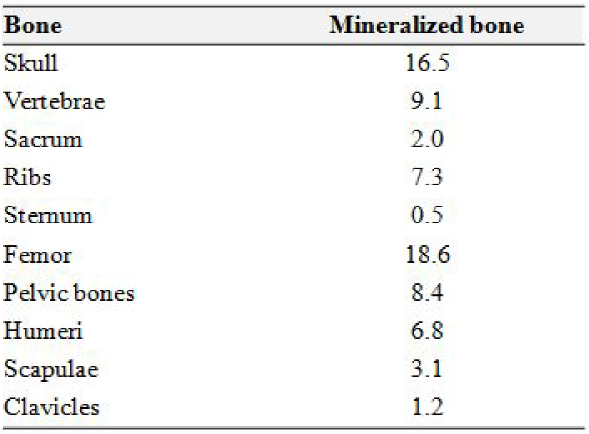

Bone	Mineralized bone
Skull	16.5
Vertebrae	9.1
Sacrum	2.0
Ribs	7.3
Sternum	0.5
Femor	18.6
Pelvic bones	8.4
Humeri	6.8
Scapulae	3.1
Clavicles	1.2

3. Results

3.1 PA-direction

Organ doses obtained from measurements and calculations are show in Table 3 , and the dataset of tube voltage of 70 kV was graphed out (Fig.2). Digital subtraction angiography was taken 4 frames per second and organ doses in Table 3, Table 4, Fig.2 and Fig.3 is absorbed dose per one frame. Each organ dose was obtained by using deposit energy ratio of each organ to x-ray entrance skin. Absorbed doses for the organs in the head and neck such as brain, lens and salivary glands were 0.02-0.50 mGy. On the other hands, absorbed doses for the organs in the trunk such as lung, liver, stomach, kidney and gonad were all less than 0.01 mGy. Maximum organ dose was brain dose, and absorbed dose for brain by the measurements was 0.208 mGy, and it by the calculations was 0.163 mGy. Entrance skin dose measurements were 0.86, 2.12, and 2.28mGy, in tube voltage of 70, 82, and 92kV, respectively. To reduce the patient exposure, Cu filter was automatically inserted at exit window of x-ray tube housing according to x-ray intensity penetrated to image receptor plane. Cu filter thickness was optimized for x-ray tube voltage associated with patient thickness. As relatively thick filter was selected for tube voltage of 70 kV, the entrance skin dose was smallest in all tube voltage.

Table 3. Absorbed doses for the organs in PA-projection

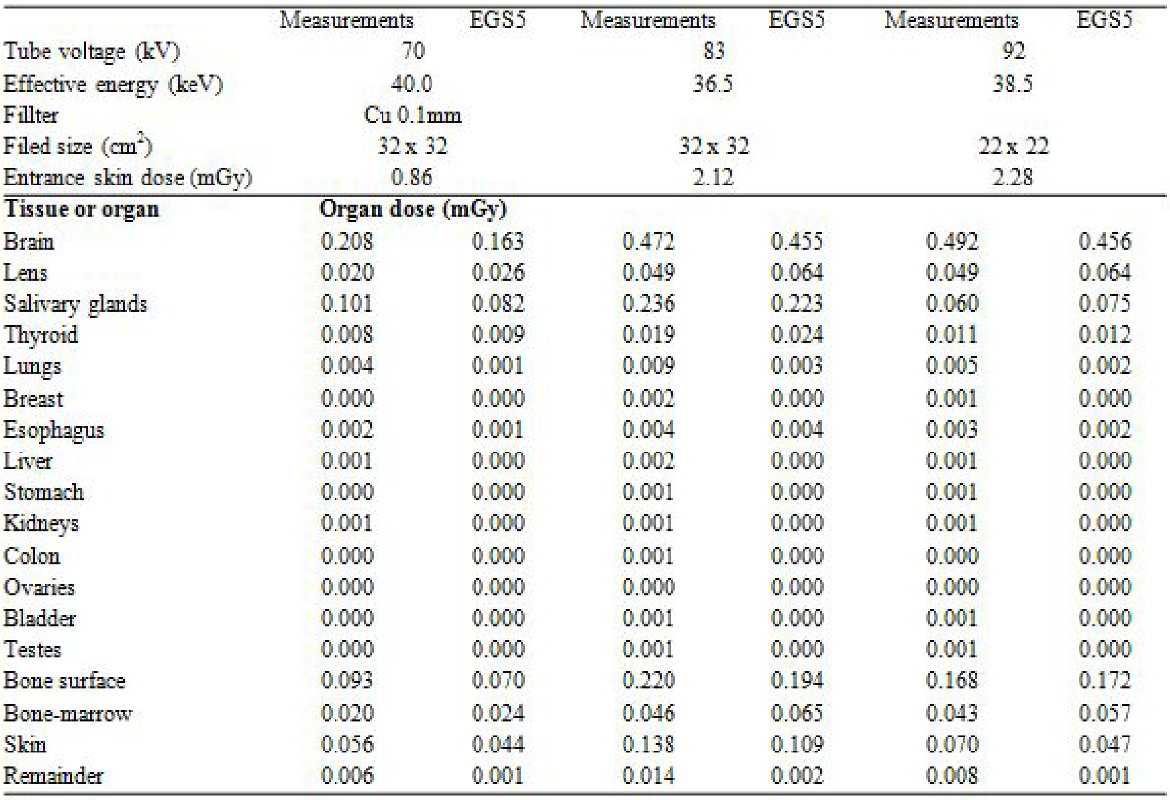

	Measurements	EGS5	Measurements	EGS5	Measurements	EGS5
Tube voltage (kV)	70		83		92	
Effective energy (keV)	40.0		36.5		38.5	
Fillter	Cu 0.1mm					
Filed size (cm^2)	32 x 32		32 x 32		22 x 22	
Entrance skin dose (mGy)	0.86		2.12		2.28	
Tissue or organ	**Organ dose (mGy)**					
Brain	0.208	0.163	0.472	0.455	0.492	0.456
Lens	0.020	0.026	0.049	0.064	0.049	0.064
Salivary glands	0.101	0.082	0.236	0.223	0.060	0.075
Thyroid	0.008	0.009	0.019	0.024	0.011	0.012
Lungs	0.004	0.001	0.009	0.003	0.005	0.002
Breast	0.000	0.000	0.002	0.000	0.001	0.000
Esophagus	0.002	0.001	0.004	0.004	0.003	0.002
Liver	0.001	0.000	0.002	0.000	0.001	0.000
Stomach	0.000	0.000	0.001	0.000	0.001	0.000
Kidneys	0.001	0.000	0.001	0.000	0.001	0.000
Colon	0.000	0.000	0.001	0.000	0.000	0.000
Ovaries	0.000	0.000	0.000	0.000	0.000	0.000
Bladder	0.000	0.000	0.001	0.000	0.001	0.000
Testes	0.000	0.000	0.001	0.000	0.001	0.000
Bone surface	0.093	0.070	0.220	0.194	0.168	0.172
Bone-marrow	0.020	0.024	0.046	0.065	0.043	0.057
Skin	0.056	0.044	0.138	0.109	0.070	0.047
Remainder	0.006	0.001	0.014	0.002	0.008	0.001

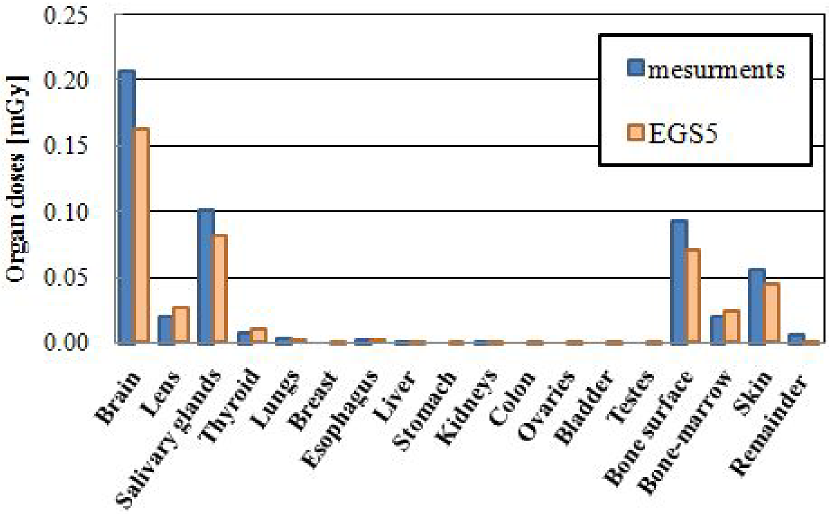

Fig 2. Absorbed doses for the organs in PA-projection for the tube voltage of 70 kV. Digital subtraction angiography was taken 4 frames per second, and organ dose is absorbed dose per one frame.

3.2 Cranio15°

Organ doses obtained from measurements and calculations are shown in Table 4 , and the dataset of tube voltage of 84 kV was graphed out (Fig.3). Absorbed doses for the organs in the head and neck such as brain, lens and salivary glands were 0.03-0.40 mGy. On the other hands, absorbed doses for the organs in the trunk such as lung, liver, stomach, kidney and gonad were all less than 0.015 mGy.

Table 4. Absorbed doses for the organs in cranio15°

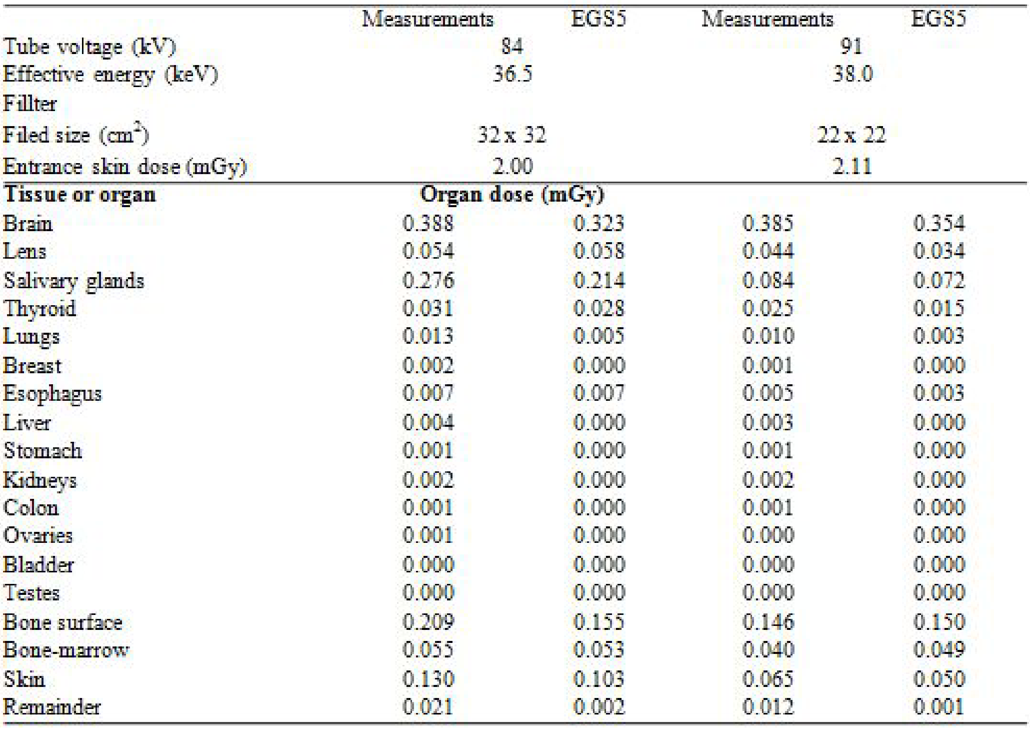

	Measurements	EGS5	Measurements	EGS5
Tube voltage (kV)	84		91	
Effective energy (keV)	36.5		38.0	
Fillter				
Filed size (cm^2)	32 x 32		22 x 22	
Entrance skin dose (mGy)	2.00		2.11	
Tissue or organ	**Organ dose (mGy)**			
Brain	0.388	0.323	0.385	0.354
Lens	0.054	0.058	0.044	0.034
Salivary glands	0.276	0.214	0.084	0.072
Thyroid	0.031	0.028	0.025	0.015
Lungs	0.013	0.005	0.010	0.003
Breast	0.002	0.000	0.001	0.000
Esophagus	0.007	0.007	0.005	0.003
Liver	0.004	0.000	0.003	0.000
Stomach	0.001	0.000	0.001	0.000
Kidneys	0.002	0.000	0.002	0.000
Colon	0.001	0.000	0.001	0.000
Ovaries	0.001	0.000	0.000	0.000
Bladder	0.000	0.000	0.000	0.000
Testes	0.000	0.000	0.000	0.000
Bone surface	0.209	0.155	0.146	0.150
Bone-marrow	0.055	0.053	0.040	0.049
Skin	0.130	0.103	0.065	0.050
Remainder	0.021	0.002	0.012	0.001

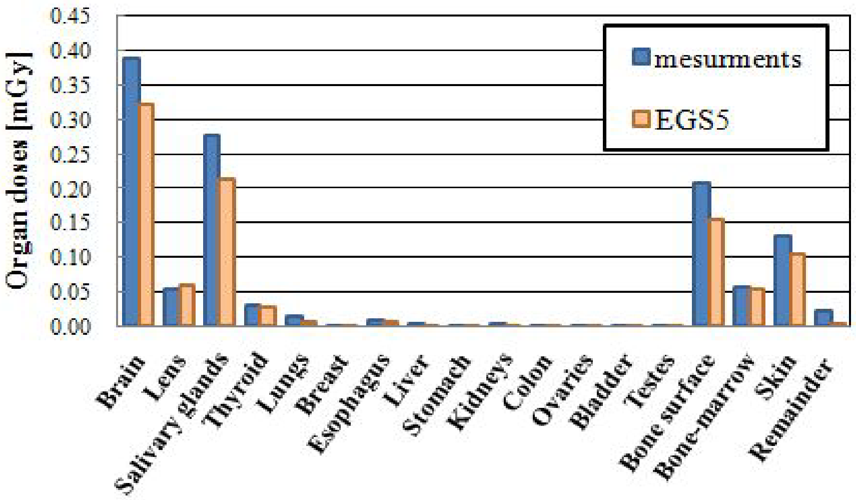

Fig 3. Absorbed doses for the organs in cranio15° for the tube voltage of 84 kV. Digital subtraction angiography was taken 4 frames per second, and organ dose is absorbed dose per one frame.

3.3 Comparison

Fig.4 and Fig.5 show difference between measured data and calculation results of EGS5. The difference is defined as follows:

$$difference = \frac{d_{EGS5} - d_{measured}}{d_{measured}} \times 100 \ [\%]$$

where d_{EGS5} and $d_{measured}$ are organ dose in EGS5 and the measurement, respectively. As shown in Fig.4 and Fig.5, the largest difference was 40 % for bone-marrow in PA-projection. In cranio15°, the largest difference was 40 % for thyroid. An irregular difference was caused in organs around the irradiation field like salivary glands and lens.

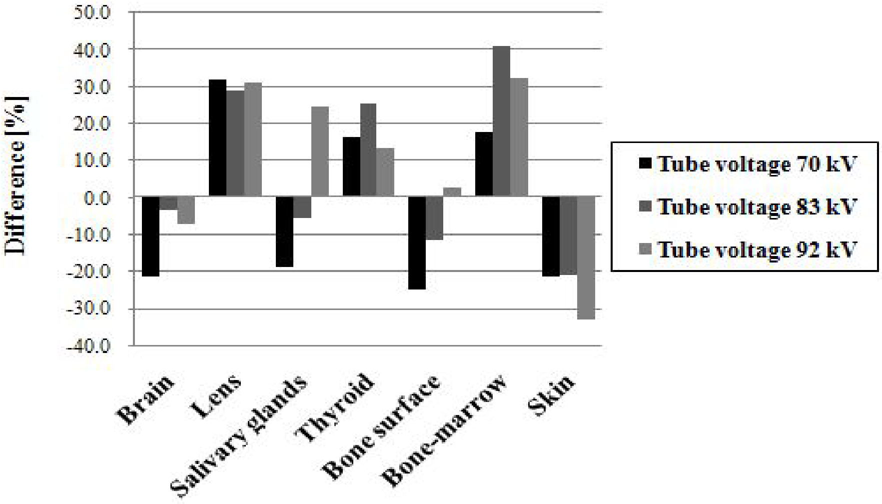

Fig 4. The difference between measurements and calculation results by EGS5 in PA-projection

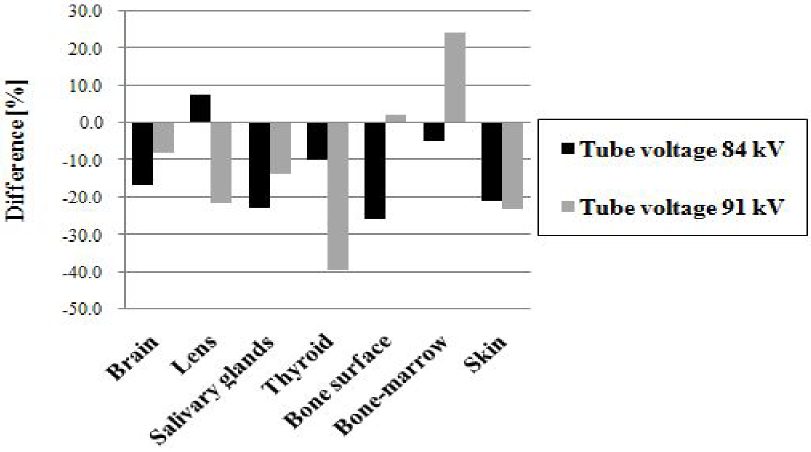

Fig 5. The difference between measurements and calculation results by EGS5 in cranio15°

4. Discussions

As show in Table 3 and Table 4, absorbed dose for the organ in the head such as brain, lens and salivary glands exposed to primary x-ray was larger than it for the organs in the trunk such as lung, liver and gonad exposed to scattered radiation.

Fig.4 and Fig.5 showed difference between measurements and calculation results and the maximum difference was 40 %. It might be caused by the difference of phantom used in the measurement and the calculation. The anthropomorphic phantom used in measurement was modeled a standard Japanese adult man, but the mathematical phantom used in calculation was modeled a standard Westerner adult. To decrease the difference between calculations and measurements, the organ parts of MIRD phantom should be resized to the size of Japanese adult. Furthermore, application of voxel phantom modeled on physical phantom will make a good agreement with those.

5. Conclusions

In this work, patient exposure doses were measured using an organ dose measuring system and calculated using EGS5 in cerebral angiography examinations and the comparison between measurements and calculations was performed. Organ dose of measurements and calculated results did not show the significant difference between each organ except for some organs. Evaluation of patient dose using Monte Carlo simulation in cerebral angiography is useful to get information of patient exposure under various conditions.

References

1) Aoyama, T., Koyama, S. and Kawaura, C.: An in-phantom dosimetry system using pin silicon photodiode radiation sensors for measuring organ doses in x-ray CT and other diagnostic radiology, Med. Phys. 29, 1504-1510 (2002).

2) International Commission on Radiation Unit and Measurements. Photon, electron, proton and neutron interaction data for body tissues. ICRU Report 46 (Bethesda, MD: ICRU) (1992)

3) International Commission on Radiation Protection. Basic anatomical &physiological data for use in radiological protection: the skeleton. ICRP Publication 70. Ann. ICRP 25(2) (Oxford: Pergarmon Press) (1995)

VALIDATION OF POINT DOSIMETRY IN ORGAN DOSE ESTIMATION IN ANTHROPOMORPHIC PHANTOM

T.Nakagawa[1], S.Koyama[2]

[1]Department of Radiological Technology, Graduate school medicine,
Nagoya University,
1-1-20 Daikou-Minami, Higashi-ku, Nagoya, 461-8673, Japan
[2]Nagoya University School of Health Sciences
e-mail: nakagawa.takuya@c.mbox.nagoya-u.ac.jp

Abstract

There have been substantial advances in helical CT since its introduction in 1989. Organ dosimetry in CT, however, has lagged behind technologic advancement. To obtain patient exposure, average organ dose was generally measured at many points in the organ evenly in an anthropomorphic phantom using thermoluminescent dosimeters (TLDs). If semiconductor dosimeter is used for the measurement, we can perform the organ dose real-time analysis. In the measurement using semiconductor dosimeter, a sufficient number of dosimeters are not usually used for the measurement at the same time, thus one or several dosimeters were placed at centroid of the organ. We formed voxel phantom from CT DICOM data of anthropomorphic phantom. To compare the dose at the centroid of the liver with an average dose in the whole liver, Monte Carlo simulation method was used. The difference between the point dose at centroid of the liver and the average dose of the whole liver which were calculated by the EGS5 was within 5%. In the evaluation of the patient exposure, we think actual measurement is more important than calculation method to obtain more accurate data. For accurate measurement of organ dose, it is better to install many dosimeters in the organ evenly. In this study, even if we cannot use sufficient number of dosimeter, it is possible to measure the organ doses accurately by optimization of dosimeter location in the phantom.

1. Introduction

There have been substantial advances in helical CT since its introduction in 1989. Organ dosimetry in x-ray CT, however, has lagged behind technologic advancement. To obtain patient exposure, average organ dose was generally measured at many points in the organ evenly in an anthropomorphic phantom using thermoluminescent dosimeters (TLDs)[1-2]. TLD read out was provided after all procedure of the measurement, thus it takes many times to get average organ dose. If semiconductor dosimeter is used for the measurement, we can perform the organ dose real-time analysis. In the measurement using semiconductor dosimeter, a sufficient number of dosimeters are not usually used for the measurement at the same time, thus one or several dosimeters were placed at centroid of the each organ[3-4]. In this study, usefulness of point dosimetry in organ dose estimation was validated using Monte Carlo simulation. We formed voxel phantom from CT DICOM data of anthropomorphic phantom. To compare the dose at the centroid of the liver with an average dose in the whole liver, EGS5 was used.

2. Materials and Methods

2.1 Voxel phantom

Voxel phantom was formed by simulating our organ dose measurement system using an anthropomorphic phantom and semiconductor dosimeters. The anthropomorphic phantom, THRA-1(Kyoto Kagaku Co., Ltd, Kyoto), is modelled on the standard Japanese adult man, 170 cm tall and 60 kg in weight. The phantom was composed of three materials; bone-equivalent, lung tissue equivalent and soft tissue equivalent. Except lung and bone structure, the phantom has no compartment of each organ. The photodiode dosimeters were installed within the phantom at the position of various organs and tissues assigned by International Commission on Radiological Protection (ICRP) definition of effective dose[5-6]. For organ with large volume such as liver, a dosimeter was set at centroid of the organ subdivided two or more equally, and these doses were averaged for determining liver dose. Figure 1 shows the location of the semiconductor dosimeter installed in the anthropomorphic phantom. The mathematical voxel phantom was constructed from CT DICOM data of the anthropomorphic phantom. Slice data was derived from thoracoabdominal CT scan with 20 slices with 1cm intervals. The slice data is consisted of 512 pixel × 512 pixel. Each voxel size was $1.875 \times 1.875 \times 10.0$ mm^3. Material of each voxel was automatically distinguished with CT value using application software made by Microsoft Visual Basic ver.6.0 (Microsoft Co, Ltd, Washington D.C.). Each voxel was assigned the materials of air, lung tissue, soft tissue, and bone, respectively. To decide region of the liver from trunk area, a schema of anatomical drawing from anatomy book was used.

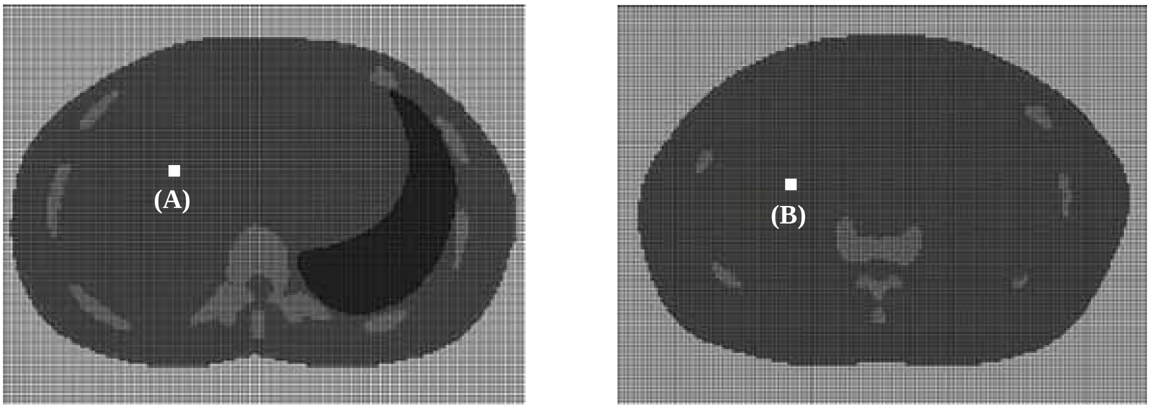

Figure 1. The location of the semiconductor dosimeter installed in the anthropomorphic phantom. (A) upper centroid of liver and (B) lower centroid of liver.

2.2 Calculation with Monte Carlo code

Dose deposited to each voxel in x-ray CT was calculated using Monte Carlo code EGS5. Number of photons was set to become less than 5% of statistical error at the region of centroid of the liver and cut-off energy of the photon was set to 5keV. The distance between isocenter and the source was set to 60cm, and the photon was expose to isocenter from point on the circumference of circle. Incident photon energy spectrum was calculated by Birch's formula on the condition of tube voltage 120kVp and target angle of 12 degree.

3. Results

3.1 The dose comparison of the liver

The organ dose in voxel phantom was estimated based on energy deposition calculated by EGS5. Table 1 shows a comparison of a point dose in the centroid of the liver (and average of (A) and (B)) and average dose of the whole liver. The difference between the point dose at centroid of liver and the average dose of the whole liver was within 5%.

Table 1. Comparison of a point dose and whole liver dose in voxel phantom

	Deposited energy [MeV]	Number of voxel	Dose per voxel [J/kg]	Percentage difference*
Point (A)	8.22	1	1.32×10^{-15}	3.1
Point (B)	7.24	1	1.16×10^{-15}	-9.4
Average of (A) and (B)	15.46	2	1.24×10^{-15}	-3.1
Whole organ dose	377738	47075	1.28×10^{-15}	-

*The difference with whole organ average dose

3.2 The dose distribution in the voxel phantom

Figure 2 shows the dose distribution in the voxel phantom and the position of the semiconductor dosimeter (Point (B)). The size of semiconductor dosimeter sensitive area is 2.8 x 2.8 mm^2. There was double difference between maximum and minimum point dose of the liver in voxel phantom. Table 2 shows the absorbed dose shift of the voxel around the centroid of liver with the location of the point. In the Figure 2, though difference of the gray level was not sufficiently expressed, large dose shift was observed in Table 2.

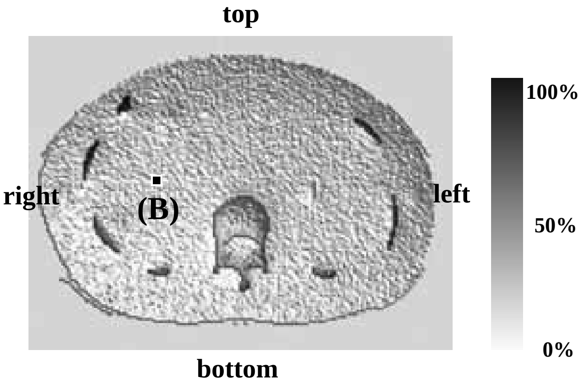

Firure 2. Dose distribution in the voxel phantom.

Table 2. Absorbed dose shift of the voxel around the centroid of liver with location of the point

Distance [mm]	Difference from centroid [%] right	top	left	bottom
5	10.4	1.1	-7.3	-1.2
10	21.0	11.7	-10.8	1.9
15	21.7	12.8	-12.8	3.6
20	32.6	15	-16.2	3.9

4. Discussion

In the Table 1, the difference between the point dose at centroid of liver and the average dose of the whole liver was within 5%. This means the dose at the centroid of the liver represented the whole liver dose. At the same time, as is obvious from the Table 2, if the dosimeter is not proper placement, it may indicate large dose shift. In this study, to optimize location of dosimeter of organ dosimetry, absorbed dose in voxel phantom was calculated by Monte Carlo code EGS5. In the evaluation of the patient exposure, we think actual measurement is more important than calculation method to obtain more accurate data. For accurate measurement of organ dose, it is better to install many dosimeters in the organ evenly. This study showed it is possible to measure the organ dose accurately when it is impossible to use a large number of dosimeters.

5. Conclusions

To measure patient exposure, it is important to install a sufficient number of dosimeters in organ in anthropomorphic phantom. We examine optimum installation of small number of dosimeters in the anthropomorphic phantom using Monte Carlo simulation method. This study shows that the absorbed dose measured at centroid of organ represent average dose for distributed in the organ entirely.

References

1) Groves AM, Owen KE, Courtney HM, et al.: 16-detector multislice CT: dosimetry estimation by TLDmeasurement compared with Monte Carlo simulation. Br J Radiol 77: 662–665(2004)
2) Yoshizumi TT, Goodman PC, Frush DP, et al.: Validation of metal oxide semiconductor field effect transistor technology for organ dose assessment during CT: Comparison with thermoluminescent dosimetry. AJR 188: 1332–1336(2007)
3) T. Aoyama, S. Koyama, C. Kawaura, An in-phantom dosimetry system using pin silicon photodiode radiation sensors for measuring organ doses in X-ray CT and other diagnostic radiology: Med. Phys. 29, 1504-1510(2002).
4) C. Kawaura, T. Aoyama, S. Koyama, et al.: Organ and effective dose evaluation in diagnostic radiology based on in-phantom dose measurements with novel photodiode-dosemeters. Radiat. Prot. Dosim. 118, 421-430(2006)
5) ICRP 1990: Recommendations of the International Commission on Radiological Protection. Publication 60. ICRP Oxford, UK, Pergamon,(1991)
6) ICRP 2007: Recommendations of the International Commission of Radiological Protection. publication 103. ICRP Oxford, UK, Pergamon,(2007)

Measurement of Monochromatic Radiation Using a Si Detector and Comparison with EGS5 Simulations

Y. Kirihara, Y. Namito†, M. Hagiwara†, and H. Hirayama†
The Graduate University for Advanced Studies, Oho1-1, Tsukuba, Ibaraki 305-0801, Japan
†*KEK High Energy Accelerator Research Organization, Oho1-1, Tsukuba, Ibaraki 305-0801, Japan*

Abstract

We have performed a mono-energetic X-ray (8 keV and 20 keV) scattering experiment at a BL-14C beam line in KEK Photon Factory. Photons scattered with Al, Si, Ti, Fe, Cu, C and Ag target were measured with a silicon PIN photo detector located at $\theta = 90°$. The measured data were compared with calculations using EGS5 code. The calculations and the measured data for K-X and L-X peak agreed within 11%, and those for Compton peak agreed within 8%.

1 Introduction

A mono-energetic photon scattering experiments using a Ge detector at KEK Photon Factory (KEK-PF) have been performed so far for evaluation of EGS5 code [1], and the EGS5 code well-reproduced a low energy characteristic X-ray ($\sim$ 8 keV) [2]. However, an efficiency of the Ge detector decrease below 10 keV due to the air and Kapton window between the detector and the target in the vacuum chamber.

Silicon PIN photo detectors (Si detector) are also used for measurements of X-ray spectrum at a low energy X-ray, and an efficiency of the Si detector does not decrease compared with that of the Ge detector because the Si detector was connected directly to the vacuum chamber. The efficiency of the Si detector and the Ge detector calculated with the EGS5 code are shown in Fig. 1.

In this paper, first, we measured the low energy characteristic X-ray with energy from 1.5 keV to 8.0 keV using the Si detector. Next, we calculated the response of the Si detector for scattered mono-energetic synchrotron photon at the angle $\theta = 90°$ on several targets. The measured spectra were compared to Monte Carlo simulations using the EGS5 code.

2 Experiments

Mono-energetic photons were delivered to a BL-14C beam line in KEK-PF. The experimental procedure is shown as follows (See also Fig. 2).

1. Synchrotron photons from a vertical wiggler were monochronized by a Si(1,1,1) double crystal monochrometer. The incident photon energy was 8 keV and 20 keV.
2. Number of incident mono-energetic photon beams were measured with a free-air ionization chamber placed in front of the target.
3. Mono-energetic photon beams were scattered with the target. Target materials were Al, Si, Ti, Fe, Cu, C and Ag (shown in Table 1).
4. The energy spectra of scattered photons were measured with the Si detector located at $\theta = 90°$.

Table 1: Target thickness and energy of the characteristic X-ray. Under lines indicate energy of the characteristic X-ray measured this experiment.

Target	Thickness [g/cm^2]	K-X energy [keV]	L-X energy [keV]
Al	0.525	1.487	-
Si	0.117	1.740	-
Ti	0.726	4.511	0.452
Fe	1.574	6.404	0.704
Cu	0.986	8.048	0.929
Ag	0.525	22.163	2.984
C	0.180	0.277	-

Table 2: Specification of the silicon PIN photo detector

Type	Window thickness [μm]	Silicon thickness [μm]	Dead layer [μm]	Resolution @5.9 keV [eV]
AMPTEK XR-100CR	12.5	300	0.15	200

Each target was installed in a vacuum chamber. The Si detector was connected directly to the vacuum chamber. A collimator of 1.5, 2.0 and 3.0 mm ϕ was placed in front of the Si detector. A distance from the surface of the target to the collimator was 222 mm. Specification of the Si detector used in the experiment is shown in Table 2.

Measured spectra were divided by number of photons irradiated to the target and the solid angle. The energy calibration was performed using two well-known energy peaks, Compton and K-X. At $\theta = 90°$, energy of Compton peak was obtained following formula:

$$E_c = \frac{E_\gamma}{1 + E_\gamma / mc^2} \tag{1}$$

where E_γ is an incident energy before scattering, and mc^2 is the rest mass of electron. The K-X energies were shown in Table 1.

2.1 The collimator size

The diameter of the collimators were determined by the accurate measurement with a microscope, and the solid angles were determined with the collimator size and the distance from the target to the collimator. The collimator size and the solid angle are shown in Table 3.

Table 3: The collimator size and the solid angle

Collimator	Measured size [mm ϕ]	Solid angle [sr]
1.5	1.448	3.465×10^{-5}
2.0	2.059	7.006×10^{-5}
3.0	2.978	1.466×10^{-4}

We measured the K-X peak yields from the Cu target for each collimator using the Si detector. The peak yields were compared with that of a previous experiment using a Ge detector and a collimator of 5.01 mm ϕ [2] shown in Fig. 3. The collimator of 3.0 mm ϕ was presumed that alignment of the collimator was the best because the number of photons of the collimator was more than that of other collimators. The geometric efficiency of the collimator of 3.0 mm ϕ was better than that of other collimators. Thus we selected the collimator of 3.0 mm ϕ for measurement scattered photons.

3 Calculations

We calculated the energy spectrum measured with the Si detector using the EGS5 code in two steps as follows.

3.1 Step 1:The energy spectrum of photon scattered from the target

The energy spectra scattered in the direction of $\theta = 90^\circ$ were calculated at a mono-energetic X-ray (8 keV and 20 keV) irradiated to the target. The EGS5 code has adopted a data of fluorescence and Coster-Kronig yields from *The Table of Isotopes eighth edition* [3]. Recently, Orion tested the K, L shell fluorescence yield and Coster-Kronig coefficients from EADL and Campbell's paper, and reported improvement of the calculated intensity [4]. Thus we calculated by the EGS5 using EADL for ω_K (K-shell fluorescence yield), and using Campbell's data for ω_L (L-shell fluorescence yield) and Coster-Kronig, respectively. The energy spectra at the incident energy of 20 keV are shown in Fig 4.

3.2 Step 2:The energy spectrum measured with the Si detector

The photon sources with distribution of the energy spectrum calculated in Step 1 were set to be uniformly distributed in the collimator ($\sim$3.0 mm ϕ). The direction of the incident photon was set parallel to the Si detector. The geometry of the Si detector is shown in Fig. 5. The photon beam enter the active region through the beryllium window, and the energy deposition ΔE in the active region was scored. The calculated peaks were broadened using Gauss function. The FWHM (full width at half maximum) of the measured data was used here, because energy resolution of the measured data was not considered in the EGS5 calculation.

4 Results and discussions

For the incident energy of 8 keV, the calculated and measured energy spectra for the Al, Si, Ti, Fe, Cu, C and Ag targets are shown in Fig. 6. The calculated spectra generally well-reproduce the measured spectra. The calculation and measurement of the K-X peaks of Al, Si, Ti, Fe and Cu targets and the L-X peak of Ag target agreed within 3%. The energy resolution of the Si detector was not enough to separate the Compton peak from the Rayleigh peak.

For the incident energy of 20 keV, the calculated and measured energy spectra for the Al, Si, Ti, Fe, Cu, C and Ag targets are shown in Fig. 7. The calculated spectra also well-reproduce the measured spectra. The calculation and measurement of the K-X peaks of Al, Si, Ti, Fe and Cu targets and the L-X peak of Ag target agreed within 11%. The Compton peaks agreed within 8%. The calculation shows overestimation for Rayleigh peak. The ratio of measured and calculated peaks are shown in Fig. 8.

References

[1] H. Hirayama, Y. Namito, A. F. Bielajew, S. J. Wilderman and W. R. Nelson, The EGS5 Code System. Report SLAC-R-730, Stanford Linear Accelerator Center, Stanford, CA, (2005).

[2] Y. Namito, H. Hirayama and S. Ban: “Improvements of Low Energy Photon Transport for EGS5”, In: *Proceedings of the 2nd International Workshop on EGS* Ed. H. Hirayama, Y. Namito and S. Ban, KEK Proc. **2000-20**,(2000) pp.11-22.

[3] Ed C. M. Lederer, V. S. Shireley, *Table of Isotopes* 7th edn (Wiley-Interscience, New York, 1978).

[4] I. Orion, Y. Namito, Y. Kirihara and H. Hirayama, *”Proceedings of the Fourteenth EGS Users’ Meeting in Japan,”* KEK Proceedings 2007-5, 33 (2007).

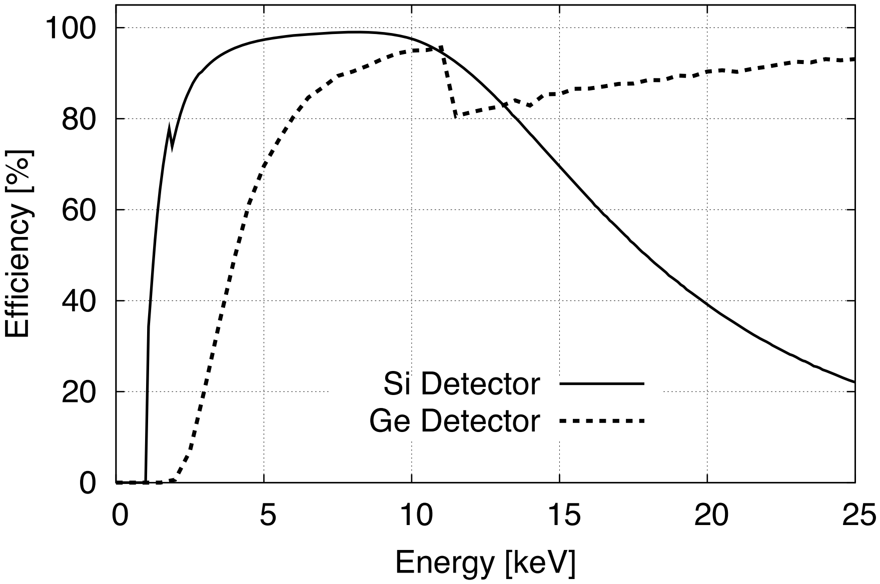

Figure 1: The peak efficiency of the detectors. The Si detector is shown by solid line. The Ge detector is shown dash line.

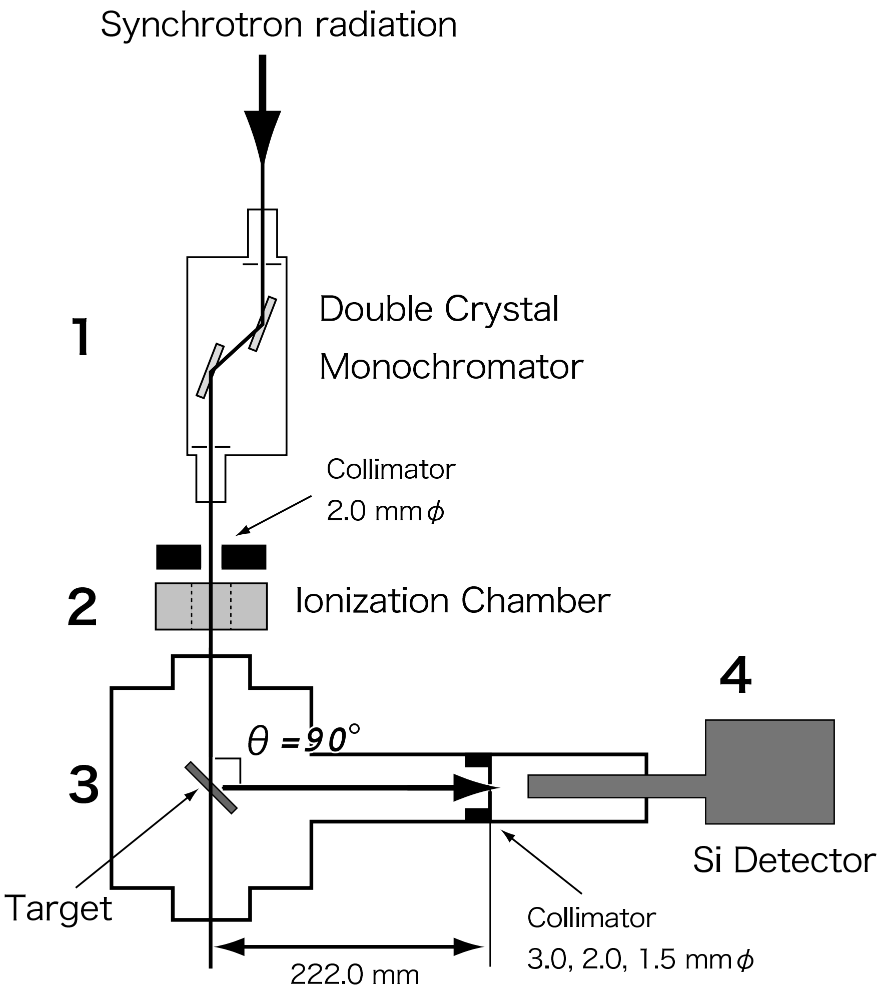

Figure 2: The PF experiment arrangement

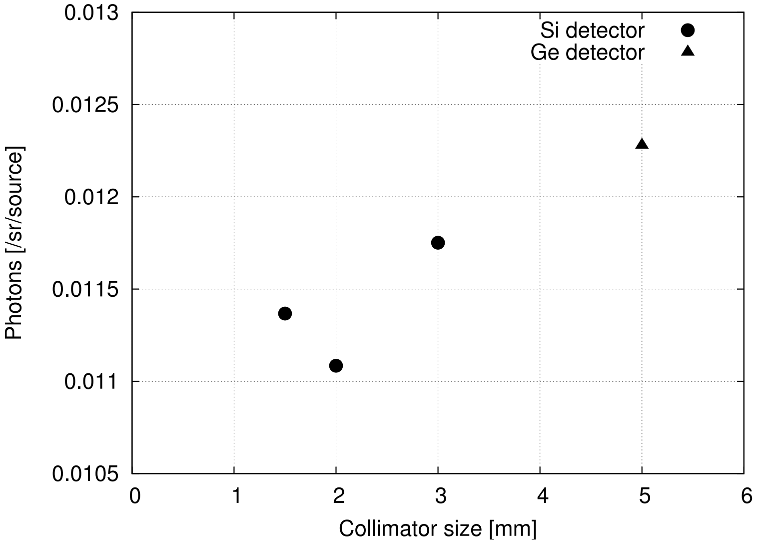

Figure 3: The count of photons when each collimator is used. The collimator of 1.5, 2.0 and 3.0 mm ϕ using the Si detector are shown in filled circles. That of 5.0 mm ϕ using the Ge detector is shown in filled triangle.

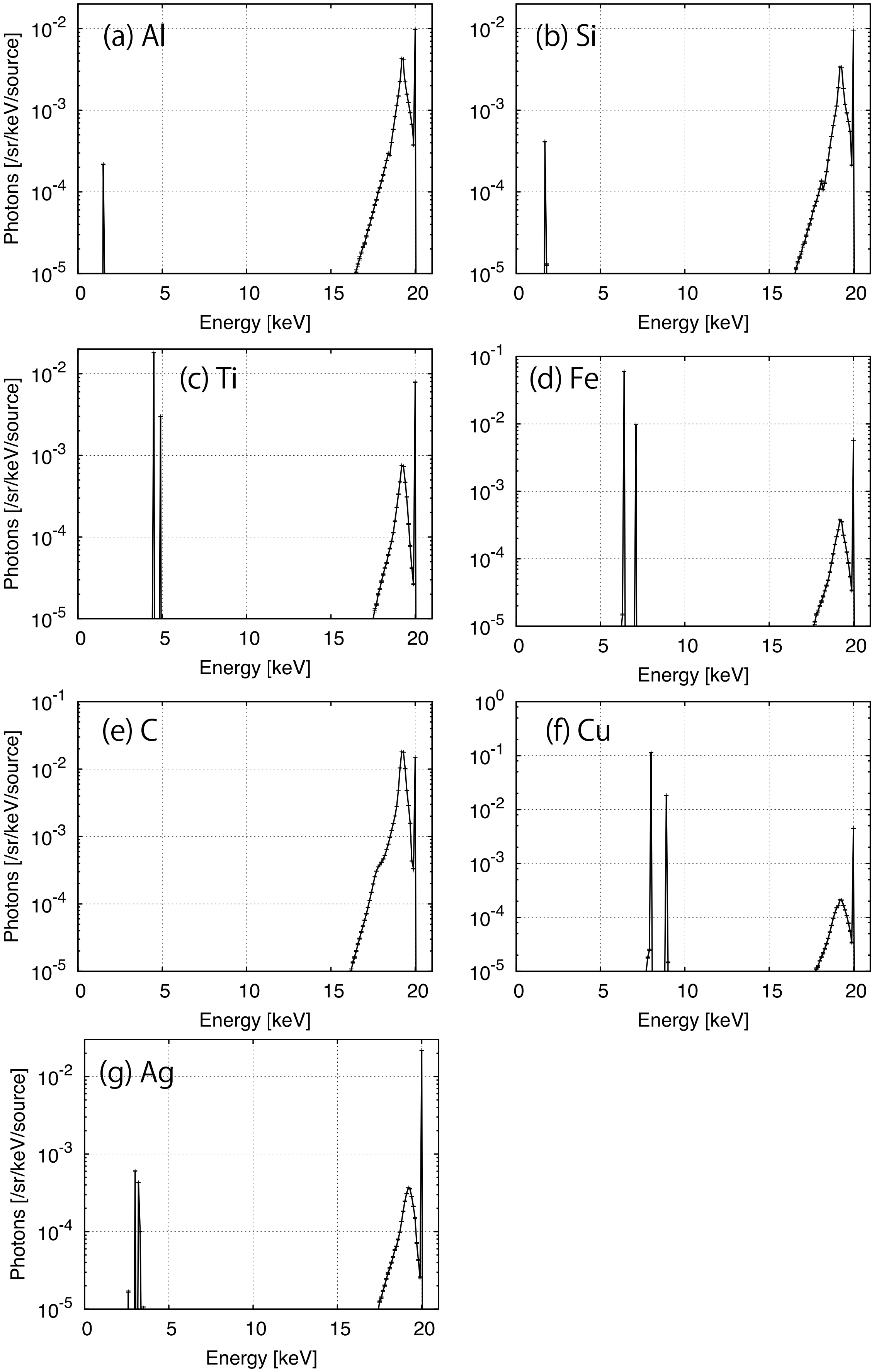

Figure 4: $\theta = 90^\circ$ scattered spectra when incident photon energies were 20 keV. Targets are (a) Al, (b) Si, (c) Ti, (d) Fe, (e) C, (f) Cu and (g) Ag.

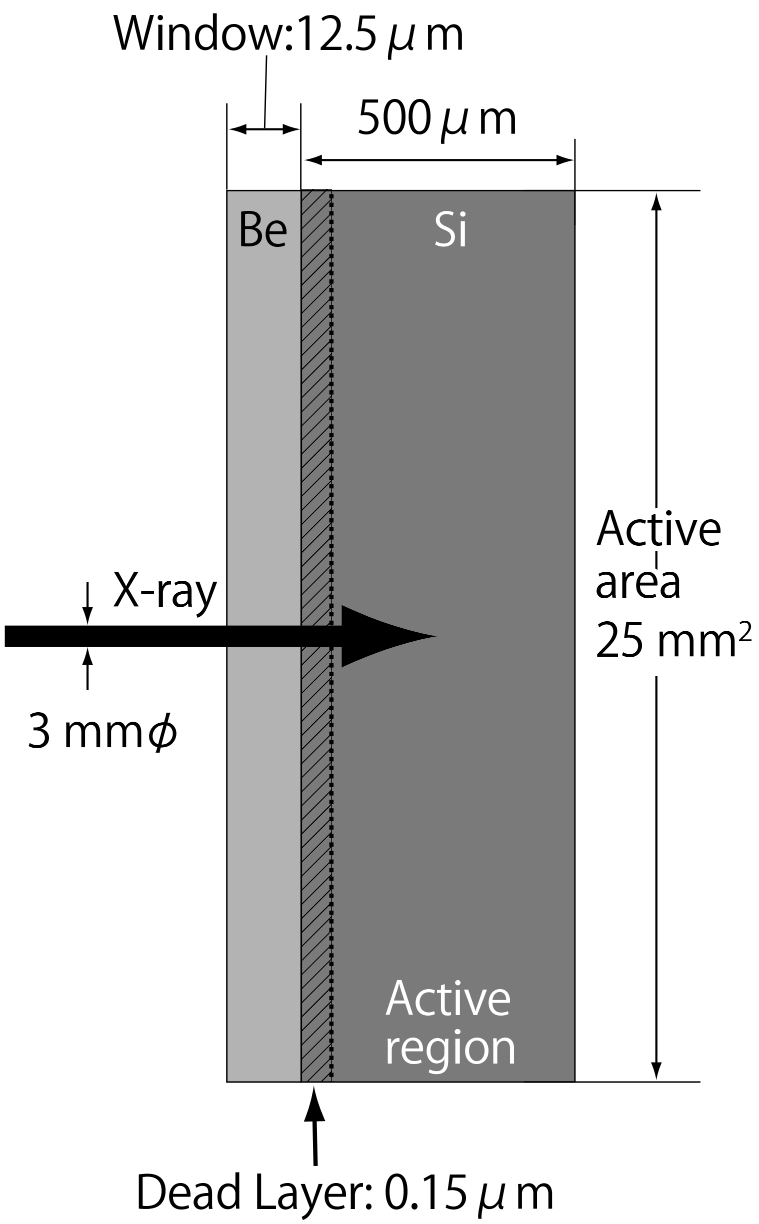

Figure 5: The geometry of the Si detector.

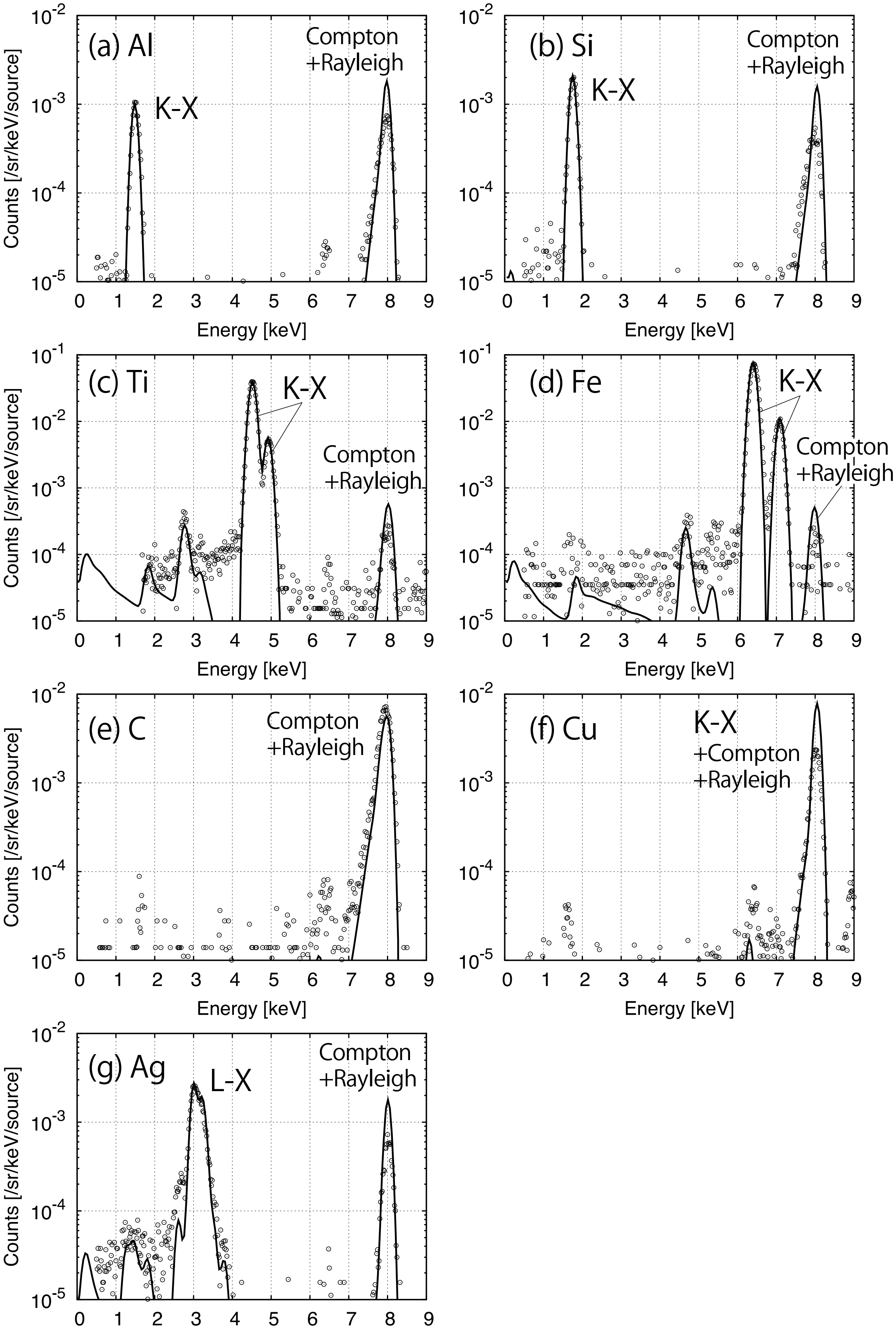

Figure 6: Comparison of the photon energy spectra for incident energy of 8 keV. Measurements are shown by open circles. EGS5 calculations are shown in lines. Targets are (a) Al, (b) Si, (c) Ti, (d) Fe, (e) C, (f) Cu and (g) Ag.

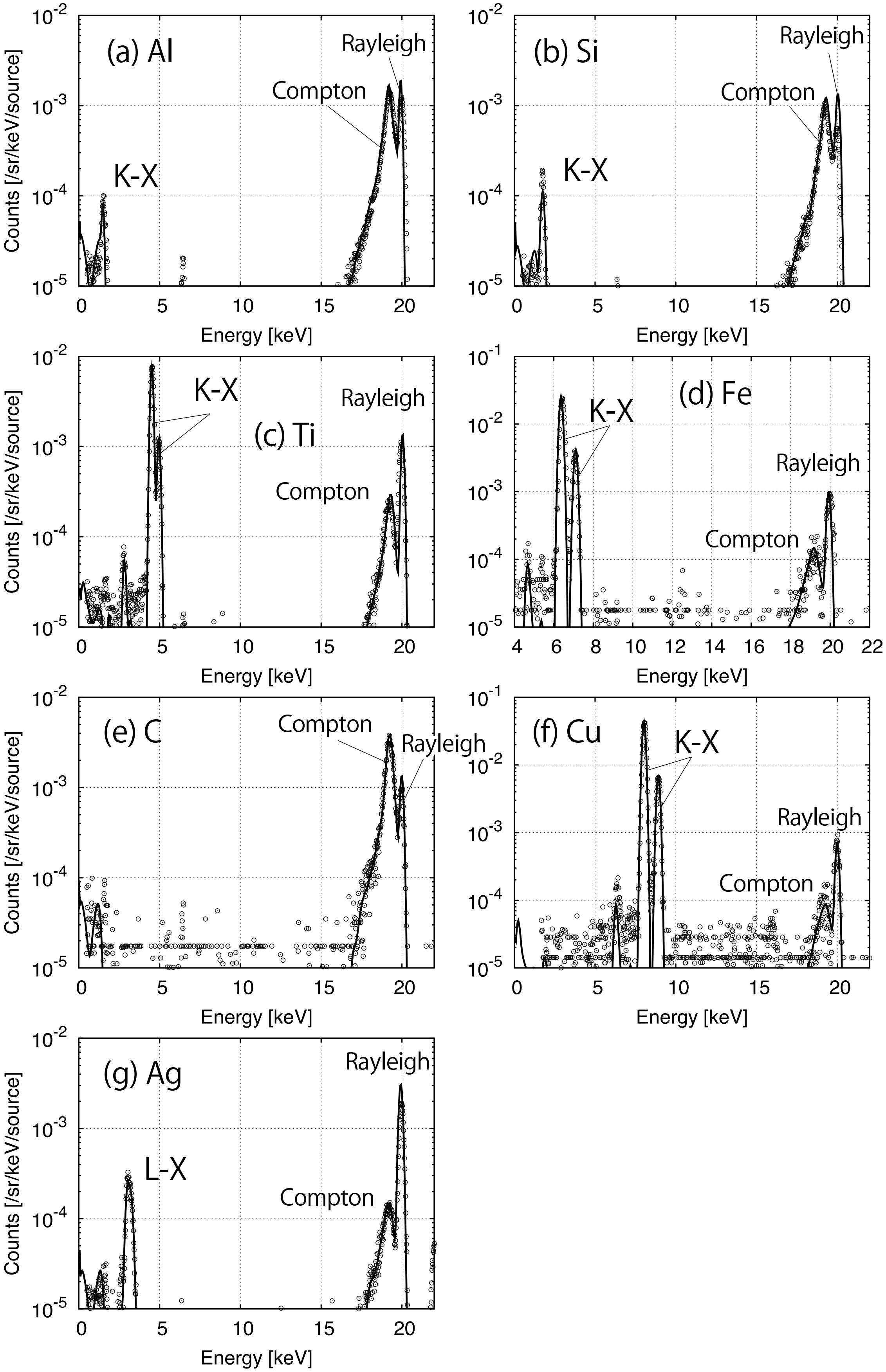

Figure 7: Comparison of the photon energy spectra for incident energy of 20 keV. Measurements are shown by open circles. EGS5 simulations are shown in lines. Targets are (a) Al, (b) Si, (c) Ti, (d) Fe, (e) C, (f) Cu and (g) Ag.

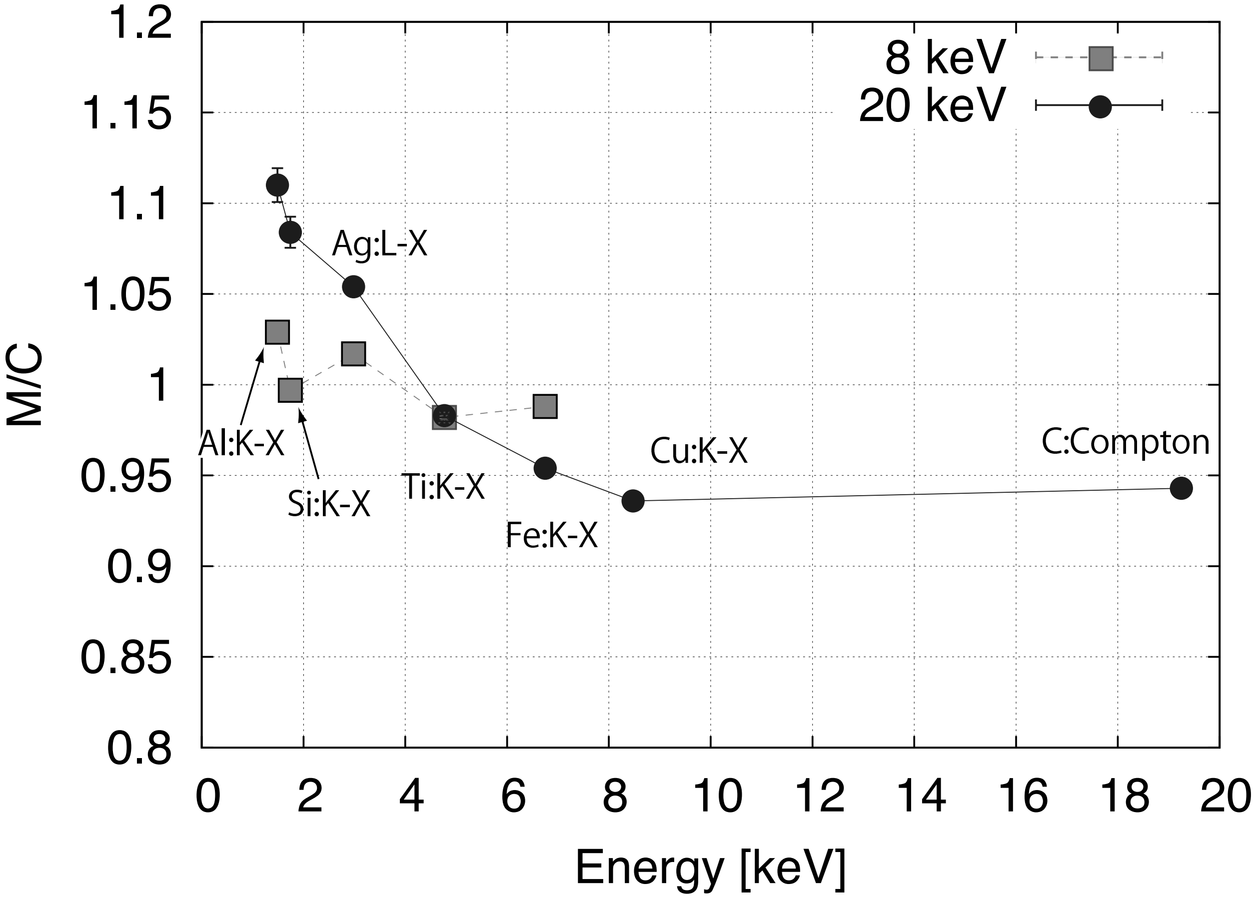

Figure 8: Ratio of measured and calculated intensity of each peak. The ratios for the incident energy of 20 keV are shown in filled circles. The ratios for the incident energy of 8 keV are shown in gray boxes.